

DISSERTATION

CHARACTERISTICS, SOURCES, AND FORMATION OF ORGANIC AEROSOLS IN THE
CENTRAL ROCKY MOUNTAINS

Submitted by

Misha Iris Schurman

Department of Atmospheric Science

In partial fulfillment of the requirements

For the Degree of Doctor of Philosophy

Colorado State University

Fort Collins, Colorado

Spring 2014

Doctoral Committee:

Advisor: Jeffrey L. Collett, Jr.

Sonia M. Kreidenweis

Charles S. Henry

Emily V. Fischer

Copyright by Misha Iris Schurman 2014

All Rights Reserved

ABSTRACT

CHARACTERISTICS, SOURCES, AND FORMATION OF ORGANIC AEROSOLS IN THE CENTRAL ROCKY MOUNTAINS

Particulate matter in the atmosphere has wide-ranging health, environmental, and climate effects, many of which are attributed to fine-mode secondary organic aerosols. High-altitude ecosystems in the Rocky Mountains are sensitive to increased nutrient, and particularly nitrogen, deposition, with documented changes in dominant diatom, lichen, and vegetative communities; visibility is also affected by fine particle pollution. Submicron particle size, composition, and source apportionment were explored at the Rocky Mountain and Grand Teton National Parks using a High-Resolution Time-of-Flight Aerosol Mass Spectrometer and Positive Matrix Factorization.

A July 2-August 31, 2010 campaign at Rocky Mountain National Park found low-concentration submicron particulate matter (max = $93.1 \mu\text{g}/\text{m}^3$, avg. = $5.13 \pm 2.72 \mu\text{g}/\text{m}^3$) of which $75.2 \pm 11.1\%$ is organic, with significant contributions from low-volatility (LV-OOA, 39.3% of PM_{10} on average) and semi-volatile oxidized organic aerosol (SV-OOA, 27.6%) punctuated by short, high-concentration biomass burning organic aerosol episodes (BBOA, 8.4%) associated with increased organic nitrogen. Nitrate (4.3%), sulfate (16.6%), and ammonium (3.9%), for which local sources are sparse, are enhanced with upslope (SW) surface winds from the densely populated Front Range; similar transport of oxidized organic aerosols is indicated by advanced oxidation and relative monodispersity (both indicative of ageing), correlation with inorganic anthropogenic tracers (LV-OOA with ammonium sulfate and SV-OOA with ammonium nitrate), and concentration correlation with upslope winds. A local BBOA source is suggested by cellulose combustion markers (m/z s 60 and 73) limited to brief, high-

concentration, polydisperse events (suggesting fresh combustion emission), a diurnal maximum at 22:00 LST, when campfires were set at adjacent summer camps, and surface wind associations consistent with local campfire locations. The particle characteristics and sources determined here represent typical conditions at the Rocky Mountain site based on analysis of inter-annual variability over the previous decade in meteorological patterns, PILS-IC, filter, and fire data.

Submicron particulate mass is lower at the Grand Teton site, averaging $2.08 \mu\text{g}/\text{m}^3$ (max = $21.91 \mu\text{g}/\text{m}^3$) of which 75.0% is organic; LV-OOA averages 48.9% of PM_{10} , with sporadic but higher-concentration BBOA events contributing another 26.1%. Sulfate (12.5%), ammonium (8.7%), and nitrate (3.9%) are low in mass. Oft-anthropogenic ammonium and sulfate have correlated time-series and association with upslope winds from the Snake River valley. A regionally disperse and/or *in situ* photochemical LV-OOA source is suggested by 1) afternoon concentration enhancement not correlated with upslope winds, anthropogenic NO_x , or ammonium sulfate, 2) smaller particle size and higher polydispersity during the day and in comparison to a biomass burning plume inferred to have travelled ~480 km, and 3) lower degree of oxidation than is usually observed in transported urban plumes. Organic nitrogen in the form of nitriles and/or pyridines is indicated during the day by CHN fragment spectra, with the addition of amines at night. Fires near Boise, ID may be the source of a high-concentration biomass-burning event on August 15-16, 2011 associated with W-SW winds (upslope from the Snake River Valley) and increased sulfate, ammonium, nitrate, and CHN fragments (nominally, amines).

Comparison of these campaigns to GEOS-Chem model simulations echoes the literature in which models under-predict organic aerosols; aqueous SOA formation is a possible, albeit poorly understood, explanation for this discrepancy. This motivates a comparison of aqueous

SOA (aqSOA) production in (1) ambient cloud water, (2) cloud water with pinonic acid added to simulate uptake of biogenic VOCs, and (3) single-precursor methylglyoxal and pinonic acid solutions; solutions were photooxidized using UVC light and added hydrogen peroxide (producing hydroxyl radical at cloud-relevant $[OH] = 4.5 \times 10^{-14}$ M) in a temperature-stabilized vessel and then continuously atomized, dried, and analyzed via AMS with 1-minute time resolution.

During photo-oxidation of cloud samples, organics increase in mass to 110-140% of the initial value and in level of oxidation (the ratio of m/z 44 (CO_2^+) to total organic aerosol mass, f_{44}) to $f_{44} \approx 0.23 \pm 0.05$, before decreasing in organic mass to 60-80% of the initial value. Decreases in organics are explained by chemical decomposition causing functional group loss in some experiments and volatile product formation in others. Pinonic acid addition appears to reduce organic mass losses and favor carbonyl formation. In contrast, the single-precursor solutions, which are similar to those used to understand aqSOA in the literature, gained 150-300% of initial organic concentrations, with a larger increase in O:C than observed in the (albeit already fairly oxidized) ambient cloud samples. Combined, these experiments illustrate an aqSOA production sequence in which organic mass is first gained through formation of lower-volatility carbonyls and acids and then either a) lost through molecular decomposition or volatile product formation, or b) maintained or increased further by addition of fresh precursors from the gas phase. These experiments also suggest that aqSOA formation in complex ambient cloud water is not well represented by the simple solutions often used for aqSOA parameterization and, further, that the rate of aqSOA production may decrease in a predictable way as oxygenation of organics increases. The high O:C and f_{44} ratios observed in aqueous SOA formed during the laboratory experiments are broadly consistent with the high degree of oxygenation in oxidized

organic aerosol (OOA) at Rocky Mountain and Grand Teton National Parks, though other mechanisms may also contribute to the observed aerosol characteristics.

ACKNOWLEDGEMENTS

My advisor, Dr. Jeff Collett, gave just the right amount of direction to keep this work on track while fostering individual inquiry, and is a font of knowledge and ideas, and an inspiring teacher. I will be always indebted for this opportunity to grow intellectually, use really cool instruments to explore interesting and relevant scientific questions, and work with such excellent people. Thank you.

Committee members Dr. Sonia Kreidenweis and Dr. Charles Henry guided this work with insightful recommendations and taught great classes, besides being all-around good folk. And thanks to Dr. Emily Fischer for joining my committee a little ‘late in the game’; her atmospheric modeling expertise helped tie this dissertation together.

I thank Dr. Taehyoung Lee deeply for his ongoing mentorship and encouragement, both scientific and personal, and for his tireless efforts in the field and lab to get great data, and for his patience as I learned to run the AMS. Ali Boris contributed long hours and rigorous thinking to the aqueous SOA experiments, and is a joy to work with.

Dr. Amy Sullivan was always (and I mean *anytime*) available for discussions and lab help, and cookies. I thank fellow students and especially Dr. Katie Benedict, Dr. Ezra Levin, Yi Li, and Ashley Evanski-Cole for their help and occasional commiseration. Everyone in the Collett and Kreidenweis groups has my thanks for their contributions to these projects.

Thank you Mom and Dad: for reading, for science camps and the microscope, for the freedom to be myself, for all the conversations (some of which were even technical!). Thanks to my late grandfather, Peter, and Grandma Judy for their support of my education, in all the forms it took. And most of all, thanks to Kevin for his support and for his patience, for his humor and playfulness, and for his total faith that I would get this done, eventually.

TABLE OF CONTENTS

Abstract.....	ii
Acknowledgements.....	vi
List of Tables.....	ix
List of Figures.....	xi
1. Background.....	1
1.1 Environmental Importance of Organic Aerosols.....	1
1.1.1 Climate Effects.....	4
1.1.2 Ecosystem and Health Effects.....	7
1.2 Organic Aerosol Formation and Ageing.....	9
1.2.1 SOA Formation from Condensing Oxidized Vapors.....	9
1.2.2 Evidence for the Importance of Aqueous SOA.....	16
1.2.3 Aqueous SOA Formation and Oxidation.....	19
1.3 Common Organic Aerosol Types and Identification Thereof.....	33
1.3.1 Aerosol Instrumentation.....	33
1.3.2 Identifying Types of Organic Aerosol: Factorization Techniques.....	40
1.3.3 Changes in Organic Composition: Elemental and Fragment Analyses.....	47
1.3.4 Aerosol Organic Nitrogen.....	53
1.3.5 Organic Aerosol Source Apportionment Using Meteorological Data.....	57
2. Methods.....	61
2.1 The High Resolution Time-of-Flight Aerosol Mass Spectrometer.....	61
2.1.1 AMS Calibrations and Instrumental Quality Control.....	64
2.1.2 Data Analysis.....	67
2.2 Positive Matrix Factorization.....	73
2.3 Aqueous SOA Experiments.....	77
3. Organic Aerosol Sources and Characteristics: Rocky Mountain National Park.....	86
3.1 Sampling Site Overview.....	86
3.2 General Particle Composition and Concentration.....	87
3.3 PMF-Derived Organic Aerosol Factors.....	91
3.4 Elemental Analysis and Organic Nitrogen.....	96
3.5 Particle Size.....	101

3.6	Source/Transport Analysis	104
3.7	Episode Analysis	112
3.8	Rocky Mountain National Park Summary and Conclusions.....	113
4.	Organic Aerosol Sources and Characteristics: Grand Teton National Park	116
4.1	Sampling Site	116
4.2	General Particle Composition and Concentration	118
4.3	PMF-Derived Organic Aerosol Factors	122
4.4	Elemental Analysis.....	128
4.5	Organic Nitrogen	132
4.6	Particle Size	135
4.7	Meteorological Analysis	136
4.8	Grand Teton National Park Summary and Conclusions	140
5.	Aqueous SOA Photo-oxidation Experiments	143
5.1	Ambient Cloud-water Photo-oxidations.....	155
5.2	Ambient Cloud-water Photo-oxidations with added Pinonic Acid Precursor.....	172
5.3	Single-Precursor Photo-oxidations: Methylglyoxal	182
5.4	Single-Precursor Photo-oxidations: Pinonic Acid.....	191
5.5	Aqueous Photo-Oxidation Conclusions	198
6.	Conclusions.....	209
6.1	Summary and Conclusions.....	209
6.2	Recommendation for Future Work	216
7.	References.....	221
8.	Appendices.....	268
8.1	AMS Instrument Function Summaries and Calibration Protocols.....	268
8.2	AMS Calibration and Data Analysis Protocols.....	269
8.3	Supporting ROM and TET Data Analyses.....	286
8.4	Alternate PMF Solutions	288
8.5	Ambient Cloud Sample Concentrations of Precursors, Oxidants, etc.....	290
8.6	On the calculation of f_{44} and f_{43} ; Additional Data Visualizations.....	291
8.7	Additional Visualizations of Aqueous Photo-oxidation Experiments	292
8.8	Normalized Family Mass Spectra	293

LIST OF TABLES

Table 1-1: Comparisons between the AMS (y) and various continuous-measurement instruments (x) for sulfate, ammonium, nitrate, organic values, and total mass. Multiple slope and correlation coefficient values indicate multiple data sets or replicates within the given reference. *HSPH: Harvard School of Public Health continuous sulfate monitor. ** (Khlystov et al. 1995). 39

Table 1-2: Published elemental ratios for given sampling conditions and/or PMF factor. *Ng e al. (2010) summarizes 43 ambient AMS datasets worldwide..... 53

Table 2-1: Measured detection limits for the given mass spectrometer mode and species; the averaging time is given by the reference. 64

Table 2-2: Experimental conditions, name, and concentration of added precursors, if applicable: ammonium nitrate (AN) and ammonium sulfate (AS; always added with AN), and/or pinonic acid (PA) or methylglyoxal (MG). Total Organic Carbon (TOC) is also included. * MGB2 & 4 not included due to instrument malfunction. In the RH column, “-“ indicates missing data, and “~0” is at or below the detection limit of the monitor. Multiple values are from replicates of the given experiment (indicated in “Name” column). 82

Table 3-1: July-August average \pm standard deviation concentrations of particulate species in $\mu\text{g}/\text{m}^3$. IMPROVE data are averaged over 1991-2012, and were accessed via the VIEWS database on 22 January 2014. *(Benedict et al. 2013) **Averaged over 2005-2012..... 89

Table 3-2: Time-series correlation coefficients (r^2) between inorganic species and organic factors calculated using the IGOR linear regression algorithm. 89

Table 3-3: Study-average component concentrations from the HR-ToF-AMS during upslope ($120\text{-}225^\circ$) and downslope ($1\text{-}120^\circ$ & $225\text{-}360^\circ$) winds, with the ratio of average upslope to average downslope concentrations; ‘G-Chem Denver PBL’ shows study-average component concentrations from the two Denver surface grid boxes thought to be a source area transported by upslope winds, while ‘G-Chem RMNP FT’ data is from the grid box immediately above the planetary boundary layer located over RMNP, representing the content of ‘free tropospheric’ aerosol during downslopes..... 111

Table 4-1: Correlations (r^2) between temporal concentration variations of given particle constituent pairs; NH_4^* refers to mass of ammonium exceeding that in stoichiometric balance with sulfate. ON_{min} is defined in Section 4.5..... 120

Table 4-2: Study-average component concentrations from the HR-ToF-AMS during upslope ($135\text{-}315^\circ$) and downslope ($316\text{-}360$ & $0\text{-}134^\circ$) winds, with the ratio of average upslope to average downslope concentrations; ‘G-Chem PBL’ shows study-average component concentrations from the Grand Teton surface grid box, while ‘G-Chem FT’ data is from the grid box immediately above the planetary boundary layer over the Grand Teton site. 139

Table 5-1: Total organic carbon carbon (TOC, $\mu\text{g}/\text{L}$) in the given ambient cloud water (TaiOx, abbreviated to ‘T’ below), pinonic acid (PA), or methylglyoxal (MG) sample solution. *Due to low sample volume, TaiOx1 is a combination of three cloud samples; TOC and pH are

estimated using averages of the three samples and assuming equal volumes. For all other samples, solute addition, etc. relied on grade-A graduated cylinders for volume determination. 143

Table 5-2: Fragments used as indicators of chemical composition; the unit mass resolution bin (m/z) is followed by the fragment formula (in parentheses) and species or compound type possibilities. Note that a given fragment may come from a variety of parent compounds; the indicated fragment does not necessarily exist in the particle phase, but may indicate the types of parent compounds present. Methylglyoxal is abbreviated 'MG.' 152

Table 5-3: Summary of delta values indicated fragments and/or functional groups, adapted from McLafferty & Turecek (1993). 153

Table 8-1: Rocky Mountain thresholds for 'high' concentrations (inclusive) used in the Conditional Probability Function equal the component average plus one standard deviation. Thresholds vary between wind levels because averaging times for components were different (to match wind data availability); longer averaging times damp the amplitude of high-concentration events, requiring different thresholds to define the same high-concentration event..... 268

LIST OF FIGURES

Figure 1-1: “Global mean RFs from the agents and mechanisms discussed in this chapter, grouped by agent type. Anthropogenic RFs and the natural direct solar RF are shown. The plotted RF values correspond to the bold values in Table 2.12. Columns indicate other characteristics of the RF; efficacies are not used to modify the RFs shown. Time scales represent the length of time that a given RF term would persist in the atmosphere after the associated emissions and changes ceased. No CO ₂ time scale is given, as its removal from the atmosphere involves a range of processes that can span long time scales, and thus cannot be expressed accurately with a narrow range of lifetime values. The scientific understanding shown for each term is described in Table 2.11.” (IPCC 2007)	6
Figure 1-2: Schematic of gaseous, particle phase, and aqueous phase SOA formation pathways adapted from Fuzzi & Andreae (2006) and Pöschl (2011).	11
Figure 1-3: Time series of inorganic particulate components from HR-ToF-AMS, PILS-IC, and URG (denuder-filter system) from July-August, 2010, at Rocky Mountain National Park (Chapter 3).	40
Figure 1-4: “Schematic diagram of bilinear factor analysis of a mass spectral matrix of an organic aerosol (ORG). The time series of the factors (ts_n) make up the matrix TS and the mass spectra of the factors (ms_n) make up the matrix MS. The differences between the measurements and the modeled results are represented as the residual matrix E.” (Zhang et al. 2011)	42
Figure 1-5: “Spectra of...PMF factors (interpreted as the denoted source profiles) calculated by...PMF.” (Lanz et al. 2007)	47
Figure 1-6: f_{43} versus f_{44} triangle diagram with typical ranges for given organic aerosol or data type from the literature, adapted from Ng et al. (2011).	48
Figure 1-7: The van Krevelen diagram with transposed ‘ambient triangle’ from Ng et al. (2011) and regions typically inhabited by the given OA type. Dashed red lines and red numbers are oxidation states of carbon ($OS_c=2*O:C-H:C$, Kroll et al. 2011); grey lines are +/- 20% error on the bounds of the triangle, from general AMS quantification error.	52
Figure 2-1: Study-average differential mobility particle sizer (DMPS) particle volume distributions (analogous to mass assuming uniform particle density) during the Rocky Mountain and Grand Teton National Parks field campaigns. The size range of near-unity transmission through the aerodynamic lens is shown in dashed red lines.	61
Figure 2-2: “Peak [resolution] comparisons for the four versions of the AMS” (Reproduced with permission from Decarlo et al. 2006). (a) Red boxes indicate the integration area for unit mass resolution data; (b) grey bars indicate exact masses of resolved fragments in HR data (at m/z 43, for example).	63
Figure 2-3: Airbeam correction factor timelines for the Rocky Mountain and Grand Teton National Parks studies. The vertical blue lines denote reference periods (selected directly after an IE calibration) used to determine the IE/AB ratio used in the airbeam correction	

factor calculation. In general, the ‘line’ of values with higher values is V-mode, which the lower is from the W-mode.	68
Figure 2-4: Residual time-lines (blue markers, in ppm) for all fragments used in m/z calibrations for (left) Rocky Mountain National Park, (center) Grand Teton National Park, and (right) the cloud water oxidation experiments. Red lines show ± 10 ppm.	69
Figure 2-5: Comparison of organics (green), sulfate (red) and nitrate (blue) concentrations from low-resolution (UMR; "Sq...") and high-resolution ("Pika ...") data from the Rocky Mountain National Park study.	70
Figure 2-6: Residuals from PMF mass reconstruct for each m/z (left) and as a histogram for example organic fragment CH_3^+ (right), for Rocky Mountain and Grand Teton National Parks studies. The difference in histogram bin width reflects the updated PMF Evaluation Tool (PET) version used for the Tetons. Boxes are the mean; whiskers 5 th and 95 th percentiles....	76
Figure 2-7: Schematic of experimental setup for bulk aqueous-phase photo-oxidation.	78
Figure 2-8: Normalized Organics/Sulfate and f_{44} (m/z_{44} /Organics) for dark (‘baseline’), photolytic, and hydrogen peroxide control experiments with conditions as noted in the legends; error bars are $\pm 28\%$ based on propagation of AMS quantification error. The remaining TaiOx samples are omitted for brevity.	85
Figure 3-1: Map showing the Rocky Mountain National Park sampling site (red star). Boulder, Denver, and other cities form the Front Range urban corridor to the east.....	86
Figure 3-2: Study-average diurnal variation of ambient temperature (red dashed line, left axis) and surface wind direction (blue line, right axis).	87
Figure 3-3: Time series of inorganic components, total organics, and organic factors (LV-OOA, SV-OOA, and BBOA) in $\mu\text{g}/\text{m}^3$. Potassium (K+) is from 17-minute-average PILS-IC samples. Pie chart shows study-average contributions for each component; the green outline contains total organics.....	88
Figure 3-4: Study-average diurnal concentrations of particulate sulfate, nitrate, ammonium, total organics, BBOA, LV-OOA, SV-OOA, $\text{C}_2\text{H}_3\text{O}^+$ (m/z 43), $\text{C}_3\text{H}_3\text{O}^+$ (m/z 55), and $\text{C}_2\text{H}_4\text{O}_2^+$ (m/z 60, levoglucosan). Solid lines are means, with $\pm 20\%$ error bars reflecting AMS quantitation error. Dashed lines are 25 th and 75 th percentiles.	90
Figure 3-5: Normalized mass spectra of organic aerosol types determined by Positive Matrix Factorization (Paatero and Tapper, 1994): Biomass Burning Organic Aerosol (BBOA), Semi-Volatile Oxidized Organic Aerosol (SV-OOA), and Low Volatility Oxidized Organic Aerosol (LV-OOA).	91
Figure 3-6: Van Krevelen-triangle diagram for time periods dominated by the given factor (as defined in Section 3.3) and for all data points. Estimated oxidation state, $\text{OS}_c \approx 2 \cdot \text{O}:\text{C}:\text{H}:\text{C}$ (Kroll et al. 2011). Red and blue lines indicate the region usually inhabited by ambient data in the f_{43} vs f_{44} plot; grey lines represent 10% error. The grey ellipse represents the typical range of ‘HOA’ factors. a: +alcohol/peroxide, $m = 0$; b: carboxylic acid + fragmentation, $m = -0.5$; c: +carboxylic acid (no fragmentation), $m = -1$; d: +ketone/aldehyde, $m = -2$ (Ng et al. 2011).	97

Figure 3-7: Time series showing select elevated-ON _{min} periods with inorganics and other organic factors from the Rocky Mountain National Park site.	99
Figure 3-8: Rocky Mountain study-average mass spectrum of CHN fragments.	100
Figure 3-9: A) Mode of the log normal size distribution fit for the indicated species or total organics during time periods dominated by the color-designated organic factor; error bars are estimations of size-dependent PToF error, compounding chopper broadening and calibration-particle size standard deviation (Supplementary Section 2). B) Log-normal width parameter with error bars equaling one standard deviation of the lognormal fit. Ammonium concentrations were too low during BBOA events for size determination.	102
Figure 3-10: 1-hour average concentrations ($\mu\text{g}/\text{m}^3$) of organic aerosol types with surface wind direction. Raw data are colored by species, average concentrations over the sixteen 22°30' wind direction bins are shown in purple, and black lines indicate the Conditional Probability Function (CPF multiplied by 10; threshold definitions in Table S1). The number of data points in each bin is shown in the lower left-hand panel.	107
Figure 3-11: 3-hour average concentrations of aerosol components with 700mb wind direction. Raw data are colored by species, average concentrations over sixteen 22°30' wind direction bins are shown in purple, and black lines indicate the Conditional Probability Function (CPF multiplied by 10, see thresholds in Table S1). The number of data points in each bin is shown in the lowest left panel.	109
Figure 3-12: A timeline subset of particle components from Rocky Mountain AMS measurements (traces, 5-minute average), GEOS-Chem free troposphere predictions (stars, 1-hour), and GEOS-Chem boundary layer predictions (horizontal bars, 1-hour), color-identified by axis; warm colors indicate upslope wind direction (colored diamonds, teal axis), while teal indicates downslope flow. Vertical lines indicate midnight (00:00 LST).	112
Figure 3-13: Timeline of species and relevant organic factor concentrations for 7-11 July 2010, plotted with 1-hour surface wind direction at the site (teal diamonds). Wind directions 90 through 180 degrees denote up-valley winds and are demarcated by dashed red lines and warm-colored diamonds. BBOA* is calculated using the six-factor reconstructions outlined in Section 3.2.	113
Figure 4-1: Map showing GrandTReNDS study site (point A).	117
Figure 4-2: Diurnal averages over AMS sampling duration of a) meteorological values ambient temperature (C), relative humidity (%), and wind direction (degrees), and b) gaseous NH ₃ , NO, NO _x , and NO _y concentrations (ppb) and particle number concentration (CN; #/m ³). Data from Tony Prenni (Prenni et al. in review).	118
Figure 4-3: Timeline of total organics (green, right axis), sulfate (red), ammonium (yellow), nitrate (dark blue), and 'excess' ammonium (NH ₄ [*] , purple) from the HR-ToF-AMS during the GrandTReNDS study. Concentrations are in $\mu\text{g}/\text{m}^3$	119
Figure 4-5: Diurnally averaged concentrations of inorganic species, total organics, and organic PMF factors (introduced below), where the solid line is the concentration mean and the	

dashed lines are 25 th and 75 th percentiles. Error bars represent 20% mass quantification error in the AMS. Concentrations are in $\mu\text{g}/\text{m}^3$	122
Figure 4-6: Mass spectra of LV-OOA and BBOA factors derived from application of PMF to high-resolution Grand Teton National Park AMS data.	123
Figure 4-7: Timelines of LV-OOA (pink) and BBOA (green) PMF organic factors and inorganics at the Grand Teton site, in $\mu\text{g}/\text{m}^3$. The pie chart depicts study average mass contributions from each component, with total organics outlined in green.....	124
Figure 4-8: Map of MODIS fire detections (yellow dots) on August 14, 2011 at 13:00 LST (height of fire intensity) from the United States Forest Service (USFS 2013); the red star is the AMS measurement site.	126
Figure 4-9: f_{43} versus f_{44} diagram featuring the August 15, 2011 biomass burning event and interesting periods during the day (1 August, 2011) and night (28 July, 2011). Ellipses indicate the approximate ranges of HOA (purple), SV-OOA (grey), and LV-OOA (pink) data in the literature (Ng et al. 2011).....	127
Figure 4-10: van Krevelen diagram showing GrandTREnds data. ‘Day’ and ‘Night’ are all data from 12:00-18:00 LST and 21:00-5:00 LST, respectively. Red and blue lines indicate the region usually inhabited by ambient data in the f_{43} vs f_{44} plot; grey lines represent 10% error. Purple ellipse: typical range of of HOA; grey ellipse = SV-OOA; pink ellipse = LV-OOA. Dashed red lines: estimated oxidation state, $\text{OSc}=2*\text{O}:\text{C}-\text{H}:\text{C}$ (Kroll et al. 2011); see Section 1.3.3. Dashed grey lines: slopes of various reaction regimes; see Section 1.3.3.....	130
Figure 4-11: Elemental ratio diurnal averages for (left) the total dataset and (right) a subset from 7:00 LST July 27 - 7:00 LST July 30. Bars depict error on elemental analysis: O:C (31%), H:C (10%), N:C (22%) and OM:OC (6%, Aiken et al. 2007).....	131
Figure 4-12: Mass spectra of $\text{C}_x\text{H}_y\text{O}_z\text{N}^+$ fragments averaged over all runs for the indicated time period during the Grand Tetons campaign. “BBOA event” refers to the higher-concentration August 15 episode.....	133
Figure 4-13: Mass spectra of $\text{C}_x\text{H}_y\text{N}^+$ fragments averaged over all runs for the indicated time period during the Grand Tetons campaign.....	134
Figure 4-14: The a) mode and b) width parameter of the lognormal fit of the average size distribution for the given component (text marker) and time period (color). ‘Day’ data averaged over 12:00-18:00 LST; ‘Night’ data averaged over 21:00-5:00 LST. Error bars on modes are error on PToF size determination as outlined in Section 2.1.2; error bars on width parameters are the standard deviation of the width parameter fit.....	135
Figure 4-15: Wind roses showing raw component concentration (colored by given component), concentration average within each of 16 wind bins (purple line), and conditional probability function in each bin (black line). Concentrations are in $\mu\text{g}/\text{m}^3$	137
Figure 4-16: Timeline showing PMF factor and inorganic component concentrations with wind speed and direction (degrees) during a subset of the Grand Teton field campaign. Concentrations are in $\mu\text{g}/\text{m}^3$	138

- Figure 4-17:** A timeline subset of particle components from Grand Teton AMS measurements (traces, 5-minute average), GEOS-Chem free troposphere predictions (stars, 1-hour), and GEOS-Chem boundary layer predictions (horizontal bars, 1-hour), color-identified by axis; warm colors indicate upslope wind direction (colored diamonds, teal axis), while teal indicates downslope flow. Vertical lines indicate midnight (00:00 LST). 140
- Figure 5-1:** Example experiment timelines showing (a) a full photo-oxidation with mass ‘spikes,’ (b) a ‘baseline’ period with increasing RH, (c) a ‘baseline’ period with steady RH (≈ 0), and (d) a full photo-oxidation with more constant output. 144
- Figure 5-2:** TaiOx: Timelines of normalized (to $t = 0$) Org/SO₄ (green) and f_{44} (red) for TaiOx 1, 2, 3, 4-1, and 7 aqueous photo-oxidations. Error bars equal 28% of the value, from propagation of 20% AMS quantification error through the indicated calculations. Experiment time approximates ambient oxidation time as discussed in Section 2.3. 156
- Figure 5-3:** TaiOx: f_{43} (mz_{43}/Org) vs. f_{44} (mz_{44}/Org) for TaiOx 1-3 and 7; the blue- and red-bounded triangle represents the range of values typically inhabited by ambient aerosols (Ng et al. 2011). 157
- Figure 5-4:** Timelines of normalized (to $t=0$ value) fragment ratios indicating level of oxidation or relative abundance of carboxylic acids (CO₂/SO₄) for TaiOx1f1, TaiOx2f1, TaiOx3f1, and TaiOx4f1. Error bars represent propagated 20% relative error for AMS mass quantitation (total propagated error = 28%). 159
- Figure 5-5:** Total organic difference mass spectra calculated via subtraction of normalized experiment beginning 5-minute average organic spectrum from experiment end spectrum. Green indicates *relative* increase of the given m/z at experiment’s end, while red indicates a decrease. 163
- Figure 5-6:** TaiOx fragment-family difference mass spectra, subtracting the normalized 5-minute average spectrum from $t=0$ from that at the experiment’s end. 165
- Figure 5-7:** TaiOx: Total normalized signal in fragments with the given delta (Δ) value in the 5-minute average experiment beginning or end total organic mass spectrum. Error bars are the normalized average signal error over all mass bins for the given experiment. 166
- Figure 5-8:** Nitrogen-to-Carbon vs Oxygen-to-Carbon ratios for ambient cloud sample aqueous photo-oxidations. Turquoise points represent baseline periods (no UV, no H₂O₂) for corresponding sample shape. Linear fits: TaiOx1: $m = 0.06$, $r^2 = 0.85$; TaiOx2: $m = 0.15$, $r^2 = 0.55$; TaiOx3: $m = 0.00$, $r^2 = 0.00$; TaiOx7: $m = 0.05$, $r^2 = 0.21$; TaiOx4-1: $m = -0.02$, $r^2 = 0.10$; TaiOx4-2: $m = -0.01$, $r^2 = 0.01$; TaiOx4-3: $m = -0.03$, $r^2 = 0.08$ 169
- Figure 5-9:** van Krevelen diagram showing (left) TaiOx1-3 full photo-oxidations and (right) TaiOx4 replicates 1-3 & TaiOx7, colored by time during experiment. Dashed red lines: Estimated oxidation state, $\text{OSc} = 2 * \text{O} : \text{C} - \text{H} : \text{C}$ (Kroll et al. 2011). Red and blue lines indicate the region usually inhabited by ambient data in the f_{43} vs f_{44} plot; grey lines represent 10% error. Linear fits: TaiOx1: $m = -0.52$, $r^2 = 0.87$ (w/out three ‘outlier’ points at exp. end: $m = 0.00$, $r^2 = 0.00$); TaiOx2: $m = -0.53$, $r^2 = 0.51$ (w/out four ‘outlier’ points at exp. end: $m = -0.36$, $r^2 = 0.70$); TaiOx3: $m = -0.28$, $r^2 = 0.64$; TaiOx7: $m = -0.33$, $r^2 = 0.14$. Linear fits:

TaiOx 4-1: $m = -0.51, r^2 = 0.46$; TaiOx 4-2: $m = -0.65, r^2 = 0.48$; TaiOx 4-3: $m = -0.65, r^2 = 0.57$	171
Figure 5-10: TaiOxPA: Timelines of Org/SO ₄ (red) and <i>f</i> ₄₄ (green) for TaiOx6PA, 7, and 7PA aqueous photo-oxidations. Error bars are not included for simplicity but equal ~28% as propagated through the indicated calculations.....	172
Figure 5-11: TaiOxPA: Timelines of normalized (to t=0 value) fragment ratios indicating level of oxidation including relative abundance of carboxylic acids (CO ₂ ⁺ /SO ₄) for TaiOx6PAf1, TaiOx7PAf1, and TaiOx7f1. Error bars represent propagated 20% relative error for AMS mass quantitation (total propagated error = 28%).	173
Figure 5-12: TaiOxPA: <i>f</i> ₄₃ (mz43/Org) vs. <i>f</i> ₄₄ (mz44/Org) for TaiOx6PA, 7, and 7PA; the blue- and red-bounded triangle represents the range of values typically inhabited by ambient aerosols (Ng et al. 2011).	174
Figure 5-13: TaiOxPA: Normalized total organic difference mass spectra calculated via subtraction of experiment beginning 5-minute average organic spectrum from experiment end spectrum. Green indicates <i>relative</i> increase of the given <i>m/z</i> at experiment's end, while red indicates a decrease.....	175
Figure 5-14: TaiOxPA: TaiOx6PA, 7, and 7PA normalized fragment-family difference mass spectra calculated via subtraction of experiment beginning 5-minute average spectrum from experiment end spectrum.	176
Figure 5-15: TaiOxPA: Total normalized signal in fragments with the given delta (Δ) value in the 5-minute average experiment beginning or end total organic mass spectrum.....	177
Figure 5-16: Nitrogen-to-Carbon vs. Oxygen-to-Carbon ratios for aqueous photo-oxidation of ambient cloud samples with and without added pinonic acid. Turquoise points represent baseline periods (no UV, no H ₂ O ₂) for corresponding sample shape. Linear fits: TaiOx6+PA: $m = -0.001, r^2 = 0.00$; TaiOx7: $m = 0.05, r^2 = 0.21$; TaiOx7+PA: $m = -0.02, r^2 = 0.02$	177
Figure 5-17: Van Krevelen diagram showing (left) TaiOx6PA, and (right) TaiOx7PA and TaiOx7 full photo-oxidations, colored by time during experiment. Linear fits: TaiOx6PA: $m = -0.65, r^2 = 0.52$; TaiOx7: $m = -0.32, r^2 = 0.14$; TaiOx7PA: $m = -0.45, r^2 = 0.26$	179
Figure 5-18: MG/MGIN: Timelines of normalized Org/SO ₄ (MGIN) or total organics (MG) and <i>f</i> ₄₄ for methylglyoxal (MG) and methylglyoxal + inorganics (MGIN) aqueous photo-oxidations.....	183
Figure 5-19: MG/MGIN: <i>f</i> ₄₃ (mz43/Org) vs. <i>f</i> ₄₄ (mz44/Org); the blue- and red-bounded triangle represents the range of values typically inhabited by ambient aerosols (Ng et al. 2011). Linear fits: MGfull1: $m = -1.01, r^2 = 0.87$; MGfull2: $m = -1.34, r^2 = 0.65$; MGINfull1: $m = -2.14, r^2 = 0.85$	184
Figure 5-20: MG/MGIN: Timelines of normalized (to t=0 value) fragment ratios indicating relative abundance of carbonyl compounds (C ₂ H ₃ O/SO ₄), carboxylic acids (CO ₂ /SO ₄), C ₂ H ₃ O ⁺ /C ₄ H ₇ ⁺ (ratio of most to least oxidized fragment at <i>m/z</i> 43), and CH ₂ O ₂ ⁺ /SO ₄ (nominally formic acid) for methylglyoxal experiments with inorganics (MGIN); ratios are	

calculated with total organics in the denominator for experiments without inorganics (MG). Formic acid is measured on the blue right-hand axes for MGfull1 and 2.	185
Figure 5-21: MG/MGIN: Normalized total organic difference mass spectra calculated via subtraction of experiment beginning 5-minute average organic spectrum from experiment end spectrum. Green indicates relative increase of the given m/z at experiment's end, while red indicates a decrease.....	186
Figure 5-22: MG/MGIN: Normalized fragment-family difference mass spectra calculated via subtraction of experiment beginning 5-minute average spectrum from experiment end spectrum. Green indicates relative increase of the given m/z at experiment's end, while red indicates a decrease. The CHON family was omitted in MGfull2 (top panel) because it contained negligible mass.	187
Figure 5-23: MG/MGIN: Total normalized signal in fragments with the given delta (Δ) value in the 5-minute average experiment beginning or end total organic mass spectrum.....	190
Figure 5-24: MG/MGIN: Van Krevelen diagram showing methylglyoxal + inorganics (MGIN, left panel) and methylglyoxal (MG, in replicate, right panel) photo-oxidations colored by time during experiment. Linear fits: MG1: $m = -0.72, r^2 = 0.93$; MG2: $m = -0.56, r^2 = 0.97$; MGIN: $m = -0.55, r^2 = 0.97$	189
Figure 5-25: MG/MGIN: Nitrogen-to-Carbon vs. Oxygen-to-Carbon ratios for (left) methylglyoxal + inorganics and (right) methylglyoxal-only aqueous photo-oxidation. Linear fits: MGIN: $m = -0.01, r^2 = 0.26$; MG1: $m = 0.00, r^2 = 0.00$; MG2: $m = -0.01, r^2 = 0.28$	190
Figure 5-26: PA/PAIN: Timelines of normalized Org/SO ₄ (for PAIN) or total organics (for PA), and f_{44} for pinonic acid and pinonic acid + inorganics aqueous photo-oxidations. PA organics are normalized to their $t = 0$ value. Error bars are 28% error from propagated 20% AMS quantification error on each measured quantity (SO ₄ , Org, etc.).	192
Figure 5-27: PA/PAIN: Timelines of normalized (to $t=0$ value) fragment ratios indicating relative abundance of carbonyl compounds (C ₂ H ₃ O/SO ₄), carboxylic acids (CO ₂ /SO ₄), C ₂ H ₃ O ⁺ /C ₄ H ₇ ⁺ (ratio of most to least oxidized fragment at m/z 43), and CH ₂ O ₂ ⁺ /SO ₄ (nominally formic acid) for pinonic acid aqueous photo-oxidations with inorganics (PAIN); ratios are calculated with total organics in the denominator for experiments without inorganics (PA).	193
Figure 5-28: PA/PAIN: Normalized total organic difference mass spectra calculated via subtraction of experiment beginning 5-minute average organic spectrum from experiment end spectrum. Green indicates relative increase of the given m/z at experiment's end, while red indicates a decrease.....	195
Figure 5-29: PA/PAIN: Normalized fragment-family difference mass spectra calculated via subtraction of experiment beginning 5-minute average spectrum from experiment end spectrum. Green indicates relative increase of the given m/z at experiment's end, while red indicates a decrease.....	196
Figure 5-30: Total normalized signal in fragments with the given delta (Δ) value in the 5-minute average experiment beginning or end total organic mass spectrum.	197

Figure 5-31: PA/PAIN: Van Krevelen diagram showing pinonic acid (PA) and pinonic acid + inorganics (PAIN) photo-oxidations in replicate colored by time during experiment. Linear fits: PA1: $m = -0.90$, $r^2 = 0.66$; PA2: $m = -0.63$, $r^2 = 0.45$; PAIN1: $m = -0.90$, $r^2 = 0.75$; PAIN2: $m = -0.83$, $r^2 = 0.58$ 197

Figure 5-32: PA/PAIN: Nitrogen-to-Carbon vs. Oxygen-to-Carbon ratios for (left) pinonic acid + inorganics and (right) pinonic acid-only aqueous photo-oxidations. Linear fits: PAFull1*: $m = -0.06$, $r^2 = 0.22$; PAFull2: $m = -0.02$, $r^2 = 0.04$; PAINfull1*: $m = -0.01$, $r^2 = 0.01$; PAINfull2: $m = -0.06$, $r^2 = 0.33$ 198

Figure 5-33: Starting concentrations of the given cloud water constituents for given sample types, where Type 3 is TaiOx2. Units are, from left to right: Cl-Ca, HCHO, & S(IV) (μN); TC-TOC (ppm); Fe & Mn ($\mu\text{g/L}$). Error bars are standard deviations where data from multiple samples of the same Type were averaged; Type 3 consists of only one sample, so error bars are omitted. 199

Figure 8-2: Comparison of AMS nitrate against that calculated from the condensation particle counter for 300nm ammonium nitrate particles; the slope of these relationships can be used to correct the BFSP ionization efficiency calibration. For equations, consult Section 5.2 of the AMS Wiki page administrated by the Jimenez Group at University of Colorado, Boulder: http://cires.colorado.edu/jimenez-group/wiki/index.php/Field_ToF-AMS_Operation#5.2_Data_processing_of_IE_calibration_.28for_DMA.2FCPC_data_analysis.29 286

Figure 8-3: Total burned area (left axis, in red) and fire-generated carbonaceous aerosol emissions (right axis, in dashed black, in PM2.5 Gg/fire season) for the given state. 287

Figure 8-4: Timelines and mass spectra from PMF six-factor recombination of the Rocky Mountain dataset. 288

Figure 8-5: Factor mass spectra for a 3-factor PMF solution of the Grand Teton dataset. The lower portions of each split axis are on the same scale to show the lack of ‘organic wave’ patterns in the ‘Factor 3’ mass spectrum. 289

Figure 8-6: Timeline of a 3-factor PMF solution of the Grand Teton dataset. 289

Figure 8-7: Correlation coefficients (R) between mass spectra and timelines of the indicated factor pairs, where 1 = Factor 3, 2 = BBOA, and 3 = LV-OOA, showing that Factor 3 is similar to BBOA in mass spectral profile and timeline. 290

Figure 8-8: Ratios of the given fragment to total organics for TaiOx1, 2, and 7PA showing that most oxidized fragment at 43 or 44 drives progression of f_{43} or f_{44} 291

Figure 8-9: f_{43} versus f_{44} for TaiOx5 and three replicates of TaiOx4..... 291

Figure 8-10: f_{43} versus f_{44} for PA and PAIN experiments..... 292

Figure 8-11: Example average total organic mass spectrum from given baseline experiment (no UV, no hydrogen peroxide) showing advanced oxidation even before photo-oxidation. 292

Figure 8-12: Timeline of TaiOx6PAfull1 showing variable atomizing system output. 293

1. Background

1.1 Environmental Importance of Organic Aerosols

Organic particulate matter is universally abundant in the atmosphere, participates in diverse biogeochemical systems, and may illustrate particle origins, transport, and environmental interactions through its content and temporal variability. This dissertation explores atmospheric particulate chemistry and sources at rural/ remote sites in the Rocky Mountains using submicron organic aerosol (OA) composition, size, and concentration from an Aerodyne High-Resolution Time-of-Flight Aerosol Mass Spectrometer (HR-ToF-AMS, or ‘AMS’); our finding that secondary formation processes (along with transport) contribute significantly to OA at these sites motivates subsequent experiments on secondary OA formation in ambient cloud water via aqueous photoreactions.

We begin by emphasizing the abundance and environmental effects of organic aerosol, with a focus on fine mode and especially submicron particles for their enhanced organic content, particular environmental impacts, and relevance to the AMS, which samples particles $\sim 0.04\text{-}1\ \mu\text{m}$ in diameter (size-dependant collection efficiency discussed later; Liu et al. 2007). Additionally, the minimum between fine- and coarse-mode particle volume size distributions (analogous to mass given constant density) is often $\sim 1\ \mu\text{m}$ in rural and remote continental ambient atmospheres such as Rocky Mountain and Grand Teton National Parks, though ‘fine’ particles are often classified as $2.5\ \mu\text{m}$ and smaller (Seinfeld & Pandis 2006; Whitby & Sverdrup 1980; Finlayson-Pitts & Pitts 2000); scanning mobility particle sizer (SMPS) average volume distributions confirmed that most fine-mode mass is submicron during both field studies (see Section 2.1).

Fine particles may contain a vast array of compounds arising from disparate sources including: water; inorganic ammonium, nitrate, and sulfate; sea salts; transition metals; and tens of thousands of organic compounds including soot and combustion products, biogenic compounds, organonitrogen and organosulfur species, organic salts, polycyclic aromatic hydrocarbons, etc. (Hamilton et al. 2004; Murphy 2005). Organics comprise ~20-90% of global fine-mode particulate mass (Saxena & Hildemann 1996; Putaud et al. 2004; Jimenez et al. 2009; Zhang et al. 2007), and the majority of non-biological (spores, bacteria, etc.) atmospheric organics are in the fine mode (Finlayson-Pitts & Pitts 2000); the organic mass fraction varies between ecosystem types, and is generally maximized over tropical forests (Andreae 1997; Roberts et al. 2001; Kanakidou et al. 2005)

In the conceptual framework describing OA chemistry, basic classifications rest on particle sources: particles emitted directly by industrial, transportation-related, and residential (biomass burning) combustion or by plants (waxes, etc., often coarse mode), as well as condensation of freshly emitted high-temperature vapors during plume cooling, are called ‘primary’ organic aerosol (POA); particles formed from condensation of atmospherically oxidized lower-volatility gases, particle coagulation, aqueous processing with subsequent droplet evaporation (leaving a particle behind), etc. is termed ‘secondary’ OA (SOA). Too light to undergo significant gravitational settling, fine particles are removed mainly through washout by precipitation and may therefore persist for days to weeks in the atmosphere, rendering the fine mode active in long-range transport of particles (Finlayson-Pitts et al. 2000 and references therein). The predominance of submicron SOA over POA in this and other similar studies and the relative development of POA as a field of study motivates a focus on SOA abundance,

composition, and sources herein (Jimenez et al. 2009; Bahadur et al. 2010; de Gouw et al. 2008; Weber et al. 2007).

We can evaluate our understanding of SOA by comparing ambient observations with models that include known sources, processing, and sinks. While the field is developing rapidly, models often fail to capture temporal, geographical, and vertical variations, composition, and climate-relevant properties of aerosols, especially of organic aerosol in remote and biomass burning-influenced areas (Tsigaridis & Kanakidou 2003; Heald et al. 2005; Heald et al. 2011). For instance, aircraft measurements in the free troposphere over Asia measured 1-2 orders of magnitude more organic carbon than predicted by the GEOS-Chem global chemical transport model; GEOS-Chem underestimates surface OC mass by ~30% compared to boundary layer IMPROVE field sites (during July-August 2004, Heald et al. 2005). Remote continental and free tropospheric field campaigns are somewhat limited due to experimental expense and logistics, and the work herein suggests that SOA formation is both important in these environs and underestimated in current models.

Much of the discrepancy between models and field campaigns may stem from incomplete parameterization of SOA formation, including underestimation of SOA from biogenic VOCs oxidized with anthropogenic plumes and omission of aqueous SOA formation, which may be a significant global source of OA (Section 1.2.3); both of these sources are explored in this work. Some of this discrepancy may also arise from prevalent wall losses in laboratory experiments, leading to underestimation of SOA yields which are then propagated through model calculations (Kokkola et al. 2013). More sophisticated and diverse studies of ambient aerosols, especially those in remote areas and influenced by aqueous processing, are therefore crucial to close these conceptual gaps. To this end, we evaluate submicron particulate characteristics at two

rural/remote field sites and explore aqSOA formation in photo-oxidizing ambient cloud water in the laboratory; the altitude and meteorology of the field sites present a unique opportunity to test model validity, as prevalent afternoon upslope winds may provide a ‘boundary layer’ sample, while nighttime boundary layer compression and downslope winds may provide access to ‘free troposphere’ particulate. In Chapters 3 and 4, our results are compared with particle concentrations in co-located surface and free troposphere grid boxes from GEOS-Chem.

Given the aforementioned gaps in the understanding of atmospheric fine particles, it is relevant to outline their known biogeochemical interactions and effects. In understanding both knowledge gaps and the relative environmental consequence of various avenues of investigation, we can best tailor future work to the most pressing scientific and environmental needs.

1.1.1 Climate Effects

Fine particles contribute to climate forcing both directly through scattering and absorption of radiation, and indirectly through their role as cloud condensation nuclei (CCN). Figure 1-1 shows radiative forcing from a variety of effects outlined in this section (IPCC 2007).

Direct effects include scattering and absorption of radiation by aerosols, the magnitude of which may vary with particle size, composition, and mixing state (Seinfeld & Pandis 2006). In short, many aerosol components, including sulfate and organics (usually the two most abundant particle constituents) scatter radiation such that they reflect sunlight back to space, reducing the amount of sunlight to the surface (IPCC 2007; Takemura et al. 2001; Reddy 2005; Hansen 2005; Chung 2002). This effect has been observed in surface temperature reductions following major sulfate-rich volcanic emissions, such as the 1991 Mt. Pinatubo eruption, which was shown to increase both scattering and cloud albedo as explained later (Minnis et al. 1993; Ramachandran et al. 2000; Rozanov 2002; Stenchikov et al. 1998). Submicron particles are especially good at

light scattering because: (1) backscatter is maximized when particle diameters and insolation wavelengths are similar, and (2) submicron particles often contain significant sulfate, which scatters light efficiently (Pilinis et al. 1995; Bergin et al. 2001; Kleefeld 2002). Conversely, some particle components, such as black carbon and, to a smaller and more variable degree, biomass burning aerosol (and other aerosols with non-soot, light-absorbing ‘brown’ organics), absorb radiation, holding heat in the atmosphere with a warming effect (Liao & Seinfeld 2005; Takemura et al. 2005). This heating may in turn affect the atmospheric temperature structure and therefore cloud structure and attendant climate effects, together termed the “semi-direct” climate effect (Hansen et al. 1997; Cook & Highwood 2004; Johnson 2005). Overall, the net direct radiative forcing from aerosols is believed to be negative. Fairly large uncertainties concerning direct aerosol forcing remain, reflecting lack of detailed global knowledge of aerosol composition, size, concentrations, and interactions (IPCC 2007).

Indirect aerosol climate effects include increases in cloud albedo, geographical extent, and lifetime due to interactions with particles, causing unknown but possibly large radiative forcing. Particle number concentration and CCN activity (influenced by size and component hygroscopicity) influence size distributions and number concentrations of cloud droplet (Seinfeld & Pandis 2006; Ramanathan et al. 2001; IPCC 2007). In general, higher particle number concentrations below clouds will increase cloud droplet number concentrations; this has been observed in clouds up- and down-wind of urban areas (Alkezweeny et al. 1993; Twomey et al. 1978) and in cloud formation induced by ship tracks (Coakley et al. 1987; Radke et al. 1989). Higher cloud droplet number concentration generally increases the albedo, lifetime (through reduced precipitation), and extent of the cloud (Lohmann & Feichter 2005). The height of

Radiative forcing of climate between 1750 and 2005

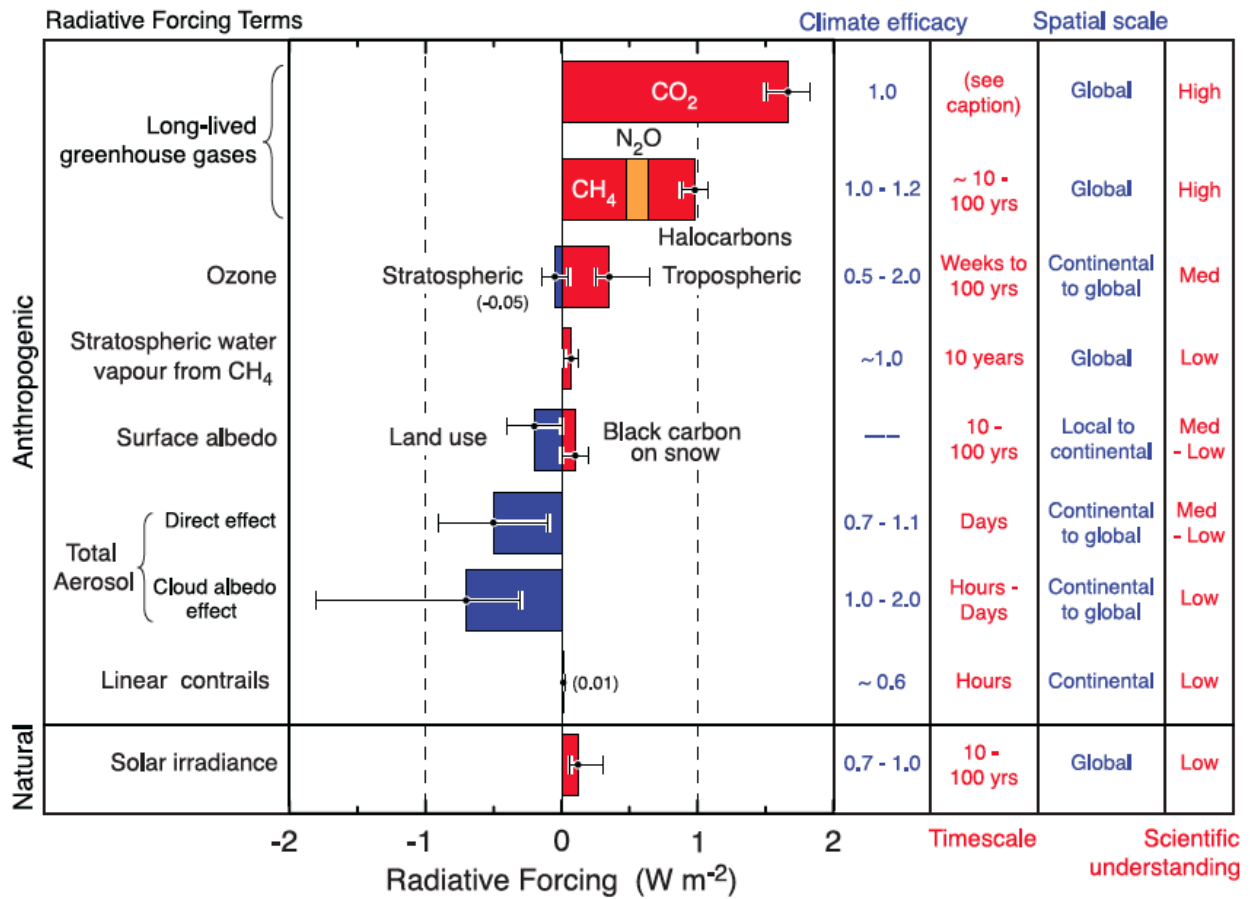


Figure 1-1: “Global mean RFs from the agents and mechanisms discussed in this chapter, grouped by agent type. Anthropogenic RFs and the natural direct solar RF are shown. The plotted RF values correspond to the bold values in Table 2.12. Columns indicate other characteristics of the RF; efficacies are not used to modify the RFs shown. Time scales represent the length of time that a given RF term would persist in the atmosphere after the associated emissions and changes ceased. No CO₂ time scale is given, as its removal from the atmosphere involves a range of processes that can span long time scales, and thus cannot be expressed accurately with a narrow range of lifetime values. The scientific understanding shown for each term is described in Table 2.11.” (IPCC 2007)

the resulting cloud is very important as low clouds generally cool the surface through solar reflectance whereas high clouds lead to surface warming; globally averaged, cloud formation from aerosol enhancement is estimated to have a net cooling affect (IPCC 2007). Lastly, deposition of absorbing aerosol (such as black carbon) onto snow pack may induce snow-melt and reduce planetary albedo, causing warming (Ramanathan & Carmichael 2008). Aerosol-cloud indirect effects, while potentially very important to Earth’s radiative balance, remain highly

uncertain, and the height, characteristics, and longitudinal location of the affected clouds are an important field of current research; Chapter 5 explores aqueous organic aerosol formation in cloud water, which may be an important source of particles active in both direct and indirect climate effects.

Lastly, and relevant to our secondary-particle focus, POA and SOA are hypothesized to have different effects on climate. POA may contain black carbon that participates in direct radiative forcing (Goldberg 1985; Masiello 2004; Mohr & Huffman 2009). SOA products (including aqueous products) may also contain light-absorbing organic compounds, or 'brown' carbon (Shapiro et al. 2009; Galloway et al. 2009; Nozière et al. 2009; Nakayama et al. 2010; Andreae & Gelencsér 2006; Chang & Thompson 2010); more importantly, their generally enhanced hygroscopicity makes for augmented CCN functionality and therefore indirect radiative forcing (Kanakidou et al. 2005; Petters & Kreidenweis 2007; Lambe et al. 2011; Jimenez et al. 2009). The High-Resolution Aerosol Mass Spectrometer can yield composition (POA vs. SOA, etc.), size, and often source information on submicron particulate; the f_{44} ratio (the ratio of signal at $m/z44$, approximating CO_2^+ from carboxylic acids, to total organics; Ng et al. 2011a) is highly correlated with O:C and often used as an indicator of hygroscopicity (Duplissy et al. 2011). Thus, the rural/remote AMS datasets presented here may be used to explore the validity and/or shortcomings of the climate and chemical models used to understand and predict global atmospheric processes.

1.1.2 Ecosystem and Health Effects

Fine particles also participate in a range of human health and environmental effects. Human health effects may stem from total particulate mass-driven lung inflammation or direct toxicity from anaerobic organic radical formation and carcinogenic compounds such as PAHs

(Rogge et al. 1993; Dzepina et al. 2007; Adler et al. 2011). Fine-mode and submicron particles in particular are especially harmful because they penetrate deeper into the lungs (Pope et al. 2002; Davidson et al. 2005; Dominici et al. 2006); in addition, fine mode particles often contain more water-soluble organic carbon (WSOC) and transition metals than the coarse mode, which contribute to oxidative DNA mutagenesis (Valavanidis et al. 2008).

Nutrient and pollutant deposition to ecosystems is another serious concern. Acidic deposition (i.e. of sulfuric and nitric acids) can cause nutrient leaching in soils, depriving vegetation of necessary nutrients (Likens et al. 1996); poorly buffered waters may acidify, harming aquatic species, while water bodies with more buffering are often subject to eutrophication driven by excess nutrient load (Bergstrom & Jansson 2006; Schindler et al. 1971). The high-altitude ecosystems in Rocky Mountain and Grand Teton National Parks are especially sensitive to the increased nutrient, and particularly nitrogen, deposition recently established in the literature, to which fine particle species contribute (Foster et al. 1997; Fenn et al. 2003; Beem et al. 2010; Malm et al. 2009; Williams et al. 2001); serious ecological changes have been documented in the Colorado Rocky Mountains including elevated nitrate in runoff and lakes and changes in dominant diatom, lichen, and vegetative communities (Fenn et al. 2003; Bowman et al. 2012; Baron et al. 2000; Malm & Hand 2007).

Scattering and absorption of visible light by fine particles contributes to reduction in visibility, reducing transportation safety and enjoyment of natural areas (Malm & Day 2001; Park et al. 2006; Gebhart et al. 2011; Park 2003; Watson 2002); visibility reduction due to aerosols has been observed at Rocky Mountain National Park, especially in the summer when particle concentrations are higher (Malm & Hand 2007; Levin et al. 2009). Scattering and

absorption by particles also prevent some insolation from reaching the surface, decreasing agricultural yields in some areas (Chameides 1999; Cohan et al. 2002).

Lastly, enhanced snow melt caused by deposition of absorbing aerosols may alter hydrological cycles (Ramanathan & Carmichael 2008) and impact the winter recreation industry. Also, reduction in cloud droplet size after introduction of fine particles may suppress precipitation in both orographic (relevant to our sites) and non-orographic clouds, though the magnitude and ubiquity of this effect is debated (Albrecht 1989; Ramanathan et al. 2001; Givati & Rosenfeld 2004; Rosenfeld & Givati 2006); precipitation suppression may occur near Rocky Mountain National Park from transported Front Range pollution (Jirak & Cotton 2006). As noted in Section 1.1.1, SOA may play an especially important role in cloud-related effects because of its generally enhanced CCN functionality.

Fine-mode aerosols factor into a wide range of climate, health, and environmental effects which are often exacerbated by smaller (submicron) size and secondary content. The longer lifetime of fine-mode particles allow widespread transport, expanding their direct and indirect climate effects to even the most pristine remote environments. Thus, a focus on sources, evolution, and characteristics of submicron organic particulate is timely in light of recent efforts to understand and mitigate climate and environmental effects. In the next section, an overview of the photochemical and aqueous SOA formation mechanisms established in the literature sets the stage for a discussion of SOA in the field and laboratory data presented here.

1.2 Organic Aerosol Formation and Ageing

1.2.1 SOA Formation from Condensing Oxidized Vapors

Secondary organic aerosol formation can be loosely organized by the mechanisms resulting in lower-volatility compounds, which may involve (1) condensation of oxidized vapors

onto preexisting particles, or (2) production of low-volatility compounds through reaction within particles or droplets (Kanakidou et al. 2005; Ervens et al. 2011). Although gas-phase photochemical oxidation with subsequent partitioning has been most extensively studied and was long thought to be the dominant SOA formation pathway (Odum et al. 1996; Hoffmann et al. 1997; Kamens et al. 1999), recent work has suggested that aqueous and particle-phase SOA formation is also quite important (Section 1.2.3); in a study encompassing a variety of atmospheric conditions and precursors, aqueous processes (in wetted particles and cloud droplets) consistently contributed 30-50% of total SOA mass (Ervens et al. 2011). In general, volatile or semi-volatile organic compounds (VOC or SVOC) are oxidized in the gas-phase to form lower volatility compounds that then condense onto preexisting particles. SOA yield through this mechanism is controlled in part by temperature as it affects vapor pressure and, in forested areas, biogenic VOC emissions (Sato et al. 2011; Leaitch et al. 2011; Ahlm et al. 2013). Enhanced relative humidity (i.e. particle wetting) also generally increases the partitioning coefficient of intermediate-volatility organic vapors by decreasing (1) the average molecular weight of the absorbing phase (MW_{OM} in Equation 1 below) and (2) the condensing compound's activity coefficient (ζ_i , Equation 1), especially for more hydrophilic compounds (Seinfeld et al. 2001; Hennigan et al. 2009); the complex heterogeneous processes involved in SOA formation are still under investigation. The partitioning coefficient is defined as (Pankow 1994; Odum et al. 1996):

$$K_p = \frac{760 R T f_{OM}}{MW_{OM} 10^6 \zeta_i P_{L,i}^\circ} \quad (\text{Equation 1})$$

where R = gas constant ($8.2 \times 10^{-5} \text{ m}^3 \text{ atm mol}^{-1} \text{ K}^{-1}$), T is temperature in Kelvin, f_{OM} is the fraction of total particulate mass that comprises the organic matter (OM)-absorbing phase,

MW_{OM} is the average molecular weight of the organic matter, and $P_{L,i}^{\circ}$ is the vapor pressure of pure compound i at the temperature of interest (torr).

Semi- and Low-Volatility OC phase partitioning may also be affected by how quickly the newly-absorbed compounds diffuse into the bulk particle, reducing the apparent concentration at the particle surface and drawing more S/LVOC into the particle through phase partitioning; oxidation of the VOC compounds within the particle can enhance this effect (Erdakos & Pankow 2004; Pfrang et al. 2011; Pöschl 2011). Third, the composition of the particles onto which SVOCs condense affects SOA yield through reactivity with the condensing compounds, water uptake (hygroscopicity), and possible partitioning effects from organic coatings, etc. (explored later, Pankow 2003; Bertram et al. 2011; Shiraiwa et al. 2013).

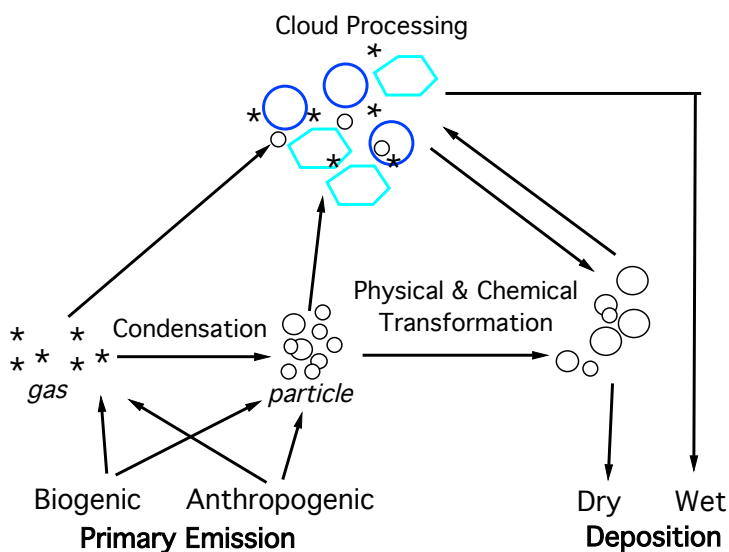


Figure 1-2: Schematic of gaseous, particle phase, and aqueous phase SOA formation pathways adapted from Fuzzi & Andreae (2006) and Pöschl (2011).

Important Compounds in SOA Formation

Good SOA precursors are abundant, form lower-volatility products with high yields, or both. Volatile organic compounds (VOCs) are generally classified by source as either biogenic (BVOC) or anthropogenic (AVOC) in order to evaluate human impact on particulate pollution

and attendant climate effects, though frequent oxidation of BVOCs by or with anthropogenic species such as NO_x , NO_3 , O_3 , etc. may complicate this kind of source apportionment as discussed below (Alfarra & Paulsen 2006; Hoyle et al. 2011). VOCs involved in SOA formation may also arise from POA volatilization; of the 20% of global OA mass that is primary, 50-75% is semivolatile and may enter the gas phase upon plume dilution (Kanakidou et al. 2005; Spracklen et al. 2011; Shrivastava et al. 2006; Robinson et al. 2007). Lastly, POA particles may act as a substrate upon which oxidized VOCs condense.

Biogenic VOCs are dominant SOA precursors globally, though of course anthropogenic VOCs may be more important in populated areas. BVOCs may include, in order of decreasing abundance, isoprene, mono-, and sesquiterpenes, alcohols and carbonyls, and alkanes, alkenes, esters, and acids, of which the isoprenoids have been studied extensively (Kesselmeier & Staudt 1999). The most abundant BVOC, isoprene, has emissions of $\sim 250\text{-}750 \text{ Tg C year}^{-1}$ contributing roughly half of total BVOC emissions (Wiedinmyer et al. 2004); isoprene and its early oxidation products are thought to form 2 to $>15 \text{ Tg}$ of SOA annually of the $8\text{-}40 \text{ Tg/yr}$ total SOA from biogenic sources (Claeys et al. 2004; Matsunaga 2005; Henze & Seinfeld 2006; Hoyle et al. 2007; Penner et al. 2001). Monoterpenes α -pinene, β -pinene, sabinene, and limonene comprise another 20-40% of total BVOCs and have major oxidation products such as glyoxal, pinonaldehyde, pinic and pinonic acids, methacrolein, and others which may be active in both gas phase and aqueous SOA formation (Guenther et al. 1995; Guenther 2000; Surratt et al. 2010; Fu et al. 2008). Other products in biogenic SOA may include di- and poly-carbonyls such as methylglyoxal.

Frequent mixing of bio- and anthropogenic OA and/or precursors widens possible products considerably. For example, biogenic isoprene and α -pinene may form sulfate esters

when photo-oxidized with ammonium sulfate (Surratt et al. 2007); organonitrogen and organosulfur species are common in SOA (Ng et al. 2008; Stone et al. 2009; Surratt et al. 2007; Froyd et al. 2010; Fry et al. 2009). Once in the particle phase, further oxidation by hydroxyl radical, organic radicals, nitrate, etc. may cause functionalization and oligomerization leading to SOA mass increases, which may be enhanced further in the presence of inorganic acids (Jang et al. 2002; Gao et al. 2004; Denkenberger et al. 2007; Müller et al. 2008). Molecular decomposition leading to higher volatility products and SOA mass loss has been observed in ambient particles undergoing photo-oxidation and will be discussed further in Section 1.2.3 and Chapter 5 (Kang et al. 2007).

Anthropogenic VOCs (excluding methane, the most abundant) include aromatics (20%), alkanes (40-45%), alkenes (10%), carbonyls and other oxygenates (10-15%), polycyclic aromatic hydrocarbons, and many others (Sawyer 2000; Placet 2000; Atkinson 2000; Atkinson & Arey 2003). Important compounds include toluene, benzene and its derivatives, formaldehyde, and cyclohexene, for which products include glyoxal, methylglyoxal, di-acids (such as adipic and glutaric acids), etc. (Tsigaridis & Kanakidou 2003; Odum 1997). Anthropogenic VOC produces much less SOA than biogenic precursors at ~4.5-6% (\pm ~2%) of global SOA production (with the highest estimates at 33%; Tsigaridis & Kanakidou 2003; Hoyle et al. 2007; Volkamer et al. 2006; Lack 2004).

Important Oxidants and Reaction Mechanisms

The dominant atmospheric oxidants of VOCs are hydroxyl radical (OH) and ozone (O₃); nitrate radical (NO₃) can be important at night and in polluted regions, with <25% of SOA in remote regions resulting from organic oxidation by nitrate (Hoyle et al. 2007; Seinfeld & Pandis 2006; Finlayson-Pitts & Pitts 2000). Chlorine is active in marine environments but will not be

discussed in the context of these continental datasets. Some organic compounds may photolyze to produce organic radicals, but SOA yields from direct organic radical reactions are thought to be low (Monod et al. 2007; Surratt et al. 2006). UV light, hydroperoxyl (HO_2), organic peroxy (RO_2), nitric oxide (NO), and nitrogen dioxide (NO_2) may be involved in oxidant generation and/or affect the yields and identity of the reaction products (especially in the case of NO_x) through competition for oxidants or reactants. NO_x may affect SOA formation in urban-influenced areas by: (1) competing with VOCs for oxidants OH and O_3 , (2) producing oxidants, as when O_3 is produced through the combination of oxygen and $\text{O}(^3\text{P})$ from NO_2 photolysis, and (3) reacting with VOC intermediate products, such as enhancement of Criegee-to-adipaldehyde pathways (pp. 665, Seinfeld & Pandis 2006; Finlayson-Pitts & Pitts 2000).

Generally, gas-phase oxidation of VOCs to form condensable species involves substitution reactions adding carboxylic acid, carbonyl, alcohol, ketone, and nitro functional groups (Seinfeld & Pankow 2003; Kroll & Seinfeld 2008). An overview of the oxidation of VOCs in the atmosphere is provided in Atkinson & Arey (2003), and major pathways will be summarized below from Finlayson-Pitts & Pitts (2000) and references therein.

Reactions between VOCs and OH are various. Alkanes often have hydrogen abstracted by the hydroxyl radical (producing water), followed by peroxide formation from O_2 addition, and terminated in acid (peroxide + HO_2), aldehyde, or organonitrate (+ NO) formation or reaction with alkylperoxy radicals to form a variety of products. For isoprene, a common alkene, OH addition to a C-C double bond forms an organic radical, which is often followed by O_2 addition to form an alkylperoxy radical (RO_2). From here, the pathway depends on the availability of NO , with which RO_2 might form a hydroxyl nitrate (minor product) or alkoxy radical (major product); these alkoxy radicals often decompose (in the case of isoprene, to methylvinylketone

and an α -hydroxy radical, which may form formaldehyde after reaction with oxygen). In the absence of NO, alkylperoxy radicals may react with HO₂ and other RO₂ radicals. End products are dominated by aldehydes (and other carbonyls) and acids, though small yields of organic nitrates may be expected, especially in forested regions (with BVOCs) impacted by NO_x-containing anthropogenic plumes, as may be the case at our Rocky Mountain site (Starn et al. 1998; Rollins et al. 2012). For aromatics reacting with OH, the dominant mechanism involves OH addition, then O₂ addition with cyclization (forming a stabilized bi-cyclic radical); from here, various ring-opening and decomposition reactions lead predominantly to dicarboxylic products such as glyoxal and methylglyoxal.

Ozone is not as important an oxidant as the hydroxyl radical, but may play an important role, especially in the oxidation of alkenes. Cyclohexene is often used as an example aromatic, and may illustrate the major reactions at play; its major products under oxidation by O₃ include pentanal, oxalic acid, and malonic acid (Kalberer et al. 2000). Briefly, the O₃ molecule adds to the aromatic ring, followed by ring-opening, after which a Criegee biradical is formed. The Criegee intermediate, which may also be formed from a variety of other atmospheric organics, is very reactive and may follow any number of pathways resulting in lower-volatility aldehydes, acids, hydroperoxides, and esters; formation of volatile formaldehyde is also common from the Criegee intermediate, which may in turn oxidize to lower-volatility products, highlighting the complex pathways leading to formation of SOA. Condensed-phase reactions including oligomerization, esterification, and aldol addition will be outlined in subsequent sections.

Past studies exploring photochemical particle formation and/or growth may be relevant to both the Rocky Mountain and Grand Teton regions, where secondary organic content is indicated as discussed in the results. Most work of this type explores particle nucleation, during which

particles grow homogeneously from clusters of vapor molecules to ultrafine (10s of nm) to ~50 nm sizes over the course of a day (Weber et al. 1997; Shi & Qian 2003; Shen et al. 2011; Makela et al. 2000; Zhang et al. 2004); these growth events occur between sunrise and sunset, suggesting that photochemical mechanisms are important, and are anti-correlated to preexisting particle concentrations, implying that condensation of oxidized vapors onto preexisting particles is favored over nucleation except in very clean environments (Kerminen et al. 2001; Kerminen & Kulmala 2002; Kulmala et al. 2004). Particle number concentrations, which increase rapidly during nucleation events, are usually used to illustrate particle nucleation, as mass concentration increases may arise from either nucleation and/or condensation of oxidized vapors onto preexisting particles. The AMS size cut (~40 nm) precludes observation of nucleation events, but increases in number concentrations (from co-located instrumentation) with commensurate growth in sizes <40 nm may indicate nucleation events as opposed to transport of a different air mass (which after ageing would be expected to have larger particle sizes); anthropogenic trace gas measurements (NO_x, etc.) are available for some campaigns and may aid in determining whether a change in air mass (due to transport, etc.) may contribute to given aerosol characteristics. Other indicators of SOA formation include enhanced *f*₄₄ (CO₂⁺ fragment/total organic mass) from carboxylic acids, which are likely to result from atmospheric oxidation through a number of mechanisms (Morgan et al. 2010; Ng et al. 2011).

1.2.2 Evidence for the Importance of Aqueous SOA

Though condensation of oxidized vapors clearly forms SOA, this mechanism fails to explain the amount, distribution, and composition of SOA observed in numerous field studies (Ervens et al. 2011). The discrepancies between the condensational model and field campaigns outlined below suggest that SOA formed through aqueous phase reactions may be comparable to

that formed through vapor condensation (Chen et al. 2007; Carlton et al. 2007; Fu et al. 2008; Fu & Jacob 2009).

First, gas-phase oxidation experiments fail to produce the molecular types generally found in ambient SOA. Oxidized, high-molecular-weight compounds (“HMWC”) with multi-functionalization and/or oligomerization contribute significantly to global OA mass (Blando et al. 1998; Romero & Oehme 2005; Fuzzi et al. 2001; Stone et al. 2009); HMWC and oligomers are found in clouds and observed to result from cloud and fog processing in ambient conditions (Collett et al. 2008; Havers et al. 1998; Facchini et al. 1999; Zappoli et al. 1999; Krivácsy 2000). Oxalate, for instance, is globally omnipresent (Kawamura & Sakaguchi 1999; Kawamura 2003; Sorooshian et al. 2006), yet unlikely to result in quantity from gaseous reactions (Warneck 2003). Also, a number of volatile compounds, including glyoxal, methylglyoxal, and glycolaldehyde, are observed ubiquitously in the particle phase, implying a formation mechanism other than vapor condensation (Tan et al. 2009; Altieri et al. 2008; Perri et al. 2010); SOA formation from aqueous oxidation of glyoxal and methylglyoxal has been indicated in modeling and ambient campaigns (Altieri et al. 2006; Loeffler et al. 2006; Carlton et al. 2007; Ervens et al. 2003; Ervens 2004; Stavrou et al. 2009).

While fragmentation within the AMS precludes measurement of specific molecules (such as HMWC and oligomers), products of condensed-vapor SOA experiments tend to under-predict AMS-measurable oxidation indicators such as f_{44} (CO_2^+ from carboxylic acids/total organic mass), O:C, etc. (Aiken et al. 2008; Ng et al. 2010). Aqueous reaction products of, for instance, glyoxal and methylglyoxal are shown here and in other studies to better reproduce observed ambient oxidation indicators (Lee et al. 2011; De Haan et al. 2009; Altieri et al. 2008; Carlton et al. 2008; Li et al. 2013).

Models including only vapor-condensation SOA also underestimate OA mass and do not capture temporal, vertical, and geographical OA variation (Tsigaridis & Kanakidou 2003; Heald et al. 2005). For instance, the GEOS-Chem model underestimates boundary layer OC by an average of 30% as compared with IMPROVE field sites and does not capture regional variability over the Northeastern U.S. (Heald et al. 2006; Park et al. 2006). Model underestimation of free-tropospheric OA is also evident; using PILS water-soluble organic carbon (WSOC), Heald et al. (2006) found that while observed WSOC was reduced by factor of 2 upon transition from the boundary layer (BL) to the free troposphere (FT), sulfate (used as a tracer of anthropogenic influence) was reduced by a factor of 10, indicating an in-situ source of WSOC. The observed FT WSOC was correlated at the 95% confidence level with methanol (a biogenic tracer, Jacob 2005) and sulfate, the majority of which is produced through aqueous reactions (Graedel & Goldberg 1983; Seigneur & Saxena 1984; Karamchandani & Venkatram 1992; McHenry & Dennis 1994). Also, biogenic SOA and anthropogenic inorganics are often correlated in field studies, in contrast to ‘dry’ biogenic VOC chamber experiments, where SOA yields are often lower when anthropogenic oxidant (such as NO_x) concentrations are increased (de Gouw et al. 2008; Weber et al. 2007; Kroll et al. 2006). These and similar findings have motivated incorporation of aqueous SOA into models, which result in better reproduction of observed SOA though many aqSOA mechanisms are still unclear and a focus of current research (Carlton et al. 2008; Chen et al. 2007a).

Ambient particle size distributions may also indicate aqueous processing. Studies evaluating SOA kinetics find that condensational growth is too slow to produce the droplet-mode particles widely observed after cloud processing events (Hering & Friedlander 1982; John et al. 1990; Meng & Seinfeld 1994; Hoppel et al. 1994). In studies of particle size distributions within

(interstitial particles) and underneath clouds, Hoppel et al. (1994) observed that the below-cloud particles had a second, larger mode (“droplet mode,” particle diameters 0.8-1 μm); they hypothesized that both a) interstitial particles are absorbed by droplets that subsequently evaporate, producing larger aggregated particles, and b) gaseous precursors are absorbed and subsequently oxidized, adding particle mass when the droplet evaporates and producing the observed “droplet mode” sizes.

Other evidence supporting the importance of aqueous processing includes higher correlation between SOA indicators (highly functionalized species, etc.) and relative humidity than between SOA and gaseous precursor concentrations (Hennigan et al. 2008; Hennigan et al. 2009; Volkamer et al. 2009). Also, aqueous photochemical reactions have also been shown to form light-absorbing organic material with absorption spectra quite like conjugated oligomers, which are not observed to form in the gas phase and appear to require a seed particle to form atmospherically (Jang & Kamens 2001; Gelencsér et al. 2003; Hoffer 2004; Chang & Thompson 2010).

1.2.3 Aqueous SOA Formation and Oxidation

Based on current knowledge of SOA content and mechanisms, aqueous reactions should form SOA in some quantity: aqueous reactions are known to form HMWC such as dicarboxylic acids (oxalic acid, etc.), oligomers, and others, which are observed in SOA; and water, sunlight, and aqueous oxidant precursors are abundant in the atmosphere, with aerosol water comprising 66-75% of aerosol mass globally (Meng et al. 1995). In the aqueous phase, the cage effect born of greater molecule proximity encourages generally faster reaction rates (Finlayson-Pitts & Pitts 2000). Furthermore, semivolatile organic compounds (SVOCs) are often hydrophilic and readily absorbed into the aqueous phase, enhancing precursor concentrations; often-hydrophobic POA is

quickly (~hours) oxidized to hydrophilic compounds that may join the SVOCs as aqueous precursors (Petters et al. 2006; Prenni et al. 2007; Ervens & Volkamer 2010; Cubison et al. 2011; Riemer et al. 2010). However, our understanding of these systems is complicated by the variety of oxidants, precursors, and solution compositions and concentrations that control reaction rates, uptake of gas-phase components at the droplet surface, and dissolution into the droplet. This section will outline known aqSOA processes in general, then summarize important precursors, products, and mechanisms.

Reactant and total solute concentration strongly influences aqSOA yield and product type. Aerosol water such as that gained through hygroscopic growth has the highest solute concentration and often forms higher molecular weight compounds such as oligomers through organic self-reaction, while lower fog- and cloud-relevant concentrations often form organic acids (Lim et al. 2010; Tan et al. 2009). Organic SOA yields may be enhanced two to three orders of magnitude in aerosol over cloud water concentrations, controlling for particle size (surface area) and liquid water content (Ervens & Volkamer 2010); this may result in part from ionic strength kinetic enhancement in more concentrated solutions (Herrmann et al. 2010; Herrmann 2003), but probably involves many of the processes outlined below as well (Ervens & Volkamer 2010).

The relationship between aerosol/droplet concentration and the solubility of gaseous precursors is complex. High strong-ion concentrations (e.g. sea salt) can reduce gaseous solubility by, essentially, out-competing low-polarity organic molecules for water molecules in their hydration shells (the "Setschenow effect," Setschenow 1889; Schwarzenbach et al. 2005). Conversely, gas solubility may be enhanced by solute dissociation and diol formation (which are included in effective Henry's Law constants), shifting the equilibrium toward dissolution of

additional gaseous molecules. Under low solution concentrations, such as in cloud water, these mechanisms seem to have little effect on the very soluble ($H > 10^4 \text{ M atm}^{-1}$), polar compounds such as glyoxal and methylglyoxal that may produce large SOA yields; Henry's law predicts partitioning of these species reasonably well, with experimental yields of 0.6–3 times those calculated using Henry's Law (van Pinxteren et al. 2005; Limbeck & Puxbaum 2000). However, the apparent solubility of hydrophobic compounds such as PAHs and alkanes is often enhanced well beyond (~40–900x) effective Henry's law values, for which proposed mechanisms include association with previously dissolved organics, adsorption at the air-water interface (for surface-active species), and/or in-droplet production from more concentrated precursors in poorly-controlled experiments (van Pinxteren et al. 2005; Glotfelty et al. 1987; Valsaraj et al. 1993; Djikaev 2003). Many SVOCs have been found to partition predominantly toward the particle phase in concentrated aerosol water and in the presence of high concentrations of gas-phase hydrophobic compounds in both lab and field studies (Matsunaga 2004; Matsunaga 2005; Gao et al. 2004).

Aqueous SOA yields may also depend on the composition of the solutes (or laboratory seed aerosol) in the droplet (as studied through laboratory glyoxal SOA, Ervens & Volkamer 2010; Volkamer et al. 2009; Galloway et al. 2011). First, increased yield may arise from enhanced radical formation, such as the CHO-initiated reactions observed in Volkamer et al. (2009); second, seed composition (along with ambient relative humidity, more weakly) affects hygroscopicity and therefore aerosol liquid water content (LWC), which has a relationship with aqSOA formation (Ervens & Volkamer 2010). The distribution of components in the droplet (mixing) is also important; for instance, some particles may have a 'shell' of soluble or insoluble organic molecules that could, respectively, have no effect on or impede gas uptake and water

evaporation (Ervens & Volkamer 2010; Xiong et al. 1998; Shiraiwa et al. 2013; Ziemann 2010); others have found that a layer of concentrated solute caused by evaporation at the particle surface may hinder organic uptake through shifting the Henry's law equilibrium (Donaldson & Vaida 2006 and references therein).

Increasing solution acidity, which may be a result of nitric, sulfuric, and/or organic acid enhancement in anthropogenically-influenced plumes (such as those explored herein), sometimes increases yields of oligomers (Gao et al. 2004), nitrogen-containing compounds such as ammonium + glyoxal (Ervens & Volkamer 2010; Surratt et al. 2007), and sulfur compounds such as aqueous-processing tracer hydroxymethanesulphonate (HMS; Kok et al. 1986; Lagrange et al. 1999; Dall'Osto et al. 2009; Jang et al. 2002). Dissociation of ammonium ion to yield H^+ may also participate in acid-catalyzed reactions, with Nozière et al. (2010) writing,

“We report that inorganic ammonium ions, NH_4^+ ... [are] efficient catalysts for the aldol condensation of carbonyl compounds... For the concentrations of ammonium and carbonate ions present in tropospheric aerosols, the aldol condensation of acetaldehyde and acetone could be as fast as in concentrated sulfuric acid and might compete with their reactions with OH radicals. For organic gases with large Henry's law coefficients, these reactions could also result in a significant uptake and in the formation of secondary organic aerosols (SOA).”

The dominant oxidant can also be affected by pH; for instance, as pH rises above pH=5, O_3 is increasingly important in reactions oxidizing S(IV) (Shen 2011). However, a number of studies also report no effect, using atmospherically relevant pH, on uptake or reaction rates for, for example, methacrolein (Nozière et al. 2006). Decreased ambient particle pH is observed under higher summer temperatures, possibly from volatilization of lower-weight compounds leaving proportionally more organic acids (Denkenberger et al. 2007); this volatilization also increases solute concentrations, leading to increased yields and oligomerization as described above. While the rates of acid-catalyzed reactions, which are thought to initiate glyoxal self-

oligomerization (Loeffler et al. 2006) and other oxidation reactions, are enhanced in acidic conditions, acidity probably has little effect on aqueous uptake of, for example, glyoxal (Kroll et al. 2005; Loeffler et al. 2006; Volkamer et al. 2009) or methylglyoxal (Zhao et al. 2006).

Lastly, droplet size can affect the vapor pressure through the Kelvin effect; the Kelvin effect is significant in ambient particles ≤ 50 nm (or ≤ 200 nm for larger organic vapors), which is significantly smaller than the cloud droplets which comprise our focus (Seinfeld & Pandis 2006). Ideally, the chemistry of aerosol, fog, and cloud water should be explored separately; in this work we focus on real cloud samples and solutions with cloud-relevant concentrations. Important aqueous oxidants and precursors are explored below.

Important oxidants, precursors, and concentrations

A number of studies have addressed aqSOA formation through field campaigns, where common approaches include comparison of interstitial particles with droplet content and/or following an air mass through cloud or fog processing. Laboratory studies fall broadly into two categories - bulk aqueous processes and chamber experiments - and employ a variety of oxidants and precursors; the most important and/or most studied reaction components are discussed below, organized by compound type. The hydroxyl (OH), nitrate (NO₃), and sulfate (SO₄) radicals are among the most important oxidants involved in aqSOA formation (Herrmann et al. 2010). Hydroxyl radical is described in depth for its importance and use in our aqueous SOA experiments. Hydrogen peroxide and HO_x (HO+HO₂) also undergo complex regenerative chemistry in both phases involving formation and reaction of organic radicals such as organic peroxides (Anastasio et al. 1994; Valverde-Canossa et al. 2005; Tilgner & Herrmann 2010).

In order to glean mechanistic and kinetic information, laboratory studies usually employ one or a very few precursors, which should be as atmospherically relevant as possible. Both

anthropogenic and biogenic precursor VOCs may be oxidized (in either phase) to form soluble carbonyl and other compounds that participate in aqSOA formation. Important anthropogenic aqSOA precursors may include aromatic and alkene compounds and their more-soluble oxidation products such as glyoxal and methylglyoxal; biogenic precursors may include isoprene, α -pinene, and other terpenes photo-oxidized to methacrolein, methylvinylketone, aldehydes, glyoxal, methylglyoxal, etc. (Lim et al. 2005). The literature on these reactants is summarized below.

Hydroxyl Radical

The hydroxyl radical (OH) is a dominant aqueous oxidant, especially for organics, with which reaction rates approach the diffusion limit (Ervens, Gligorovski, et al. 2003). In the atmosphere, OH can be absorbed from the gas phase or formed in the aqueous phase from photolysis of hydrogen peroxide (H_2O_2 ; Zellner et al. 1990; Graedel & Goldberg 1983), $\text{Fe}(\text{OH})^{2+}$ (Weschler et al. 1986; Arakaki & Faust 1998), HONO (Fischer & Warneck 1996; Arakaki & Faust 1998), and HNO_3 (Graedel & Weschler 1981); photolytic processes may contribute up to 33% of $\text{OH}_{(\text{aq})}$ (Ervens et al. 2003; Arakaki & Faust 1998), and have been observed in ambient particles (Shen & Anastasio 2011). Fenton reactions may produce OH in the absence of UV given $\text{Fe}^{2+}/\text{Cu}^+$ content (see citations above), which is possible in our ambient cloud samples and motivated our no-UV control experiments (see Section 2.3). Lastly, H_2O_2 may be generated by a number of non-photolytic oxidation reactions including HO_2 self-reaction (Finlayson-Pitts & Pitts 2000). H_2O_2 in ambient aerosol water is up to 100 times greater than predicted Henry's law concentrations, implying that photochemical and other reactions produce significant hydrogen peroxide (Arellanes et al. 2006; Wang et al. 2010). Direct photolytic oxidation of organics is also possible in aqueous solutions (Guzman et al. 2006); this includes

both oligomerization and lysing reactions, products of which may form OH in turn through HO_x cycling.

OH is a popular laboratory oxidant for its importance and relative ease of generation using added H₂O₂ and UV light (as in this work), but its concentration is rarely measured in ambient aerosol or cloud water. Complicating factors in [OH] estimation include matrix-enhanced organic oxidation rates (and thus OH turnover time), OH sink uncertainty, and the effect of solute concentration and composition uniformity (organic shells, etc.) on oxidant absorption and transport within the bulk particle (Ervens et al. 2003). Ervens et al. (2003) used the CAPRAM 2.4 model to estimate concentrations of $\sim 10^{-13}$ M in clouds and $\sim 10^{-12}$ M in aerosol water, which is approximately reproduced in the aqSOA experiments in Chapter 5 ($\sim 10^{-14}$ M) and consistent with the best estimates of cloud [OH] (see Section 2.3, Ervens & Volkamer 2010; Jacob 1986). Previous analysis of our ambient cloud samples by Shen (2011) revealed that H₂O₂ was present (and the dominant S(IV) oxidant), though organic chemistry was not explored; concentrations of H₂O₂ measured in the cloud samples upon collection were generally within one order of magnitude of concentrations added in the aqueous photo-oxidations, with a few samples with [HOOH] about one order of magnitude lower (Table 8-4). Though other aqueous oxidants may be important at night, such as nitrate radical (Herrmann et al. 2010) and organic peroxides (Valverde-Canossa et al. 2005), the experiments herein focus on aqueous OH photoreactions for their projected high yield and comparative relevance to the field components of this dissertation (i.e. daytime SOA formation) and use control experiments to explore dark hydrogen peroxide and photolytic organic reactions (without H₂O₂).

Glyoxal

Glyoxal is widely used as a ‘model’ SOA precursor for its abundance, ubiquity, and chemical relevance to other dicarbonyl molecules (Volkamer et al. 2001). Fu et al. (2008) use GEOS-Chem and IMAGES (v2) to estimate global glyoxal formation between 45-108 Tg y⁻¹ (Fu et al. 2008; Stavrou et al. 2009); glyoxal is a primary and higher-order product of photo-oxidation of both anthropogenic VOCs such as toluene and acetylene (Jang & Kamens 2001; Fu et al. 2008) and biogenic VOCs like isoprene, which produces 47% of total glyoxal in the Fu model (Atkinson et al. 2006; Fu et al. 2008). In more recent work, updated precursor budgets and glyoxal yields have revised gas-phase glyoxal production slightly downward to ~21 Tg y⁻¹ (Liu et al. 2012), though this estimate omits recently suggested and possibly significant glyoxal (and methylglyoxal) sources from oxidation of aromatics including PAHs (Wang et al. 2007; Chan et al. 2009; Nishino et al. 2010). Regardless, the most important aqueous glyoxal source is probably in-droplet glycolaldehyde oxidation, producing ~79% of [Gly]_{aq}; gas-to-liquid exchange delivers the remaining aqueous glyoxal (Liu et al. 2012). Glyoxal has been detected over oceans (Warneck 2003), suggesting a marine source since the estimated atmospheric lifetime of glyoxal is short (~3 hrs), though longer-range transport of precursors is possible (Fu et al. 2008; Kawamura et al. 2005).

Glyoxal chemistry has been studied extensively in the lab, and may provide a model of the reaction mechanisms important for the carbonyl compounds. Glyoxal reacts with OH to form glyoxylic, oxalic, acetic, formic, and other carboxylic acids, and may react with inorganic or organic species to form acetal oligomers, imidazoles, and other high molecular weight compounds (Carlton et al. 2007; Loeffler et al. 2006; De Haan et al. 2009; Galloway et al. 2009; Tan et al. 2009). Under low precursor concentrations of ~0.03-1 mM, these acids are the

dominant end products (Tan et al. 2009; Lim et al. 2010); at higher concentrations (~1-3mM), oligomers and HMCW have been observed (Carlton et al. 2007; Lim et al. 2010). Glyoxal may also react directly with H₂O₂ to form glyoxylic acid after photooxidation of intermediate 2-hydroxy-2-hydroperoxyethenal (Lee et al. 2011); glyoxylic acid, in turn, may react with OH to form oxalic acid (Lim et al. 2010), or with H₂O₂ to produce formic acid (Tan et al., 2009), which largely volatilizes upon droplet evaporation (Lee et al., 2011). These findings motivate our hydrogen peroxide-only control experiments in Sections 2.3 and 5.

Dark hydration and oligomerization reactions also occur with carboxylic compounds, causing partitioning into the particle phase (Kroll et al. 2005; Galloway et al. 2009; Ip et al. 2009). However, the thermal, reversible nature of these reactions, along with the lower number of oligomer subunits (as compared to photochemical products) allows easy re-evaporation, which, together with low formation rates, marginalizes the contribution of dark carboxyl-compound reactions to aqSOA mass (<1% of SOA mass; Ervens & Volkamer 2010). Aldol reactions may not be important due to their low rate constants in ambient conditions (Casale et al. 2007; Minerath & Elrod 2009), though conflicting studies exist (Lim et al. 2010; Nozière et al. 2010). Lastly, glyoxal and other carbonyls may react with ammonium and amines in the dark, but estimated yields for such reactions are ~10 times lower than total photochemical oxidation (Ervens & Volkamer 2010).

Methylglyoxal

Methylglyoxal (abbreviated Mgly) is another important aqSOA precursor formed – possibly in greater mass than glyoxal - from myriad anthropogenic and biogenic sources in amounts estimated at ~140 Tg y⁻¹ (Fu et al. 2008; Kawamura et al. 2005; Atkinson & Arey 2003; Liu et al. 2012); about 79% of methylglyoxal production is thought to arise from isoprene

oxidation, with acetone contributing significantly as well (Fu et al. 2008). In the aqueous phase, reaction with OH is the main methylglyoxal sink and produces compounds and oligomers similar to glyoxal (Altieri et al. 2008; Tan et al. 2010; Tan et al. 2012). At high concentrations (and especially in complex ambient mixtures), OH-organic reactions may also form organic radicals that react further and enhance HMWC complexity and mass (Ervens et al. 2011). Esterification of methylglyoxal has also been observed under OH oxidation (Altieri et al. 2008). While photolytic and hydrogen peroxide-initiated reactions may occur as discussed extensively in Chapter 5, they are not as important as hydroxyl radical reactions (Tan et al. 2012). While extremely abundant and ubiquitous, methylglyoxal is less studied than glyoxal; it is used in aqueous experiments as a proxy for early-generation oxidative products of common emissions (aromatics, monoterpenes, etc.).

Other Biogenic Compounds

Biogenic VOCs and biomass burning products are also involved in aqueous SOA formation. Isoprene oxidation forms glyoxal and other carbonyls as mentioned above, but also significant methacrolein (MACR) and methylvinylketone (MVK), which are less soluble than the carbonyl compounds (Iraci et al. 1999) but produce similar aqSOA yields in solution through surface reactions (Zhang et al. 2010; Huang et al. 2011; Liu et al. 2009). Also, O₃-MACR/MVK reactions, while slow and minimally productive in terms of aqSOA formation, produces hydrogen peroxide (H₂O₂), which can produce OH through photolysis (and/or Fenton reaction with Cu⁺ or Fe₂⁺), which in turn initiates further organic oxidation reactions producing aqSOA (Chen et al. 2007; Stefan & Bolton 1999). Soluble aldehydes formed in clouds from interstitial isoprene oxidation may also contribute to aqSOA (Lim et al. 2005). Total aqSOA from isoprene

is estimated to contribute 4-20% of global biogenic SOA mass, and may be more important, or even dominant, over forested areas (Lim et al. 2005).

Aqueous isoprene OH oxidation yields glyoxal and methylglyoxal at low concentrations ([isoprene] \approx 0.05 mM, Liu et al. 2009; Chen et al. 2007) and glyoxylic acid with carboxylic acid oligomers at higher concentrations (2-5 mM, El Haddad et al. 2009), with pyruvic acid as an intermediate compound that may react further with OH (Altieri et al. 2006). Some compounds, like pyruvic acid, may also photolyze to produce similar carboxylic acids or oxidants such as OH and H₂O₂ (Chen et al. 2007a; Guzman et al. 2006).

α -pinene

α -pinene and its major oxidative products pinonaldehyde (first generation) and pinonic acid (multiple generations possible) also form significant aqSOA (Kanakidou et al. 2005; Jang 1999). α -pinene has been used widely to represent ‘biogenic monoterpenes,’ and comprises \sim 25% of global monoterpene emissions, which themselves contribute up to 50% of emitted biogenic VOCs (depending on vegetation type, Kanakidou et al. 2005). Reaction with OH produces predominantly pinonaldehyde and pinonic acid isomers (Jang 1999; Vinckier et al. 1997), forming 50-80% of product mass (along with an unidentified carboxylic acids) during one dry chamber OH oxidation experiment (Winterhalter et al. 2003). As with glyoxal, OH oxidation may form a plethora of products including aldehydes, carboxylic acids, dicarboxylic acids, and possibly hydroperoxides (Hakola et al. 1994; Aschmann et al. 1998; Vinckier et al. 1997; Winterhalter et al. 2003; Nozière et al. 1999); a recent nuclear magnetic resonance study on bulk α -pinene aqueous oxidation (no aerosolization or drying) established major reaction products *trans*-sobrerol (alcohol functional groups), campholenic aldehyde (carbonyl-) and *trans*- and *cis*-carveol (alcohols; Bleier & Elrod 2013). Though O₃ is a dominant gas-phase α -pinene oxidant

(Nakayama et al. 2010), α -pinene products resulting from non-ozone reactions have been identified in ambient aerosol, suggesting that these other pathways may be more important (Claeys et al. 2004; Edney et al. 2003; Kubátová et al. 2000). α -pinene may also react productively with hydrogen peroxide in the gas phase (Claeys et al. 2004). That said, few studies have explored α -pinene aqueous chemistry, or that of its early oxidation products pinonaldehyde and pinonic acid; we employ pinonic acid, which has been observed in both chamber and ambient SOA (Yu et al. 1999; Kavouras et al. 1998).

Inorganic Precursors

Laboratory aqSOA experiments have also employed inorganic precursors and oxidants to better reflect the ubiquity of these compounds in the ambient atmosphere. Sulfate, nitrate, and ammonium are the most important ambient inorganic constituents, and have all been observed in aqSOA; we employ ammonium nitrate and ammonium sulfate salts in some of our single-precursor oxidations as explained in the relevant methodological and results sections.

Sulfur Compounds

Sulfate is fairly ubiquitous in tropospheric water, with sources including anthropogenic sulfur dioxide (SO_2) in urban areas and dimethyl sulfide from phytoplankton emissions in marine environments (Laj et al. 1997; Finlayson-Pitts & Pitts 2000; Seinfeld & Pandis 2006; Lovelock et al. 1972). Photo-oxidations of sulfate solutions with added glyoxal, methylglyoxal, α -pinene, and isoprene (among others) produce organosulfates and new HMWC with sulfate groups, likely after sulfate radical (SO_4^-) formation from reaction with OH (Nozière et al. 2010; Perri et al. 2010; Gómez-González et al. 2008); acid-catalyzed reactions are also thought to be important for organosulfur species formation, though acidity reduces the effective Henry's law constant for SO_2 (and yields of biogenic aqSOA formation in general, Froyd et al. 2010; Lim et al. 2010; Jang

et al. 2002; Valverde-Canossa et al. 2005; Tan et al. 2009; Surratt et al. 2007; Hatch et al. 2011b; Seinfeld & Pandis 2006). Nighttime organosulfate production from temperature-driven sulfur-species partitioning followed by aqueous oxidation may be significant (Hatch et al. 2011a). Esters of sulfate and IEPOX, a major isoprene oxidation product, have been found to comprise “one of the most abundant single organic compounds measured in atmospheric aerosol” (Froyd et al. 2010). Sulfate esters were observed in ambient aerosol and formed significantly in acidic α -pinene and isoprene + OH reactions by Surratt et al. (2007, not aqueous), though this is contradicted in the experiments of Zhao et al. (2006). Organosulfate species may act as aqueous processing tracers; for instance, hydroxymethanesulphonate (HMS) has been identified in ambient fog-processing events and found to form only through aqueous processes (Dall’Osto et al. 2009; Herckes et al. 2007) and favored at high pH (Rao & Collett 1995). Contributions of organosulfates to ambient OA may be significant. Perri et al. (2010) estimated that aqueous processing of glycolaldehyde by sulfate radical resulted in organosulfates comprising ~1% of total aqueous organic mass at cloud-relevant concentrations, but likely much more in aerosol water; we stress that this yield reflects only one of an array of abundant precursors, likely making the value above a lower bound on organosulfate contributions. As will be discussed in Chapter 5, organosulfur species fragment to HSO_x fragments in the AMS, precluding exploration of organosulfur formation here.

Nitrogen Compounds

Particulate nitrogen is also omnipresent and can be classified roughly into ammonium/amine (reduced) and nitrate/organonitrate (oxidized) species. Aqueous reaction of glyoxal with ammonium and amines may form imines and imidazoles in the first generation, which may form N-containing oligomers with themselves, glyoxal, and, significantly, aldehydes in the second

generation (De Haan et al. 2011; Carlton et al. 2007; Galloway et al. 2009; Shapiro et al. 2009; De Haan et al. 2009; De Haan et al. 2009; Nozière et al. 2009; Nozière et al. 2010; Kua et al. 2011). Amines, nitrate esters, nitroso compounds, and peptides have been identified in ambient fog (Herckes et al. 2007; Herckes et al. 2013). NO_x chemistry also contributes to aqSOA; for instance, high NO_x favors the production of carboxylic compounds (glyoxal, methylglyoxal) from monocyclic aromatic compounds (benzene, toluene, xylene; Sun et al. 2010), but suppresses SOA yield in the gas phase (Ng et al. 2007), suggesting that aqSOA and gasSOA may be important in different locations and conditions. Organonitrogen species often contribute significantly to wet deposition of nitrogen, which is of interest at our Rocky Mountain and Grand Teton National Park sites (Beem et al. 2010; Benedict et al. 2013; Williams et al. 2001), and techniques for estimating organic nitrogen from AMS data will be presented in Section 1.3.4.

Overall, the literature suggests that atmospheric conditions of high biogenic VOC, NO_x, humidity, and cloud water will form the most aqSOA mass (Ervens et al. 2011).

Common Difficulties in Aqueous SOA Experiments

One of the greatest shortcomings of the current aqSOA literature is the lack of atmospheric relevance in precursor and oxidant concentrations. It is well established that solution concentration has a large effect on both yields and product types, but experimental solution concentrations are somewhat constrained by current methodology, which must balance time resolution needs with sampling methodology (such as atomization used here) and instrument mass sensitivity.

Next, the simplified solutions used in many experiments may not reflect matrix effects (e.g. on mass yields), including complex organic oxidant cycling, that occur in ambient atmospheric water; the aqueous experiments herein have been designed to address this

shortcoming by exploring aqSOA production in collected ambient cloud water. The high aqSOA yields observed in ambient studies (and laboratory mixtures) have been attributed to unspecified ‘combinations of surface and bulk effects,’ but surface effects (i.e. rates of gaseous uptake at the surface and diffusion into the bulk droplet as affected by solute composition) have not been thoroughly investigated; an approach for evaluating surface effects is presented in Future Work.

Lastly, it is difficult to maintain suspended droplets in a reactor for atmospherically relevant photo-oxidation time; the relatively slower reactions occurring in dilute droplets (vs. aerosol water) may not have time to complete before the droplet is lost to the walls or sample lines; increasing [OH] to speed reactions may produce unrealistic reaction regimes. That said, short droplet lifetimes in clouds (~minutes) might render even short-residence-time experiments useful.

In the study of aqueous SOA production, mechanistic and kinetic information is possible only in controlled laboratory experiments; little is known about mass production in the complex ambient matrix. Chapter 5 presents aqueous SOA production from photo-oxidations of ambient cloud samples with and without added pinonic acid precursor as a first step toward reconciling laboratory kinetics and real atmospheric behavior (Section 2.3 and Chapter 5).

1.3 Common Organic Aerosol Types and Identification Thereof

1.3.1 Aerosol Instrumentation

It is difficult, to say the least, to find an instrument that captures the diversity of atmospheric particles, which range in size, concentration, content (refractory versus non-refractory, inorganics, and millions of organic compounds and isomers, Goldstein & Galbally 2007), and phase and participate in rapid transport and chemistry. The ideal instrument accurately determines particle size and molecular composition at high time resolution in low

concentration conditions for a broad range of particle types (organics, inorganics, refractory material, etc.). This section will review common analysis techniques for fine particles and defend the use of the high-resolution time-of-flight aerosol mass spectrometer (HR-ToF-AMS) for the applications presented here; a number of OA measurement reviews are available (Jacobson et al. 2000; McMurry 2000; Rudich et al. 2007; Hallquist 2009).

Filters

Filters have long been used to collect atmospheric particles. Advantages include generally lower cost (depending on analysis) and the ability to subject the filter and/or extracts to wide variety of analytical techniques (some of which may give high degrees of chemical specificity). Unfortunately, there are some serious caveats to filter use. First, the time-resolution of filter samples is generally low (~many hours-days) due to higher sample mass requirements for analytical techniques and/or low ambient concentration. Longer filter exposure times generally increase sampling artifacts such as contamination, adsorption of gases, and volatilization (McDow & Huntzicker 1990; Turpin et al. 1994). Denuding the sample stream to separate gaseous and particle phases generally enhances organic volatilization (Kamens & Coe 1977; Eatough et al. 1996); denuders for organic compounds exist but are often expensive, time-consuming to use, and have lower time resolution, though methods are improving (Krieger & Hites 1992; Fan et al. 2003; Tobias et al. 2007; Rowe & Perlinger 2010). During filter extraction (appropriate to the analytical technique), solubility compatibility between sample and solvent is necessary for complete extraction, limiting analysis of, for instance, insoluble species in a water-based solvent (Grosjean 1975). Detailed sizing is rarely accomplished in filter sampling beyond PM_{2.5} (for fine-mode) size cuts at the cyclone, with the exception of multi-stage impactors such as the MOUDI (Marple & Rubow 1984; McMurry & Zhang 1989).

Analytical techniques used with filters (and sometimes on their own, in on-line capacities) include nuclear magnetic resonance (NMR) spectroscopy and Fourier transform infrared spectroscopy (FTIR, capable of functional group quantitation), which may identify many compound classes but have poor time resolution and (often) quantitation (Havers et al. 1998; Decesari et al. 2000; Decesari et al. 2001; Decesari et al. 2007). Gas chromatography/mass spectrometry (GC/MS) and associated techniques (GCxGC/MS, etc.) achieve molecular identification (with fair time resolution if coupled with an ambient inlet instead of a filter sample), but capture only a small percentage of total ambient compounds (Hamilton et al. 2004; Welthagen et al. 2003). Electrospray ionization (ESI, often combined with mass spectrometry) uses liquid sample and so can be paired with liquid chromatography, capillary electrophoresis, etc. beforehand for great molecular specificity, but quantitation is difficult and time resolution is limited by the initial separation (Iinuma et al. 2004; Gómez-González et al. 2008; Surratt et al. 2008; Altieri et al. 2009). Ion and other liquid chromatography (IC and LC, paired with MS, conductivity, or pulsed amperometric detection) gives detailed chemical information, but has, again, a liquid-sample requirement and lower time resolution (Anttila et al. 2005; Römpf et al. 2006; Iinuma et al. 2007; Surratt et al. 2007). Various thermal/optical carbon analysis techniques such as the ubiquitous Sunset Labs instrument can determine elemental versus organic carbon (EC vs. OC), etc. from filter samples (Bae et al. 2004).

To study the transport and chemical evolution of OA, higher measurement time resolution than can be achieved with filters is required. Continuous particle measurement systems are summarized below.

Particle-into-Liquid-Sampler (PILS)

The PILS instrument continuously collects ambient particles, grows them into droplets in a super-saturated environment, and collects the droplets via impaction into a liquid stream; the liquid sample stream can be analyzed for inorganics, water-soluble organic carbon (WSOC), or more specific organic molecules using liquid chromatography at a time resolution of ~10-17 minutes (Weber et al. 2001; Orsini et al. 2003; Sullivan 2004; Sorooshian et al. 2006). The PILS is a great advancement in on-line analysis; however, the bulk WSOC is molecularly non-specific.

Mass Spectrometers

Mass spectrometers are popular for on-line analysis because of their high mass- and time-resolution and potential for quantitative analysis. The most common is the aerosol mass spectrometer (examined later in this section), but many other variations exist (Noble & Prather 2000; Sullivan & Prather 2005; Canagaratna et al. 2007). Briefly, ambient particles are focused into an interior vacuum (except CIMS, below) and separated from attendant gases, vaporized, ionized, and detected via (commonly) quadrupole or time-of-flight mass spectrometry. Sample types may include single-particle analysis, as in laser-ablation single-particle mass spectrometers with ToF-MS detection (McKeown et al. 1991; Noble & Prather 1996; Murphy et al. 2006; Gross et al. 2006), and total (submicron) particulate as in the Aerodyne AMS with light-scattering or Particle-Time-of-Flight (PToF) size determination. Sampled particle sizes are often limited to ~60-600nm, as discussed later, though the nano aerosol mass spectrometer (NAMS) may be used for particles < 20nm (Smith et al. 2005; Wang et al. 2006).

The ionization technique used in a given mass spectrometer determines the types of data produced and therefore the proper application of the instrument. 'Hard' techniques such as the electron impact (EI) ionization used in the AMS produce high signal, which improves the limit

of detection (important in low-mass ambient conditions) but fragments parent organic compounds, obliterating much chemical information; statistical multivariate techniques such as positive matrix factorization must be used to determine types of organic molecules present, as outlined in Section 1.3.2. The history and ubiquity of EI has led to development of mass spectral databases which can be used to explore chemical content; EI within the AMS produces spectra quite similar to these databases, “albeit with more fragmentation [which is notable in] the greatly enhanced intensity of the CO_2^+ ion for species such as carboxylic acids in the AMS, likely due to pyrolysis occurring on the vaporizer” (Aiken et al. 2007).

‘Soft’ ionization techniques preserve more chemical information but are often specific to a certain molecule type (preventing broad composition determination) or incompatible with the sample and inlet types used for ambient particles (for instance, electrospray ionization uses liquid sample). The thermal-desorption chemical ionization mass spectrometer (TD-CIMS) was recently developed to operate at ambient inlet pressure, preventing the drying that may accompany high vacuum in other instruments (Zelenyuk et al. 2006), but with a more limited range of analytes than the AMS (Slusher 2004; Turnipseed et al. 2006; Wolfe et al. 2009; Zheng et al. 2011). Other soft ionization techniques currently in use include vacuum ultraviolet (VUV) photo-ionization, and proton transfer reaction mass spectrometry (PTR/MS, another form of chemical ionization, Northway et al. 2007; Dreyfus & Johnston 2008; Hearn & Smith 2006; Hellén et al. 2008). The recently developed Extractive ESI-MS couples electrospray ionization/mass spectrometry with a continuous ambient sample stream, yielding extremely high mass- and time- resolution (~seconds) measurements of aerosols and/or gases and is quantitative for SOA in which all particle components are soluble in the ESI solvent (such as in published lab experiments, Horan et al. 2012; Doezema et al. 2012; Gallimore & Kalberer 2013). Ambient

aerosols have not been measured using this system; quantitiveness and/or comprehensive characterization could be compromised if particles are not completely soluble in the chosen ESI solvent.

The Aerodyne High Resolution Time-of-Flight Aerosol Mass Spectrometer (HR-ToF-AMS)

The Aerodyne High Resolution Time-of-Flight Aerosol Mass Spectrometer (HR-ToF-AMS) measures size and composition of submicron non-refractory particles with high time- and mass-resolution (Jayne et al. 2000; Drewnick et al. 2005; Decarlo et al. 2006). Briefly, an aerodynamic lens focuses ambient aerosol into the interior vacuum, where gases diffuse from the particle beam and are discarded. Groups of particles isolated by a spinning chopper wheel are separated by size inertially as they traverse the Particle Time-of-Flight region. Particles are vaporized in a 600 °C oven and ionized via 70 eV electron impact ionization; the resulting fragments are separated by mass in the Time-of-Flight Mass Spectrometer and counted with a Multichannel Plate Detector. More detail is given in Section 2.1.

Extensive comparison of HR-ToF-AMS to established measurement techniques suggests the AMS to be capable of quantitative measurements of a breadth of compounds, given proper calibration (Section 2.1, Table 1-1). Sulfate, ammonium, and nitrate generally agree quite well with the PILS-IC instrument, even with the difference in size cut (\sim PM₁ for AMS, while PILS usually has a PM_{2.5} cyclone; agreement may arise from a primarily submicron fine mode in the cited works). Figure 1-3 shows inorganic species measured via AMS, PILS-IC, and 24-hour average filter (with PM_{2.5} cyclone and backup filters/denuders for volatilized particulate) at the Rocky Mountain National Park site; no PILS data are available for the Grand Teton or aqueous SOA campaigns. Sizing is consistent with SMPS and DMA (Jayne et al. 2000; Zhang et al. 2005a).

Table 1-1: Comparisons between the AMS (y) and various continuous-measurement instruments (x) for sulfate, ammonium, nitrate, organic values, and total mass. Multiple slope and correlation coefficient values indicate multiple data sets or replicates within the given reference. *HSPH: Harvard School of Public Health continuous sulfate monitor. **(Khlystov et al. 1995).

Species	Instrument	Slope	r ²	Citation
Sulfate	PILS	1.01	0.91	(Drewnick et al. 2003)
	PILS	~1	0.79	(Jimenez 2003)
	PILS	0.90,1.24	0.85,0.88	(Takegawa et al. 2005)
	PILS	1.04	0.56	(Allan et al. 2004)
	PILS	0.99,1.32	0.91,0.91	(Hogrefe et al. 2004)
	PILS	1.00	0.88	herein, Rocky Mountains
	R&P 8400S	1.01	0.92	(Drewnick et al. 2003)
	R&P 8400S	0.99,0.99	0.89,0.92	(Hogrefe et al. 2004)
	R&P 8400S	0.75	0.69	(Zhang et al. 2005)
	HSPH*	1.03	0.94	(Drewnick et al. 2003)
Ammonium	PILS	1.10	0.57	(Allan et al. 2004)
	PILS	0.95,1.26	0.96,0.89	(Takegawa et al. 2005)
	PILS	0.80	0.50	herein, Rocky Mountains
	5-hr PM _{2.5} Steam Sampler**	1.07	0.72	(Zhang et al. 2005)
Nitrate	PILS	1.15,1.81	0.95,0.61	(Hogrefe et al. 2004)
	PILS	1.00	0.37	(Allan, Bower, et al. 2004)
	PILS	1.12,0.81	0.99,0.95	(Takegawa et al. 2005)
	PILS	1.29	0.76	herein, Rocky Mountains
Total Mass	TEOM PM _{2.5}	0.66	0.71	(Zhang et al. 2005)
	TEOM PM _{2.5}	0.59	0.91	(Drewnick et al. 2003)
Size Distributions	SMPS, MOUDI	Qualitatively good, mass disagreement from size cut		(Zhang et al. 2005)
Organic C	Sunset EC/OC	1.14,1.21	0.72,0.87	(Kondo et al. 2007)
Organic Mass	FTIR	1.06	0.84	(Russell et al. 2009)

Organic mass and organic carbon measurements are harder to evaluate because most OM & OC measurements are made with much lower time resolution, but favorable comparisons have been made by averaging AMS data to match filter sampling times (using sunset OC, Zhang et al. 2005a; Kondo et al. 2007). More recently, consistent OM measurements have been derived between FTIR and AMS (Russell et al. 2009). Few direct comparisons between AMS ON and other instruments have been made, largely because methods for quantifying ON with AMS are not reliable. The AMS is also not able to vaporize non-refractory material such as elemental

carbon, but since refractory fresh combustion products (hydrocarbon-like organic aerosol, or HOA, which might indicate the presence of non-refractory material) are not observed at these relatively remote sites, there is probably little effect on organic quantitation herein.

The field campaigns herein are motivated by the impacts of nutrient deposition on sensitive environments, which necessitates a complex analysis of particle chemical evolution and transport; it is important to capture as much chemical and sizing detail as possible with high time resolution in order to combine the data with meteorological information for source apportionment. Filter-based techniques are eliminated for their low time resolution and artifacts; the AMS is selected over PILS-IC for its sizing capability, higher time resolution, and more comprehensive speciation.

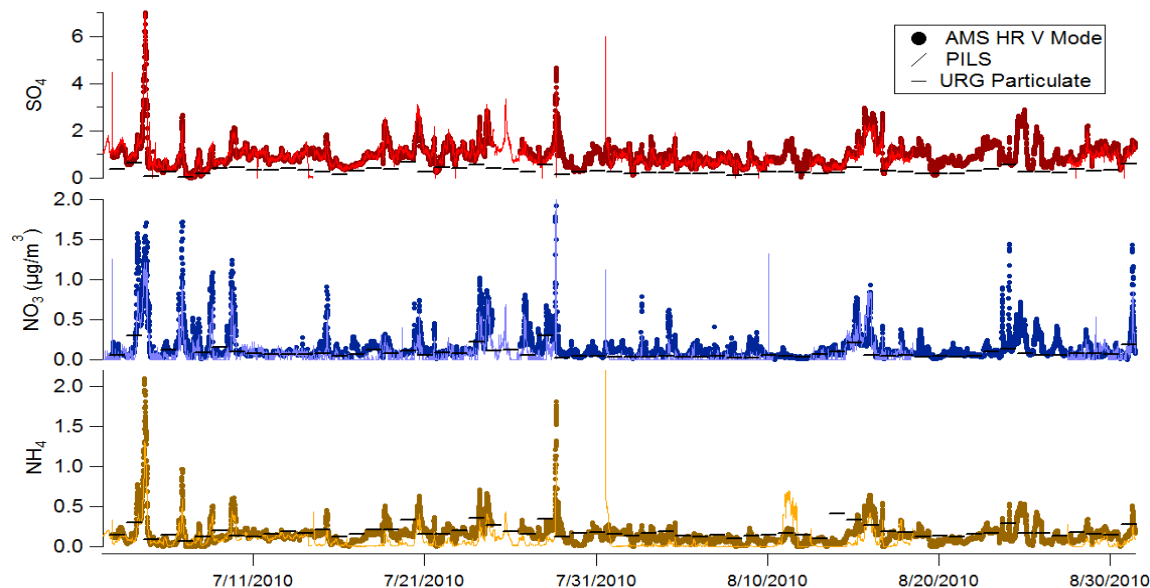


Figure 1-3: Time series of inorganic particulate components from HR-ToF-AMS, PILS-IC, and URG (denuder-filter system) from July-August, 2010, at Rocky Mountain National Park (Chapter 3).

1.3.2 Identifying Types of Organic Aerosol: Factorization Techniques

As outlined above, the AMS has many advantages for exploring ambient aerosol; however, the fragmentation induced by electron impact ionization destroys organic parent

molecules in the particle, leaving a complex mixture of fragments. To glean more organized chemical information, statistical multivariate techniques such as Positive Matrix Factorization (PMF) and Multiple Component Analysis (MCP) may be used to separate fragments into component types, or ‘factors,’ contributing to the receptor dataset as a function of time; each factor has a static chemical profile of time-correlated species (for instance an organic mass spectrum or particular combination of elements) that varies in contribution to total mass over time. High-resolution data (individual fragment masses in the form of mass spectra) are used for PMF input. Since we have only receptor data, use (and therefore review) of source-receptor techniques such as Chemical Mass Balance (CMB) is precluded.

AMS data form a matrix ‘ORG’ of mass spectra (columns, where vector elements are high-resolution fragment masses) versus time (rows, where vector elements are sample time). Multivariate techniques define factor mass spectra (MS) with varying time series (TS) such that the original input matrix ORG is reconstructed, with residual mass E (see Figure 1-4 from: Ulbrich et al. 2009; Zhang et al. 2011). In matrix notation:

$$\text{ORG} = \text{TS} \times \text{MS} + \text{E} \quad (\text{Equation 2})$$

Factorization algorithms vary based on how they solve Equation 2 for TS and MS while minimizing E, usually through some sort of iterative least-squares regression. There are multiple possible solutions for any given input matrix as linear transformations, or ‘rotations,’ of the solution matrix reallocate mass between the factor mass spectra and time lines; each factorization technique has a different way of determining the ‘best’ rotation or solution space for a given dataset. Common multivariate techniques are outlined broadly below; additional details on PMF are provided in Section 2.2.

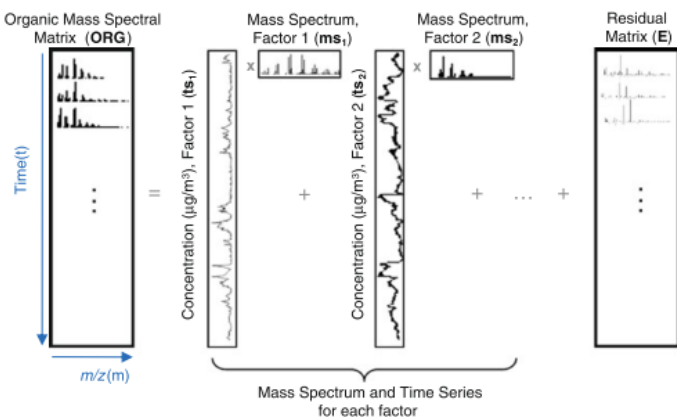


Figure 1-4: “Schematic diagram of bilinear factor analysis of a mass spectral matrix of an organic aerosol (ORG). The time series of the factors (ts_n) make up the matrix TS and the mass spectra of the factors (ms_n) make up the matrix MS. The differences between the measurements and the modeled results are represented as the residual matrix E.” (Zhang et al. 2011)

Principal and Multiple Component Analysis (PCA & MCA)

Principal component analysis is an eigenvector-based technique that, in effect, uses error in a row or column to scale (weight) the given row or column in the least-squares regression, minimizing residual over the row- or column- as a whole (not for individual data points in the matrix, see Hopke 2003); this approach may reduce precision, leading to data-matrix reconstructions that are not as accurate as the technique used in PMF, below, since data values with low error, and thus greater physical value, are down-weighted along with less-precise values (Paatero & Tapper 1993). PCA analysis of AMS observations typically uses time series of m/z 44 (mostly CO_2^+ from oxygenated compounds such as carboxylic acids) and m/z 57 ($C_4H_9^+$ from hydrocarbons) as *a priori* indicators of oxygenated OA (OOA) and hydrocarbon-like OA (HOA, as a proxy for primary OA), respectively, in a two-factor solution (Zhang et al. 2005; Zhang, Alfarra, et al. 2005; Volkamer et al. 2006; Takegawa et al. 2006). Though PCA is useful to distinguish primary and secondary organic fractions, more than two organic factors are often present; OOA, especially, is often comprised of two or more oxygenated sub-types as will be explored later in this section.

Multiple component analysis is a variation of PCA capable of separating ≥ 2 factors that has been widely applied to ambient AMS datasets (Zhang et al. 2007; Bae et al. 2007; Cottrell et al. 2008; Ziemba et al. 2010). MCA has been found to compare well with PMF for a number of ambient datasets (Ulbrich et al. 2006; Canagaratna et al. 2007), although PMF is sometimes able to resolve more factors in a given dataset (Ng et al. 2011). UNMIX is another version of PCA that uses the times when a factor is not contributing to component mass to bound a potential solution space and other physical constraints to choose reasonable solutions (Henry 1987; Henry & Kim 1990; Kim & Henry 1999; Kim & Henry 2000).

Positive Matrix Factorization (PMF)

Positive matrix factorization is a positivity-constrained, receptor-only (no *a priori* inputs) error-weighted (fragments with low signal:noise have less weight in the construction of factor mass spectra than those with strong signal), least-squares regression algorithm (Section 2.2, Paatero & Tapper 1994; Paatero 1997; Paatero & Hopke 2003; Lanz et al. 2007; Slowik et al. 2010). In contrast to PCA, scaling in PMF is performed on each data point in the matrix (through the error estimate for that point), improving data matrix reconstruction by giving more weight to species that are known with more precision (Paatero & Tapper 1993). The positivity constraint is enforced by applying a ‘penalty function’ to solution points that approach zero, increasing their error value and thus steering the solution away from the near-zero value (Paatero et al. 2002; Currie et al. 1984). PMF factorizations are found to be optimized for input containing more than 100 samples (Pandolfi et al. 2008; Norris & Vedantham 2008); the Grand Teton and Rocky Mountain studies had ~4,600 and 15,200 samples used in PMF, respectively. A three-dimensional version of PMF incorporating particle size has been developed, but was not applied to these datasets (Ulbrich et al. 2012); another PMF algorithm variation deals with datasets

containing different time resolutions, such as daily filters analyzed alongside online techniques (Zhou et al. 2004).

Two main PMF algorithms have been developed: PMF2, used here, and ME2 (multilinear engine 2, Paatero 1999). PMF2 is older and somewhat more constrained in possible input formats, while the ME2 allows two or more indexes (only two – time and mass – are used in the diagram shown in Figure 1-4) on each array, allowing a much broader combination of input types such as particle size (Zhou 2005), gaseous component concentrations (Rizzo & Scheff 2007; Wu et al. 2007), and/or meteorological information (Paatero 1999; Buzcu-Guven et al. 2007; Chan et al. 2011).

The main criticism of PMF is that the user must define the most appropriate number of factors based on somewhat subjective comparisons of factors to each other, ‘common’ factors from other studies, and ancillary data such as inorganic tracers (discussed in methods Section 2.2). However, PMF has been shown to correctly factorize synthetic datasets, and the reliability of PMF analyses can be enhanced greatly through careful attention to data preparation and interpretation techniques (Allan et al. 2004; Ulbrich et al. 2009; Paatero & Hopke 2003; Paatero et al. 2002); Zhang et al. (2011) provide a workflow to optimize PMF analysis based on other works (Reff et al. 2007; Ulbrich et al. 2009). Through the improved scaling technique described above, PMF is more quantitative and resolves more abundant and physically realistic factors than MCA (Huang et al. 1999), and compares well to CMB and other apportionment techniques (Zhang et al. 2005; Takegawa et al. 2006; Docherty et al. 2008; Aiken et al. 2009); PMF also runs faster than some of its contemporary programs, including the Alternating Least Squares algorithm (Hopke et al. 1998). Lastly, PMF can resolve comparatively low-mass factors contributing $\geq 5\%$ of total mass (Ulbrich et al. 2009).

There are two main types of PMF2 algorithms; they differ mainly in how non-negativity and missing data points are managed (Chan et al. 2011). For the AMS PMF Evaluation Tool (PET, $\geq v2.03A$, Ulbrich et al., 2009) used herein, values approaching zero are subject to a progressive penalty function such that the solution is ‘steered’ away from the edges of the positive solution space as described above. In contrast, the EPA PMF algorithm merely requires that the solution is non-negative, allowing some solutions that might be disallowed in PET PMF (Kim & Hopke 2007; Norris & Vedantham 2008). In the PET PMF, non-existent AMS data points contain not-a-number (nan) values. Since AMS data sets are very large (~5,000 mass spectra/month, herein), all nan values are simply removed from the analysis (Paatero & Hopke 2003; Ulbrich 2011). In contrast, the US EPA PMF tool inserts the median value of the given component into nan data points and increases the error to 4x the median value, down-weighting the point in the least-squares regression and possibly affecting the average mass contribution of the given components in the factor (Norris & Vedantham 2008; Chan et al. 2011). However, despite these differences and resulting slight inconsistencies between average factor concentrations in datasets analyzed with both programs, PET and EPA PMF algorithms produce factors similar in number and content that are within 5-95% uncertainty of each other and result in similar conclusions about sources of local aerosol (Kim & Hopke 2007).

Common Organic Factors Derived from PMF

PMF is useful for resolving types of organics (though not flawless, as will be explored in our Rocky Mountain dataset). The remainder of this section summarizes common organic factors relevant to the current work derived from the >125 published manuscripts on the subject (compiled in: Zhang et al. 2007; Zhang et al. 2011; Ulbrich 2011).

Many studies have sought to find reliable markers for the combustion or oxidation of various materials and species, including biomass burning, which is a significant source of atmospheric content (both gaseous and particulate) globally. Biomass burning organic aerosol (BBOA) may be identified by fragments of levoglucosan ($C_6H_{10}O_5$) and other anhydrosugars, which are products of cellulose combustion, in the ambient mass spectra at m/z 60 ($C_2H_4O_2^+$), m/z 73 ($C_3H_5O_2^+$), m/z 137, and m/z 167 (Simoneit et al. 1999; Schneider et al. 2006; Weimer et al. 2008; Alfarra et al. 2007; Mohr & Huffman 2009); laboratory studies indicate that these spectral markers are consistent across a wide range of wood types and combustion conditions (Weimer et al. 2008; Grieshop et al. 2009). Ambient PMF-derived factors that contain these markers are called ‘biomass burning organic aerosol’ (BBOA, Alfarra et al. 2007; Weimer et al. 2008; Aiken et al. 2009). BBOA is sometimes correlated with potassium (K), another known biomass combustion tracer (Fuzzi et al. 2007; Echalar et al. 1995; Lee et al. 2010).

Other common classifications are based on organic compounds’ degrees of oxidation. Least oxidized is Hydrocarbon-like Organic Aerosol (HOA), which is produced chiefly by fuel combustion, distinguished by hydrocarbon chains at m/z 57 ($C_4H_9^+$), often used as a proxy for primary organic aerosol, and not observed in the campaigns herein (Figure 1-5, Zhang et al. 2005b & 2005c; Lanz et al. 2007 & 2008; Mohr et al. 2009). Semi-Volatile Oxidized Organic Aerosol (SV-OOA or OOA-II) is somewhat oxidized and its spectrum is characterized by the predominance of m/z 43 ($C_3H_7^+$ or CH_3CO^+) over m/z 44 (CO_2^+) (Lanz et al. 2007; Ulbrich et al. 2009). Lastly, Low-Volatility Oxidized Organic Aerosol (LV-OOA or OOA-I) describes highly oxidized aerosol with signal at m/z 44 (CO_2^+) greater than that at m/z 43 (Lanz et al. 2007; Ulbrich et al. 2009). Due to oxidation during transport, OOA factors are observed more

frequently than HOA factors in rural areas (Zhang et al. 2007). Thus, organic factors illustrate the aerosol's degree of oxidation, which may help to identify important particulate sources.

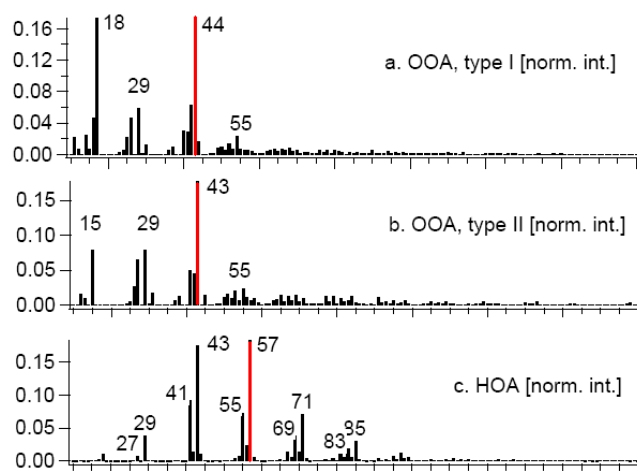


Figure 1-5: “Spectra of...PMF factors (interpreted as the denoted source profiles) calculated by...PMF.” (Lanz et al. 2007)

1.3.3 Changes in Organic Composition: Elemental and Fragment Analyses

While the factors identified by PMF can provide valuable information about aerosol transport and possible sources, they have, by definition, static mass spectra, which preclude direct observation of changes in organic composition during, for example, biomass burning events (which are observed in both field campaigns herein). Ratios of content-indicating fragments to total organic mass may be used to explore organic evolution; elemental analysis (EA) can be applied to AMS data to explore changes in oxygenation and, in laboratory studies, important reaction regimes (carboxyl group addition, etc.) through movement in the van Krevelen (O:C vs. H:C) diagram.

Fragment Ratios to Total Organic Mass

The ratios of total mass at m/z 43 or m/z 44 to total organics (f_{43} or f_{44} , respectively) are among the most widely used oxygenation metrics for AMS data. Mass at m/z 43 is overwhelmingly $C_3H_7^+$ from hydrocarbons and $C_2H_3O^+$ from carbonyls, while CO_2^+ from

carboxylic acids usually dominates at m/z 44, though $C_2H_4O^+$ (~carbonyls) may also contribute (Allan 2003; Alfarra 2004; Alfarra et al. 2004; Allan et al. 2004; Zhang et al. 2004; Canagaratna et al. 2004; Zhang et al. 2005; Duplissy et al. 2011); while it is important to use total mass at a given m/z (not dominant fragment mass) in f -ratio calculations for consistency with the literature, either low- and high-resolution UMR data may be used fairly equivalently. Ambient aerosols are generally observed to inhabit a triangular region in f_{43} vs. f_{44} space and progress toward higher f_{44} and lower f_{43} (the ‘top’ of the ‘ambient triangle’) as they are oxidized from hydrocarbons to carbonyls, and from carbonyls to carboxylic acids, indicating that oxidation increases composition homogeneity (Figure 1-6, Ng et al. 2011). Movement in this space will be discussed in more detail in the results chapters.

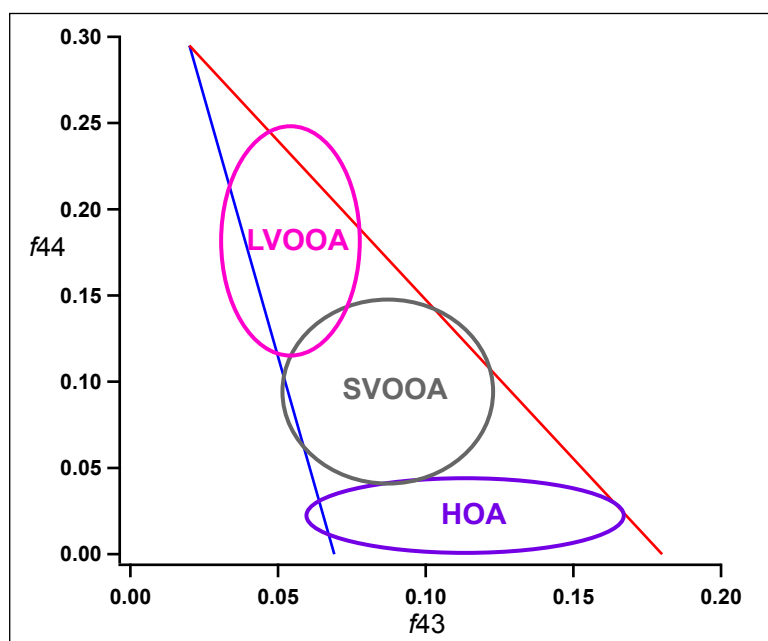


Figure 1-6: f_{43} versus f_{44} triangle diagram with typical ranges for given organic aerosol or data type from the literature, adapted from Ng et al. (2011).

Elemental Analysis of AMS Data

The Analytic Procedure for Elemental Separation (APES) software used for AMS EA counts elemental contributions from CH, CHO, CHON, CHN, and CS fragment families

($\geq 1.04A$, Donna Sueper, based on Aiken et al. 2007; Aiken et al. 2008). The mass of a given element X (M_x) is quantified via (Chhabra et al. 2010):

$$M_x = \sum_i^{m/z_{\max}} I_i \frac{m_x}{m_i} \quad (\text{Equation 3})$$

where I_i is signal from the i^{th} X-containing ion, m_x is the atomic mass of X, and m_i is the mass of the i^{th} singly charged fragment. Then, elemental ratios such as O:C or, more generally, X/Y, can be expressed as:

$$X/Y = \alpha_{X/Y} \frac{M_x/m_x}{M_y/m_y} \quad (\text{Equation 4})$$

where $\alpha_{X/Y}$ is a calibration factor arising from differential ionization probability of given elements, which has been determined in the laboratory by comparing NIST to AMS spectra for a range of 59 atmospherically-relevant organic standards including hydrocarbons (saturated, unsaturated, and aromatics), alcohols, carboxylic acids, aldehydes, esters, peroxides, anhydrides, carbohydrates, amines/amides, organic nitrites, and nitriles (Aiken et al. 2007).

Under electron impact ionization, single or plural positive ionization of a molecule may induce fragmentation (single or plural) leaving one or more fragments with a positive charge; the remaining neutral fragments are not held by the induced electromagnetic field and are thus lost to the vacuum. A number of papers have explored the preferential loss of electronegative groups in neutral fragments, finding that elements are lost in a fairly predictable and therefore correctable way (Aiken et al. 2007; Aiken et al. 2008; Chhabra et al. 2010; Rollins et al. 2010; Chhabra et al. 2011). Generally, as compounds fragment under electron impact ionization, O is lost to the neutral fragment preferentially because of its electronegativity (though not overwhelmingly; the slope with thermal EA is ~ 0.86 , Aiken et al. 2007); a dearth in hydrogen may arise from neutral

losses and/or the failure to report $m/z < 20$ fragments in the NIST mass spectra (and $m/z < 12$ in the AMS).

Corrections ($\alpha_{X/Y}$) are built into the AMS elemental analysis software, which also quantifies organic oxygen (as opposed to that in gas-phase and inorganic molecules); in the APES EA software, corrections include: $\text{CO}^+ = \text{CO}_2^+$; $\text{H}_2\text{O}^+ = 0.225 * \text{CO}_2^+$; $\text{HO}^+ = 0.25 * \text{H}_2\text{O}^+$; $\text{O}^+ = 0.04 * \text{H}_2\text{O}^+$ (Aiken et al. 2008). Some researchers have preferred to remove the influence of oxygen for other applications, but the oxygen content of ambient aerosol is highly relevant to its content and chemistry (Pang et al. 2006). The fragmentation table is altered on a case-by-case basis to correct for other elemental contributions from gaseous CO_2 , etc. as discussed in the methods (Aiken et al. 2008). Error estimates for the elemental ratios are: O:C (31%), H:C (10%), N:C (22%), and OM/OC (6%) (Aiken et al. 2007).

EA does not attempt to estimate organic contributions to nominally inorganic fragments such as NO^+ , NO_2^+ , SO^+ , and SO_2^+ that may arise from both organic and inorganic parents, assuming a relatively small contribution of organic N and S in ambient aerosol (Surratt et al. 2007). This may be a fair assumption during periods when inorganic sulfate and nitrate are highly dominant, but ambient aerosols sometimes contain significant organic nitrogen (ON) and organic sulfur (OS) as outlined earlier; ON is explored through relevant fragment timelines and other techniques as presented in Section 1.3.4, while OS species overwhelmingly fragment to nominally inorganic HSO_x in the AMS and thus cannot be quantified (Farmer et al. 2010). Another source of EA error is differences in relative ionization efficiency (RIE) between reduced and oxidized species, which are normally not differentiated in the fragmentation table governing such calculations (Jimenez 2003); new software updates allow differentiation of PAHs, but since fairly oxygenated species were observed in the experiments herein, this option was not

employed. Lastly, while AMS EA is not as accurate as traditional thermal methods, it is also not subject to artifacts such as organic adsorption to and volatilization from filters and requires far less sample mass (Turpin et al. 1994; Aiken et al. 2008).

The van Krevelen Diagram: O:C vs. H:C Space

The van Krevelen diagram (O:C vs. H:C) can indicate bulk changes in oxygenation in ambient datasets and may be used to explore reaction mechanisms in isolated air masses, such as chamber reactions (van Krevelen 1950; Kim et al. 2003; Heald et al. 2010; Ng et al. 2011).

Details regarding interpretation of the van Krevelen diagram and comparison to existing ambient datasets will be expanded in relevant results sections, but a general overview is provided here. In short, common OA types (to which PMF factors can be analogized) inhabit given regions in the diagram: HOA generally has H:C of >1.5 with $O:C < 0.4$; SV-OOA ranges from $H:C = \sim 1.3-1.6$ and $O:C = \sim 0.1-0.6$; while for LV-OOA, $H:C = \sim 1.1-1.5$ while $O:C = \sim 0.5-1.1$ (Figure 1-7, Pang et al. 2006; Aiken et al. 2008; Kroll et al. 2009; Ng et al. 2010; Huang et al. 2011). A summary of elemental analysis of ambient AMS datasets can be found in Table 1-2.

As an isolated particle population oxidizes, the slope of movement in van Krevelen space can be indicative of general reaction mechanisms (Figure 7, e.g. Heald et al. 2010). Cognizing that these reactions usually involve replacement of a hydrogen atom, a slope of 0 (line a, Figure 1-7) would indicate alcohol or peroxide addition, which add O without changing the number of H. Slopes of -0.5 (line b, Figure 1-7) are indicative of either carboxylic addition with C-C bond breakage or addition of both acid and alcohol/peroxide functional groups without fragmentation (total 1 H loss per 2 O addition). Slope = -1 is indicative of carboxylic acid or hydroxycarbonyl addition (line c, Figure 1-7), while slope = -2 arises from the replacement of aliphatic carbon by a carbonyl group to form an aldehyde or ketone (-2 H + 1 O, line d, Figure 1-7).

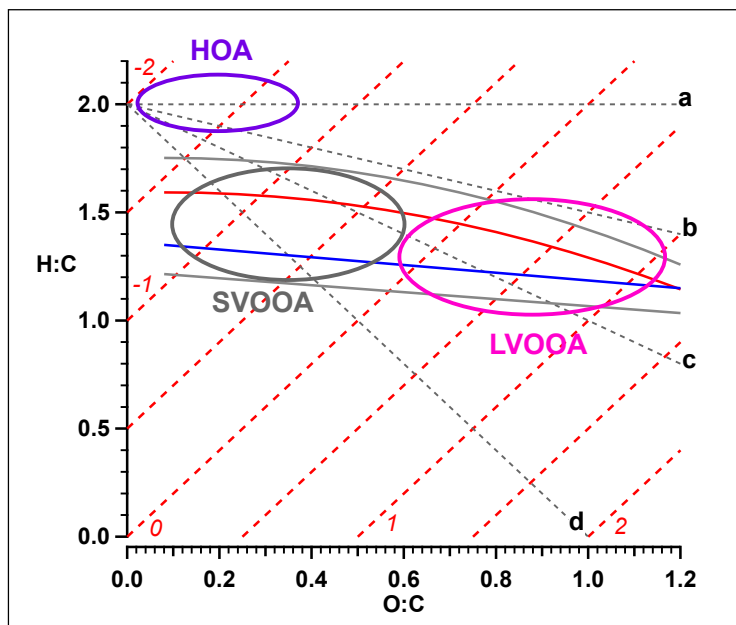


Figure 1-7: The van Krevelen diagram with transposed ‘ambient triangle’ from Ng et al. (2011) and regions typically inhabited by the given OA type. Dashed red lines and red numbers are oxidation states of carbon ($OS_C = 2 \cdot O:C - H:C$, Kroll et al. 2011); grey lines are +/- 20% error on the bounds of the triangle, from general AMS quantification error.

Elemental analysis can also be compared to other oxidation metrics such as f_{43} versus f_{44} , which was recently transposed onto the van Krevelen diagram by empirical parameterization of f_{43} versus H:C (polynomial) and f_{44} versus O:C (linear) for a wide range of ambient and chamber OA that were analyzed via high-resolution AMS (Aiken et al. 2008; Docherty et al. 2008; Aiken et al. 2009; DeCarlo et al. 2010; Chhabra et al. 2010; Ng et al. 2011; Chhabra et al. 2011; Sun et al. 2011). At very low levels of oxidation (high f_{43}), this parameterization does not seem to hold, probably because the dominant molecular types - simple aromatics without alkyl groups - have an $H:C \approx 1$, while only slightly more oxidized molecules may have $H:C \approx 1.5$ in a roughly stepwise relationship (Ng et al. 2011); Ng et al. found the parameterization to be valid when $f_{43} < \sim 0.20$ (and/or $f_{44} > 0.05$), which holds for most ambient datasets including those herein. Since all datasets in this work are high resolution, we do not use this parameterization for

data analysis, but merely to transpose the ambient triangle into van Krevelen space for comparison with the literature.

Table 1-2: Published elemental ratios for given sampling conditions and/or PMF factor. *Ng et al. (2010) summarizes 43 ambient AMS datasets worldwide.

Ratio	Value or Range	OA Type	Reference
OM:OC	1.55	BBOA	(Huang et al. 2011)
	1.65	SV-OOA	(Huang et al. 2011)
	1.6-1.87	Urban Ground Site	(Aiken et al. 2008)
	1.8-2.0	SV-OOA (downwind urban)	(Aiken et al. 2008)
	1.99	LV-OOA	(Huang et al. 2011)
	2.3-2.5	LV-OOA (downwind urban)	(Aiken et al. 2008)
	2.4-2.8	Downwind/Aged Urban	(Aiken et al. 2007)
O:C	<0.05	HOA	(Ng et al. 2010)*
	0.05-0.1	HOA	(Aiken et al. 2008)
	0.16-0.76	Ambient Urban	(Aiken et al. 2008)
	0.3-0.4	Biomass Burning	(Aiken et al. 2008)
	0.26	BBOA	(Huang et al. 2011)
	0.35±0.14	SV-OOA	(Ng et al. 2010)*
	0.39	SV-OOA	(Huang et al. 2011)
	0.5-0.6	SV-OOA	(Aiken et al. 2008)
	0.64	LV-OOA	(Huang et al. 2011)
	0.73±0.14	LV-OOA	(Ng et al. 2010)*
	0.8-1	LV-OOA	(Aiken et al. 2008)
	1-1.2	Downwind/Aged Urban	(Aiken et al. 2007)
	H:C	0.6-1	LV-OOA
1.3		LV-OOA	(Huang et al. 2011)
0.8-1.1		SV-OOA	(Aiken et al. 2007)
1.48		SV-OOA	(Huang et al. 2011)
1.62		BBOA	(Huang et al. 2011)
1.4-1.9		Urban	(Aiken et al. 2008)
N:C	0.00-0.09	Urban	(Aiken et al. 2008)
	0.01-0.03	Rural	(Huang et al. 2011)

1.3.4 Aerosol Organic Nitrogen

Ecological impacts stemming from nitrogen deposition have been documented in the Colorado Rocky Mountains (Fenn et al. 2003; Baron et al. 2000; Davidson et al. 2005), and aerosols containing nitrates cause between 18-50% of local visibility reduction (Malm et al.

2007). While most research has focused on inorganic nitrogen such as nitric acid and ammonia, organic nitrogen (ON) is estimated to average $30 \pm 16\%$ of total atmospheric nitrogen loading worldwide (Neff et al. 2002; Zhang 2002; Mace et al. 2003; Duan et al. 2009), and contribute roughly one-fifth to one-third of fine particulate mass (Zhang 2002; Lin et al. 2010).

ON species may exist as gases and in wet or dry aerosol and move readily between phases (Galloway et al. 2004; Galloway et al. 2008; Cape et al. 2011). Dissolved organic nitrogen contributes significantly to total nitrogen deposition in Rocky Mountain National Park and elsewhere (Timperley et al. 1985; Gorzelska et al. 1992; Williams et al. 2001; Beem et al. 2010; Benedict et al. 2013). ON compounds found in aerosols include amines and imines (Murphy et al. 2007; Malloy & Qi 2009), uric, amino, and other organic acids (Cornell et al. 2003), and organic nitrates (Brown et al. 2009; Paulot et al. 2009; Bruns et al. 2010). Like emissions of inorganic nitrogen, which more than doubled since the 1970s, environmental levels of organic nitrogen species have been increasing (Fenn et al. 2003; Galloway et al. 2004; Burns 2003).

A number of techniques can be used to measure aerosol ON; for example, filter samples analyzed via thermal combustion techniques can yield water-soluble organic nitrogen, though weekly time resolution is required for adequate sample mass in all but the most polluted environments (Facchini et al. 2008). The Steam Jet Aerosol Collector coupled to a TC/TN analyzer is capable of 30-minute time resolution (which still may not resolve atmospheric events), but cannot speciate ON (Lin et al. 2010).

Unfortunately, quantifying organic nitrogen via AMS is difficult because nominally ‘nitrate’ and ‘ammonium’ molecules often fragment from organic parent compounds (broadly, organonitrates and amines, respectively) under EI ionization, leaving much organic nitrogen

mass indistinguishable from inorganic nitrogen (Rollins et al. 2010; Farmer et al. 2010). Attempts to determine organic contributions to nominally inorganic fragments are fraught with assumptions. For instance, one could define as inorganic the amount of ammonium needed to stoichiometrically balance sulfate and/or nitrate; however, sulfate can form, for example methylammonium-sulfate (Galloway et al. 2009; Shapiro et al. 2009; Nozière et al. 2009; De Haan et al. 2011), and trimethylamine-nitrate salts are also possible, though probably not abundant (Silva et al. 2008). As a result, most studies (including this one) treat all measured nitrate and ammonium as inorganic, though we make an attempt to apportion nitrate fragments to ON based on timeline associations between ‘stoichiometric excess’ nitrate and organic PMF factors for the Tetons dataset (Chapter 4).

Fortunately, some nominally organic-nitrogen fragments in the CHN (~amine) and CHON (~organonitrate) families are often preserved. From these it is sometimes possible to identify classes of compounds present (e.g. amines and pyridines/nitriles in the Tetons data, Chapter 4); the total mass of the CHN and CHON fragments also provides a lower bound on the ON concentration (ON_{\min}), which can be calculated using elemental ratios derived from said fragments and total organic mass through:

$$ON_{\min} = (\text{Org}/\text{OM}:\text{OC}) * \text{N}:\text{C} * (14/12) \quad (\text{Equation 5})$$

If NH_4 or NO_3 in excess of that stoichiometrically balanced in ammonium-nitrate or ammonium-sulfate exists, we assume that it is organic (sodium- and calcium nitrate have also been observed, though often in supermicron particle sizes; Lee et al. 2004; Lee et al. 2008). First, we determine the amount of ammonium or nitrate excess of stoichiometric balance, as shown for ammonium sulfate:

$$\text{NH}_{4(\text{S})} = \text{SO}_{4(\text{tot})} \times \frac{\mu\text{mol}}{96.07\mu\text{g SO}_4} \times \frac{18.0385\mu\text{g NH}_4}{\mu\text{mol}} \times \frac{2 \mu\text{mol NH}_4}{1 \mu\text{mol SO}_4} \quad (\text{Equation 6})$$

$$\text{NH}_4^* = \text{NH}_{4,\text{total}} - \text{NH}_{4(\text{S})} \quad (\text{Equation 7})$$

NO_3^* , or nitrate in excess of stoichiometric balance with NH_4^* , may be calculated analogously:

$$\text{NO}_{3(\text{A})} = \text{NH}_4^* \times \frac{\mu\text{mol}}{18.0385\mu\text{g NH}_4} \times \frac{62.0049\mu\text{g NO}_3}{\mu\text{mol}} \quad (\text{Equation 8})$$

$$\text{NO}_3^* = \text{NO}_{3,\text{total}} - \text{NO}_{3(\text{A})} \quad (\text{Equation 9})$$

These equations assume that a) ammonium preferentially forms ammonium sulfate over ammonium nitrate (i.e. there are no sulfate-containing acids in the given sample), and b) ammonium, nitrate, and sulfate are internally mixed, which are not universally true depending on particle sources; however, as seen in Chapter 4, associations between NO_3^* and the BBOA PMF factor may provide qualitative support for conclusions about ON drawn therein.

ON content may be indicated by the presence of PMF factors that are associated with ON or ON precursors in the literature. Biomass burning is well suited to this approach since it produces a common, unique factor (BBOA, indicated by m/z 60) and is correlated to the precursors of aerosol ON including VOCs produced by combustion itself and by increased isoprenoid emission from the heated vegetation (Grieshop et al. 2009). Chamber studies have shown significant aerosol ON yield from oxidation of vegetative emissions α - and β -pinene (Alfarra & Paulsen 2006; Fry et al. 2009; Bruns et al. 2010) and isoprene by NO_3 under realistic conditions (Starn et al. 1998; Ng et al. 2008; Brown et al. 2009); organic nitrates are major products of these reactions (Bruns et al. 2010; Desyaterik et al. 2013).

Other Methods for ON Determination from AMS Data

A review of these methods, and others with less potential for success, can be found in Farmer et al. (2010). Organic nitrates may be quantified from HR data via $\text{NO}^+:\text{NO}_2^+$ ratios, which vary between inorganic and organic nitrates, but unfortunately also between instruments and sampling locations (Fry et al. 2009; Bruns et al. 2010; Farmer et al. 2010); this necessitates fragmentation ratio calibration for each instrument and for the given ON content, which is unknown in ambient aerosols, though fragmentation ratios from ON standards have been applied to ambient data (Farmer et al. 2010). Also, ratios may suffer from interferences from sodium nitrate, calcium nitrate, and non-nitrate ON including amides, and are statistically distinguishable from ammonium nitrate only if organic nitrates comprise more than 15% of total nitrate (Bruns et al. 2010). An analogous technique using the ratio of HNO_3^+ to NO_x^+ has been explored, but has higher uncertainty and many of the same caveats as the $\text{NO}^+:\text{NO}_2^+$ ratio (Farmer et al. 2010).

Nominally organic-N fragments have been used to explore ON content; Rollins et al. found recently that for a range of organic nitrate standards, “58% of the [organic] N is detected at CHN^+ and CHNO^+ fragments” (2010), but it is unknown if this fragmentation ratio holds for differing instruments and ambient particles. Detection of amines and organonitrates through CHN and CHON spectra is explored in detail in the results (Chapters 3-5).

1.3.5 Organic Aerosol Source Apportionment Using Meteorological Data

Chemical source apportionment is often supported by meteorological information; many studies have used various associations with wind direction, the HYbrid Single-Particle Lagrangian Integrated Trajectory (HYSPLIT) model, residence time analysis, the potential source contribution function, and other back-trajectory products to map source regions and

transport (Chan et al. 2011; Sun et al. 2011; Tanner et al. 2005; Gebhart et al. 2011; Ashbaugh et al. 1985; Malm et al. 1986); a review may be found in (Hopke 2003).

The HYSPLIT model combines gridded meteorological data consisting of wind shear, horizontal field, and vertical diffusivity of the given constituent (gas or particle) to construct back-trajectories and/or dispersion maps of a given sampled air parcel with grid resolutions of several to tens of kilometers (Draxler & Hess 1998; Stein et al. 2007; Ziemba et al. 2010); its accuracy has been verified against tracers from Chernobyl and volcanic eruptions, balloon trajectories, and ambient studies of gaseous tracers (Draxler & Hess 1998).

Here, complex flow over mountainous terrain produces back-trajectories that may be useful in aggregate but lack the geographical specificity needed to study individual transport events (Gebhart et al. 2011). For the Rocky Mountain study, links between increased NO_x and ammonia concentrations and low-level upslope flow from the Front Range indicate that less complex meteorological analysis may aid source apportionment (Parrish et al. 1990; Langford & Fehsenfeld 1992). Thermally-induced afternoon upslope (NE-S, 45° - 180°) and nighttime downslope (SW-N, 225° - 360°) winds are well established in the Rocky Mountains in the summer and may transport urban plumes toward or away from the RMNP site, respectively (Bossert & Cotton 1994; Bader et al. 1987; Bossert et al. 1989; Jirak & Cotton 2006); the co-located National Park Service ROMO met station records hourly surface observations. Synoptic scale circulations may also drive relevant winds, and Denver 700 mb winds are used to represent regional flow (Gebhart et al. 2011). Wind observations are preferred to models, and daily 0Z and 12Z Denver soundings were retrieved (station #: 72469, University of Wyoming Database 2012). However, the rapid, sometimes brief changes in aerosol composition observed at the site demand greater meteorological time resolution; therefore, 3-Hourly NCEP North American Regional

Reanalysis (NARR) Composites were used for 3Z, 6Z, 9Z, 15Z, 18Z, and 21Z 700mb vector winds (NOAA 2012). Similar behavior may be indicated in the Grand Teton study as outlined in Chapter 4; a portable meteorological station with hourly time resolution was employed there.

There are a number of methods used to assimilate concentration and meteorological data. The Conditional Probability Function (CPF) used herein identifies wind directions contributing high constituent concentrations and is well supported in the literature (Lestari & Mauliadi 2009; Xie & Berkowitz 2007; Kim & Hopke 2004; Ashbaugh et al. 1985; Kim et al. 2003); the CPF equals the number of concentrations points greater than a threshold (Appendix Section 8.1, **Table 8-1**) measured in a given wind sector divided by the number of data points in that sector. Commonly used thresholds include the 25th (Lestari & Mauliadi 2009), 50th (Buzcu-Guven et al. 2007), and 90th percentiles for the given constituent (Benedict et al. 2013); here, thresholds are the species average plus one standard deviation, computed using AMS data averaged to the time resolution of the meteorological data (1 or 3 hours for surface or regional winds, respectively).

An obvious caveat to CPF arises when wind counts in a certain bin are low, allowing one or a few above-threshold measurements to produce an arbitrarily high CPF value; depending on thresholding, CPF may also filter out lower-concentration events that are yet connected with a certain wind direction (Zhou et al. 2004). Other wind-association approaches can be used in such cases, including simple wind-rose plots (Chueinta et al. 2000) and nonparametric regression.

In short, nonparametric regression (NPR) estimates the mean value of a dependent variable (component concentration) given one or more predictor values such as wind direction and/or speed, without making assumptions about the mathematical relationship between the variable or the statistical distribution of the data (Härdle 1992; Wand & Jones 1995; Henry et al. 2002); recent applications of NPR have integrated wind speed as well as wind direction, which

helps to resolve source regions for which transport time to the receptor is variable (Yu et al. 2004).

2. Methods

2.1 The High Resolution Time-of-Flight Aerosol Mass Spectrometer

The HR-ToF-AMS determines the size- and time-resolved composition of non-refractory submicron particles (Drewnick et al. 2005; Decarlo et al. 2006; Jayne et al. 2000). An instrument description follows; experiment and instrument function specifics are discussed in the results chapters and Appendix Section 8.1, respectively. During field measurements, ambient sample is first drawn at ~ 3 LPM through a $PM_{2.5}$ cyclone (using a backing pump to meet the cyclone flow requirements), of which the AMS samples ~ 0.09 LPM; the cyclone was omitted in the aqueous laboratory experiments as described in Section 2.3. The AMS aerodynamic lens focuses ~ 60 - 600 nm particles with unit transmission efficiency into a beam ~ 100 μm in diameter (Drewnick et al. 2005; Liu et al. 2007); the lens transmits the majority of the submicron mass at both field sites ($\sim 98.7\%$ at Rocky Mountain), as demonstrated using DMPS study-average size distributions in Figure 2-1 (Ezra Levin, personal communication, 22 November, 2011).

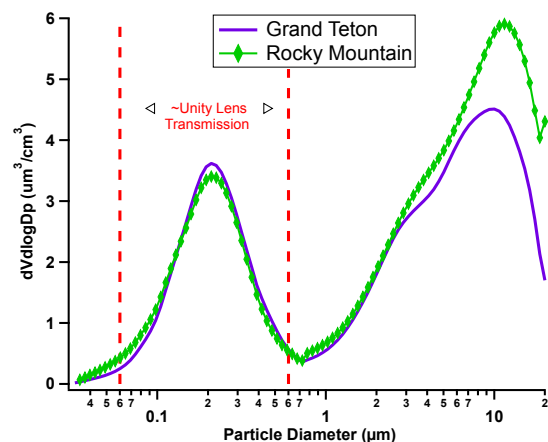


Figure 2-1: Study-average differential mobility particle sizer (DMPS) particle volume distributions (analogous to mass assuming uniform particle density) during the Rocky Mountain and Grand Teton National Parks field campaigns. The size range of near-unity transmission through the aerodynamic lens is shown in dashed red lines.

As the focused aerosol beam enters the high interior vacuum, the pressure differential causes the particle/gas mixture to accelerate; gases diffuse trans-axially more rapidly than

particles, and are ‘skimmed’ from the particles as the aerosol beam passes through a conical aperture into the Particle Time of Flight (PToF) chamber. Then, the semi-denuded particle beam encounters a rotating, slitted “chopper” wheel, which allows 1% of the particles into the PToF region (2% chopper used for the Grand Teton study). There, the resulting group of particles is separated by aerodynamic size via differences in particle inertia and Stokes’ drag force (Jimenez 2003); chopper transmission and vaporizer arrival times are recorded, giving particle velocity, which can be used to determine the particles’ aerodynamic diameters (Drewnick et al. 2005). Within each averaging period (described below), the chopper toggles between the open and closed positions, collecting ambient aerosol data (open) and gaseous and instrument background (closed), where the difference between the two is the net ambient particulate. The ‘chopping’ position aligns the chopper slits with the particle beam for size determination.

A porous, conical ~600 °C oven (located inside the 70 eV electron impact ionizer) vaporizes the particles, with vapors often undergoing thermal decomposition. The vapor molecules are then fragmented and ionized under electron bombardment in the ionizer; the resulting (mostly) singly charged fragments are focused into the ToF-MS extraction region. Here, a high-voltage EM pulse impels the charged fragments into the mass spectrometer fragment time-of-flight (ToF) region; since most fragments are singly charged, the force imparted on each fragment is the same and fragments are separated by mass inertially (Drewnick et al. 2005).

During their flight, the fragments’ flight trajectories are guided by ion reflectrons into either a ‘V’ or ‘W’ shape before hitting the multi-channel plate (MCP) detector; this increases the flight path, enhancing fragment separation. In ‘V’ mode, the flight is short, detection is fast, and fewer fragments are lost in transit ($LOD_{NO_3} = 0.003 \mu\text{g}/\text{m}^3$, Table 2-1). This makes the V

mode ideal for analyzing PToF samples, which require very high time resolution for sizing, or for sampling low concentrations. The longer flight path in the W mode allows higher mass resolution and thus more detailed chemical information, but fragment loss is higher ($LOD_{NO_3} = 0.05 \mu\text{g}/\text{m}^3$) and each mass spectrum takes longer to record; the W mode is not ideal for sizing or low mass conditions. A complete mass spectrum (m/z 1-300) is obtained with resolution of $\sim 2000 \text{ m}/\Delta\text{m}$ for the V mode and $\sim 5000 \text{ m}/\Delta\text{m}$ in the W mode in $12 \mu\text{s}$; these are averaged over 2-5 minutes in field campaigns and 1 minute in the laboratory experiments to balance signal-to-noise and time resolution requirements.

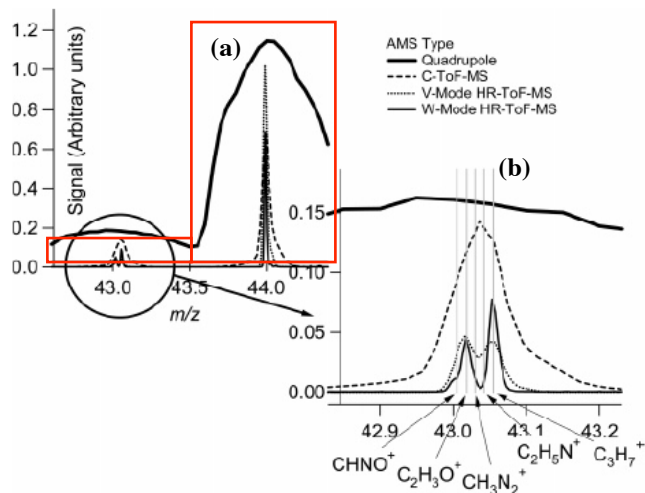


Figure 2-2: “Peak [resolution] comparisons for the four versions of the AMS” (Reproduced with permission from Decarlo et al. 2006). (a) Red boxes indicate the integration area for unit mass resolution data; (b) vertical grey bars indicate exact masses of resolved fragments in HR data (at m/z 43, for example).

The difference in resolution between V and W modes can be seen in Figure 2-2(b). These modes produce two main data types. Unit mass resolution (UMR) data can be used to quantify major component (sulfate, nitrate, ammonium, total organics) concentrations at given particle sizes; Figure 2-2(a) shows how UMR data are integrated. High-resolution data can resolve individual fragments within the same nominal mass bin, allowing quantitation of given fragments and elemental analysis (Aiken et al. 2009); high-resolution data is used in Positive

Matrix Factorization (PMF, Section 2.2). The programs used to generate each data type are described in Section 2.1.2. The ToF-AMS DAQ v 1.7.2B software was used for data acquisition.

The detection limits of the AMS have been measured, using filtered air, as three times the standard deviation of the signal noise for each species in a number of studies measured (Table 2-1).

Table 2-1: Measured detection limits for the given mass spectrometer mode and species; the averaging time is given by the reference.

Species	V Mode	W Mode	Reference
Sulfate	0.0052	0.11	1-min, Decarlo et al. 2006
	0.011	-	5-min, Ge et al. 2012
	0.003±0.0003	-	30-sec, Drewnick & Hings 2009
Nitrate	0.0029	0.032	1-min, Decarlo et al. 2006, AMS manual
	0.008	-	5-min, Ge et al. 2012
	0.003±0.0003	-	30-sec, Drewnick & Hings 2009
Ammonium	0.038	0.15	1-min, Decarlo et al. 2006
	0.030	-	5-min, Ge et al. 2012
	0.030±0.006	-	30-sec, Drewnick & Hings 2009
Organics	0.022	0.36	1-min, Decarlo et al. 2006
	0.060	-	5-min, Ge et al. 2012
	0.025±0.006	-	30-sec, Drewnick & Hings 2009

2.1.1 AMS Calibrations and Instrumental Quality Control

AMS data quality is enhanced by mass spectrometer tuning, aerodynamic lens alignment, and calibrations pertinent to electron multiplier gain, flow rate, particle sizing, and ionization efficiency (IE); quality assurance during sampling includes periodic HEPA filtration (to verify inlet integrity, etc.), mass spectrometer *m/z* calibrations, chopper position checks, IE calibrations, ancillary data collection, and logs chronicling instrument function, weather, vehicular traffic, fires, etc. These steps are summarized below with detailed protocols found in Appendix Section 8.2; particle collection efficiency determination is discussed in Section 2.1.2.

The first calibration performed is the electron multiplier calibration, which determines the relationship between multichannel plate detector (MCP) signal and the number of fragments impacting the MCP, allowing calculation of the number of ions from the total signal (Aerodyne Research 2005). The MCP multiplies the current induced by the impact of the ion on the MCP via electron cascade. MCP power (electron cascade signal multiplication) is adjusted to maximize signal-to-noise without unnecessarily degrading the MCP surface. The mass spectrometer is tuned by adjusting the extraction pulse, ion reflectrons, etc. to the desired balance of resolution and signal strength; tuning is checked before every measurement campaign.

The flow rate calibration is necessary when temperature or pressure changes significantly; volumetric flow is related to the pressure differential between ambient conditions and the AMS interior by noting interior pressure while adjusting flow using a needle valve at the inlet; after calibration, the valve is replaced by a micro-orifice (100-130 μM) such that flow is ~ 1.47 cc/min, as required for proper functioning of the aerodynamic lens. Next, the aerodynamic lens must be aligned with the vaporizer; this is achieved by observing signal intensity of NO^+ from generated ammonium nitrate particles while scanning lens positions. This produces a rough ‘circle’ of high signal intensity (mirroring the opening of conical vaporizer and/or interposed apertures), the middle of which is the optimal focus point to minimize particle bounce out of the cone.

The ionization efficiency (IE) calibration is of utmost importance, since it affects the interpretation of signal intensity, and is performed regularly (\sim weekly; Aerodyne Research 2005). An initial estimate of IE is made by generating ammonium nitrate particles of known size such that single-particle mass is known (using a differential mobility analyzer, or ‘DMA,’ TSI Electrostatic Classifier, model #3080; see Section 2.3) and observing signal from single particle

vaporization events; this is called the brute-force single particle ionization efficiency calibration (BFSP-IE). The BFSP-IE is determined using V mode sampling; the ratio of V and W mode air beam measurements can be used to calculate the W mode IE. These IEs can be checked, and corrected if necessary, by comparing AMS reported mass (usually for nitrate from 300 nm NH_4NO_3 particles) to that calculated from the concurrently sampled condensation particle counter number concentration (CPC, TSI model 3010), assuming that all discrepancy arises from error in the BFSP-IE (not different line losses between instruments, etc.). If the BFSP ionization efficiency is incorrect, the slope of the relationship between AMS and CPC nitrate mass, sampled in the V and W modes, can be used to correct the IE value for the corresponding mode (Appendix Section 8.2, **Figure 8-2**).

The particle sizing calibration uses either DMA-sized ammonium nitrate particles or polystyrene latex spheres. Particle travel time between the chopper and the vaporization oven is recorded; particle speed and density are then known, and aerodynamic particle diameter (d_{va}) can be calculated (Appendix Section 8.2). If NH_4NO_3 particles are used, a shape factor corrects for non-sphericity in the d_{va} calculation; however, there are no corrections for the reductions in aerodynamic lens transmission that may be caused by non-sphericity (Allan et al. 2004). The affect of non-sphericity on vaporizer retention is accounted for in the collection efficiency determination described later. The servo (chopper) position check is performed each field maintenance day (~every two days) and uses signal intensities to determine open, closed, and chopping servo positions as described earlier.

During sampling, a number of calibrations and checks are performed regularly for data quality assurance. Periodic sampling of ambient air through a HEPA filter verifies inlet integrity and can be used to check air beam values (gaseous species in such great abundance that some

molecules reliably make it past the skimmer, e.g. N_2^+) and resolution for a number of species used for m/z calibrations (Aerodyne Research 2005). Filtered air is sampled for ~30 minutes every other day in the field. The mass spectrometer m/z calibration is also checked and corrected each field maintenance day, for both V and W modes. Three peaks are user-identified (usually air peaks and tungsten from the instrument background) by their intensity relative to surrounding fragments and related to flight time through the mass spectrometer ToF region; a record of every m/z calibration is kept using screen shots. Values related to the IE and instrument function, including air beam values, resolutions of various species, and filament emission current, are tracked for each mode on log sheets. Pump spin frequency and current consumption are also recorded continuously along with computer, electronics, and vaporizer temperature.

Additionally, sample stream temperature and relative humidity are measured before the flow-control orifice; enclosure (mobile laboratory for field experiments) temperature was held constant. As both gaseous and particulate CO_2 contribute to signal at m/z 44, gaseous concentrations must be quantified to isolate particulate CO_2^+ mass. At the Rocky Mountain site, a HEPA filter was periodically placed over the inlet; at Grand Teton, a LI-COR LI-820 monitored inlet CO_2 continuously. Copper tubing (1/4 inch ID) was used for inlet extensions when necessary.

2.1.2 Data Analysis

Data analysis utilized the SQUIRREL ($\geq v1.51H$), PIKA ($\geq v1.10H$, Sueper et al., 2011), and PET ($\geq v2.03A$, Ulbrich et al., 2009) tools in Igor Pro 6.22A (WaveMetrics Inc., Lake Oswego, OR). A general overview of data analysis is provided below. See Appendix Section 8.2 (Data Analysis Protocols) and the packed IGOR experiments (-.pxp) and full datasets on the included compact discs for greater detail.

Unit Mass Resolution Analysis

Primary data processing integrates the results of all calibrations, logged events, and background data (air beam, etc.) with raw data to produce the initial unit mass resolution (UMR) data; Figure 2-3 shows the airbeam (AB) correction factor, which integrates fluctuations in ionization efficiency, flow, etc. into mass calculations, for the field studies herein. The W-mode experienced periodic malfunctions prefaced by deteriorating ionization efficiency (manifested as increasing AB correction factor) and attributed to bugs in the TPS software; data from periods before malfunction were used with the corrections shown above and compare well to ‘normal’ periods in air beam signal, etc. Corrections to m/z calibrations, baseline signal, and single ion signal areas are applied (to all UMR, HR, and PToF data types) and error is determined. The accuracy of the m/z calibration is expressed in terms of ppm of the given species, for which the community standard is ± 10 ppm for all species used in the calibration; this standard was achieved in all datasets herein, using 6 or more calibration points (Figure 2-4).

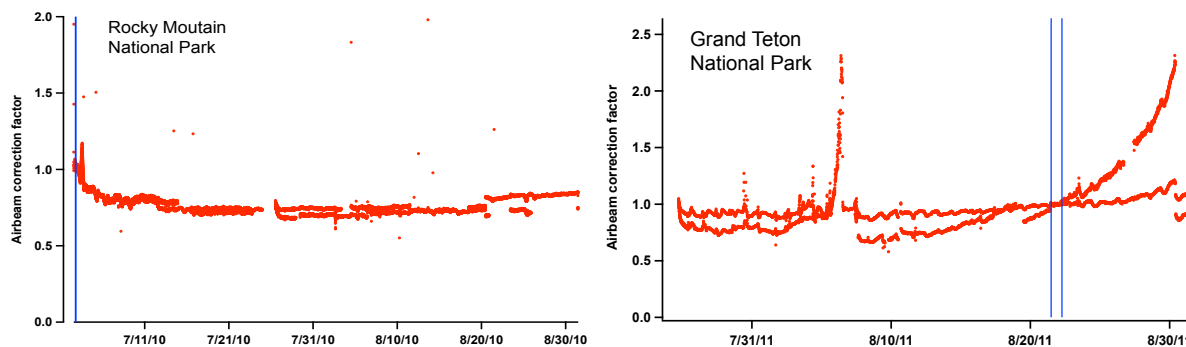


Figure 2-3: Airbeam correction factor timelines for the Rocky Mountain and Grand Teton National Parks studies. The vertical blue lines denote reference periods (selected directly after an IE calibration) used to determine the IE/AB ratio used in the airbeam correction factor calculation. In general, the ‘line’ of values with higher values is V-mode, which the lower is from the W-mode.

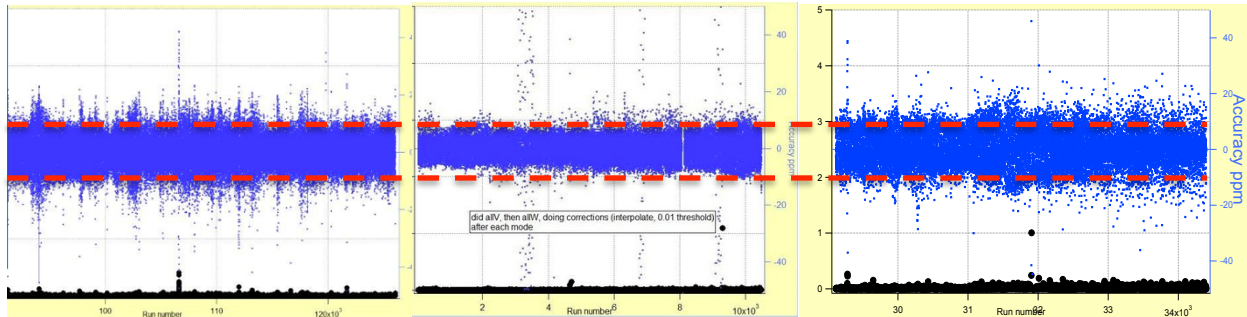


Figure 2-4: Residual time-lines (blue markers, in ppm) for all fragments used in m/z calibrations for (left) Rocky Mountain National Park, (center) Grand Teton National Park, and (right) the cloud water oxidation experiments. Red lines show ± 10 ppm.

Next, the baseline and peak integration regions are optimized for each m/z (m/z s 11-110 in field data; m/z s 12-200 in aqSOA experiments, enabled by greater mass at high m/z s); in each month of field data, baseline and integration region were examined in three to five raw spectra for each of the two mass spectrometer modes. An effort was made to examine high and low ambient aerosol concentrations because concentration affects total signal and therefore the optimum integration region. While there is no quantitative measurement of the "goodness of fit" for the baseline, errors made in this step may manifest as illogical species ratios or time-series, allowing the analyst to identify and redo unsatisfactory baseline sections.

In the UMR data, the mass of a given species is ascribed as a fraction of total unit mass based on the 'fragmentation table,' which may be adjusted to fit a given dataset; for instance, a priori knowledge of molecular content (as in laboratory studies) may be used to apportion more or less mass to a given species. Elemental isotope ratios are determined in the fragmentation table, as well as gaseous contributions to various fragments to which both particulate and gaseous species contribute. Lastly, for sized particle composition, PToF 'background' periods (containing no particle arrivals) are used to set the particle time-of-flight data (PToF) signal baseline. The resulting UMR data may be used to explore species charge balance (particle acidity) and changing relationships between, for instance, an inorganic species and total organics

that may indicate changes in particle composition warranting further exploration. Primary data products include UMR species timelines, average diurnal variations, component size distributions, and UMR mass spectra.

High-Resolution Analysis

Secondary data processing involves reconstructing high-resolution (HR) peak shape by adjusting average peak shape (constant) and width (m/z -dependent function) and choosing fragments to fit such that the half-width, half-max rule is maintained and the residual between reconstructed and measured signal is minimized (Appendix Section 8.2, **Figure 8-1**); the resulting high resolution data often has more organic mass but little change in inorganics in comparison to UMR data (Figure 2-5).

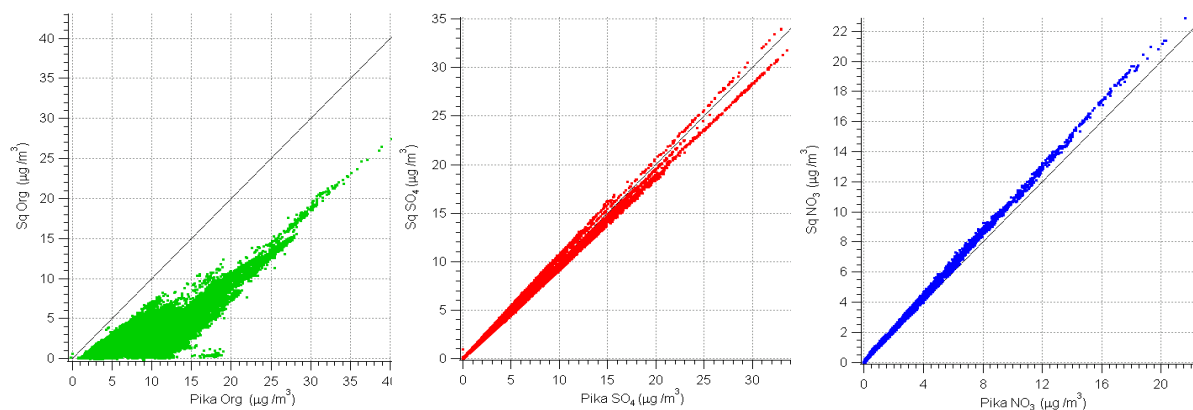


Figure 2-5: Comparison of organics (green), sulfate (red) and nitrate (blue) concentrations from low-resolution (UMR; "Sq...") and high-resolution ("Pika ...") data from the Rocky Mountain National Park study.

High-resolution data can be analyzed for individual fragment and species timelines, diurnal concentration patterns, and elemental analysis; the matrix containing fragment masses versus time is used as Positive Matrix Factorization input. The following HR data products will be used throughout this dissertation: organic aerosol types from Positive Matrix Factorization (PMF); elemental ratios (O:C, H:C, etc.) from elemental analysis (EA); fragment and species

timelines and correlations with wind and other particle components; and mass spectra (both total organic and organic family, as described later) for various periods and/or experiment types.

Collection Efficiency Determination

The AMS particle collection efficiency may be reduced by particle bounce out of the vaporizer and must be determined for mass quantitation. Bounce is minimized by particle sphericity, which in turn is influenced by particle composition, especially as it increases hygroscopicity and therefore water content (Allan et al. 2004; DeCarlo et al. 2004; Matthew et al. 2008; Huffman et al. 2005). Recent work by Middlebrook et al. (2012) has shown that the AMS collection efficiency, which is usually ~ 0.5 for ambient studies, increases with aerosol acidity (as determined by the ratio of measured ammonium to that predicted by stoichiometric balance with sulfate, nitrate, and chloride, $\text{NH}_4/\text{NH}_{4,\text{predict}} < 0.75$; Allan, 2004), ammonium nitrate fraction ($\text{ANMF} > 0.4$), and relative humidity in the inlet ($\text{RH} > 80\text{-}90\%$; at lower RH, drying upon exposure to the AMS interior high vacuum may induce efflorescence; Zelenyuk et al. 2006).

In the Rocky Mountain study (for example), $\text{NH}_4/\text{NH}_{4,\text{predict}} = 0.8$ ($r^2 = 0.96$), $\text{ANMF} = 0.11 \pm 0.15$, and the inlet relative humidity averages $52 \pm 22\%$ (88% of hourly data points are below 80% RH, using Clausius-Clapeyron with ambient temperature, ambient RH, and the mobile lab thermostat setting of 15.56 °C for enclosure temperature); none of these should increase C.E. given the thresholds listed above. A model of CE integrating particle acidity, ANMF, and inlet relative humidity was used to calculate the CE at each time point for all datasets (Middlebrook et al. 2012); both field studies and the aqueous experiment using dried cloud-water particles (Chapter 5) had calculated CEs near 0.5 with little variability. Comparison to PILS-IC sulfate supports this CE choice, with a slope of unity between AMS vs. PILS sulfate at the Rocky Mountain site ($m=1.00$, $r^2=0.88$; NO_3 : $m=1.29$, $r^2=0.76$), which is consistent with

other studies (Middlebrook et al. 2012; Takegawa et al. 2005). This favorable comparison between the AMS and 17-minute PILS-IC during the Rocky Mountain study corroborates proper AMS sampling and data analysis practices; 24-hour URG inorganic concentrations also compare well except for comparatively lower sulfate (**Figure 1-3**). The PILS-IC malfunctioned during the Grand Teton study and was not used during laboratory experiments.

Estimation of PToF Sizing Error

PToF sizing error estimates were constructed for each dataset (not to be confused with PToF mass error calculations in Ulbrich et al. 2012). Sources of error in PToF size determination include, but are not limited to, 'chopper broadening' caused by the spread in particle arrival times caused by the time it takes the chopper slit to pass through beam (particles at end of transmission time enter flight slightly later than ones at beginning); since differently sized particles fly at different velocities, this error is size dependent (Allan et al. 2003). For a 1% chopper at 150Hz (2% used for Grand Teton study), the amount of time that the chopper is open, which influences the spread of the sized particles arriving at the vaporizer, can be calculated by:

$$\left(\frac{6.7 \text{ ms}}{\text{revolution}}\right) \left(\frac{0.01 \text{ open chopper}}{\text{revolution}}\right) \left(\frac{\text{revolution}}{2 \times 0.5\% \text{ slits}}\right) = 0.034 \frac{\text{ms}}{\text{revolution}} \quad (\text{Equation 10})$$

For each particle size, the chopper transmission time can be compared to total particle flight time to determine chopper-broadening error. The particle PToF flight time can be calculated via:

$$\text{Velocity} = p_3 + \frac{(p_0 - p_3)}{(1 + (D_{va}/p_1)p_2)} \quad (\text{Equation 11})$$

where p_0 = velocity of the gas *after* the aerodynamic lens, $p_1 = D^*(nm)$ coefficient, $p_2 = b$ coefficient, p_3 = velocity of the gas *in* the aerodynamic lens (determined during the size calibration). For example, using RoMANS size calibration values, a 300 nm-particle flight time

of 0.003136 seconds yields an error of $0.000034 \text{ s}/0.003136 \text{ s} = 0.011$ or 1.1%. For the 2% chopper, this is ~2.1% using the size calibration for the Grand Teton study.

Chopper broadening error is exacerbated by error in PSL or DMA-selected ammonium nitrate used for sizing (error about the size calibration curve); since these errors have different units, each is calculated as a percentage of diameter at each given size and compounded via:

$$\text{Total Error (\% of diameter)} = \sqrt{\sum_i e_i^2} \quad (\text{Equation 12})$$

where e is the % error for each relevant process (Skoog et al. 2006; Harris 2007). Polystyrene latex spheres (PSL, Duke Scientific Corp.) are used for size calibration points at 70, 100, 200, 300, 400, 500, and 700 nm, and have precisions of 1.5-9 nm, depending on size. For example, 300nm PSL particles have a diameter standard deviation of 5 nm or 0.0167 (1.7%) of particle size. Compounding chopper broadening and calibration errors yields a total 2.7% error in size determination for 300 nm particles during the RoMANS study; these calculations were iterated at the diameters listed above for each field experiment (size was not calculated for the laboratory study since it would be a function of atomizer output, not ambient size distributions). Other possible PToF errors and caveats to a complete PToF error determination are outlined in Ulbrich et al. (2012). The PToF size resolution is $5\text{-}10 D_{\text{aero}}/\Delta D_{\text{aero}}$ (FWHM) over the size range of aerodynamic lens transmission (Aerodyne Research Inc. 2004).

2.2 Positive Matrix Factorization

Positive Matrix Factorization (PMF) is a positivity-constrained, receptor-only, least-squares regression algorithm used to deconvolve the matrix containing run-average (2-5 min) organic mass spectra versus time into a chosen number of spectrally-static organic ‘factors’ whose contributions to total organic mass vary over time (Paatero 1997; Paatero & Tapper

1994). Spectral factors returned by PMF may be analyzed with meteorological data or anthropogenic inorganic tracers and compared to ‘typical’ spectra from various sources and/or degrees of processing to examine local chemistry; Ulbrich and coworkers have compiled an online database of AMS spectra spanning a broad range of sources, species, and sampling conditions (Ulbrich et al. 2009). Although the choice of number of factors introduces subjectivity to PMF analysis, correct factorization of synthetic datasets and comparison to other factorization algorithms support PMF use for source apportionment (Ulbrich 2011; Reff et al. 2007; Engel-Cox & Weber 2007). Error and HR data matrix preparations followed Ulbrich et al. (2009). In particular, time series for all fragments used in PMF were evaluated for discernible trends (as opposed to noise around zero), and meaningless fragments were discarded (Paatero & Hopke 2003); those of uncertain usefulness were included at least until their S:N ratios were evaluated against the discard and down-weight thresholds discussed below.

The selection of number of PMF factors is based on factors’ spectral and timeline dissimilarities, comparison to ‘established’ factor types, and correlation with tracers (such as anthropogenic inorganic species concentrations) as will be explored in the results chapters (Ulbrich et al. 2012); factor number choice may be supported using Q (a parameter describing residuals) and other statistics. Q is defined as (Paatero et al. 2002):

$$Q = \sum_i \sum_j (e_{ij}/\sigma_{ij})^2$$

where e is residual not fit by the algorithm and σ is the estimated error over all rows (i , MS fragments) and columns (j , time) of the data and corresponding error matrices. For the Rocky Mountain study, a three-factor solution is supported by a large (36%) reduction in Q between two- and three-factor solutions, indicating that the three-factor solution describes considerably more of the variability in the dataset, but diminishing reduction ($\leq 21\%$) in Q when 4 or more

factors are chosen; for the Tetons, mass spectral and timeline comparisons suggested a two-factor solution, yielding an 8% Q reduction, similar to the 5% reduction for 3 factors and emphasizing the low utility of this statistic in determining factor number. A second variable, Q_{exp} , equals the degrees of freedom (for AMS data, approximately the number of data points in the input data matrix) and $Q/Q_{\text{exp}} = 0.08$ for Rocky Mountain, while $Q/Q_{\text{exp, Tetons}} = 0.79$ for Grand Teton (Ulbrich et al. 2009; Paatero & Tapper 1993). As described in the literature, $Q/Q_{\text{exp}} \ll 1$ indicates an overestimation of error (Paatero et al. 2002; Ulbrich et al. 2009). The Tetons dataset error estimation compares well with published analyses (Ulbrich et al. 2012); however, the Rocky Mountain Q/Q_{exp} is much lower. We hypothesized that the low total signal contributes to reduced signal-to-noise ratio overall, putting a larger percentage of data points (mass of a fragment at a given time) under the S:N ($S:N = \sqrt{\sum \text{signal}^2 / \sum \text{err}^2}$) thresholds that recommend down-weighting (increasing the error) during error matrix preparation; points with $S:N < 0.2$ (“bad”) are excluded from the analysis and those with $0.2 < S:N < 2$ (“weak”) are down-weighted by a factor of 2 (Paatero & Hopke 2003). All of the ‘bad’ fragments featured time series dominated by noise with no evident trends, and thus their exclusion was sustained. The down-weighting factor for weak fragments was subsequently reduced to 1.2, resulting in $Q/Q_{\text{exp}} = 0.1$ for a three-factor solution. The Q/Q_{exp} improvement is minimal and the ensuing factors are nearly identical to those presented in Chapter 3, so the original analysis (down-weight factor of 2) was used. Residual mass between input and PMF reconstruction was low and fairly constant between fragments suggesting that the overestimation in error is uniform across fragments; the approximately Gaussian distribution about zero for most fragments indicates accurate mass reconstruction (example shown for CH_3^+ , Figure 2-6).

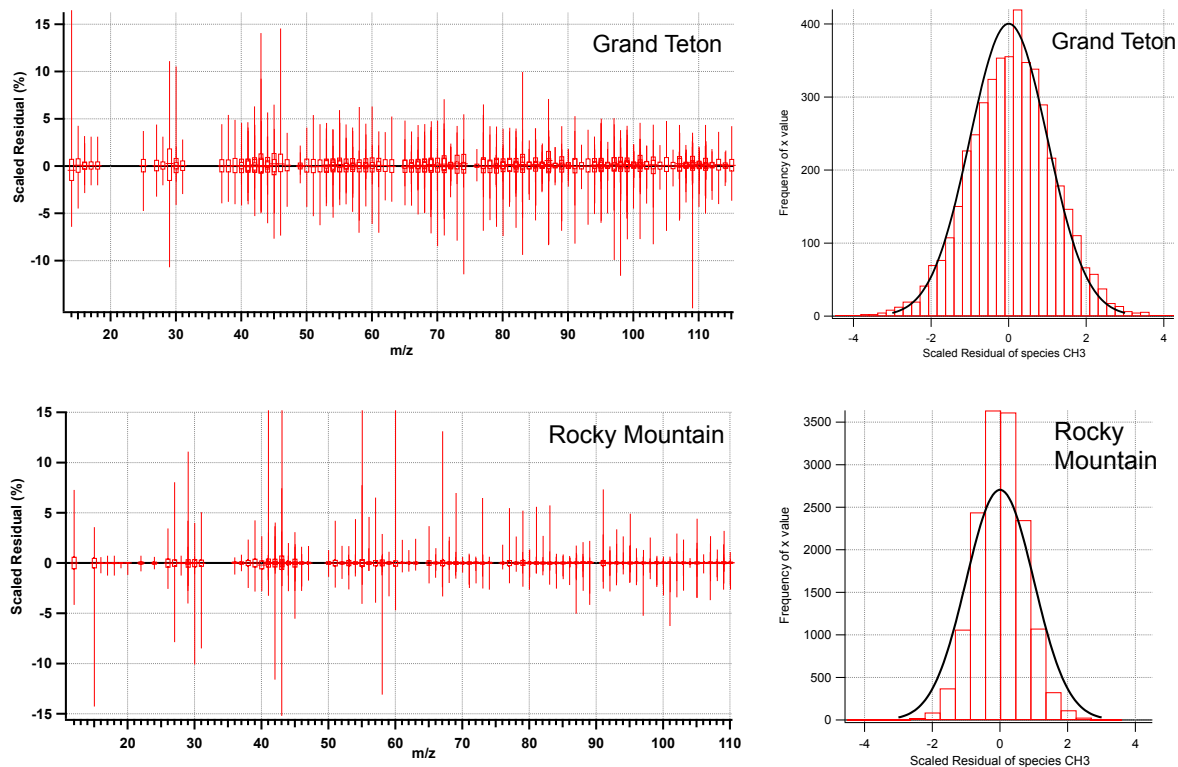


Figure 2-6: Residuals from PMF mass reconstruct for each m/z (left) and as a histogram for example organic fragment CH_3^+ (right), for Rocky Mountain and Grand Teton National Parks studies. The difference in histogram bin width reflects the updated PMF Evaluation Tool (PET) version used for the Tetons. Boxes are the mean; whiskers 5^{th} and 95^{th} percentiles.

The FPEAK parameter is used to explore linear transformations, or ‘rotations,’ of the PMF solution matrix that redistribute mass between the factor mass spectra and time lines while maintaining the positivity constraint (Ulbrich et al. 2009). FPEAK was varied from -1 to 1 (within which Q/Q_{exp} varied less than 10% for both Rocky Mountain and Grand Teton; see Ulbrich et al., 2009), but none of these solutions improved description of the aerosol characteristics at the Rocky Mountain site; these rotations are examined further in Chapter 3. Thus, $\text{FPEAK} = 0$ was selected for Rocky Mountain; RotMat, which describes the rotational freedom of the solution, or number of possible MS-time series combinations, is also minimized with $\text{FPEAK} = 0$ as recommended by Paatero and Hopke (2003) and others (Lanz et al. 2007). The Rocky Mountain PMF analysis was repeated twice from HR fragment selection onward and

twice with different error constraints with very similar results. For the Grand Teton site, FPEAK = -0.2 produced the most logical separation between the biomass burning and oxidized organic aerosol factors (see Chapter 4); its RotMat value was approximately equal to the minimum value at FPEAK=0 (within 0.01%).

2.3 Aqueous SOA Experiments

The mass and composition of aqueous SOA (aqSOA) formed in clouds is a topic of current research, but is usually studied in simple solutions in the laboratory in order to constrain reaction rates and mechanisms; the atmospheric relevance of the resulting aqSOA (in composition and amount) is unknown. Under the hypothesis that matrix effects in real, complex ambient cloud water lead to higher SOA production via formation of more functionalized products than observed in single-precursor laboratory studies, the experiments in Chapter 5 compare bulk aqueous photo-oxidation of ambient cloud and single-precursor solutions at similar starting TOC concentrations; hydrogen peroxide is added and photolyzed to produce $\text{OH}_{(\text{aq})}$, one of the most important oxidants of aqueous organics (see introduction), at atmospherically-relevant concentrations. This methods section will introduce the experimental setup, including instrumentation, solution preparation, and control experiments; data quality and interpretation, and the relevance of the experimental setup to the atmosphere will be discussed in Chapter 5 to better contextualize the results.

An opaque box contained the photoreactor system, which includes a stir-bar plate for continuous solution mixing, the photoreactor, and a UV lamp (Figure 2-7). The transparent glass photoreactor (custom-made for this application) features a beaker-like receptacle for the reacting solution surrounded by a continuously circulating water sheath for solution temperature control; the coolant is drawn from an external water tank at ~22 C labeled 'T Control' in the schematic

and circulated by an AquaBox fish-tank pump (Model AA2005). Both photo-reactor and stir bar were cleaned with DI and air-dried between each experiment. The UV lamp (Green Killing Machine, Model AAUV09W-UVC, 254 nm peak wavelength) fit into the photoreactor with a loose flange, covering but not hermetically sealing the vessel opening.

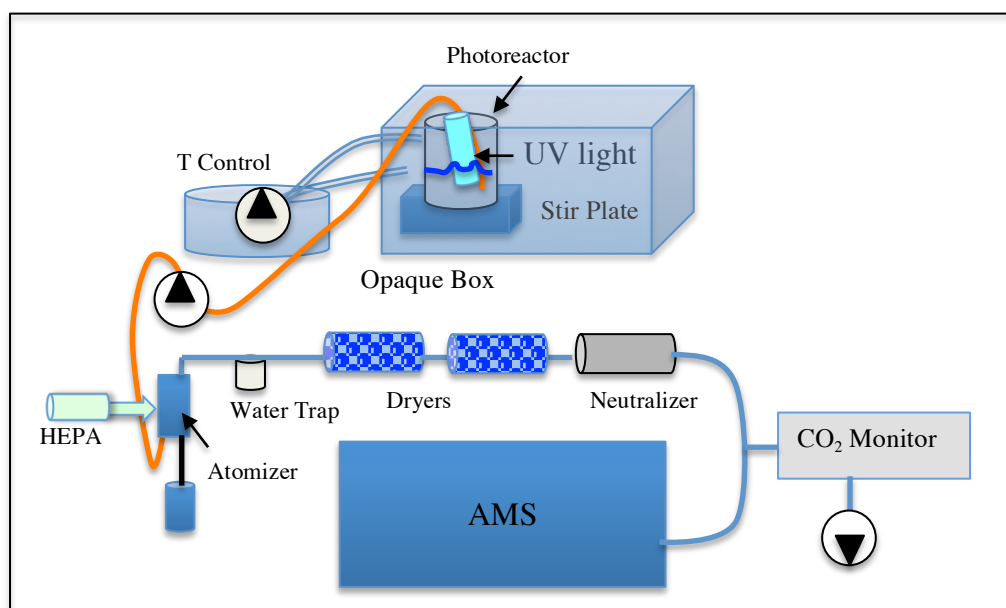


Figure 2-7: Schematic of experimental setup for bulk aqueous-phase photo-oxidation.

The reacting solution was sampled continuously via PET tubing and analyzed with the AMS after Lee et al. (2011). During the first methylglyoxal experiment set (MG1; Table 2-2), a Dionex GP50 IC gradient pump at 0.5 mL/min delivered the reacting solution to the TSI 3076 Constant Output Atomizer, which was operated with 15 psi HEPA-filtered (Pall #12144) compressed air; when the gradient pump broke and replacement parts were not immediately available, it was replaced with an Ismatec IPC peristaltic pump at the same flow rate. The atomized sample was dried using two diffusion dryers with Dryrite substrate, which was refreshed approximately daily, and electrostatically neutralized with a ²¹⁰Po neutralizer before splitting flow (without dilution) between a LICOR-820 CO₂/humidity monitor and the AMS; see

Chapter 5 for relative humidity of the sample stream and effects thereof on particle collection efficiency, etc. Due to sporadic visible water at the atomizer outlet, a simple ‘T’ water trap was installed for experiments Tox7full1, MGfull2, MGINfull1 and attendant control experiments (Table 2-2); the errors introduced by irregular atomizer function are discussed in Chapter 5. Briefly, this atomizing-drying method is hypothesized to mimic the evaporation of a cloud droplet to form droplet mode aerosol (Lee et al. 2011; El Haddad et al. 2009; De Haan et al. 2009; Loeffler et al. 2006), with further drying of questionable atmospheric relevance as the sample stream enters the high vacuum in the AMS (Zelenyuk et al. 2006; see Chapter 5 for further discussion). DI water was flushed through the atomizing system between each experiment (controls and full oxidations) until no mass was seen in the AMS (usually ~2 minutes at ~1 mL/min); the atomizer was dismantled and cleaned thoroughly when concentrations were still high after the DI flush.

Atmospheric Relevance of Approach

Sample information including concentrations of added hydrogen peroxide and precursors can be found in Table 2-2; Appendix Section 8.4 lists ambient cloud sample collection information. Methylglyoxal (MG) and pinonic acid (PA) were selected as precursors for their likely importance in ambient clouds (see introduction) and chemical similarity to other early VOC oxidation products; use in previous studies, especially of methylglyoxal, allows verification of our techniques and results against the literature. Added methylglyoxal concentrations are 60 and 500 μM (MG2 and 1, respectively), which fall within the range measured in ambient cloud water (~1-100s μM , Ervens et al. 2003; Tan et al. 2009; De Haan et al. 2009; Ervens et al. 2013; Collett et al. 1990; Munger et al. 1990); the methylglyoxal concentrations >1 mM often used in the literature may be less representative of ambient cloud

water than those here (Tan et al. 2010; Yasmeen et al. 2010; De Haan et al. 2011). While pinonic acid concentrations have rarely been evaluated in cloud water, experimental PA yields from α - and β -pinene aqueous oxidation are similar, at ~ 0.1 - 1% aerosol mass, to yields of pinic acid (~ 1 - 5%) and pinonaldehyde (~ 0 - 1%) from the same precursors (Yu et al. 1999); pinic acid and pinonaldehyde have been measured in concentrations of 0.11 and $0.8 \mu\text{M}$, respectively, in ambient cloud (van Pinxteren et al. 2005), and a similar molarity for pinonic acid is assumed herein based on similarity of yields. In an effort to represent aqSOA formation from total monoterpene oxidation products (and have sufficient S:N in the AMS), $30 \mu\text{M}$ pinonic acid solutions were used, which may be somewhat more atmospherically relevant than previous similar experiments ($500 \mu\text{M}$; Lee et al. 2012).

Hydroxyl radicals were produced via photolysis of hydrogen peroxide, which was added to achieve $[\text{HOOH}]_{\text{aq}} = 300 \mu\text{M}$. The resulting $[\text{OH}]_{\text{aq}}$ was quantified by tracking absorption of 410 nm light (via UV/visible absorption spectrometry) by 4-nitrophenol ($50 \mu\text{M}$; Acros Organics, Pittsburgh PA) during reaction with $250 \mu\text{M}$ hydrogen peroxide and the UV lamp introduced above, and using the second-order rate constant for degradation of 4-nitrophenol (Oturán et al. 2000) to find $[\text{OH}]_{\text{aq}} = 5.4 \pm 0.5 \times 10^{-14} \text{ M}$ (Alexandra Boris, personal communication, 25 January 2014); solution composition was determined using electrospray ionization high-resolution time-of-flight mass spectrometry (ESI-HR-ToF-MS). Before hydrogen peroxide addition, the ambient cloud samples contained $[\text{HOOH}]_{\text{aq}} = 1$ - $100 \mu\text{M}$; assuming that the rate constant for OH production by hydrogen peroxide photolysis used herein holds in this complex matrix, and that OH-organic reaction rate increases are linear within the given [OH] concentration range (currently under investigation), this initial hydrogen peroxide produces concentrations of $[\text{OH}]_{\text{aq}} \approx 10^{-15}$ – 10^{-14} M with which the supplementary hydrogen peroxide is

additive, giving total $[\text{OH}]_{\text{aq}} \approx 10^{-14}$ M. The $[\text{OH}]_{\text{aq}}$ used here is similar to that modeled in ambient cloud water ($\sim 10^{-14}$ – 10^{-13} M; Arakaki & Faust 1998; Ervens et al. 2003; Ervens & Volkamer 2010; Jacob 1986; Deguillaume et al. 2005), and 1-2 orders of magnitude lower than used in similar laboratory experiments (Lim et al. 2010; Lee et al. 2011a). Lastly, without the large droplet surface area-to-volume ratio to maximize O_2 absorption, dissolved oxygen levels in the bulk aqueous solution may be lower than the modeled complete saturation in ambient cloud droplets; continuous mixing may add oxygen to some extent, but oxygenation was not monitored during the experiments and may diverge from atmospheric behavior.

As discussed in the introduction and Chapter 5, precursor and especially oxidant concentrations may affect aqSOA production and content (Tan et al. 2009; Lee et al. 2011a); the component concentrations herein may be among the most atmospherically relevant of their kind to date, making experiment time approximately equivalent to atmospheric oxidation time. The total experiment time for ‘full’ oxidations (UV+ H_2O_2) was between ~ 100 - 140 minutes, which often captures the initial aqSOA reactions (product formation and composition change tend to slow at ~ 40 - 100 minutes into reaction, albeit with higher oxidant and precursor concentrations, in Volkamer et al. 2009; Lee et al. 2011a); ambient sample volume also limited reaction time. For the ambient samples herein, clouds were present for 0-10 hours (average = 3 ± 4 hrs) preceding collection and the persisted for an average of 6 ± 4 hours after collection, with only one sample (one of the three mixed to create TaiOx1) from a cloud persisting less than the experimental oxidation time of ~ 2 hours. Thus, experiments herein are atmospherically relevant in both oxidation time and oxidant intensity, though they will not in general capture more advanced stages of oxidation near the end of the cloud’s lifetime. Many controlled aqueous experiments (all precursors added at $t=0$) often continue to undergo SOA mass and composition

changes well beyond 140 minutes in experiments lasting up to 7 hours, and precursor concentrations in these experiments often well exceed those in the real atmosphere, implying longer reaction times in less-concentrated ambient solutions, in general (Carlton et al. 2007; Zhang et al. 2010; Lee et al. 2011a; Lee et al. 2011b). Also, interstitial vapors in clouds are potentially continuous sources of ‘fresh’ precursors that could extend the ‘reaction time’ within the cloud up to the lifetime of the cloud. Thus, the experiments herein may represent lower-bound estimations of aqSOA formation in photooxidized clouds.

Table 2-2: Experimental conditions, name, and concentration of added precursors, if applicable: ammonium nitrate (AN) and ammonium sulfate (AS; always added with AN), and/or pinonic acid (PA) or methylglyoxal (MG). Total Organic Carbon (TOC) is also included. * MGb2 & 4 not included due to instrument malfunction. In the RH column, “-” indicates missing data, and “~0” is at or below the detection limit of the monitor. Multiple values are from replicates of the given experiment (indicated in “Name” column).

Experimental Conditions	Name	PA or MG (uM)	AN&AS (uM)	HOOH (uM)	TOC (mg/L)	RH (%)
MG + UV	MGuv1 & 2	496.83597	0	0	17.90	-, ~0
MG + H ₂ O ₂	MGho1	496.83597	0	300	17.90	-
MG no H ₂ O ₂ no UV	MGb1	496.83597	0	0	17.90	-
MG + UV + H ₂ O ₂	MGfull1	496.83597	0	300	17.90	-
PA + UV	PAuv1 & 2	30.00	0	0	3.60	-, ~0
PA + H ₂ O ₂	PAho1 & 2	30.00	0	300	3.60	-, ~0
PA no H ₂ O ₂ no UV	PAb1, 2, 3, & 4	30.00	0	0	3.60	-, ~0, 0.20±0.36,0
PA + UV + H ₂ O ₂	PAfull1 & 2	30.00	0	300	3.60	-, ~0
PA + inorgs + UV	PAINuv1 & 2	30.00	50	0	3.60	36.33 ±1.25
PA + inorgs + H ₂ O ₂	PAINho1 & 2	30.00	50	300	3.60	42.57 ±0.51
PA + inorgs no H ₂ O ₂ no UV	PAINb1, 2, 3, & 4	30.00	50		3.60	-, 0, 0
PA + inorgs + UV + H ₂ O ₂	PAINfull1&2	30.00	50	300	3.60	-, ~0
Tai-Ox 1 no H ₂ O ₂ no UV	Tox1b1	0	0	0	~20	45.11 ±1.61
Tai-Ox 1 + UV	Tox1uv1	0	0	0	~20	51.14 ±0.69
Tai-Ox 1 + H ₂ O ₂	Tox1ho1	0	0	2982.1	~20	53.68 ±0.28
Tai-Ox 1 + UV + H ₂ O ₂	Tox1full1	0	0	3017.4	~20	22.60 ±3.52
Tai-Ox 2 no H ₂ O ₂ no UV	Tox2b1	0	0	0	24.10	27.87

						±2.31
Tai-Ox 2 + UV + H ₂ O ₂	Tox2full1	0	0	3002.7	24.10	38.29 ±2.93
Tai-Ox 3 + UV + H ₂ O ₂	Tox3full1	0	0	292.40	2.86	47.36 ±1.86
Tai-Ox 3 + H ₂ O ₂	Tox3uv1 & 2	0	0	303.57, 300.00	2.86	53.12 ±0.90, 29.67 ±1.94
Tai-Ox 3 + UV	Tox3ho1 & 2	0	0	0	2.86	23.09 ±2.84, 38.61 ±1.31
Tai-Ox 3 no H ₂ O ₂ no UV	Tox3b1				2.86	35.19 ±1.42
Tai-Ox 4 + H ₂ O ₂ + UV	Tox4full1,2, & 3	0	0	301.37, 298.70, 300.83	1.73	33.89± 4.73, ~0,~0
Tai-Ox 4 no H ₂ O ₂ no UV	Tox4b1 & 2	0	0	0.00	1.73	21.79± 1.15, 0
TaiOx6 + PA no H ₂ O ₂ no UV	Tox6PAb1	30.00	0	0	9.15	~0
TaiOx 6 + PA +UV	Tox6PAuv1	30.30	0	0	9.15	~0
TaiOx 6 + PA + H ₂ O ₂	Tox6PAho1	30.36	0	303.57	9.15	~0
TaiOx 6 + PA +UV+ H ₂ O ₂	Tox6PAfull1	30.49	0	304.88	9.15	~0
TaiOx 7+PA no H ₂ O ₂ no UV	Tox7PAb1	30.49	0	0	10.06	~0
TaiOx 7+ PA +UV+ H ₂ O ₂	Tox7PAfull1	30.49	0	304.88	10.06	~0
MG + UV + H ₂ O ₂	MGfull2	60	0	300	2.16	
MG no H ₂ O ₂ no UV	MGb3, 5, & 6*	60	0	0	2.16	
MG + UV	MGuv3	60	0	0	2.16	~0
MG + H ₂ O ₂	MGho2	60	0	300	2.16	~0
MG + inorgs + UV + H ₂ O ₂	MGINfull1	60	50	300	2.16	~0
MG + inorgs no H ₂ O ₂ no UV	MGINb1 & 2	60	50	0	2.16	~0
MG + inorgs + UV	MGINuv1	60	50	0	2.16	~0
MG + inorgs + H ₂ O ₂	MGINho1	60	50	300	2.16	~0
Tai-Ox 7 no H ₂ O ₂ no UV	Tox7b1	0	0	0	6.40	~0
Tai-Ox 7 + UV + H ₂ O ₂	Tox7full1	0	0	297.52	6.40	~0
Tai-Ox 7 + UV	Tox7uv1	0	0	0	6.40	~0
Tai-Ox 7 + H ₂ O ₂	Tox7ho1	0	0	300	6.40	~0

Control Experiments

As outlined in the introduction, aqueous organic mass may be formed from a variety of reactions. For instance, Fenton reactions could contribute to OH formation from H₂O₂ without

photolysis (Arakaki & Faust 1998; Deguillaume et al. 2005); methylglyoxal can photolyze to form organic radicals (although this mechanism generally does not compete with OH-initiated reactions; Tan et al. 2010; Tan et al. 2012) or form oligomers through dark hydration (Loeffler et al. 2006; Zhao et al. 2006; Krizner et al. 2009). To investigate the reaction regimes forming aqSOA, control experiments evaluated contributions of dark (noUV/noH₂O₂, ‘baseline’), photolytic (+UV/noH₂O₂), or hydrogen peroxide-initiated (noUV/+H₂O₂) reactions to aqSOA (Figure 2-8). For both ambient cloud samples from Mt. Tai, China (TaiOx) and single-precursor solutions (PA and MG), neither organic mass (Total Organics/Total Sulfate, normalized to t = 0 as described in Chapter 5) nor oxidation indicator *f*₄₄ (mass at *mz*₄₄/Total Organics, normalized to t = 0) change significantly under any of the control conditions; we may conclude that any change in aqSOA mass and/or composition in the full photo-oxidation arises from OH-initiated reactions and that Fenton reactions, etc. do not produce significant amounts of OH. Noise in the methylglyoxal and pinonic acid experiments complicates interpretation, but mass does not appear to change for any species or control scenario save possible *f*₄₄ decrease in the baseline pinonic acid + inorganics experiment (no added hydrogen peroxide or UV light). The noise in the methylglyoxal and pinonic acid baseline experiments may reflect observed, sporadic variable mass output from the atomizer; normalization to sulfate is used to correct for these fluctuations, which are discussed in detail in Chapter 5.

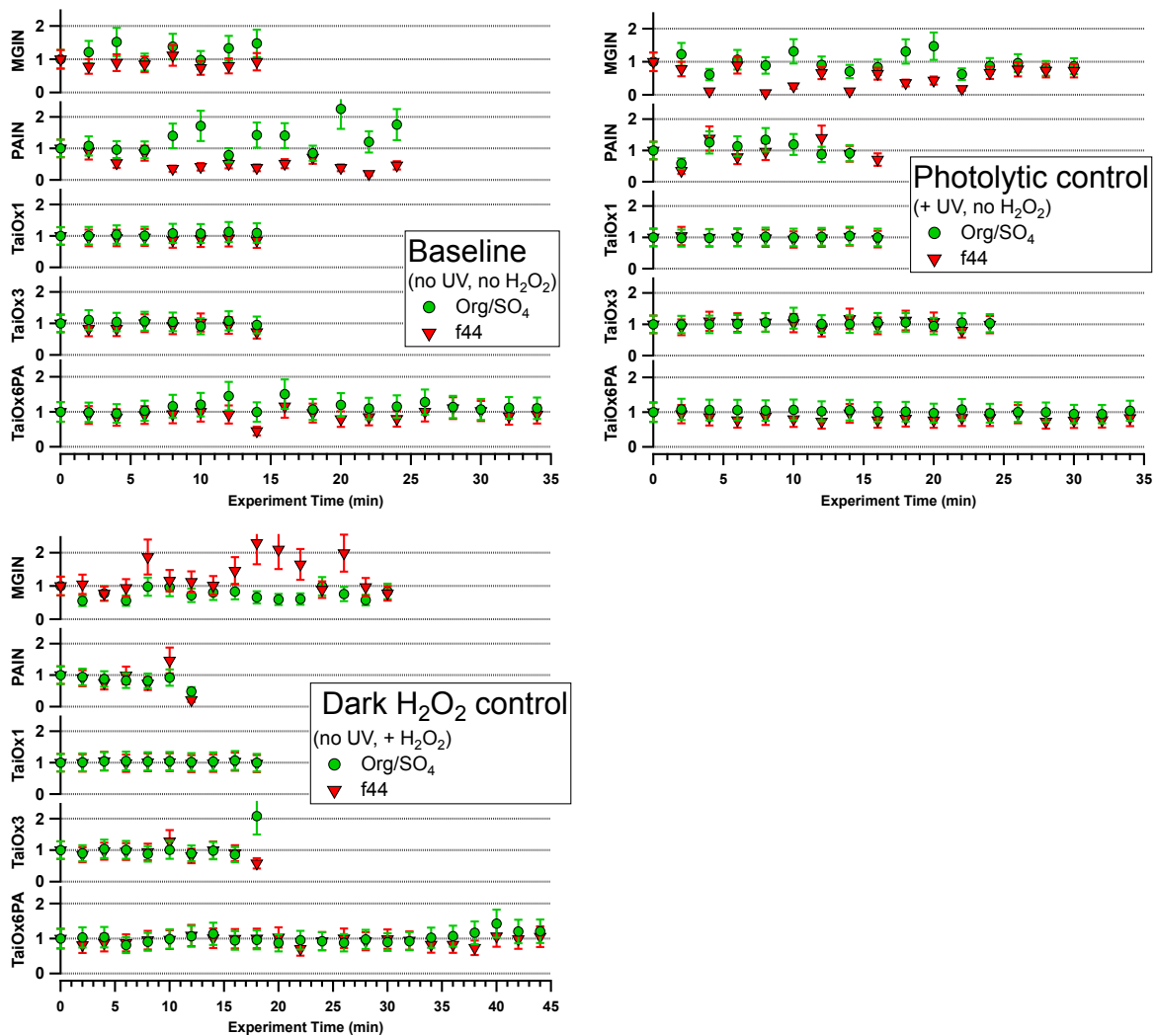


Figure 2-8: Normalized Organics/Sulfate and *f44* (*mz44*/Organics) for dark ('baseline'), photolytic, and hydrogen peroxide control experiments with conditions as noted in the legends; error bars are $\pm 28\%$ based on propagation of AMS quantification error. The remaining TaiOx samples are omitted for brevity.

3. Organic Aerosol Sources and Characteristics: Rocky Mountain National Park

3.1 Sampling Site Overview

Fine particles were sampled in a valley on the SE side of Rocky Mountain National Park between the towns of Estes Park and Allenspark, CO at ~2,740 m (Lat: 40.2778, Long: 105.5453, Figure 3-1).

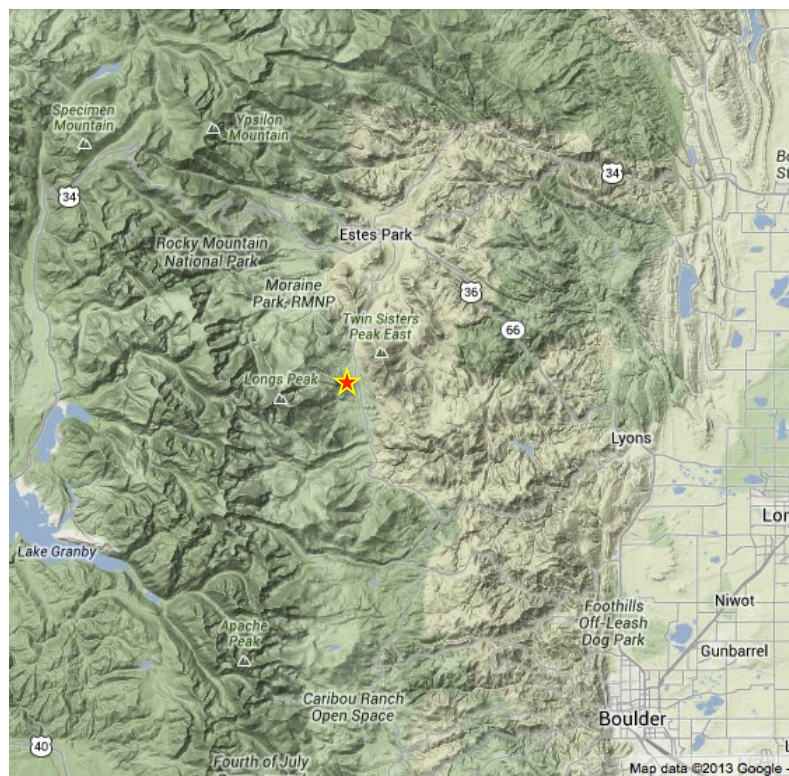


Figure 3-1: Map showing the Rocky Mountain National Park sampling site (red star). Boulder, Denver, and other cities form the Front Range urban corridor to the east.

The sampling site is adjacent to the Salvation Army High Peak, Covenant Heights, Timberline, and Aspen Lodge Resort camps, but removed from urban centers and considered rural; traffic on the nearby CO Hwy 7 is light. The HR-ToF-AMS was deployed from 2 July through 31 August 2010; the particle concentrations, deposition, and visibility effects that motivate this work are consistently greater in summer (Malm et al. 2009; Beem et al. 2010; Levin et al. 2009), when mountain-valley circulations cause afternoon upslope (~S) and

nighttime downslope (~NW) winds which may transport urban plumes toward or away from the RMNP site, respectively (Figure 3-2, Bossert & Cotton 1994; Bader et al. 1987; Bossert et al. 1989; Jirak & Cotton 2006). Co-located instruments include meteorological, CASTNet, and IMPROVE (designator: ROMO) stations, a particle-into-liquid sampler (PILS-IC, Orsini et al. 2003; Weber et al. 2001), Hi-Vol filter samplers, URG annular denuders, a differential mobility particle sizer (DMPS; TSI 3085), an optical particle counter, an aerodynamic particle sizer, and an automated precipitation sampler. Levin et al. (2009), Beem et al. (2010), and Benedict et al. (2013) present site maps and results using some of above instrumentation.

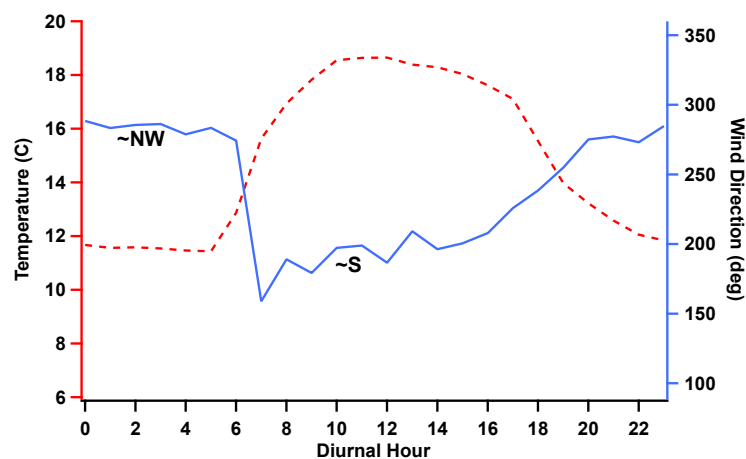


Figure 3-2: Study-average diurnal variation of ambient temperature (red dashed line, left axis) and surface wind direction (blue line, right axis).

3.2 General Particle Composition and Concentration

The total aerosol mass concentration during these summer measurements was fairly low, with an average of $5.13 \pm 2.72 \mu\text{g}/\text{m}^3$, but comparable to average $\text{PM}_{2.5}$ measurements from the IMPROVE network during July and August from 1991 to 2012 ($4.87 \pm 2.37 \mu\text{g}/\text{m}^3$, CIRA 2013; most $\text{PM}_{2.5}$ was submicron during this study). Total organics dominate with frequent higher-concentration events manifested in both brief, high-amplitude spikes, and longer-duration, lower-intensity increases (max = $93.09 \mu\text{g}/\text{m}^3$, average $3.86 \pm 2.66 \mu\text{g}/\text{m}^3$, Figure 3-3); organics

contribute $75.2 \pm 11.1\%$ of total submicron mass on average, which is consistent with the organic contribution to 24-hour average $PM_{2.5}$ found in the summer of 2006 ($60 \pm 12\%$; Levin et al. 2009). Sulfate is lower and less featured (max = $7.45 \mu\text{g}/\text{m}^3$, average $0.85 \pm 0.48 \mu\text{g}/\text{m}^3$), and nitrate and ammonium are also low (NO_3 : max = $5.37 \mu\text{g}/\text{m}^3$, average $0.22 \pm 0.24 \mu\text{g}/\text{m}^3$; NH_4 : max = $2.05 \mu\text{g}/\text{m}^3$, average $0.20 \pm 0.14 \mu\text{g}/\text{m}^3$, Figure 3-3). These values are statistically similar to previous datasets covering 1991-2012, showing low inter-annual variability in major species and total particulate mass (Table 3-1); thus, this study may illustrate ‘typical’ particle characteristics and sources at the site.

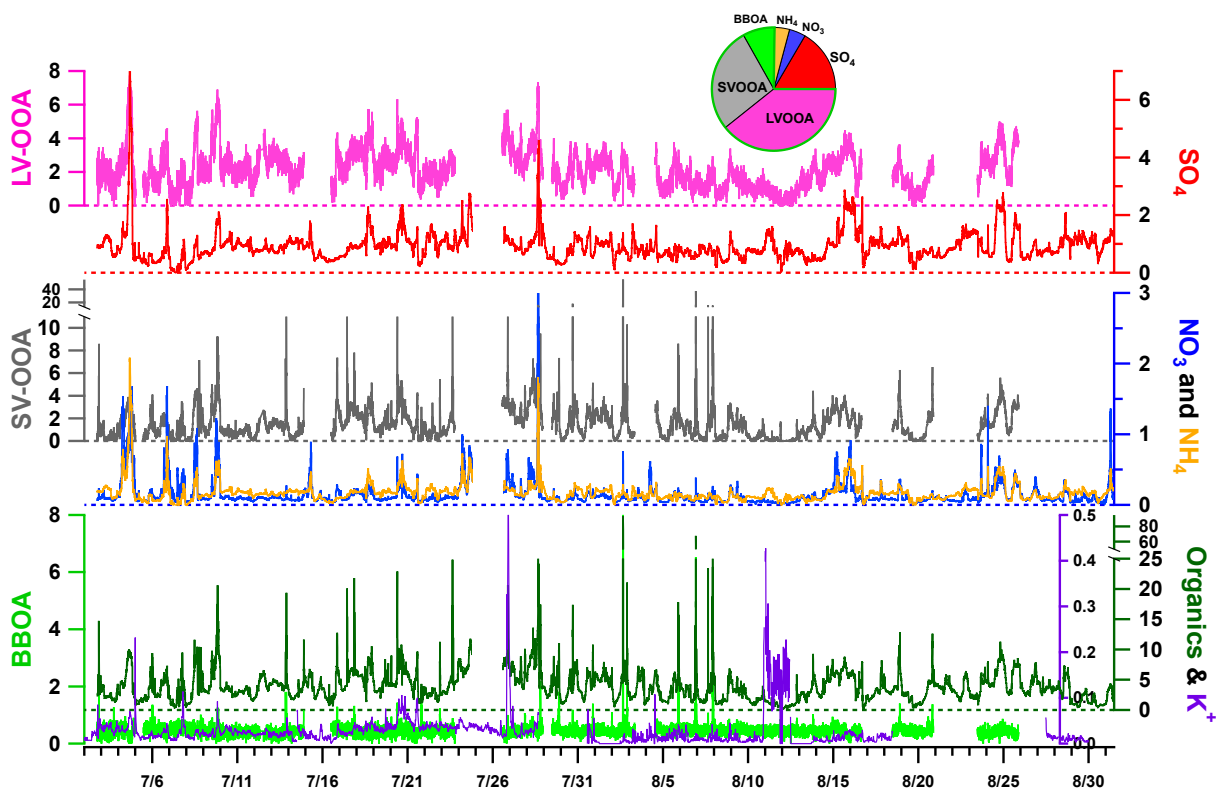


Figure 3-3: Time series of inorganic components, total organics, and organic factors (LV-OOA, SV-OOA, and BBOA) in $\mu\text{g}/\text{m}^3$. Potassium (K^+) is from 17-minute-average PILS-IC samples. Pie chart shows study-average contributions for each component; the green outline contains total organics.

Table 3-1: July-August average \pm standard deviation concentrations of particulate species in $\mu\text{g}/\text{m}^3$. IMPROVE data are averaged over 1991-2012, and were accessed via the VIEWS database on 22 January 2014. *(Benedict et al. 2013) **Averaged over 2005-2012

	NO₃	SO₄	NH₄	OM	PM_{2.5}
this study	0.22 \pm 0.24	0.85 \pm 0.48	0.20 \pm 0.14	3.86 \pm 2.66	PM ₁ : 5.13 \pm 2.72
Summer 2006*	0.12	0.99	0.32		
Summer 2010*	0.08 \pm 0.06	0.31 \pm 0.14	0.18 \pm 0.07		
IMPROVE	0.17 \pm 0.19	0.76 \pm 0.30	0.05 \pm 0.06	2.28 \pm 1.52**	4.87 \pm 2.37

Time-series correlations indicate ammonium-nitrate ($r^2 = 0.89$) and ammonium-sulfate ($r^2 = 0.97$) mixtures; ammonium nitrate and ammonium sulfate commonly arise in ambient particles produced from ageing of agricultural, industrial, and other anthropogenic sources. The low correlation between nitrate and sulfate ($r^2 = 0.34$, Table 3-2) may indicate that they are not regularly internally mixed in the local aerosol. Formation mechanisms for particulate ammonium nitrate and ammonium sulfate may differ: ammonium nitrate may arise from condensation of nitric acid and ammonia with subsequent particle-phase salt formation, or, less commonly, gas-phase salt formation with subsequent partitioning to the particle phase, and can involve dry or wet particles, or droplets; in possible contrast, because aqueous processing is responsible for most S(VI) formation, the presence of sulfate suggests that at least a portion of the particles (i.e. those containing ammonium sulfate) may have undergone cloud processing (Lelieveld & Heintzenberg 1992; Barth et al. 2000; Seinfeld & Pandis 2006); this will be explored further in following sections.

Table 3-2: Time-series correlation coefficients (r^2) between inorganic species and organic factors calculated using the IGOR linear regression algorithm.

	LVOOA	SVOOA	BBOA	SO₄	NO₃
SO₄	0.77	0.18	0.05		0.34
NO₃	0.33	0.41	0.02	0.34	
NH₄	0.76	0.72	0.03	0.97	0.89

Diurnal concentration patterns are explored in Figure 3-4; inorganic diurnal means increase but the 25th and 75th percentiles increase only slightly (though in similar profile to the oxidized organics, in the next section), indicating that the mean values are driven by fewer, high-concentration events; i.e. the diurnal variations in inorganic species are not consistent. The afternoon increases in the means of sulfate and ammonium have a pattern different than that of nitrate, supporting the suggestion that events and/or mechanisms driving concentrations of ammonium sulfate differ from those influencing nitrate. Nitrate has a bi-modal mean similar to total organics (see Section 3.2) and presaging the organic nitrogen content explored in Section 3.3. For total organics and inorganics on average, concentrations begin to increase at ~10:00-12:00 LST, approximately 2-4 hours after the ~8:00 LST initiation of upslope winds (Figure 3-2), consistent with typical lags observed in episode analysis (Section 3.7).

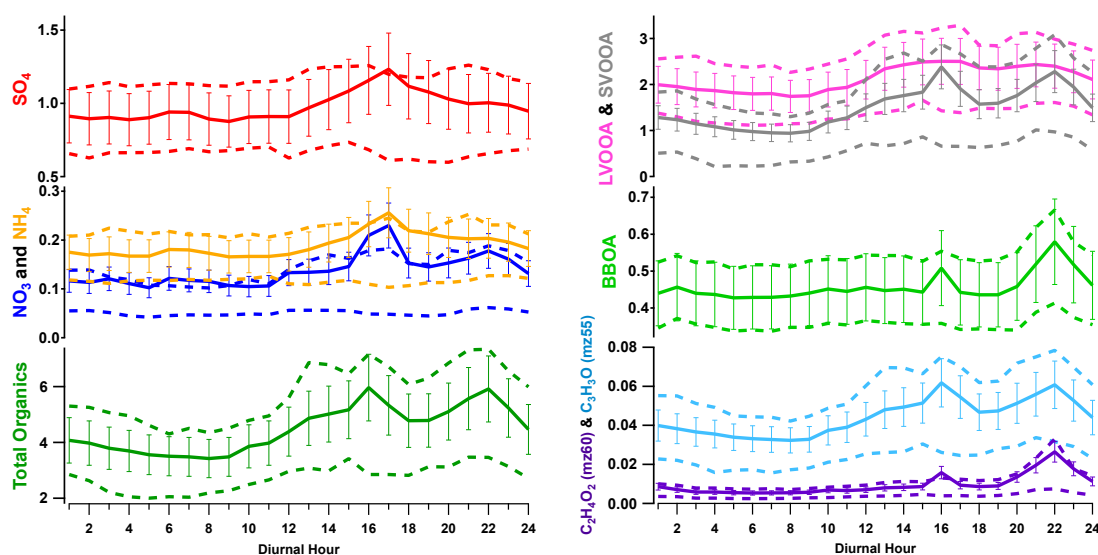


Figure 3-4: Study-average diurnal concentrations of particulate sulfate, nitrate, ammonium, total organics, BBOA, LV-OOA, SV-OOA, $C_2H_3O^+$ (m/z 43), $C_3H_3O^+$ (m/z 55), and $C_2H_4O_2^+$ (m/z 60, levoglucosan). Solid lines are means, with $\pm 20\%$ error bars reflecting AMS quantitation error. Dashed lines are 25th and 75th percentiles.

3.3 PMF-Derived Organic Aerosol Factors

Positive Matrix Factorization suggests a three-factor solution with Biomass Burning Organic Aerosol (BBOA, **Figure 3-5**; Simoneit et al. 1999) and two types of oxidized organics, Low-Volatility Oxidized Organic Aerosol (LV-OOA) and Semi-Volatile Oxidized Organic Aerosol (SV-OOA; Lanz et al. 2007; Ng et al. 2010).

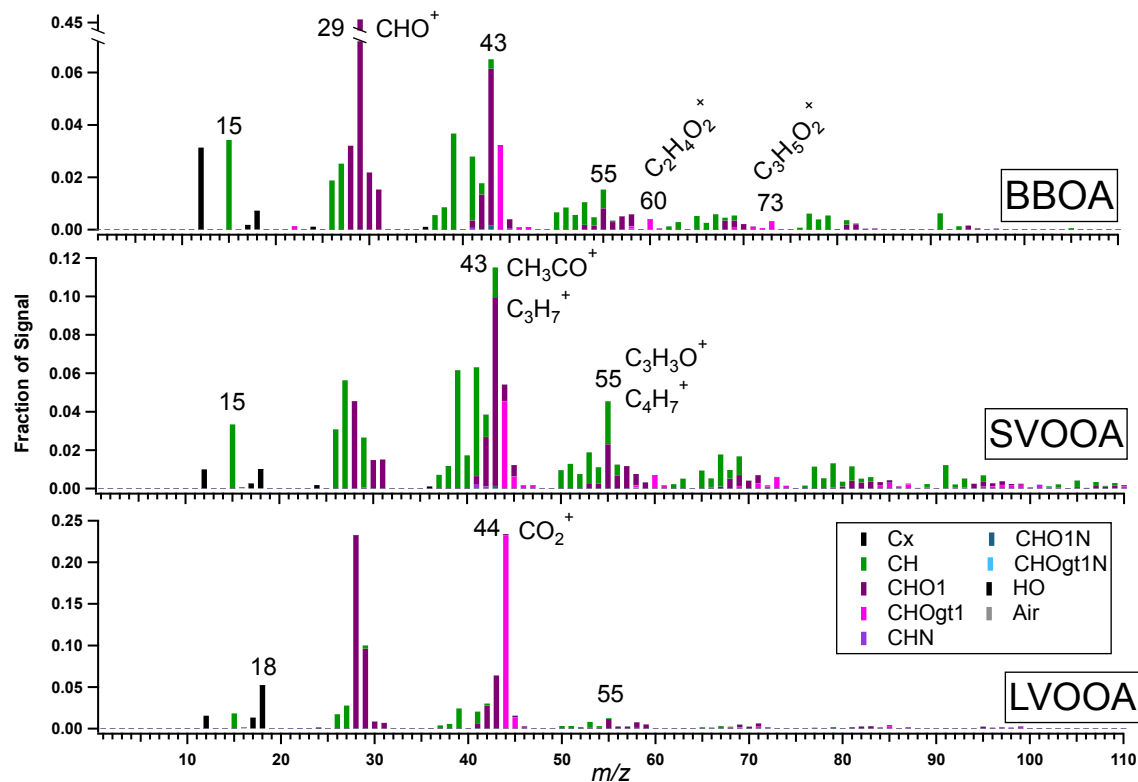


Figure 3-5: Normalized mass spectra of organic aerosol types determined by Positive Matrix Factorization (Paatero and Tapper, 1994): Biomass Burning Organic Aerosol (BBOA), Semi-Volatile Oxidized Organic Aerosol (SV-OOA), and Low Volatility Oxidized Organic Aerosol (LV-OOA).

The factor mass spectra display classic features of the given organic type as defined in numerous papers: SV-OOA (or OOA-II) is indicated by greater signal at m/z 43 (C₃H₇⁺ and CH₃CO⁺) than at m/z 44 (CO₂⁺) and has a peak at m/z 55 (C₄H₇⁺ and C₃H₃O⁺), while LV-OOA (or OOA-I) is highly oxidized, with a dominant peak at m/z 44 (CO₂⁺) (Lanz et al. 2007; Ulbrich et al. 2009); the BBOA factor features prominent fragments of cellulose and hemi-cellulose combustion products at m/z 60 (C₂H₄O₂⁺) and m/z 73 (C₃H₅O₂⁺) (Alfarra et al. 2007; Weimer et

al. 2008; Aiken et al. 2009). These biomass burning marker compounds are released from all wood burning and therefore cannot – by themselves - be used to differentiate campfires and wildfires; however, meteorological and temporal analyses may be used to suggest fire types as discussed later in this chapter. All of these factors are quite oxidized, with significant CH_3CO^+ (at m/z 43) and CO_2^+ (at m/z 44); oxygenated fragments often dominate signal at a given m/z (note fragment families CHO and CHOgt1 in Figure 3-5).

The three-factor solution is supported by meaningful dissimilarities in the time series (Figure 3-3), diurnal profiles (Figure 3-4), and average mass spectra (Figure 3-5) of the factors. LV-OOA is generally most abundant (average = $2.15 \pm 1.11 \mu\text{g}/\text{m}^3$), and features longer duration (~6-11 hour), low amplitude (2-3 times average) elevated-concentration events. The LV-OOA time series is correlated with sulfate and ammonium (Table 3-2), similar to studies with LV-OOA factors from anthropogenically-influenced secondary aerosol formation (Jimenez et al. 2009; Lanz et al. 2007; Ulbrich et al. 2009; Zhang et al. 2011). Internal mixing of sulfate and low-volatility OA may arise from similar oxidation pathways; S(VI) species result mainly from atmospheric oxidation of S(IV) species, and thus particles containing sulfate have been subject to advanced oxidative processing, which also tends to produce low-volatility OA (Jimenez et al. 2009). Aqueous processing is known to efficiently produce both low-volatility organic compounds and S(VI) species.

LV-OOA increases consistently in the afternoon (diurnal mean mode at 14:00-15:00 LST) and nighttime (mode at 22:00 LST, Figure 3-4). The afternoon increase may arise from transport with upslope winds, as will be explored below; the nighttime concentration maximum begins to form at ~16:00 LST, when temperatures start to drop (Figure 3-2), suggesting effects from boundary layer compression and/or thermal partitioning. Both OOA factors also feature a subtle

8:00 LST minimum, which may be attributed to thermal boundary layer expansion before an influx of particles associated with afternoon upslope winds; fine-mode particles persist long enough (4-8 days) in the absence of precipitation to undergo concentration changes due to boundary layer compression and expansion (Benkovitz et al. 1994; Tanner et al. 2005).

While SV-OOA is lower in general, it is more variable (average = $1.51 \pm 1.63 \mu\text{g}/\text{m}^3$); the SV-OOA timeline is punctuated by longer duration, low amplitude concentration increases similar to (and often accompanied by) LV-OOA increases, but also short, high-amplitude (4-10 times average, max = $64 \mu\text{g}/\text{m}^3$) periods commensurate with increasing BBOA. Like LV-OOA, SV-OOA has two modes in the diurnal average; however, the evening increase is more pronounced than that of LV-OOA (discussed below). SV-OOA is correlated with ammonium and, more weakly, nitrate (Table 3-2), suggesting influence from urban areas and/or agriculture. These semivolatile species indicate a less-aged aerosol, and may indicate different processing pathways, as will be discussed further in Section 3.5.

BBOA is generally very low (average $0.46 \pm 0.21 \mu\text{g}/\text{m}^3$), but has brief (~1-2 hour), higher-concentration episodes; these events occur in the evenings and the occasional afternoon, producing a consistent diurnal mode at ~22:00 LST commensurate with nighttime campfires at adjacent summer camps and an outlier-driven mean increase at ~16:00 LST (Figure 3-4, High Peak Camp manager Russ Chandler, personal communication, 9 September 2012). BBOA is not correlated with other AMS-determined aerosol components or 17-minute PILS-IC potassium ($r^2 = 0.01$); however, the K^+ timeline periodically tracks BBOA. Because K^+ is emitted mainly during the fire flaming phase (versus smoldering), it often lacks correlation with anhydrosugar fragments at m/z 60, etc., which are more consistent biomass burning markers across burn and

fuel types (Lee et al. 2010; Sullivan et al. 2008); the intermittent association between potassium and BBOA suggests that the campfires exhibited a range of flaming phases.

We reiterate that PMF solutions are subjective since they involve qualitative user inputs such as number of factors; indeed, characteristics inconsistent with the anticipated behavior of anthropogenically-influenced, transported SV-OOA (see Section 3.5) lead us to hypothesize that some 'BBOA' mass may be misallocated to SV-OOA by the algorithm. The most compelling evidence is that the SV-OOA mass spectrum contains some m/z 60 and m/z 73, but average mass spectra of all high-SV-OOA periods with no commensurate increase in BBOA do not contain mass at m/z 60 and m/z 73; therefore, an SV-OOA mass spectrum containing these markers does not represent the vast majority of elevated-SV-OOA periods.

Also, the amplitude and duration of some high-concentration SV-OOA events is inconsistent with the expected behavior of transported aerosol. Dilution during transport (Section 3.5) tends to damp high-concentration events and, in general, OOA factors see gradual, sustained, and moderate (\sim 2-3 times average) concentration increases accompanied by inorganics. The appearance, then, of brief, high-amplitude 'SV-OOA' events commensurate with BBOA but not with inorganics is inconsistent with the likely behavior of transported, aged aerosols. Brief, high-amplitude events might, however, be expected from a local (low dilution), sporadic point source such as campfires, so the appearance of these 'spikes' in SV-OOA supports the hypothesis that some BBOA mass is inappropriately assigned to SV-OOA (see example: period A, Figure 10). Diurnal patterns echo the timeline idiosyncrasies; the 22:00 LST increase in BBOA is mirrored in the modes of m/z 60 and SV-OOA. In a PMF run excluding periods with BBOA events (not shown), SV-OOA increases only slightly at night and is similar

to LV-OOA in amplitude and pattern; apportionment of some BBOA mass to SV-OOA would account for the enhancement in SV-OOA's nighttime mode.

Matrix rotation in PMF redistributes mass between the factors, presenting alternate solutions (Ulbrich et al. 2009). Positive FPEAK (discussed in the Methods) allocates less m/z 60 and m/z 73 to SV-OOA and more to BBOA, but also re-allots mass at other m/z s to BBOA; this renders the BBOA time line increasingly like that of SV-OOA, which is unphysical because it suggests that BBOA increases during periods when no biomass burning markers are present in the mass spectra, as explained above. Matrix rotation therefore fails to provide additional information about the local aerosol and the original (FPEAK=0) solution is presented here.

In an effort to better resolve the BBOA episodes, the factor number was increased (beyond the three-factor solution defended earlier) to isolate mass spectral features such as m/z s 60 and 73 that seemed to be partially misallocated. Using 'typical' BBOA and SV-OOA mass spectra as a guide, six factors were recombined based on timeline similarity to produce three factors with mass spectra and timelines closer to the 'expected' patterns explained earlier. The resulting BBOA spectrum contains the vast majority of m/z 60 and m/z 73 mass, and the SV-OOA timeline is free of BBOA-like concentration spikes (Appendix Section 8.3, **Figure 8-4**). The resulting OOA factors are not as well correlated with their inorganic counterparts as in the original analysis (Appendix Section 8.3, **Table 8-3**); however, the general pattern of better correlations between LVOOA-ammonium-sulfate and SVOOA-ammonium-nitrate is preserved. Since this factor recombination method introduces additional subjectivity and is untested in the literature, the original PMF analysis is used herein.

All of the PMF methods attempted yield similar conclusions about the nature of particles at the Rocky Mountain site; LV-OOA is associated with ammonium sulfate, SV-OOA with

ammonium nitrate, and BBOA has sporadic, high amplitude events. These similarities suggest that the analysis is useful for interpreting the local particulate despite the imperfect factorization of BBOA and SV-OOA. PMF factors are mass-spectrally static; to explore the behavior of and variability within each type of OA, periods dominated by a given factor were subject to elemental, size, and wind-rose analyses which will be presented below; "LV-dominated" periods are indicated when $[LV] \geq 2*[SV]$, "SV-dominated" periods when $[SV] > [LV]$, and "BBOA-dominated" episodes when $[BB] \geq 2*0.46 \mu\text{g}/\text{m}^3$ (twice the average concentration).

3.4 Elemental Analysis and Organic Nitrogen

Elemental analysis of high-resolution mass spectra utilized the updated AMS fragmentation table for ambient OA in Aiken et al. (2008). The ratio of organic mass to organic carbon (OM:OC) averages 1.99 ± 0.16 and indicates highly oxidized OA consistent with other non-urban sites (Turpin & Lim 2001; Aiken et al. 2008); O:C averages 0.66 ± 0.13 and H:C averages 1.27 ± 0.09 . N:C is determined from CHN and CHON fragments, excluding nominally inorganic fragments such as NO_2^+ that may also arise from fragmentation of organic nitrogen (ON) molecules; N:C averages 0.01 ± 0.01 (max = 0.55).

On the van Krevelen-triangle diagram (Figure 3-6), the data position in the apex of the triangle space (higher O:C and lower H:C) indicates highly oxidized particles consistent with other ambient datasets (Ng et al. 2011; Heald et al. 2010); data points are colored by the dominant PMF factor as defined above. SV-OOA- and BBOA-dominated periods occupy similar ranges, while LV-OOA events are more oxidized with lower H:C. During BBOA-dominated periods, O:C ranges from ~ 0.2 , consistent with the literature (usually ~ 0.3 - 0.4), to ~ 0.65 , which is higher than often observed (Aiken et al. 2007; Aiken et al. 2008; Heringa et al. 2012); this relative oxygenation may arise from the ubiquity of OOA at the site, and/or from additional

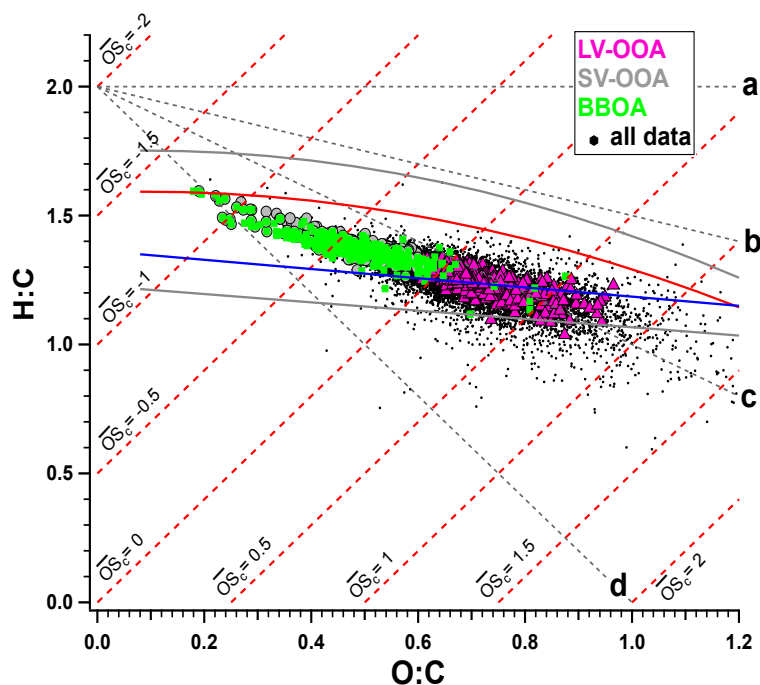


Figure 3-6: Van Krevelen-triangle diagram for time periods dominated by the given factor (as defined in Section 3.3) and for all data points. Estimated oxidation state, $\overline{OS}_c \approx 2 * O:C - H:C$ (Kroll et al. 2011). Red and blue lines indicate the region usually inhabited by ambient data in the $f43$ vs $f44$ plot; grey lines represent 10% error. a: +alcohol/peroxide, $m = 0$; b: carboxylic acid + fragmentation, $m = -0.5$; c: +carboxylic acid (no fragmentation), $m = -1$; d: +ketone/aldehyde, $m = -2$ (Ng et al. 2011).

partitioning of oxidized organics onto the new biomass burning particles. The unsorted total dataset is also shown to demonstrate the constancy of high oxidation; there are no points in the ‘HOA/POA’ region of the graph indicated by a grey ellipse. The overlap between LV- and SV-OOA-dominated data points in van Krevelen space and the concomitance of SV- and LV-OOA time-series ($r^2 = 0.59$) suggest that, *purely in terms of oxidation*, SV- and LV-OOA are somewhat arbitrary delineations between air masses whose oxidation varies continuously. However, the different inorganic mixtures (and sizes, Section 3.4) associated with LV-OOA and SV-OOA validate treating them separately.

Linear regressions of O:C/H:C are sometimes used to investigate oxidation mechanisms; for instance, a slope of -0.5 arises from 1 H loss per 2 O addition which is indicative of either carboxylic addition with C-C bond breakage or addition of both acid and alcohol/peroxide

functional groups without fragmentation (Heald et al. 2010). However, the reaction mechanisms producing these slopes are constrained only when observing air masses isolated during reaction, a doubtful assumption for any ambient dataset and especially one of this length. Nonetheless, these slopes are provided for reference. Slopes during periods dominated by each factor are all close to -0.5 ($m_{LV} = -0.54$; $m_{SV} = -0.56$; $m_{BB} = -0.53$), consistent with other ambient aerosol studies (Ng et al. 2011). The photo-oxidation of α -pinene also produces this slope, consistent with possible biogenic contributions discussed in Section 3.5, although other reactions can of course yield similar slopes and air masses herein are not isolated (Chhabra et al. 2011; Lambe et al. 2011).

A lower bound on organic nitrogen mass can be estimated using Equation 5 ($ON_{min} = (Org/OM:OC)*N:C*(14/12)$, where ‘Org’ is total organic mass); ON mass may be underestimated using this method because N:C includes only N from CHON and CHN fragments, omitting ‘inorganic’ nitrate (NO_n^+) produced by ON fragmentation. ON_{min} is small (max = $1.04 \mu g/m^3$; average = $0.02 \pm 0.02 \mu g/m^3$). The few, modest ON_{min} events are accompanied by BBOA (although not all BBOA increases are accompanied by ON_{min}) and total nitrate with no commensurate sulfate or ammonium (Figure 3-7); ON such as nitrophenols (Iinuma et al. 2007), urea (Mace et al. 2003), nitriles, and amines/amides (Simoneit et al. 2003) have been associated with biomass burning in the literature.

Though fragmentation in the AMS precludes identification of organic molecules, series of CHN fragments at m/z s 30 and 58 (with additional peaks at m/z s 72, 86, and 100) have been observed in mass spectra from laboratory and field data with amine content (Murphy et al. 2007; Silva et al. 2008); CH_4N^+ (m/z 30) may result from amine re-arrangement after electron impact ionization (Murphy et al. 2007). Here, prominent CHN fragments are noted at m/z s 30, 41, 53,

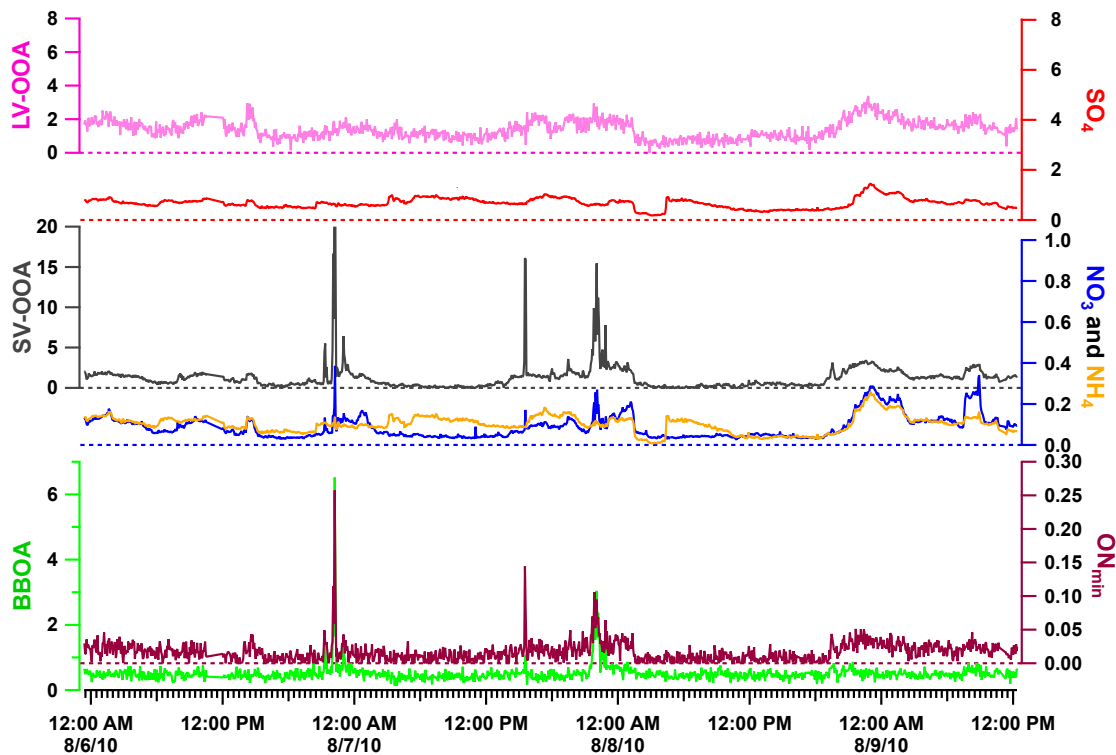


Figure 3-7: Time series showing select elevated-ON_{min} periods with inorganics and other organic factors from the Rocky Mountain National Park site.

58, 63, 67, 77, 81, 79, 91, and 95 and are organized into the ‘wave’ pattern often seen in organic spectra (m/z s 53, 67, 81, and 95, ‘Series 1’ in Figure 3-8), which arises from the tendency of organic molecules to lose CH_2 groups sequentially during fragmentation and results in peaks separated by 14 amu. Because multiple parent molecules may produce a given fragment under electron impact ionization, parent CHN molecules cannot be determined through fragmentation ratios, etc.; however, empirical formulae at m/z s 53, 67, 81, and 95 belong overwhelmingly to nitrile and/or pyrrole (heterocyclic) molecules, suggesting that these are (or fragment from) important ON compounds in the local particulate. Fragments at m/z s 63, 77, and 91 form another methylene-subtraction series (‘Series 2,’ Figure 3-8), for which empirical formulae also suggest nitriles and/or heterocyclic compounds, including pyridine, which is often used to stabilize

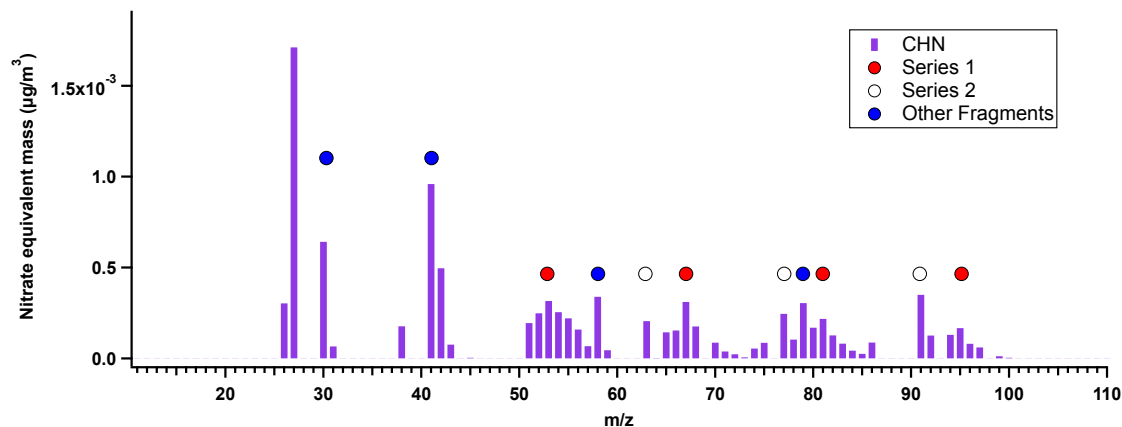


Figure 3-8: Rocky Mountain study-average mass spectrum of CHN fragments.

agricultural fertilizers and is produced in small amounts in biomass burning (McKenzie et al. 1995).

This CHN series, while not found in the literature, is similar to fragments observed in a similar high-altitude site near Grand Teton National Park (*m/z*s 30, 41, 55, 58, 67, 79, 91; see Chapter 4). The average CHN mass spectrum for elevated- ON_{\min} periods (not shown) has higher CHN signal than average total, LV-OOA, and SV-OOA spectra, but no appreciable difference in fragment patterns, indicating a concentration increase but likely minimal change in CHN composition. The concurrence of increases in ON_{\min} and BBOA suggests that ON content, and especially nitrile and/or hetero-aromatics, is enhanced in biomass burning plumes. Although CHON fragments (nominally, ‘organonitrates’) were fit in the high resolution analysis, they contained very little mass and no clear fragmentation patterns, precluding use for organonitrate exploration (Farmer et al., 2010).

Organic nitrogen content is evident in the presence of CHN fragments. Also, the presence of organic bases such as amines may be suggested by the dearth of inorganic cations indicated by a measured-to-predicted ammonium ratio less than one ($\text{NH}_4_{\text{meas:pred}} = 0.80$, $r^2 = 0.96$, where predicted ammonium is in stoichiometric proportion to $\text{NO}_3^- + \text{SO}_4^{2-} + \text{Cl}^-$); indeed, the amine

(and/or heterocyclic) compounds suggested in the mass spectra are basic, and amine salts with nitrate and sulfate have been observed in chamber photo-oxidations (Murphy et al. 2007). The study average cation-to-anion ratio is 0.74 ± 0.16 , which compares well to average spring-time (0.9 ± 0.2) and poorly to summer-time (1.2 ± 0.2) $PM_{2.5}$ filter data in a co-located, though not contemporaneous, study (Levin et al. 2009); Levin et al. attributed their summertime ‘excess ammonium’ to ammonium oxalate, of which we find no evidence; the high fragmentation in the AMS precludes detection of specific molecules such as oxalate. Quantification of ON from AMS data is also prevented by fragmentation of ON to nominally inorganic fragments, the inconsistency of this fragmentation between instruments, and the vast array of possible ON parent compounds in ambient particles.

3.5 Particle Size

Whereas PMF factors are comprised of individual fragments (many of which may contribute to a given m/z), particle size is determined for unit mass resolution data, making size analysis of high-resolution PMF factors challenging. However, size determination of marker m/z s and of time periods heavily dominated by a given factor (as described above) can be useful. Lognormal fits of aerosol component size distributions allow better statistical comparison of factor-dominated periods (Whitby 1978; Remer & Kaufman 1998; Dubovik et al. 2002) and were constructed using the standard Igor fitting algorithm; lognormal fits also allow size mode estimation in low-signal species such as ammonium and nitrate that suffer from lower signal:noise in the raw size distributions. Lognormal fit parameters include: $x_0 = D_g$ (geometric diameter), width = $2 \cdot \ln^2 \sigma_g$, $A = [\mu\text{g}/\text{m}^3] / (\ln \sigma_g \sqrt{2\pi})$, where σ_g = geometric standard deviation (Smith & Jordan 1964; Raabe 1971).

High-LV-OOA events have larger particles (~425 nm mode) than SV-OOA episodes (~350 nm mode), while BBOA may be slightly smaller (~300 nm mode, Figure 3-9). As indicated by the lognormal width parameter, LV-OOA events are also more monodisperse than SV-OOA; the tendency of condensation and coagulation during oxidation to make particles larger and more monodisperse suggests that the OOA factors spend time in transit from their source (Zhu et al. 2002; Seinfeld & Pandis 2006), and further that LV-OOA particles undergo more oxidative processing than SV-OOA particles, as mean radius increases continuously with ageing (Dubovik et al. 2002; Reid et al. 2005; Dinar et al. 2008; Grieshop et al. 2009).

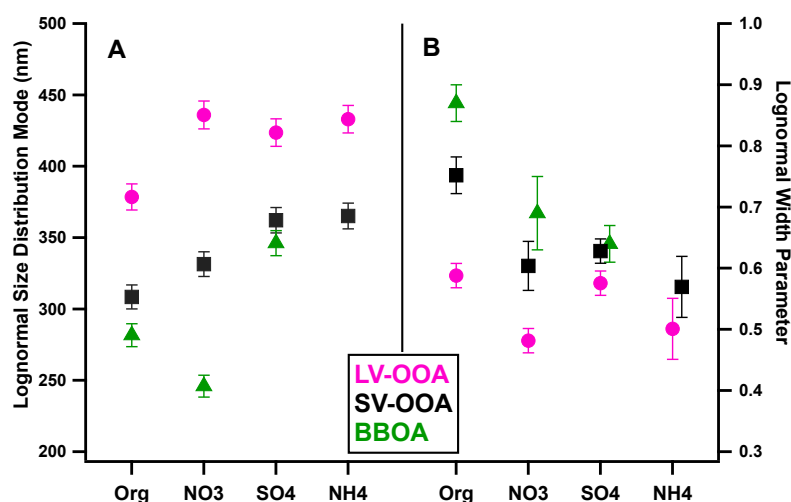


Figure 3-9: A) Mode of the log normal size distribution fit for the indicated species or total organics during time periods dominated by the color-designated organic factor; error bars are estimations of size-dependent PToF error, compounding chopper broadening and calibration-particle size standard deviation (Supplementary Section 2). B) Log-normal width parameter with error bars equaling one standard deviation of the lognormal fit. Ammonium concentrations were too low during BBOA events for size determination.

The similar size distributions and time-series of LV-OOA, ammonium, and sulfate suggest an internal mixture of these components. While SV-OOA and LV-OOA are often coincident, SV-OOA-dominated periods feature smaller particle sizes and a correlation with ammonium nitrate. As mentioned earlier, differences in atmospheric processing of the given components may lead to these distinct mixtures. SV-OOA and ammonium nitrate, all semivolatile species, may arise in the particle phase through condensation of vapors. While

oxidized nitrogen species and semi-volatile organics also may participate in aqueous chemistry, such processing tends to produce lower-volatility organics and would result in internally mixed sulfate. This implies that the SV-OOA/ammonium nitrate particles undergo, if any, less aqueous processing than the LV-OOA/ammonium sulfate particles.

As mentioned earlier, sulfate is used as an aqueous processing tracer, and its correlation with LV-OOA suggests evidence of aqueous organic processing. Size distributions of cloud/fog-processed particles tend to be larger than observed here (Hering & Friedlander 1982; John et al. 1990; Meng & Seinfeld 1994; Hoppel et al. 1994), but many of these studies feature heavy, prolonged cloud/fog cover and meteorology and chemistry (e.g. higher aerosol concentrations) which may differ from that in the Front Range. Aqueous reactions in wetted particles are also feasible; the deliquescence relative humidity of mixed ammonium sulfate-organic particles is ~30-70% (depending on organic fraction and type) and the ambient RH varied from 4-100% during the study with an average of $59 \pm 31\%$ (Takahama et al. 2007; Smith et al. 2011; Smith et al. 2012); this is consistent with the historical July-August average RH of ~50%, based on monthly-average data (during 1991-2012, CIRA 2013).

BBOA events are smaller and more polydisperse than other organic factors, higher in amplitude, and not coincident with inorganic species, reflecting a fresher, local particle population given less time to grow by condensation and/or coagulation. With an average organic mode of ~280 nm, the biomass burning aerosol at this site is consistent with fresh BB plumes from temperate forests, which range in mode from 86-300 nm (Reid & Hobbs 1998; Reid et al. 2005 and references therein; Adler et al. 2011). 2-D time and size images for some BBOA events (not shown) reveal growth of total organics from 100-200 nm to ~350 nm over the course of the event, consistent with observations of similar biomass burning events and explained by rapid

coagulation (Adler et al. 2011). The size distributions of particles during SV-OOA events with and without concurrent BBOA increase were similar. The level of oxidation (average $f_{44} = 0.09 \pm 0.02$ during BB-dominated periods) is consistent with literature SV-OOA; together, the relatively large size (in comparison to some biomass combustion, e.g. mode = 100 nm in Adler et al. 2011, though mode may vary with burn type) and advanced oxidation may be explained by the presence of ‘background’ OOA and/or rapid condensation of semivolatile VOCs onto the increased particle surface area provided by the BB plume (Grieshop, Donahue, et al. 2009; Adler et al. 2011).

3.6 Source/Transport Analysis

The chemical and size data indicate that oxidized organic aerosol is mixed in varying combinations with inorganic anthropogenic tracers nitrate, sulfate, and ammonium. The level of oxidation argues for prolonged reaction time in the atmosphere; also, limited local habitation precludes high emissions of inorganic anthropogenic tracers. Together, these suggest transported, anthropogenically-influenced OOA particles, which could arise from either anthropogenic OA and SOA precursors, and/or anthropogenic OA and oxidation products of biogenic organics, such as BVOC oxidation in the presence of NO_x (Rollins et al. 2012; Kiendler-Scharr et al. 2009; Ng et al. 2008; Surratt et al. 2010). Correlations between secondary OA mass and temperature may indicate which precursors and mechanisms are at play: in many urban/downwind ambient observations, a negative correlation arises from thermodynamically-driven partitioning effects, but in heavily forested areas, increased SOA-precursor BVOC emissions from increasing temperature can overwhelm thermodynamic partitioning reduction, causing an overall increase in secondary mass (Leitch et al. 2011; Pierce et al. 2012; Ahlm et al. 2013). These studies are usually episode-focused and establish the isolation of the given air mass using meteorology and

anthropogenic trace gases; at Rocky Mountain, the average relationship between temperature and SOA concentration is determined for periods with up-slope and down-slope winds.

Concentrations of LV-OOA, SV-OOA, 'SOA' (LV+SV), and BBOA have no relationship with ambient temperature during either upslope or downslope winds ($r^2 \approx 0$, $m \approx 0$; **Table 8-2**); this could a) indicate a balance, on average, between thermodynamic partitioning and BVOC precursor emission effects on SOA mass, and/or b) be a product of the inconsistent lag between wind direction and concentration changes (see below). Episode analysis concerning temperature and partitioning was not performed.

Fragmentation within the AMS prevents the molecular specificity needed to determine which of these mechanisms is at play. However, co-located (though not concurrent) carbon isotope work indicates that ~88% of summer $PM_{2.5}$ carbon is contemporary (Schichtel et al. 2008). From the PMF factors, biomass burning OA (which contains contemporary carbon) contributes a study average of ~11-16% of submicron OC, depending on whether the original or recombined PMF solutions are used for BBOA mass and OM:OC, respectively (in the original solution, misallocation of BBOA mass to SV-OOA makes this a lower-bound estimate). Even during the highest-concentration BBOA episode, BB comprises only 5.77-14.45% of the 24-hour average OC. Thus, biomass burning does not appear to provide all of the observed contemporary C, assuming that the contemporary-C fractions of PM_1 and $PM_{2.5}$ do not differ greatly (reasonable since most fine mass is submicron), and that inter-annual contemporary carbon fraction variability is low (which depends on wildfire variability); in 2010, total burned area from the NCAR FINN model and fire contributions to surface $PM_{2.5}$ are quite similar to values in the years 2003-2011 in Colorado (high-fire-event years occurred in 2002 and 2012, Figure 8-3; Val Martin et al. 2013). The contemporary carbon and partitioning evidence presented above

suggest that biogenic VOCs may contribute to local OA formation. Levin et al. (2012) described particle growth from condensation of organics in summer at a similar forested Colorado site; concomitant size increase and κ (hygroscopicity parameter) decrease during particle formation events is an indicator of organic condensation (Dusek et al. 2010). Lastly, the brief biomass burning events feature small, polydisperse particles not correlated with anthropogenic tracers and likely derived from nearby campfires during the studied time period.

Associating meteorology with component concentrations and diurnal patterns supports these source indications. Surface winds are funneled by the valley topography and are predominantly down-valley from the WNW (48%) or up-valley from the SE (16%, Figure 3-10); this pattern is consistent inter-annually, with similar wind roses produced by data from 1995-2005 (Malm et al. 2009). Raw and directionally-averaged concentrations of aerosol components plotted against surface wind direction over sixteen 22°30' wind direction bins are shown with conditional probability functions (CPFs) in Figure 3-10. High inorganic concentrations are associated with local SE winds indicating up-valley movement from the Front Range barring complex flow and are very similar in both CPF value and meteorological association to co-located PM_{2.5} measurements (note that CPFs are multiplied by 10 to share a scale with concentration; Benedict et al. 2013). CPFs for OOA factors also have an association with southeasterly winds, and higher average concentrations are associated with S-SE winds for all components (including BBOA, though from a different source; see below). While increases in inorganics are always accompanied by LV- and SV-OOA, OOA sometimes increases independently with Northwesterly winds. This may indicate regional OOA content (i.e. “background” organics), possibly aged biogenic SOA from forest emissions, which could originate from the west over the mountains and be unassociated with Front Range emissions.

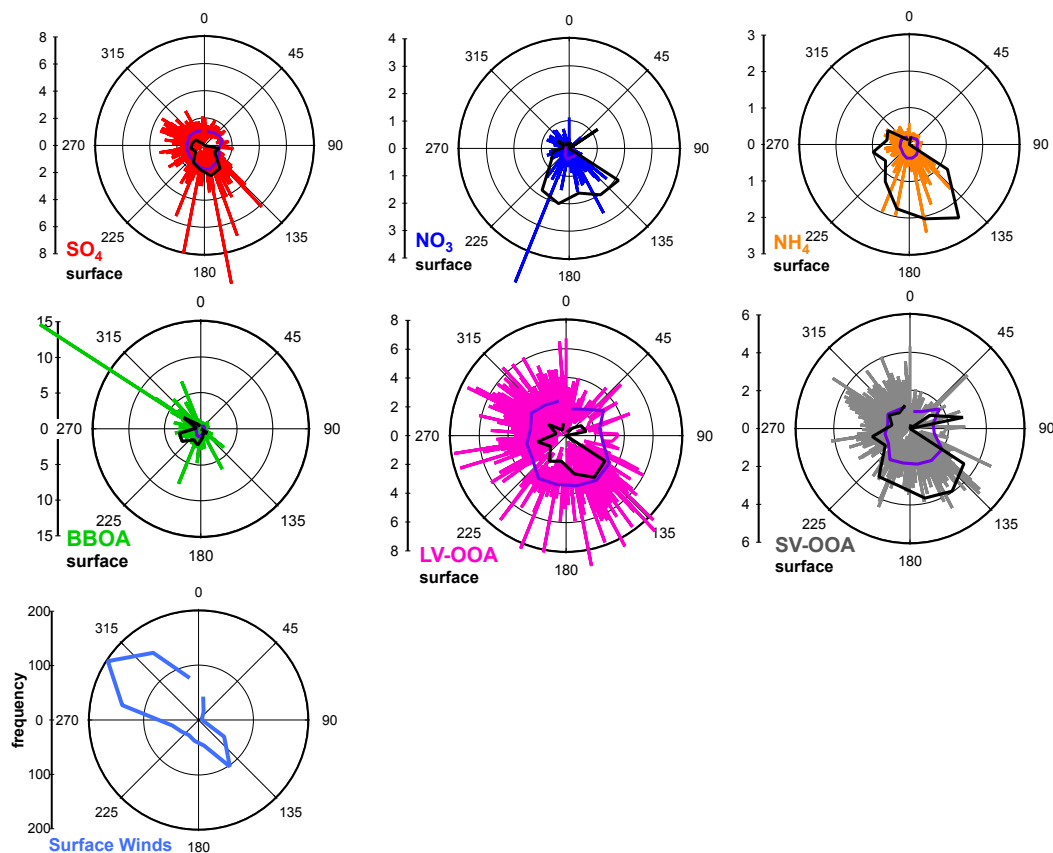


Figure 3-10: 1-hour average concentrations ($\mu\text{g}/\text{m}^3$) of organic aerosol types with surface wind direction. Raw data are colored by species, average concentrations over the sixteen $22^\circ 30'$ wind direction bins are shown in purple, and black lines indicate the Conditional Probability Function (CPF multiplied by 10). The number of data points in each bin is shown in the lower left-hand panel.

Ratios of average concentrations during upslopes (wind from $120\text{--}225^\circ$) to those during downslopes (all other directionalities) are 1.56 for SV-OOA, 1.25 for LV-OOA, 1.37 for total organics, and 1.21-2.08 for inorganics, indicating that ‘regional background’ concentrations are ~48-82% of those associated with upslope winds; these background concentrations are somewhat higher than found in Benedict et al. (2013), where the upslope-downslope ratio of, for example, ammonium in summer 2009 was 2.4 (versus 1.44 herein).

High BBOA concentrations are usually associated with NW or SW-to-S surface winds. The closest campfire source is ~200m WNW of the sampling site; the shorter transport (and therefore dilution) time may explain the higher concentrations in BBOA events from the WNW.

Three other camps are placed ~0.5-1 km due south; the increased number and distance of the fires explains the higher average but lower maximum concentrations associated with SW-to-S winds. The Conditional Probability Function (CPF) analyses indicate higher concentrations with up-valley S to SE surface winds for all constituents except BBOA, which has a weak S through NW dependence consistent with the placement of the campfire sources.

Denver 700mb winds may represent regional flow and are predominantly (56%) from the west (Figure 3-11). Down-slopes (SW-N) often occur in the nighttime and morning, with upslope flow in the afternoon (SSW-SE; 28% of data points). Enhanced LV- and SV-OOA CPFs and bin averages are associated with NE-ESE 700 mb winds (Figure 3-11); other constituents show no obvious directional dependence in either raw or averaged data, though CPFs for inorganic species indicate NE-SSE (upslope) directionality. BBOA shows little relationship to regional winds, which is logical given the local sources. The weak relationship between concentrations and regional winds may be affected by the high averaging time needed to match AMS data to 700mb winds (3 hours, damping high amplitude events and possibly brief but important changes in regional flow). Lastly, the transport time lag between changes in regional or surface flow and concentration increase (or suppression) at the site is variable. Attempts at time-lag correction using various offsets (1-3 hr) did not lead to better correlations between concentrations and wind direction; transport times ranging as low as 1 hour were found in this and co-located studies (Figure 27; Benedict et al. 2013).

Overall, the OOA-inorganic mixtures described earlier are linked with upslope flow from the Front Range via their association with up-valley surface winds and afternoon concentration increases. All elevated inorganic concentrations are accompanied by E to SE surface winds and LV- and SV-OOA increases; depressed concentrations of inorganics are accompanied by

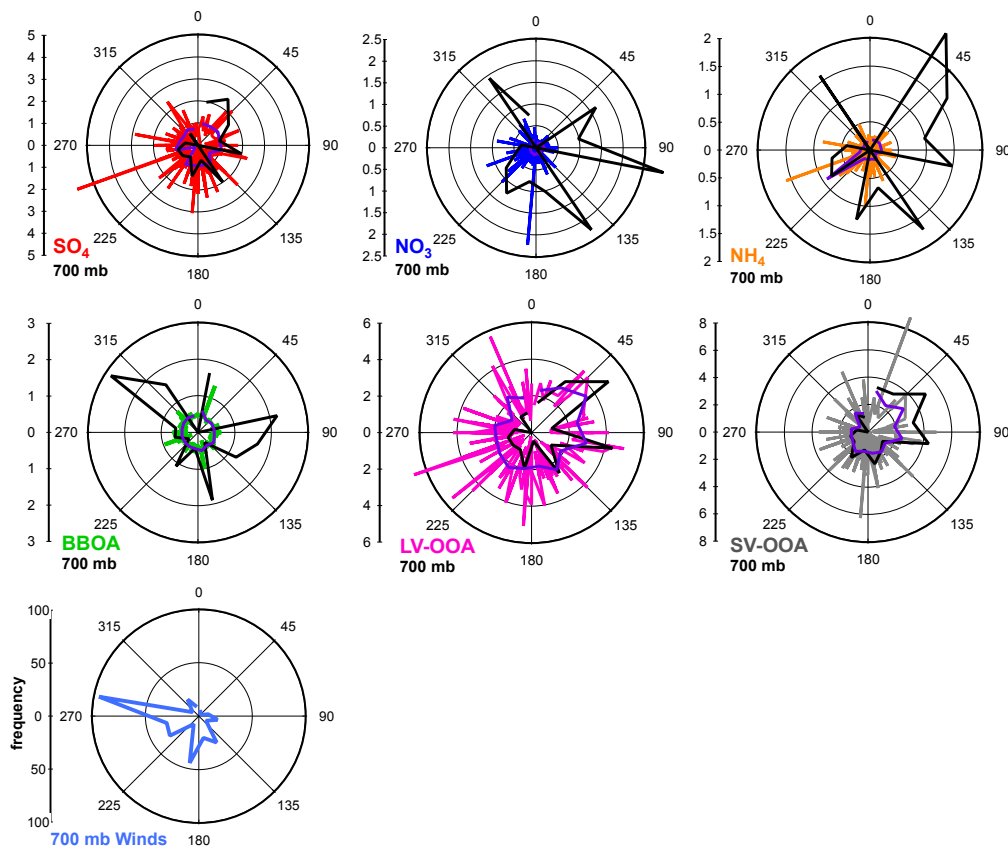


Figure 3-11: 3-hour average concentrations of aerosol components with 700mb wind direction. Raw data are colored by species, average concentrations over sixteen 22°30' wind direction bins are shown in purple, and black lines indicate the Conditional Probability Function (CPF multiplied by 10). The number of data points in each bin is shown in the lowest left panel.

westerly to northerly flow, though some increases in OOA ('regional background') occur during NW flow. Diurnal averages indicate increased afternoon concentrations of most constituents, consistent with the pattern of afternoon upslope flow. BBOA from local sources is transported by surface winds and not associated with regional flow or inorganic species.

Rocky Mountain data were also compared to $0.5 \times 0.66^\circ$ nested U.S. GEOS-Chem model runs (which simulate mountainous regions better than other resolutions, Wainwright et al. 2012), using two Denver surface grid boxes for comparison to upslope periods and a 'free tropospheric' box above the planetary boundary layer (PBL) over RMNP for comparison to downslope data (Bonne Hotmann, personal communication, 20 August, 2013). The model was run with 2010

emissions data and meteorology. During summer months, boundary layer and free tropospheric influence are often indicated during up- and downslopes, respectively, at similar mountainous sites including Storm Peak, Colorado (Obrist et al. 2008), Whistler Mountain (2,182 m; Gallagher et al. 2011), three volcanic island mountains (2.4-3.7 km, Kleissl et al. 2007), and the Jungfrauoch Sphinx research station (Baltensperger et al. 1997; Nyeki et al. 1998; Collaud Coen et al. 2011). Data used to differentiate between BL and FT influence include water mixing ratio (Weiss-Penzias et al. 2006; Obrist et al. 2008), air temperature (caveats include the influence of local surface heating, Grant et al. 2005), and aerosol concentration (Baltensperger et al. 1997; Nyeki et al. 1998; Collaud Coen et al. 2011; Gallagher et al. 2011). The diurnal profile of OOA at Rocky Mountain is very like that of particle number concentration at Whistler Mountain and Jungfrauoch, which were used to evidence the diurnal cycle of afternoon PBL (increase in [CCN]) and nighttime FT influence (decrease in [CCN], Gallagher et al. 2011). Here, though the PBL height modeled by GEOS-Chem during the study (avg. = $1,061 \pm 239$ m) is lower than the site elevation (2,740 m) and so implies ubiquitous free-tropospheric influence, the AMS data suggests that transport of anthropogenically-influenced boundary-layer air from the Front Range is important (and modeled PBL heights may be underestimated due to the lack of topography in the model); evidence for FT influence at night includes the significant depression in OOA concentrations, though this could also arise from downslopes transporting cleaner PBL 'regional background' air masses.

Modeled study-average Denver $PM_{2.5}$ inorganics (SO_4 , NO_3 , and NH_4) and organics are ~50% and ~12% of AMS averages during upslope winds, respectively (Table 3-3; AMS measures PM_{10} , but most fine mass is submicron at this site); however, though the model is similarly low during downslope periods, inorganics are within a standard deviation of the AMS

Table 3-3: Study-average component concentrations from the HR-ToF-AMS during upslope (120-225°) and downslope (1-120° & 225-360°) winds, with the ratio of average upslope to average downslope concentrations; ‘G-Chem Denver PBL’ shows study-average component concentrations from the two Denver surface grid boxes thought to be a source area transported by upslope winds, while ‘G-Chem RMNP FT’ data is from the grid box immediately above the planetary boundary layer located over RMNP, representing the content of ‘free tropospheric’ aerosol during downslopes.

	Upslope ($\mu\text{g}/\text{m}^3$)	Downslope ($\mu\text{g}/\text{m}^3$)	Ratio AMS Up:Down	G-Chem Denver PBL ($\mu\text{g}/\text{m}^3$)	G-Chem RMNP FT ($\mu\text{g}/\text{m}^3$)	Ratio G-Chem BL:FT
SO₄	1.08 ± 0.74	0.89 ± 0.38	1.21	0.49 ± 0.32	0.33 ± 0.11	1.48
NH₄	0.23 ± 0.22	0.16 ± 0.09	1.44	0.20 ± 0.18	0.12 ± 0.05	1.66
NO₃	0.25 ± 0.32	0.12 ± 0.12	2.08	0.07 ± 0.21	0.01 ± 0.05	7.00
Organics	5.54 ± 3.04	4.05 ± 2.20	1.37	0.68 ± 0.31	0.32 ± 0.29	2.12
BBOA	0.48 ± 0.18	0.46 ± 0.10	1.04	-	-	
SV-OOA	2.03 ± 1.70	1.30 ± 1.03	1.56	-	-	
LV-OOA	2.49 ± 1.17	2.00 ± 0.92	1.25	-	-	

values for both upslope and downslope periods. The significant under-estimation of modeled organics, especially in the free troposphere, is similar to that in Heald et al. (2006); in that study, the underestimation of organics coupled with relatively good prediction of anthropogenic constituents that are transported to the FT (e.g. sulfate) implied an *in situ*, secondary (possibly aqueous) OA source (Heald et al. 2006; Heald et al. 2011). Here, local biomass burning, which is not included in the model, may also contribute to the discrepancy in particulate organics.

Modeled concentrations in the surface grid box at RMNP have very similar biases (not shown).

A timeline subset showing GEOS-Chem predictions and Rocky Mountain AMS data is shown in Figure 3-12. None of the grid boxes capture diurnal variations and timeline trends, which is unsurprising given the fact that RMNP particle concentrations are driven by biomass burning events and up/downslope transport not captured in the model (Wainwright et al. 2012). Upslope winds followed by enhanced AMS concentrations can be seen clearly most afternoons, while model organics are generally increased in the morning. Model predictions of nitrate and sulfate are quite low and less featured, while ammonium better resembles AMS measurements, especially during downslope winds. This suggests that the Denver surface grid boxes under-

predict ammonium, since AMS ammonium is increased beyond model predictions during upslope winds; however, there are a few periods (8/15-16, 8/24) where Denver boundary layer nitrate and ammonium increase with AMS-observations during upslope periods.

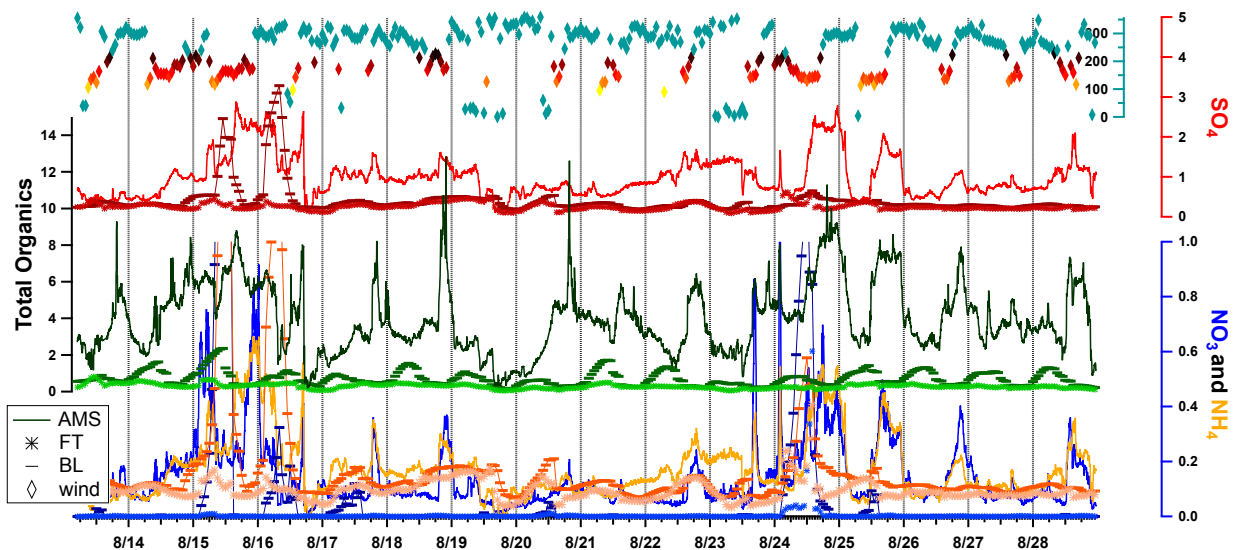


Figure 3-12: A timeline subset of particle components from Rocky Mountain AMS measurements (traces, 5-minute average), GEOS-Chem free troposphere predictions (stars, 1-hour), and GEOS-Chem boundary layer predictions (horizontal bars, 1-hour), color-identified by axis; warm colors indicate upslope wind direction (colored diamonds, teal axis), while teal indicates downslope flow. Vertical lines indicate midnight (00:00 LST).

3.7 Episode Analysis

The aerosol characteristics summarized previously are demonstrated in a series of high-concentration periods interrupted by concentration suppression during July 7-11, which clearly show the transport of OOA and inorganics by SE surface winds (Figure 3-13). Initiation of SE flow is followed by marked concentration increases after ~3 hours, suggesting a 3-hour transport time between the Front Range and RMNP during this subset. A similar lag applies between down-valley flow initiation and concentration decreases. The fact that the 1-3 hour offsets described above did not improve correlation between wind direction and species concentrations indicates that transport time is, not surprisingly, variable. The abrupt decreases in all components' concentrations following NW wind initiation reveals the relative cleanliness of the

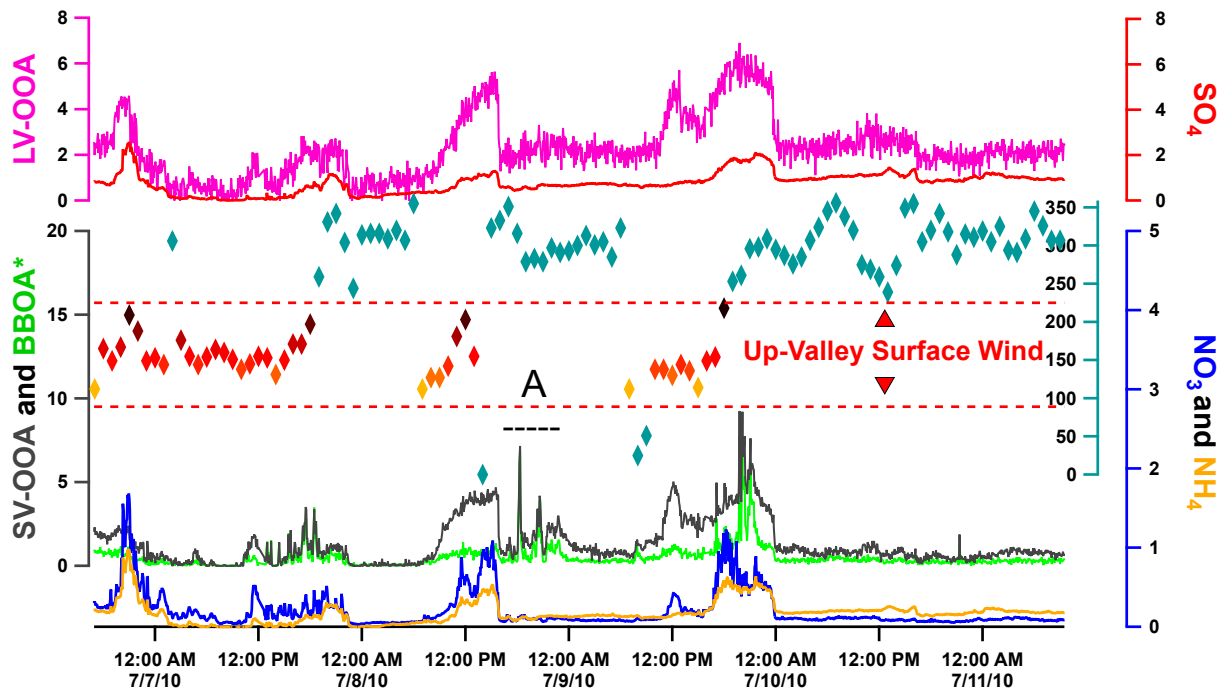


Figure 3-13: Timeline of species and relevant organic factor concentrations for 7-11 July 2010, plotted with 1-hour surface wind direction at the site (teal diamonds). Wind directions 90 through 180 degrees denote up-valley winds and are demarcated by dashed red lines and warm-colored diamonds. BBOA* is calculated using the six-factor reconstructions outlined in Section 3.2.

air coming over the mountains during these periods. Lastly, note the apparent discrepancy during period A, where ~NW winds are accompanied by sharp spikes in SV-OOA; this is thought to be an entanglement of BBOA mass with SV-OOA (Section 3.2) as evidenced by the short, high-amplitude concentration increase, enhancement of m/z 60 in the mass spectrum (not shown), and lack of attendant increase in anthropogenic inorganics; this is corroborated by an increase in BBOA in the recombinant-factor PMF analysis (Figure 3-13) and the NW placement of the campfire source (as winds are from the north).

3.8 Rocky Mountain National Park Summary and Conclusions

The ambient submicron aerosol at the Rocky Mountain National Park ROMO site during 2 July - 31 August 2010 is low in concentration (total average $PM_{10} = 5.13 \pm 2.72 \mu\text{g}/\text{m}^3$), dominated by highly oxidized organics (LV-OOA and SV-OOA), and punctuated by short

biomass burning (BBOA) episodes. Mixtures of LV-OOA with ammonium sulfate and SV-OOA with ammonium nitrate are indicated by consistent size distributions and time-series correlation. Inorganic species (nitrate, sulfate, and ammonium) are established anthropogenic emission tracers for which sparse population precludes a strong local source. High inorganic concentrations are concurrent with southeasterly surface (and, weakly, Denver 700mb) winds that indicate upslope flow from the Front Range. A biogenic contribution, possibly from oxidation of anthropogenic species (such as NO_x and SO_x) with BVOCs as Front Range plumes are transported over forest, is suggested by the fact that contemporary carbon contributed by local biomass burning may not account for total contemporary carbon at the site (Schichtel et al. 2008). Organic nitrogen is associated with BBOA and may indicate amine, nitrile, and/or heterocyclic aromatic content, but is low in mass; BBOA is not correlated with any measured inorganic species.

Transport of oxidized organic aerosols from the Front Range is indicated by advanced oxidation and relative monodispersity (both indicative of ageing), association with inorganic anthropogenic tracers, and concentration correlation with surface upslope flow from the Front Range; the presence of sulfate, periodic high relative humidity and cloud cover, and advanced oxidation of the LV-OOA may suggest aqueous processing for a portion of the particle population, while growth by vapor condensation may be more likely for SV-OOA/ammonium nitrate particles. Boundary layer compression and/or partitioning due to decreased temperature may cause evening increases in OOA. A local BBOA source is suggested by cellulose combustion markers (m/z s 60 and 73) limited to brief, high-concentration, polydisperse events (suggesting fresh combustion emission), association with local S or NW winds consistent with

campfire locations, no association with regional winds, and an unequivocal diurnal maximum at 22:00 LST, when campfires were set at adjacent summer camps.

The particle characteristics and sources determined here represent typical conditions at the Rocky Mountain site, based on analysis spanning the previous decade of inter-annual variability in meteorological patterns, IMPROVE (total $PM_{2.5}$, sulfate, nitrate, ammonium, and OC), PILS-IC ($PM_{2.5}$ sulfate, nitrate, and ammonium), filter ($PM_{2.5}$ sulfate, nitrate, and ammonium), and fire (burned area, contribution to surface $PM_{2.5}$) data.

4. Organic Aerosol Sources and Characteristics: Grand Teton National Park

4.1 Sampling Site

The Grand Teton sampling site was located at 2,722 m (8,930 ft) under the summit of Peaked Mountain, just outside the western boundary of Grand Teton National Park (lat.: 43.7928° N, lon.: 110.9592° W, Figure 4-1). The site lies on a west-facing slope looking over the Snake River Valley, which is dominated by agricultural operations; the closest sizeable population is Driggs, ID (population = 1,660 in 2011), approximately 16 km (10 mi) away at the foot of the mountain; Idaho Falls (metropolitan population = 136,108 in 2011) is ~93 km (58 mi) distant. The instruments were housed in a camouflaged (per U.S. Forest Service regulations) mobile laboratory parked at the Sacajawea Ski Lift, with access provided by the Grand Targhee Ski Resort. The laboratory contained a suite of instrumentation including the AMS (for which measurements span 25 July – 31 August, 2011), particle sizing rack with an aerodynamic particle sizer (APS, TSI 3021), optical particle counter (OPC, LASAIR 1003), and differential mobility particle sizer (DMPS, TSI 3085), a gaseous-instrument rack with CO (& Teledyne-API Inc., Model 300EU), NO, NO_x, NO_y (Teledyne-API Inc., Models 200EU and Model 201E) and two ammonia (NH₃) measurements (Particle Measuring Systems Air Sentry II Ion Mobility Spectrometer & Picarro G1103 Analyzer), and a meteorological station measuring wind direction and speed, temperature, and relative humidity. Hi-Vol samplers collected PM_{>2.5} and PM_{2.5} on filters for Sunset Labs OC:EC, ion and HPAEC-PAD chromatography analysis, yielding elemental, inorganic, and carbohydrate information organics with 24-hour time resolution. 24- and 12-hour URG denuders collected ammonia and nitric acid, with filter packs and backup denuders for particulate and volatilized particulate, respectively. This site was one of eleven in

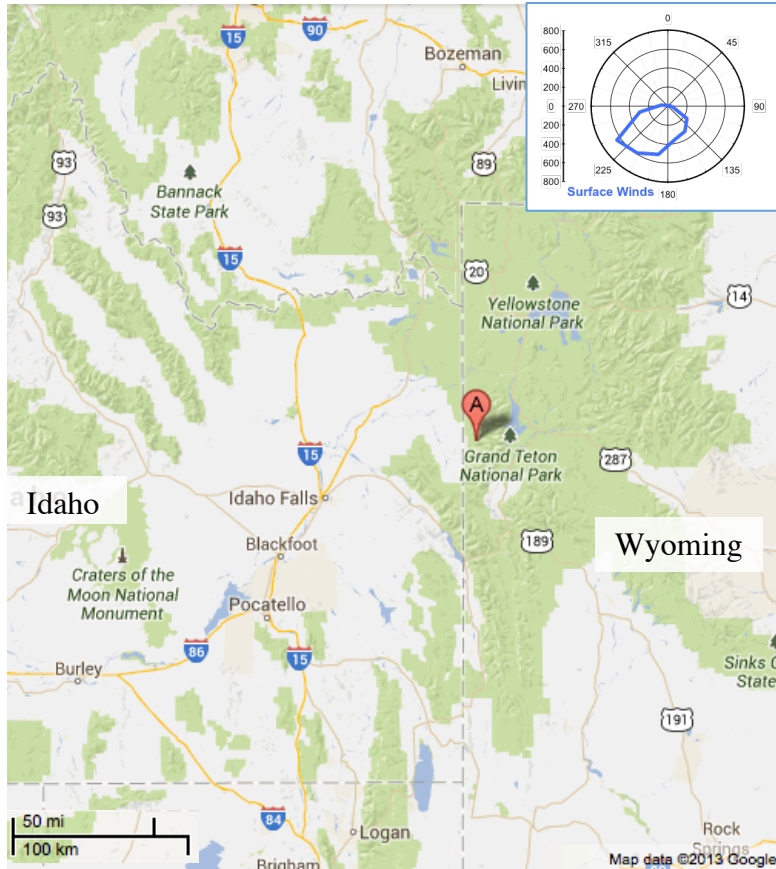


Figure 4-1: Map showing GrandTREnds study site (point A).

the wider Grand Teton Reactive Nitrogen Deposition Study (GrandTREnds) aimed at quantifying reactive nitrogen sources and deposition in Grand Teton National Park.

Meteorological and gas-phase data illustrate prevalent conditions and transport at the site (Figure 4-2, Prenni et al. in press). Hourly diurnal averages of wind direction reveal steady SSE winds ($\sim 175^\circ$) overnight (22:00-09:00 LST) that shift abruptly to the WSW ($\sim 250^\circ$) direction in the afternoon (11:00-20:00 LST); this is characteristic of the thermally driven mountain-valley circulations common in such terrain, and echoes the afternoon up-slopes in Rocky Mountain National Park. NO_x and NO_y are produced primarily by human activities; their enhancement at the onset of the daytime upslope wind suggests the import of anthropogenically-influenced air masses (through thermal upslope flow and/or boundary layer expansion) and is mirrored in

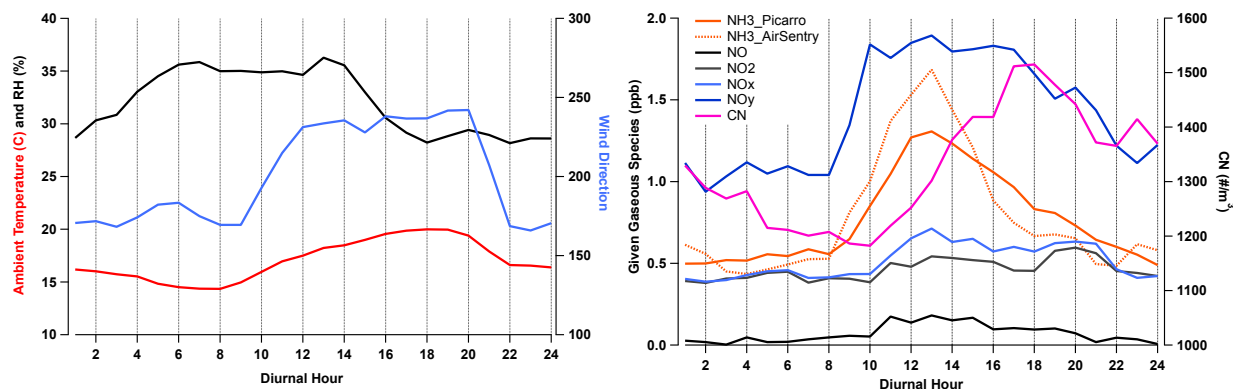


Figure 4-2: Diurnal averages over AMS sampling duration of a) meteorological values ambient temperature (C), relative humidity (%), and wind direction (degrees), and b) gaseous NH₃, NO, NO_x, and NO_y concentrations (ppb) and particle number concentration (CN; #/m³). Data from Tony Prenni (Prenni et al. in review).

gaseous ammonia, which features noon-time enhancement in both Picarro and Air Sentry instrument measurements, though the ammonia maximum may be enhanced by thermally-driven partitioning to the gas phase during the heat of the day.

Maximum particle number concentration occurs at ~17:00 LST, lagging well behind the beginning of the upslope winds. This particle number increase could arise from import of aerosols formed or emitted in the valley during the day or from in-situ formation, as may be indicated below in the AMS size and composition data; whatever mechanisms are at play, the 10:00 LST particle number minimum may arise from thermal boundary layer expansion before afternoon particle transport or in-situ formation. Lastly, HYSPLIT back-trajectories reveal dominant air transport routes through the Snake River Valley and from the south (including Northern Utah) during the campaign (Benedict et al. in press). Historical meteorology is not available.

4.2 General Particle Composition and Concentration

Atmospheric particulate is low in mass concentration and consists primarily of organics, with two periods of enhanced ($>[\text{avg} + \text{std.dev.}]$) concentration coinciding with regional

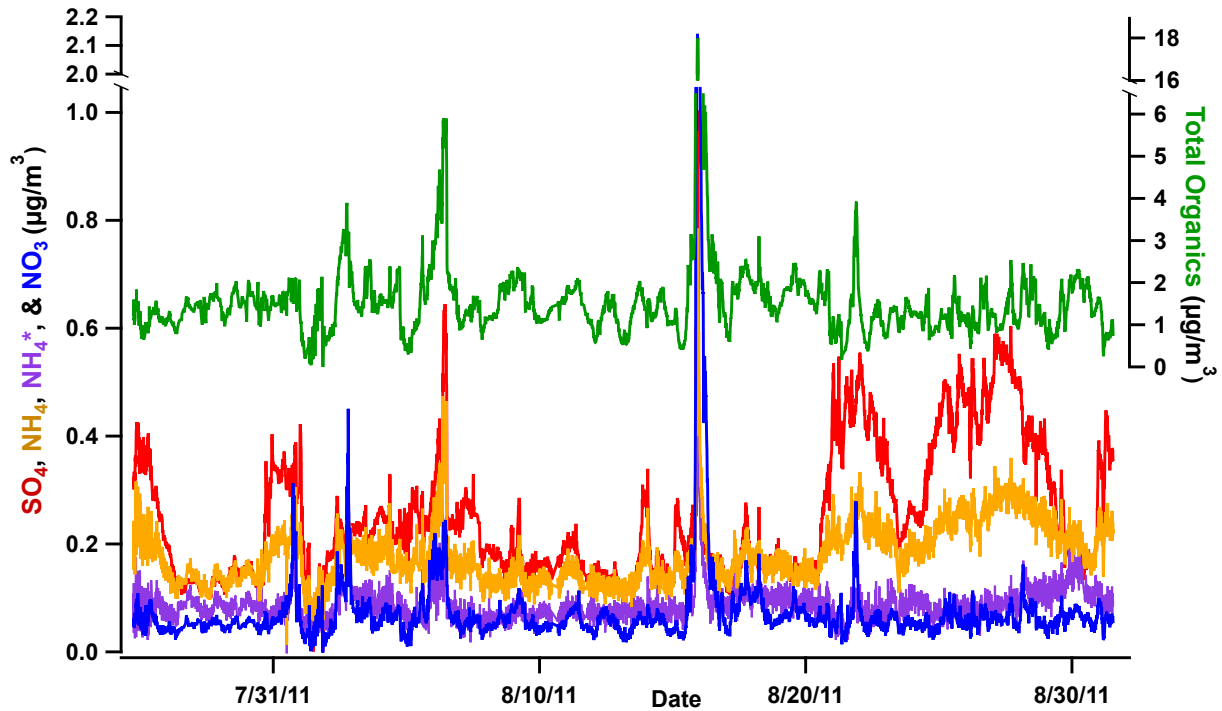


Figure 4-3: Timeline of total organics (green, right axis), sulfate (red), ammonium (yellow), nitrate (dark blue), and ‘excess’ ammonium (NH_4^* , purple) from the HR-ToF-AMS during the GrandTREND study. Concentrations are in $\mu\text{g}/\text{m}^3$.

wildfires (total organics: max. = $17.98 \mu\text{g}/\text{m}^3$; avg. = $1.56 \pm 1.19 \mu\text{g}/\text{m}^3$ or 75.0 % of average AMS mass). Inorganic species are lower in concentration; sulfate (max. = $1.00 \mu\text{g}/\text{m}^3$; avg. = $0.26 \pm 0.12 \mu\text{g}/\text{m}^3$) and ammonium (max. = $0.78 \mu\text{g}/\text{m}^3$; avg. = $0.18 \pm 0.06 \mu\text{g}/\text{m}^3$) are greater in general than nitrate (max. = $2.14 \mu\text{g}/\text{m}^3$; avg. = $0.078 \pm 0.12 \mu\text{g}/\text{m}^3$). High nitrate concentrations are accompanied by increased organic mass (Figure 4-3). The closest site with which to compare these data is the Yellowstone National Park IMPROVE station, for which July-August average concentrations over 1996-2012 are: organic mass = $3.90 \pm 6.11 \mu\text{g}/\text{m}^3$; nitrate = $0.10 \pm 0.10 \mu\text{g}/\text{m}^3$; sulfate = $0.46 \pm 0.21 \mu\text{g}/\text{m}^3$; ammonium = $0.03 \pm 0.03 \mu\text{g}/\text{m}^3$; and $\text{PM}_{2.5}$ = $5.04 \pm 3.78 \mu\text{g}/\text{m}^3$, generally like those observed here. Yellowstone organics are generally $<10 \mu\text{g}/\text{m}^3$ with periodic high-concentrations events (~ 1 -2 events/month; organic data span 1996-2012);

however, the Yellowstone site is ~40 miles from the site presented here and across the Teton range, with different topography and presumably meteorology, and thus not directly comparable.

Time-series correlation suggests an internal mixture of ammonium and sulfate ($r^2 = 0.72$), for which the overall slope (NH_4 vs. SO_4) = 0.41; the stoichiometric slope for pure ammonium sulfate by mass is 0.38, suggesting that ammonium sulfate may be an important form of both species. However, there are also periods during which the concentration of ammonium equals or exceeds that of sulfate; in these periods, ammonium fragments may arise from ammonium nitrate, amines, carboxylate-ammonium salts such as ammonium oxalate (Malm et al. 2005; Wang et al. 2010), and/or other organic nitrogen compounds as discussed in Sections 4.4 and 4.6. To explore the form of this ‘excess’ ammonium (NH_4^*), mass of ammonium exceeding that in stoichiometric balance with sulfate ($\text{NH}_{4(\text{S})}$) was calculated via:

$$\text{NH}_{4(\text{S})} = \text{SO}_{4(\text{tot})} \times \frac{\mu\text{mol}}{96.07 \mu\text{g SO}_4} \times \frac{18.0385 \mu\text{g NH}_4}{\mu\text{mol}} \times \frac{2 \mu\text{mol NH}_4}{1 \mu\text{mol SO}_4} \quad (\text{Equation 13})$$

$$\text{NH}_4^* = \text{NH}_{4,\text{total}} - \text{NH}_{4(\text{S})} \quad (\text{Equation 14})$$

NH_4^* may have a weak correlation with nitrate and often has a similar time series (Table 4-1); at other times, NH_4^* may exceed nitrate, indicating possible amine contributions, or nitrate may exceed NH_4^* , suggesting enhanced organonitrates or soil-influenced species such as calcium

Table 4-1: Correlations (r^2) between temporal concentration variations of given particle constituent pairs; NH_4^* refers to mass of ammonium exceeding that in stoichiometric balance with sulfate. ON_{min} is defined in Section 4.5.

	LV-OOA	BBOA	SO₄	NO₃
SO₄	0.02	0.02		
NO₃	0.00	0.89	0.04	
NH₄	0.00	0.22	0.70	0.27
NH₄[*]	0.00	0.38	0.02	0.46
ON_{min}	0.22	0.09		

nitrate (Lee et al. 2004; Lee et al. 2008). Figure 4-4 shows the relationship between NH_4^* and NO_3 colored by concentration of organics. Points above the line of ammonium nitrate stoichiometry indicate an excess of ammonium for which possible forms include amine and/or organic ammonium salts as mentioned above. Data below the line are indicative of excess nitrate and occur only when $[\text{Org}] > \sim 8 \mu\text{g}/\text{m}^3$, during the August 15 elevated-concentration event identified as biomass burning by PMF (see Section 4.3); the association between biomass burning and organonitrates is discussed further in Section 4.5. The predominance of data points with ‘excess ammonium’ suggests that amines may be more important than organonitrates, which is echoed in analysis of nominally organic nitrogen fragments in Section 4.5. Nitrate and total organics are time-series correlated ($r^2 = 0.89$); lack of correlation between other species combinations may indicate external mixture (or at least unrelated sources and transport) between ammonium-sulfate and organic/ammonium*-nitrate particle types (Table 4-1).

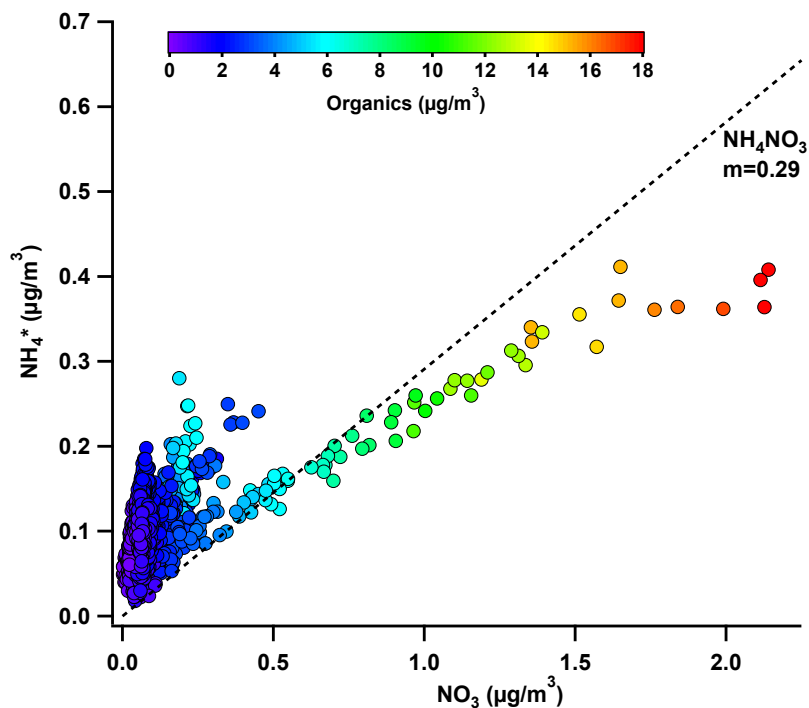


Figure 4-4: Ammonium in excess of stoichiometric balance with sulfate (NH_4^*) versus nitrate. The dashed line indicates the stoichiometric mass ratio of pure ammonium nitrate.

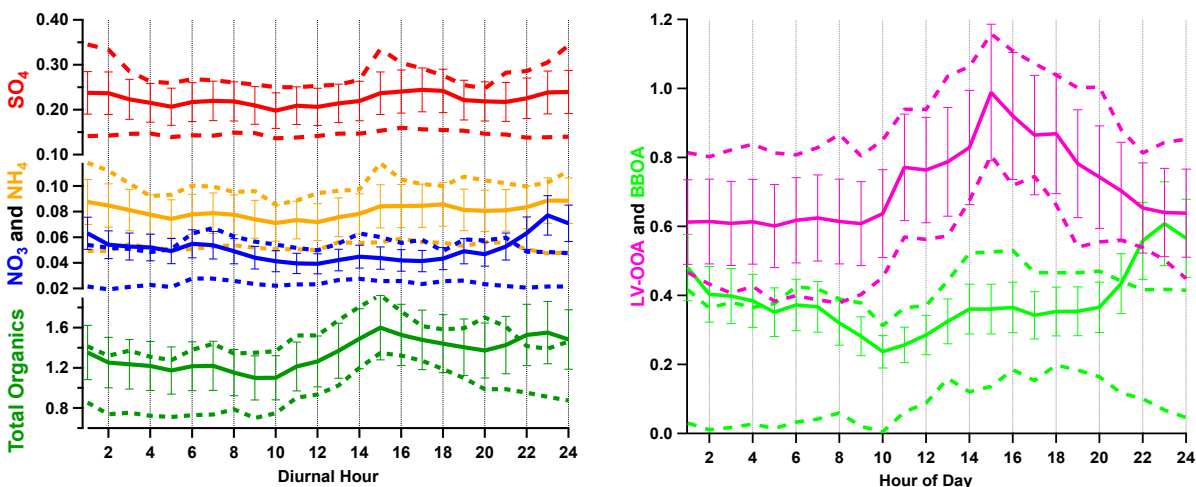


Figure 4-5: Diurnally averaged concentrations of inorganic species, total organics, and organic PMF factors (introduced below), where the solid line is the concentration mean and the dashed lines are 25th and 75th percentiles. Error bars represent 20% mass quantification error in the AMS. Concentrations are in $\mu\text{g}/\text{m}^3$.

Ammonium and sulfate have weak average diurnal maxima in the afternoon and overnight (Figure 4-5); the 75th percentile concentrations follow similar patterns for both species, indicating that higher concentrations occur consistently in the afternoon and nighttime (i.e. means are not influenced by outliers). Nighttime concentration increases may result from boundary layer compression or partitioning driven toward the particle phase by lower temperatures. Nitrogen has an inconsistent maximum at 23:00 LST; a mean increase without commensurate 25th and 75th percentile increases indicates that the mean is driven by high-concentration events (in this case, the August 15 BBOA episode, explored below). Total organics increase consistently and significantly in the afternoon (mode at 15:00 LST), with another event-driven mean maximum at ~23:00 LST; these patterns are examined in depth below.

4.3 PMF-Derived Organic Aerosol Factors

Positive Matrix Factorization was applied to high-resolution organic mass spectra from the entire 25 July-31 August data set; despite low mass, signal-to-noise was sufficient throughout the campaign to apply the same down-weighting thresholds ($S:N < 2 = \text{'weak,}'$ $S:N < 0.2 = \text{'bad}'$)

used in previous analyses and recommended by Paatero & Hopke (2003). A two-factor solution was indicated by good reconstruction of mass (within $\pm 5\%$ of total organics) and the failure of additional factors to produce meaningful mass spectra or disparate time series (Figure 4-6). As noted in Chapter 2, relatively minor changes in PMF statistics with changing factor number rendered statistics less useful than qualitative comparisons for factor number determination for this dataset. Appendix Section 8.2 includes a 3-factor solution for reference (Figure 8-5, Figure 8-6, Figure 8-7).

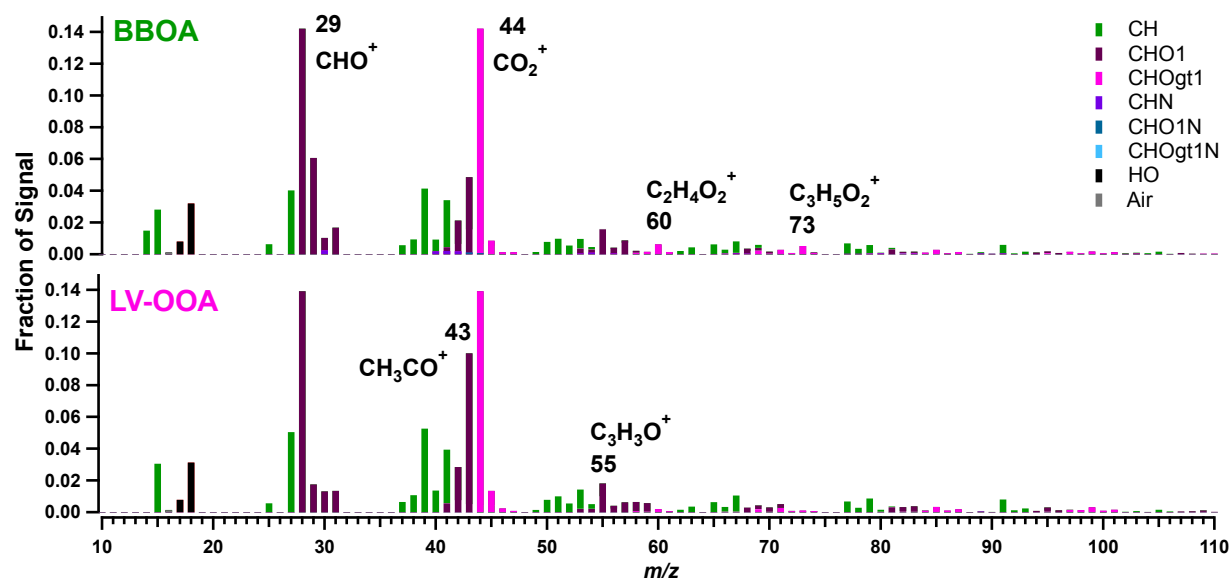


Figure 4-6: Mass spectra of LV-OOA and BBOA factors derived from application of PMF to high-resolution Grand Teton National Park AMS data.

The two-factor solution consists of one oxidized organic factor (Low Volatility Oxidized Organic Aerosol, or LV-OOA) and one biomass-burning factor (BBOA) with meaningful dissimilarities in factor mass spectra (Figure 4-6), time-series (Figure 4-7), and diurnal profiles (Figure 4-5). Like the OA observed in Rocky Mountain National Park (Section 3.2), LV-OOA is identified by the predominance of mass at m/z 44 over that at m/z 43; however, the LV-OOA spectrum at Grand Teton has greater relative signal at m/z 43 in comparison to that at Rocky Mountain, indicating a less oxidized low-volatility aerosol. Prominent levoglucosan fragments

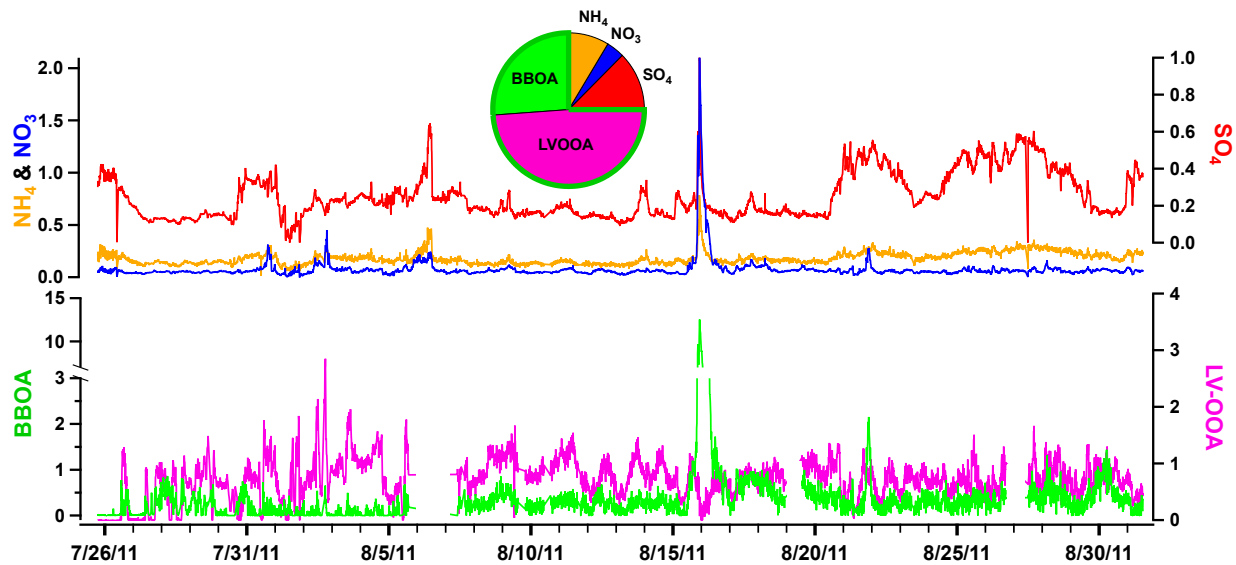


Figure 4-7: Timelines of LV-OOA (pink) and BBOA (green) PMF organic factors and inorganics at the Grand Teton site, in $\mu\text{g}/\text{m}^3$. The pie chart depicts study average mass contributions from each component, with total organics outlined in green.

($\text{C}_2\text{H}_4\text{O}_2^+$ at m/z 60 and $\text{C}_3\text{H}_5\text{O}_2^+$ at m/z 73) differentiate a second, BBOA factor, for which enhanced oxidation relative to Rocky Mountain BBOA is indicated by abundant signal at m/z 44.

LV-OOA dominates submicron particulate mass, contributing 49% of average particle mass (max. = $3.37 \mu\text{g}/\text{m}^3$; avg. = $1.02 \mu\text{g}/\text{m}^3$, Figure 4-7),¹ with a consistent, significant diurnal maximum in the midafternoon ($\sim 15:00$ LST, Figure 4-5) but few other episodic features. This afternoon increase could be driven by photochemistry, which can produce condensable SVOCs from gaseous precursors within minutes to hours after sunrise (Section 1.2.1), by transport by the consistent upslope flow beginning at $\sim 9:00$ LST, and/or by boundary layer fluctuations, in which the BL expands to encompass the sampling site, bringing with it generally higher particle concentrations (Section 3.6). The diurnal pattern of LV-OOA resembles that of NO_x , which might suggest anthropogenic air-mass impact, but LV is not correlated to NO_x ($r^2 = 0.001$) or any inorganic species (Table 4-1); while this does not rule out transport of OOA, it may suggest a

¹ Reconstructed mass from PMF is approximate. For average percentage contribution to total organic mass, mass

local (or regionally disperse) source, which could arise from photochemical oxidation of biogenic VOCs in this forested area (discussed further in Section 4.6). Organic composition is fairly static, with little variation in the organic mass spectrum (as represented by fragment ratios f_{43} and f_{44} described later in this section) apart from biomass burning and two other events, described below.

BBOA is dominant during wildfire smoke events on August 15 and 21 and comprises roughly a third of total organic mass on average (max. = $17.88 \mu\text{g}/\text{m}^3$; avg. = $0.54 \mu\text{g}/\text{m}^3$); historically, 2011 was a relatively low fire year in Idaho, with ~ 20 Gg carbonaceous aerosol emitted ($\text{PM}_{2.5}$) against the 2002-2012 average of 30 ± 40 Gg (**Figure 8-3**; data courtesy Maria Val Martin, 2013). From MODIS data, the only fire activity around August 15 within the HYSPLIT back-trajectory source regions (ID, WY, MT, UT, or CO) was a cluster of large fires SE of Boise, including the South Pen, Union, Squaw, Blair, Big Hill, and Morrow fires spanning August 14-16 with 77,000 burnt acres combined (Forest Service Remote Sensing Application Center database, Figure 4-8); these were approximately 480 km (~ 300 mi) from the site at the other end of the Snake River Valley, which may conduct surface flow toward the site as is observed in Rocky Mountain National Park.

The August 15 episode drives a BBOA diurnal mean maximum at $\sim 23:00$ LST that is not reflected in the 25th or 75th percentiles, indicating that BBOA follows no consistent diurnal pattern; BBOA at this site is episodic, consistent with sporadic regional fires and low regional BBOA background (Figure 4-7). An internal mixture of BBOA and (nominally inorganic) nitrate fragments is indicated by correlated time-series ($r^2 = 0.89$ with NO_3), diurnal pattern, size (Section 4.6), and wind association (Section 4.7); BBOA may also be sporadically accompanied by ammonium*-nitrate (Table 4-1), but is not correlated with ammonium-sulfate. Due to PILS-

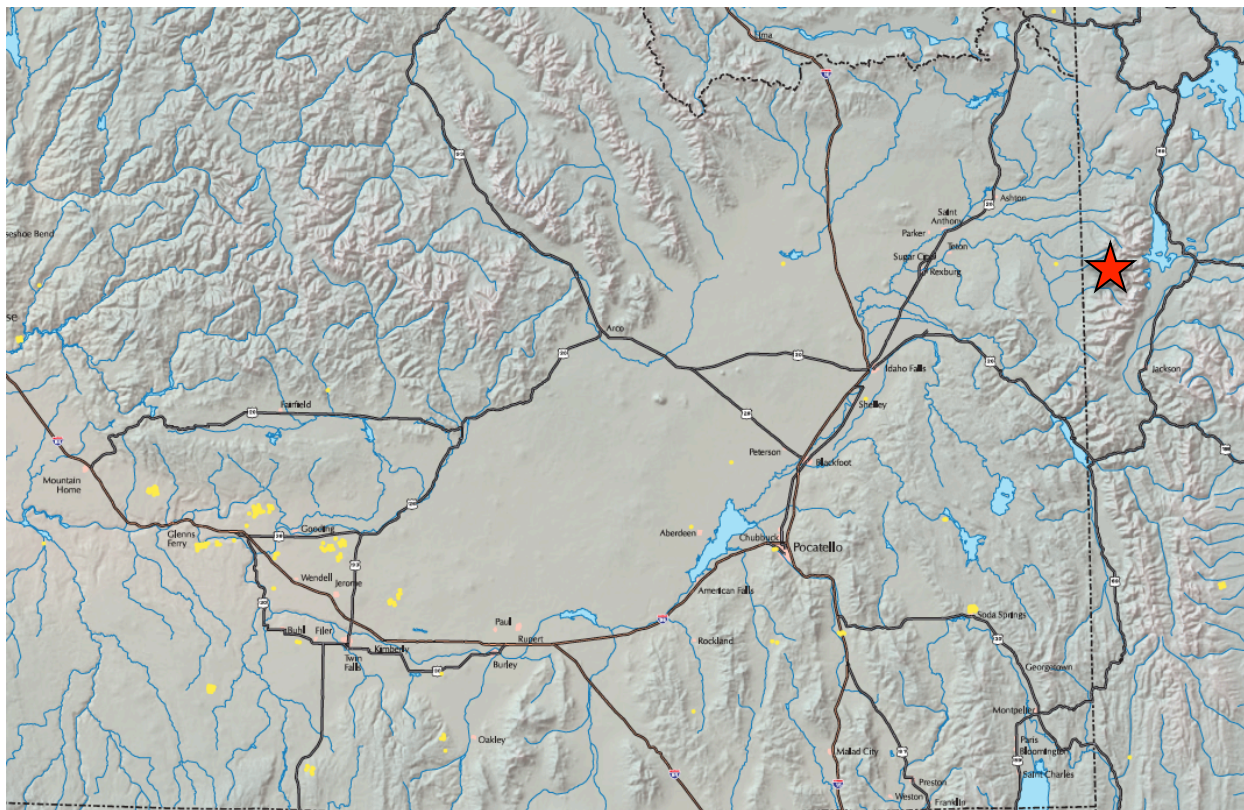


Figure 4-8: Map of MODIS fire detections (yellow dots) on August 14, 2011 at 13:00 LST (height of fire intensity) from the United States Forest Service (USFS 2013); the red star is the AMS measurement site.

IC malfunction, no potassium data are available for correlation with BBOA; in any case, potassium emission is dependent on the fire flaming phase and therefore is not always correlated with other, more reliable BBOA markers such as m/z 60 (Echalar et al. 1995; Silva et al. 1999; Weimer et al. 2008; Lee et al. 2010; Cubison et al. 2011).

In the f_{43} - f_{44} triangle diagram (**Figure 4-9**; Ng et al. 2011), the majority of the data fall in the SV-OOA (grey ellipse)/LV-OOA (pink ellipse) overlap region, indicating a somewhat static level of oxidation over the study period. The August 15 biomass burning event is shown colored by time and reveals a decrease in oxidation as the event progresses, which may have a variety of causes. First, transport times may have decreased toward the event end, though wind speed at the site did not change significantly (see Figure 4-16). Second, the event spanned an

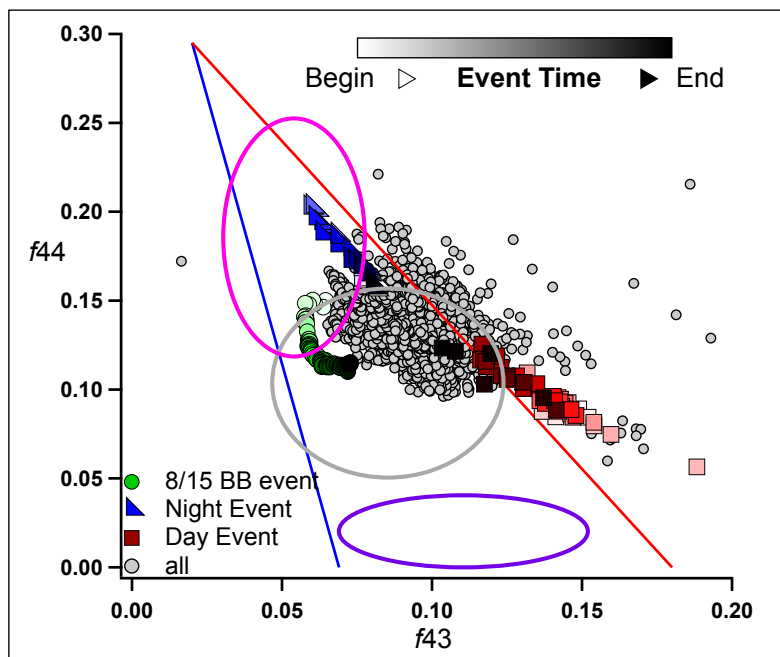


Figure 4-9: f_{43} versus f_{44} diagram featuring the August 15, 2011 biomass burning event and interesting periods during the day (1 August, 2011) and night (28 July, 2011). Ellipses indicate the approximate ranges of HOA (purple), SV-OOA (grey), and LV-OOA (pink) data in the literature (Ng et al. 2011).

overnight period, starting at ~19:15 LST August 15 (with sunset at 20:49 LST) and ending at ~09:40 August 16 (with sunrise at 06:50 LST), so reduction in photochemical oxidation as the sun set could explain the decrease in oxygenation over time; if true, this also suggests that photochemical oxidation is dominant at the site (for example, over nitrate radical), at least for this event. Lastly, an influx of high-concentration particulate matter could provide substrate for condensation of continuously oxidizing plume VOCs; since SVOCs are often less oxidized than the carboxylic acid species found in the particulate phase (especially as particles are oxidized during transport), SVOC condensation could increase hydrocarbons and/or carbonyls relative to acid species, reducing the f_{44} value as discussed in Section 1.3.3 and producing the movement observed in Figure 4-9 (Pankow 1987; Pankow 1994; Shrivastava et al. 2006). However, the multiplicity of factors that could contribute to this reduction in oxidation renders mechanistic evaluation difficult.

Two periods - one during the daytime and one at night - stand out in Figure 4-9 for their interesting progressions in level of oxidation. On August 1, the particulate organics become more oxidized (lower f_{43} , higher f_{44}) over the course of the afternoon (12:00-21:00 LST). No meteorological data is available during this event,* making it difficult to conjecture whether transport of new aerosol (which might be accompanied by a change in wind direction and/or speed), in-situ oxidation, or some combination thereof is at play. In the nighttime example, the particles become more and then progressively less oxidized between ~21:00 LST on July 28 and 07:00 LST July 29. The early increase in oxygenation seems precipitated by an abrupt shift in wind direction from due west to south-southeast at 21:40 LST. Then, the wind shifts again to the southwest at 02:20 LST, after which the particles start to become less oxygenated. This association with wind direction seems to imply transport of differing air masses.

* The meteorological station was not logged (or was incorrectly downloaded), and data from meteorological stations located at the ski lifts and a nearby airport are not logged. The possibility of locally complex, terrain-influenced flow discourages use of meteorological data from further afield.

4.4 Elemental Analysis

The ratio of organic matter to organic carbon (OM:OC) may be used as a metric of aerosol oxidation and averages 1.81 ± 0.15 in total and 1.78 ± 0.07 during biomass burning periods. Aiken et al. (2008) found a similar value (~1.8) for their PMF-derived SV-OOA factor from a site near Mexico City, but higher values (~1.9-2.1) as the plume traveled to more remote regions; OM:OC for urban aerosols typically measure ~1.3-1.6, while values of 2-2.5 have been observed at rural sites with anthropogenic influence (Turpin & Lim 2001; Aiken et al. 2008). Given the distance from major population centers, our relatively low OM:OC implies that Tetons OOA may not arise solely from transported anthropogenic particles, which we would expect to be more aged; it is also possible that oxidation per unit time during transport is reduced in

comparison to those studies, as by rapid transport or lower oxidant concentrations, etc. For the biomass burning event, OM:OC=1.78 ± 0.07; other studies, many of which were urban and/or in closer proximity to the burn have measured OM:OC=1.6-1.7 for biomass burning events (Turpin & Lim 2001; Fuzzi et al. 2007; Aiken et al. 2008; Chen et al. 2009), consistent with the values found here.

O:C averages 0.50 ± 0.11 in total, consistent with published SV-OOA factors (Section 1.3.3), and suggesting that though the mass spectrum identifies the bulk of the local aerosol as ‘low volatility’ OOA, it is in fact less oxygenated than many observed LV-OOA factors. O:C during the biomass burning events is not significantly different than the total average (avg_{BB} = 0.49 ± 0.05), but is higher than other published BBOA events (~0.26-0.4, which may have spent less time in transport than in this case), possibly reflecting the ubiquity of OOA at the site or oxidation during transport (Aiken et al. 2008; Huang et al. 2011).

H:C averages 1.32 ± 0.15, which is on the cusp between literature SV-OOA and LV-OOA values (Table 1-2) and lower than that measured in urban primary or hydrocarbon-like OA (for which H:C = ~1.4-1.9, Aiken et al. 2008; Huang et al. 2011). N:C averages 0.031 ± 0.081 (max = 0.63, avg_{BB} = 0.012 ± 0.004) indicating low nominally organic nitrogen content (CHON and CHN fragments) at the site overall, as is discussed in Section 4.5; this is on the higher end of the range supported in the literature, which contains no value over N:C=0.09 for a field campaign to our knowledge (though N:C reporting is relatively uncommon, Aiken et al. 2008; Huang et al. 2011). However, the maximum value herein (0.63) is a clear indicator that there are periods when nominally organic nitrogen fragments are very abundant, justifying a more complex analysis of organic nitrogen in the next section.

In van Krevelen space (Figure 4-10), the positioning of the data in the middle of the triangle indicates a moderately oxidized aerosol. Elemental ratios for daytime and nighttime particles are largely similar, though isolated points during day and night are less and more oxidized, respectively. Elemental ratio diurnal averages are also remarkably un-featured (left panel, Figure 4-11).

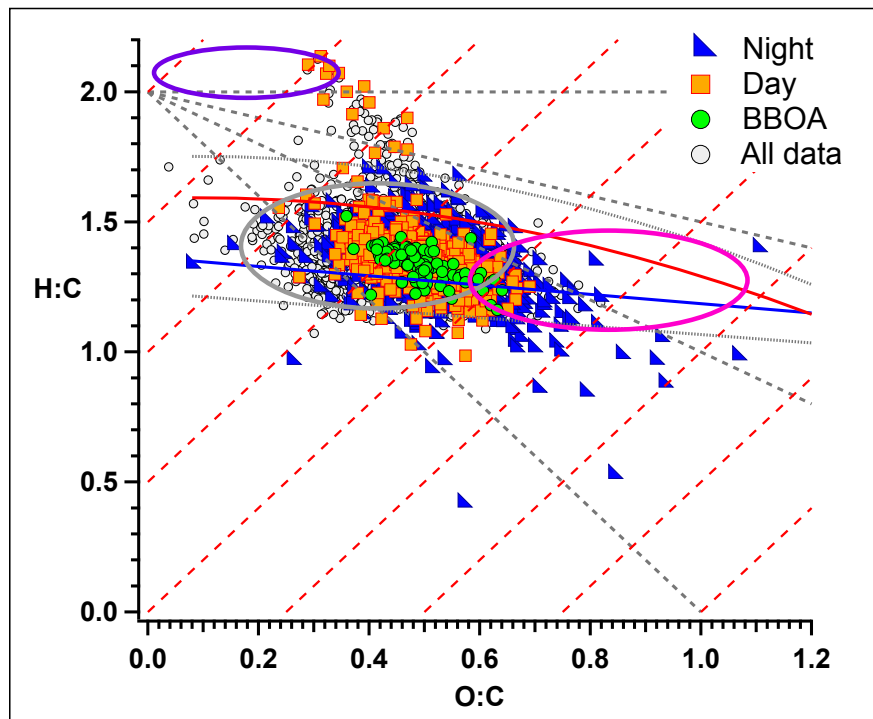


Figure 4-10: van Krevelen diagram showing GrandTREnds data. ‘Day’ and ‘Night’ are all data from 12:00-18:00 LST and 21:00-5:00 LST, respectively. Red and blue lines indicate the region usually inhabited by ambient data in the f_{43} vs f_{44} plot; grey lines represent 10% error. Purple ellipse: typical range of HOA; grey ellipse = SV-OOA; pink ellipse = LV-OOA. Dashed red lines: estimated oxidation state, $OSc=2*O:C-H:C$ (Kroll et al. 2011); see Section 1.3.3. Dashed grey lines: slopes of various reaction regimes; see Section 1.3.3.

This static composition is more consistent with a ubiquitous (‘regional background’) in situ source than it would be with transported plumes, since the daytime upslope winds are quite consistent and commensurate changes in composition would be expected. However, it is also possible that averaging a range of event types, including the high-amplitude biomass burning and other transport events, with the ‘regional background’ dampens features. For instance, a subset from 27-30 July does show some interesting diurnal variation in elemental ratios (though none of

the fluctuations are statistically significant; right panel, Figure 4-11); H:C increases at ~10:00 and 12:00 LST with commensurate decreases in O:C, which could arise from transport of less-oxidized particles and/or condensation of less-oxidized SVOCs. This is followed by small increases in O:C and OM:OC and a significant increase in N:C (CHON and CHN fragments), which could arise from either *in situ* oxidation or transport. However, overall, PMF resolves only the LV-OOA and BBOA factors, implying that if multiple mechanisms produce OOA, additional factors account for less than 5% of OA mass and/or produce chemically indistinguishable particles, given the data types produced by the AMS.

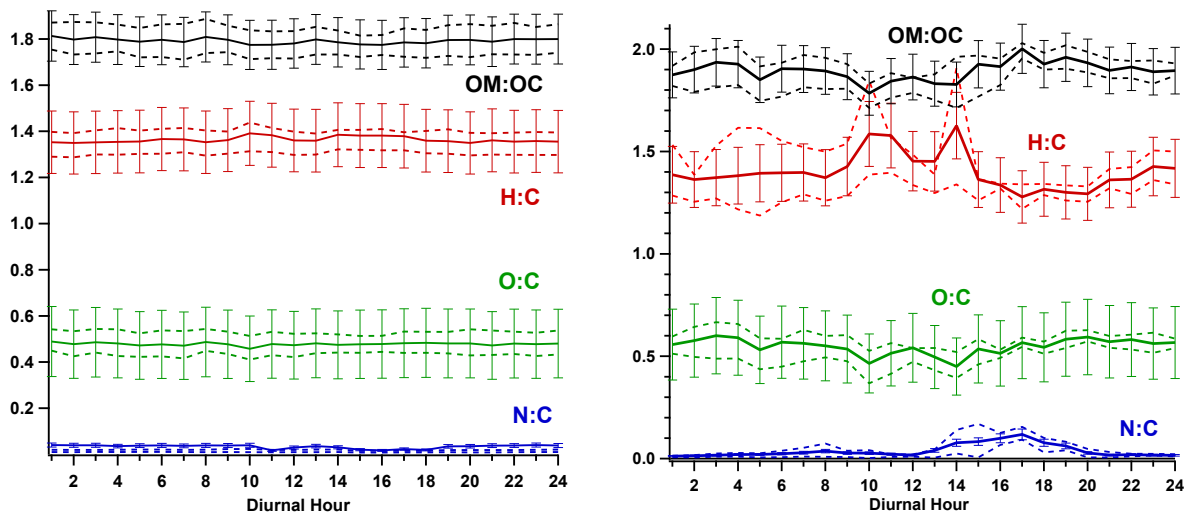


Figure 4-11: Elemental ratio diurnal averages for (left) the total dataset and (right) a subset from 7:00 LST July 27 - 7:00 LST July 30. Bars depict error on elemental analysis: O:C (31%), H:C (10%), N:C (22%) and OM:OC (6%, Aiken et al. 2007).

In the van Krevelen diagram, BBOA events have elemental ratios similar to day, night, and total particles, though higher than literature BBOA as discussed above. As noted in Section 1.3.3, fitting slopes to ambient van Krevelen data in order to describe reaction regimes is discouraged because of possible confusion by the transport of new air masses.

4.5 Organic Nitrogen

There is evidence of organic nitrogen content in Grand Teton aerosol in the form of organonitrates and, more significantly, amine species. As seen in Figure 4-12, nominally organonitrate fragments ($C_xH_yO_zN^+$ family, ‘CHON’ hereafter) form clear ‘wave’-like mass spectral patterns, which arise from successive fragmentation of methylene bridges ($-CH_2-$) and indicate that these fragments are not errors in the high-resolution signal fitting (see Section 1.3.4). However, the signal intensity of these fragments is about 100 times lower than that for other organics ($C_xH_y^+$ and $C_xH_yO_z^+$ families). Adding CHON fragment mass yields an average $ON_{\min,CHON}$ of $0.02 \pm 0.03 \mu\text{g}/\text{m}^3$ (maximum = $0.22 \mu\text{g}/\text{m}^3$ or 1.2% of total OM during BBOA period), which is at the detection limit for the W mode; high resolution V mode data, which have a lower detection limit, are not used because the resolution is not great enough to quantify these low-abundance fragments, which often overlap somewhat with larger neighboring peaks even in the W mode (half-width/half-max is maintained during fitting). However, the association between nitrate and biomass burning events (which are often associated with nitrophenols, nitriles, amines, etc., Fry et al. 2009; Rollins et al. 2009; Ng et al. 2008; Bruns et al. 2010; Mace et al. 2003), the presence of nitrate in excess of that stoichiometrically balanced with NH_4^+ (NO_3^-), and the lack of correlation with anthropogenic tracers ammonium-sulfate, suggests that some of the nominally inorganic nitrate signal arises from organonitrates.

CHON fragment signal intensities are consistent between the study average and BBOA-event mass spectra apart from enhanced $CHNO^+$ (at m/z 43) and CH_2NO^+ (at m/z 44) mass in the study average, which could be a product of the curve fitting algorithm (Figure 4-12); during the high-concentration BBOA event, high signal from CH_3CO^+ and CO_2^+ overwhelms these relatively small CHON peaks, making them difficult to quantify. Regardless, the consistency of the CHON

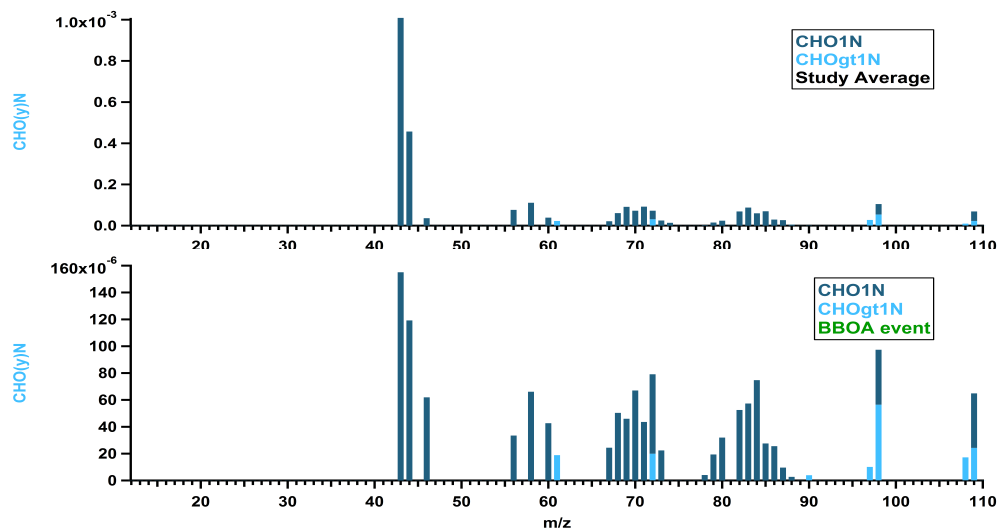


Figure 4-12: Mass spectra of $C_xH_yO_zN^+$ fragments averaged over all runs for the indicated time period during the Grand Tetons campaign. “BBOA event” refers to the higher-concentration August 15 episode.

mass spectrum and signal intensity over the study period, observed from fragment timelines and a sampling of mass spectra throughout the duration (not shown), suggests that organonitrates comprise part of the regional background aerosol.

CHN ions comprise the most abundant nominally organic nitrogen fragments (Figure 4-13), with about two times the signal intensity of the CHON family. Unlike CHON, CHN fragments vary in both signal intensity and mass spectral patterns. The average daytime spectrum contains a $C_xH_5N^+$ series at m/z s 55, 67, 79, and 91 indicative of nitriles and/or pyridine-type fragments (which have the same empirical formula) in 70 eV reference spectra, which are generally comparable to fragmentation in the AMS (NIST Webbook; Dzepina et al. 2007; Alfarra 2004). Pure nitriles are distinguishable from pure pyridines due to fragmentation variations caused by their differing structures; unfortunately, the complexity of the ambient mass spectra and the likelihood of several compounds contributing to a given fragment make compound identification difficult in this case. Pyridine compounds are common in the atmosphere and emitted from combustion and soil, to which they are applied to inhibit fertilizer

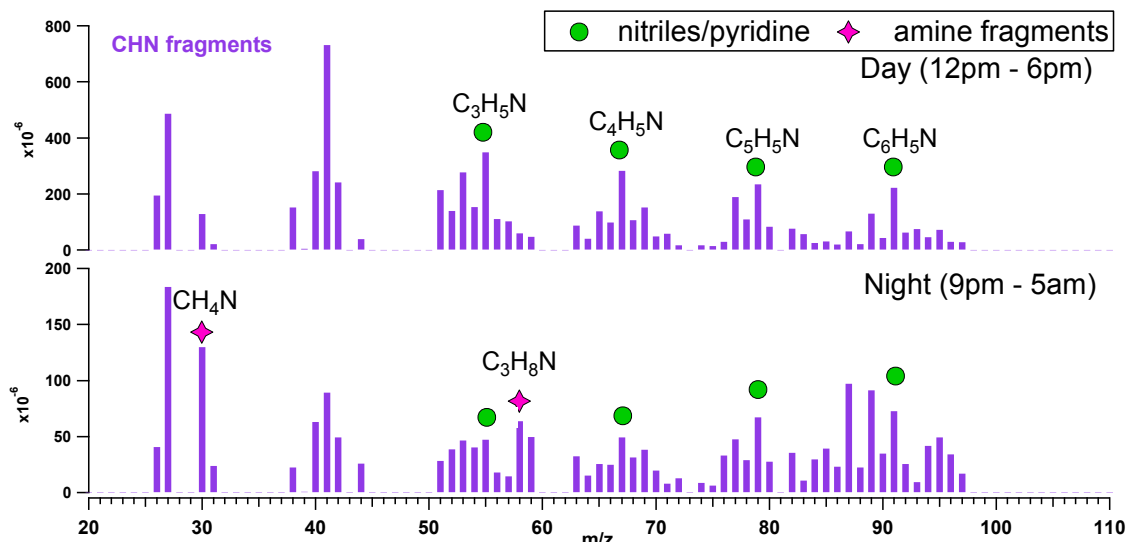


Figure 4-13: Mass spectra of $C_xH_yN^+$ fragments averaged over all runs for the indicated time period during the Grand Tetons campaign.

volatilization from crops, with an atmospheric lifetime of ~ 5 -59 days allowing wide dispersion (Atkinson et al. 1987; Schulte & Arnold 1990); also, a number of nitriles are used as herbicides, so regional agricultural sources could contribute pyridine and/or nitriles. While pyridine is fairly volatile and does not readily condense under atmospheric temperatures (Chirico et al. 1996), absorption may occur in the presence of sufficient organic substrate (Eisele 1988; Schulte & Arnold 1990; Tanner & Eisele 1991; Murphy et al. 2006); pyridine is abundant in both boundary and free tropospheric layer particles (Eisele 1988; Schulte & Arnold 1990; Tanner & Eisele 1991; Murphy et al. 2006).

The daytime CHN spectrum (tentatively identified as pyridine/nitriles above) differs from published spectra of, for example, common ambient component trimethylamine (m/z s 30, 58, 72, and 86, etc.; Silva et al. 2008) and chamber amine SOA experiments (m/z s 30, 31, 58, 88, and 118 for various amine precursors; Murphy et al. 2007). However, some of these amine fragments are enhanced in the nighttime average spectrum, suggesting the presence of amine compounds; of particular note is CH_4N^+ at m/z 30, which Murphy et al. (2007) suggest results from amine re-

arrangement after electron impact ionization. Following the CHON analysis, average $ON_{\min,CHN} = 0.04 \pm 0.06 \mu\text{g}/\text{m}^3$ (max = $0.38 \mu\text{g}/\text{m}^3$); giving a total average $ON_{\min} = ON_{\min,CHN} + ON_{\min,CHON} = 0.06 \mu\text{g}/\text{m}^3$ (max = $0.60 \mu\text{g}/\text{m}^3$).

4.6 Particle Size

As in the Rocky Mountain dataset, lognormal distributions were fitted to average size distributions for various time periods to describe their size modes and width parameters (Figure 4-14), where the width parameter indicates relative polydispersity. Particles were notably larger and more monodisperse during BBOA events, suggesting an aged aerosol consistent with ~480 km (300 mi) transport from the fires near Boise, ID. In contrast, the smaller size and relative polydispersity of the total aerosol ('all' in Figure 4-14), suggests fresher particles; this is consistent with the hypothesis, which arose from the lack of correlation between OOA and anthropogenic tracers, that local formation may be more important than transport for OOA.

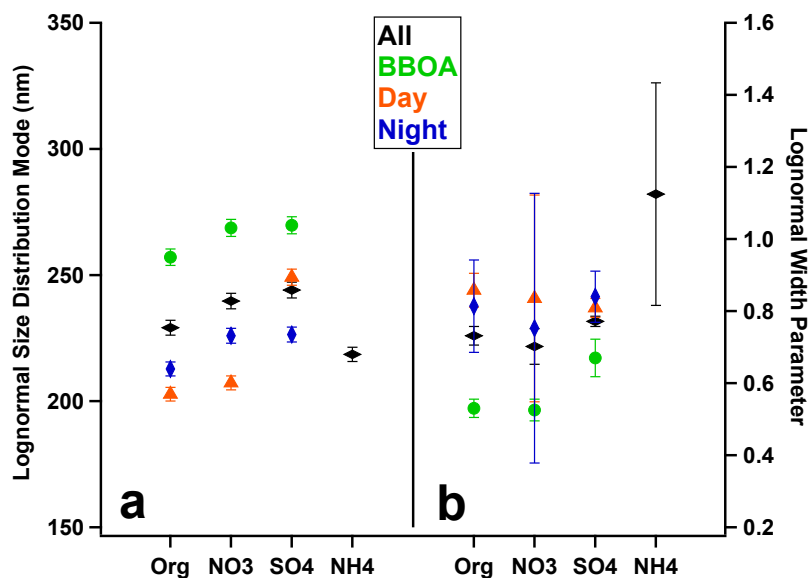


Figure 4-14: The a) mode and b) width parameter of the lognormal fit of the average size distribution for the given component (text marker) and time period (color). ‘Day’ data averaged over 12:00-18:00 LST; ‘Night’ data averaged over 21:00-5:00 LST. Error bars on modes are error on PToF size determination as outlined in Section 2.1.2; error bars on width parameters are the standard deviation of the width parameter fit.

The daytime aerosol is slightly smaller and more polydisperse than during the night, which could arise from photochemical formation. Also, sulfate, which is thought to be transported from anthropogenic sources in the valley, is significantly larger than organics and nitrate, implying an external mixture; however, import of fresher (than the overnight-aged) aerosol from the near valley floor could also produce a reduction in mode size, as could loss of semi-volatile species during warmer daytime temperatures. OOA has no correlation to temperature on average ($r^2 = 0.04$, slope = 0.02). A positive correlation may indicate that SOA formation from BVOCs is dominant, as vegetative emissions increase with temperature, while a negative correlation may indicate prevalent thermal partitioning; a slope of ~ 0 may indicate a balance between the two, on average, but this analysis is best applied to isolated air masses, which is not the case here. In all, since the BBOA is with some certainty transported from near Boise, we can conclude only that the OOA is either photochemical or transported from sources nearer (or with less equivalent oxidation time) than Boise.

4.7 Meteorological Analysis

The evidence shown so far for transported BBOA and locally-formed and/or ‘regional background’ OOA can be supported by relating component concentrations to wind direction. Wind roses with raw data, average concentrations over each of 16 directional wind bins, and conditional probability functions are shown in Figure 4-15. LV-OOA is constant with respect to wind direction at $\sim 1.5 \mu\text{g}/\text{m}^3$; this is reflected in the average concentration trace and the CPF, which suggests no directionality apart from a single high value to the $\sim\text{NEE}$, which is largely a function of the low wind count in that bin (a caveat to using CPF, see Section 1.3.5). LV-OOA concentration also fails to increase following upslope wind initiation on the timeline, lending credence to our in-situ formation/regional background hypothesis. For instance, in Figure 4-16,

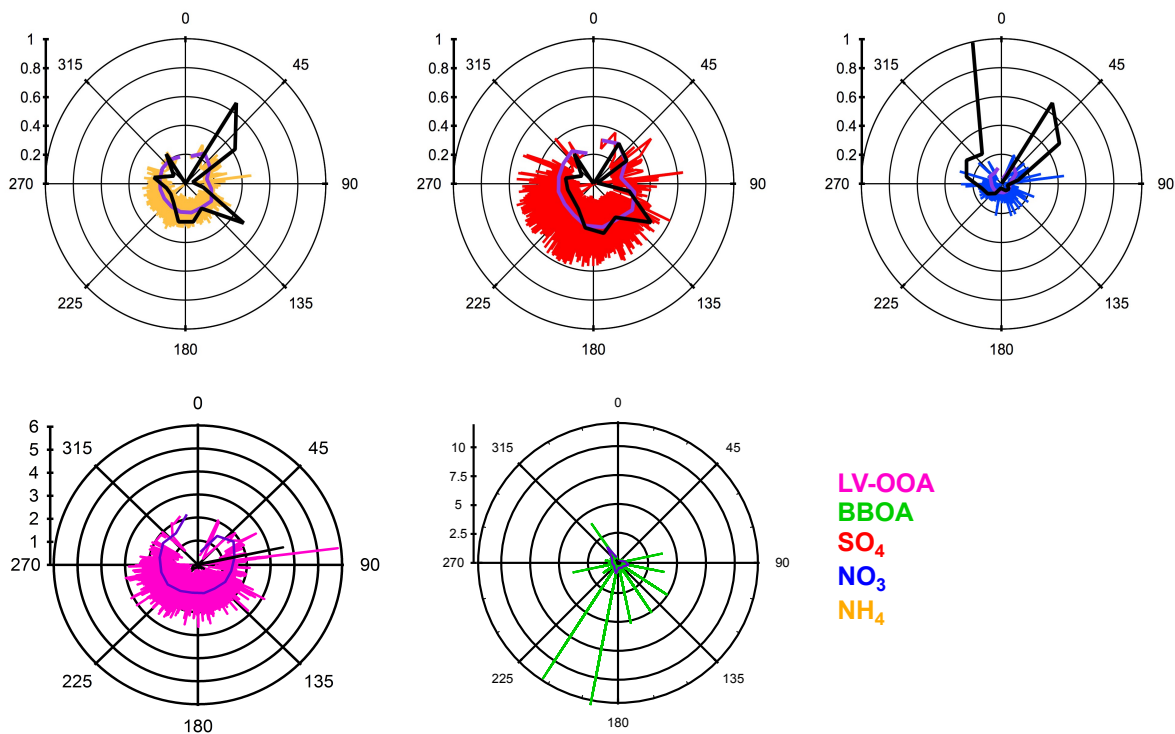


Figure 4-15: Wind roses showing raw component concentration (colored by given component), concentration average within each of 16 wind bins (purple line), and conditional probability function in each bin (black line). Concentrations are in $\mu\text{g}/\text{m}^3$.

the wind is fairly steadily from the SW-W (upslope, geographically) before, during, and after the BBOA event evident on the night of 15-16 August, but there is little change in LV-OOA (the slight decrease during the BBOA event could arise from PMF apportionment of mass to BBOA based on the strength of mass spectral signifiers, e.g. m/z 60). Further, over a two-day period (midnight to midnight August 16-18; Period A, Figure 4-16), wind direction changes from westerly to northeasterly and back around the compass with no change in LV-OOA concentration. Increasing wind speed is sometimes accompanied by increasing inorganics during the time period shown, but bears little relation to LV-OOA. The episodic, transported nature of BBOA is reflected in a few scattered high-concentration events in the raw data with CPFs near zero because only one or a few data points in each bin exceeded the threshold.

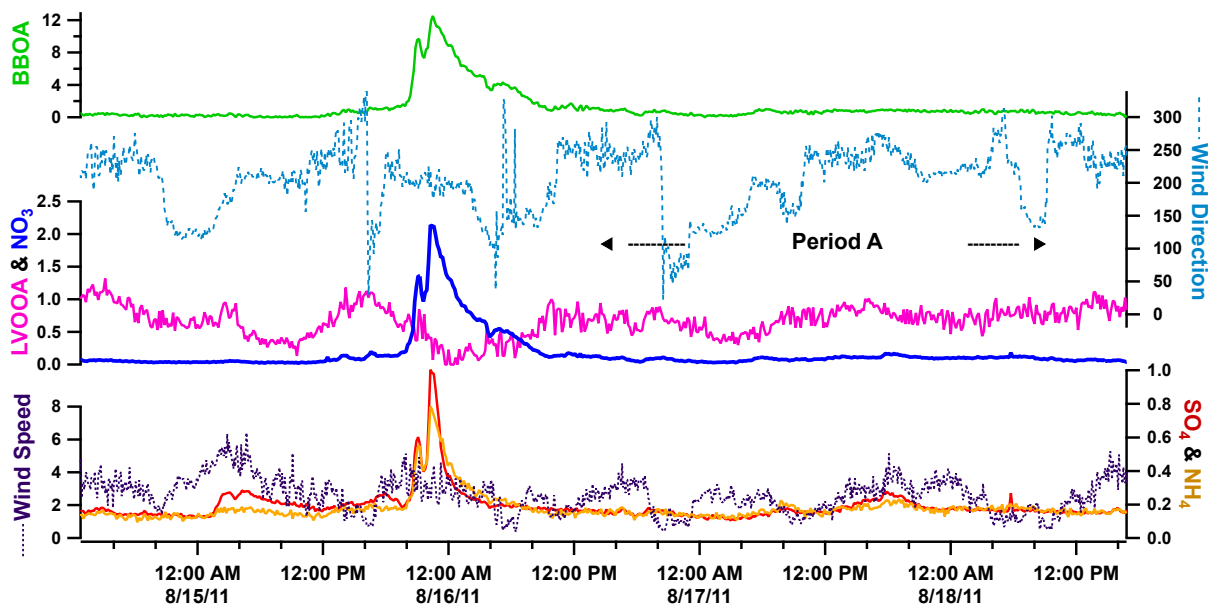


Figure 4-16: Timeline showing PMF factor and inorganic component concentrations with wind speed and direction (degrees) during a subset of the Grand Teton field campaign. Concentrations are in $\mu\text{g}/\text{m}^3$.

On the other hand, both ammonium and sulfate show enhanced raw, average, and CPF traces with S-SE wind, which is approximately parallel to the plane of the mountain's slope (Figure 4-15); this suggestion of upslope transport from the Snake River Valley is supported by:

- a) slight afternoon increases in inorganics, commensurate with diurnal upslope wind patterns,
- and b) the chiefly anthropogenic sources of inorganics, for which sparse population precludes a local source. For all inorganic species, high CPF values from the NE (and NW for nitrate) may come from low wind bin counts, as above. Nitrate concentration is universally low.

Grand Teton data were also compared to GEOS-Chem using grid boxes at the surface and immediately above the planetary boundary layer (PBL) comparison to upslope and downslope data, respectively (Bonne Hotmann, personal communication, 13 August, 2013). The model was run with 2011 emissions data and meteorology. This technique may be sub-optimal if boundary layer expansion to encompass the site is important (in comparison to the topographically-funnel flow at Rocky Mountain, for instance), for which placement in the BL or FT may not be

indicated by local wind direction; also, since the majority of wind direction measurements come are upslope (88% or n=2614, Figure 4-17), analysis of downslope data is hindered by lower sample number (n=341).

As in the Rocky Mountain study, the GEOS-Chem modeled boundary layer during the study (avg. = 984 ± 137 m) is lower than the site elevation (2,722 m), suggesting constant free-tropospheric influence; however, clear afternoon increases in NO_x suggest periodic transport of anthropogenically-influenced boundary-layer air (Table 4-2).

Table 4-2: Study-average component concentrations from the HR-ToF-AMS during upslope (135-315°) and downslope (316-360 & 0-134°) winds, with the ratio of average upslope to average downslope concentrations; ‘G-Chem PBL’ shows study-average component concentrations from the Grand Teton surface grid box, while ‘G-Chem FT’ data is from the grid box immediately above the planetary boundary layer over the Grand Teton site.

	Upslope ($\mu\text{g}/\text{m}^3$)	Downslope ($\mu\text{g}/\text{m}^3$)	Ratio AMS Up:Down	G-Chem PBL ($\mu\text{g}/\text{m}^3$)	G-Chem FT ($\mu\text{g}/\text{m}^3$)	G-Chem PBL:FT
SO₄	0.28 ± 0.13	0.25 ± 0.12	1.12	0.35 ± 0.10	0.39 ± 0.11	0.90
NH₄	0.20 ± 0.06	0.18 ± 0.05	1.11	0.13 ± 0.04	0.15 ± 0.04	0.87
NO₃	0.08 ± 0.15	0.09 ± 0.10	0.89	0.00 ± 0.00	0.01 ± 0.02	-
Organics	1.56 ± 1.41	1.57 ± 1.06	0.99	1.21 ± 0.73	0.25 ± 0.10	4.84
BBOA	0.50 ± 1.08	0.34 ± 0.22	1.47	-	-	
LV-OOA	0.63 ± 0.33	0.68 ± 0.27	0.93	-	-	

There are no significant differences in concentrations of either total organics or inorganic species between periods with upslope and downslope winds, though upslope values tend to be higher; however, timeline features are somewhat dissimilar (Figure 4-17). BBOA, which is likely transported from the Snake River Valley, has a higher average during upslope winds, while LV-OOA has the same average during up- and downslopes, reinforcing the assertion that *in situ* or regionally disperse sources are important for oxidized OA. In the timeline subset in Figure 4-17, total organics appear to follow wind direction, with the highest organic concentrations concurrent with WSW-WNW upslope winds (perpendicular to slope plane); however, if transport is a source

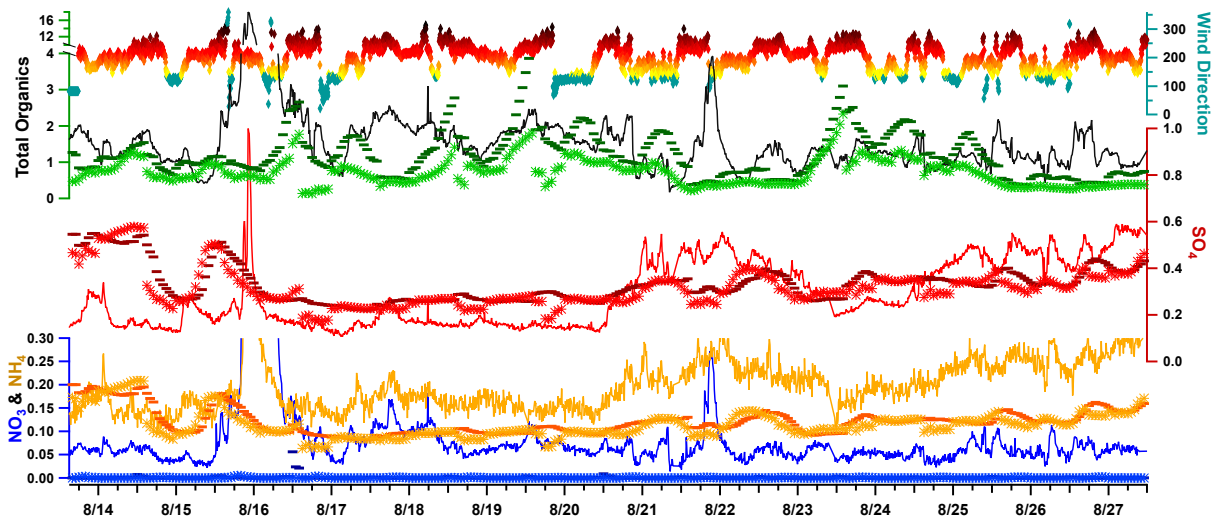


Figure 4-17: A timeline subset of particle components from Grand Teton AMS measurements (traces, 5-minute average), GEOS-Chem free troposphere predictions (stars, 1-hour), and GEOS-Chem boundary layer predictions (horizontal bars, 1-hour), color-identified by axis; warm colors indicate upslope wind direction (colored diamonds, teal axis), while teal indicates downslope flow. Vertical lines indicate midnight (00:00 LST).

of organics, it cannot be statistically differentiated from regional background. Organics are significantly different between GEOS-Chem predictions for the ‘free troposphere’ and the Grand Teton ‘downslope’ data with no significant differences in other constituents, implying a missing ‘free tropospheric’ organic source (if the site is indeed in the free troposphere periodically); in GEOS-Chem simulations in Heald et al. (2005, Section 1.2.2), anthropogenic constituents such as sulfate that are transported to the FT are well-predicted but organics are not, leading the authors to suggest an *in situ*, secondary OA source.

4.8 Grand Teton National Park Summary and Conclusions

Submicron particulate mass is low, averaging $2.08 \mu\text{g}/\text{m}^3$ (75% organic) with sulfate dominating inorganic mass and low ammonium and nitrate. Ammonium and sulfate have correlated time-series and CPF-indicated association with upslope winds from the Snake River valley, suggesting transport from an anthropogenic source. Concentrations of both were low with no significant diurnal patterns, though a weak afternoon maximum was observed.

Ammonium sulfate appears to be the dominant form of particulate nitrogen, with ammonium in excess of stoichiometric balance with sulfate and nitrate (NH_4^*) possibly contributing to amine/nitrile/pyridine mass and one episode (during the Aug. 15 BBOA event) with evidence of organonitrate content where nitrate is excess of stoichiometric balance with NH_4^* .

PMF analysis produces two organic types: low-volatility oxidized organic aerosol (LV-OOA) and episodic biomass burning aerosol (BBOA). LV-OOA contributes ~49% of total mass on average, with fairly static mass spectral composition and concentrations (usually ~0.5-1.5 $\mu\text{g}/\text{m}^3$). Though CO_2^+ fragments are more abundant than CH_3CO^+ (which is the definition of a 'low-volatility' aerosol), OM:OC, O:C, and data placement in f_{43} vs. f_{44} -space indicate that the data overlap both SV-OOA and LV-OOA ranges, a relatively lower degree of oxidation than is often observed in, for instance, highly aged urban plumes. LV-OOA is enhanced in the afternoon, but not correlated with upslope winds, anthropogenic NO_x , or ammonium sulfate; OOA at the site is also smaller and more polydisperse a) during the day, and b) in comparison to a biomass burning plume inferred to have travelled ~480 km. These data evoke *in situ* photochemical organic aerosol formation and/or growth (perhaps from local biogenic VOCs), though transported anthropogenic OA and/or gaseous precursors cannot be excluded if they are regionally disperse.

A high-concentration biomass-burning event on August 15-16, 2011 is thought to be transported from fires near Boise, ID evident in MODIS fire maps. This event is associated with W-SW winds (upslope from the Snake River Valley) and increased sulfate, ammonium*, nitrate, and CHN fragment abundance (nominally, amine compounds), suggesting enhanced organic nitrogen content. Particles were larger and more monodisperse during this time period, consistent with extended transport and oxidation time.

In general, the CHN spectra indicated nitrile and/or pyridine content during the day with the addition of amines at night. Nominally organonitrate (CHON) fragment intensities were constant throughout the campaign; lack of enhancement with BBOA events suggests that organonitrates are part of the regional LV-OOA background, though enhanced nominally inorganic nitrate fragments during the BBOA event in excesses of balance with ammonium indicate compounds such as organonitrates or calcium nitrate² that do not fragment to CHON. Agriculture abounds locally and may contribute both amines (though natural sources are also possible) and pyridines/nitriles, which come from combustion and agricultural processes (Section 4.6); photochemical oxidation reactions (in particular of biogenic SVOCs) may result in organonitrates, and calcium nitrate may arise from reaction of nitric acid (or its precursors) with particulate calcium carbonate.

² The effect in the AMS of refractory calcium on vaporization of nitrate from calcium nitrate has not been recorded in the literature.

5. Aqueous SOA Photo-oxidation Experiments

We hypothesize that matrix effects in real, complex ambient cloud water lead to higher SOA production via formation of more functionalized, lower-volatility products; the experimental setup addresses this hypothesis by comparing aqueous photo-oxidation of ambient cloud samples and single-precursor solutions at similar starting total organic carbon (TOC) concentrations (Table 5-1). Briefly, cloud or solution samples were photooxidized using UVC light and added hydrogen peroxide (producing hydroxyl radical, OH) in a temperature-stabilized vessel, and the continuously sampled solution was atomized, dried, and analyzed via AMS with 1-minute time resolution (see Section 2.3). Cloud samples were collected atop Mt. Tai, China, which lies in an industrialized province near metropolitan areas but disallows motorized vehicles locally, using a Caltech Active Strand Cloudwater Collector (CASCC) or a size-fractionating CASCC during the summer of 2008 (Demoz et al. 1996; Rao & Collett 1995; Collett et al. 1998; Rattigan et al. 2001; Reilly et al. 2001). Sample collection was begun when the cloud liquid water content exceeded 100 mg/m^3 , with collection bottles changed every 1-2 hours and samples stored frozen (Shen 2011); see Appendix Section 8.4 for more information on individual samples. To explore aqSOA production and type in the photooxidized solutions (ambient cloud water and single-component standards), we must quantify organic mass production and at least relative change in organic composition.

Table 5-1: Total organic carbon (TOC, $\mu\text{g/L}$) in the given ambient cloud water (TaiOx, abbreviated to ‘T’ below), pinonic acid (PA), or methylglyoxal (MG) sample solution. *Due to low sample volume, TaiOx1 is a combination of three cloud samples; TOC and pH are estimated using averages of the three samples and assuming equal volumes. For all other samples, solute addition, etc. relied on grade-A graduated cylinders for volume determination.

	MG1	MG2/MGIN	PA/ PAIN	T1	T2	T3	T4	T6PA	T7/7PA
TOC	18.01	2.16	3.60	~20*	24.1	2.86	1.73	9.17	6.40/10.06
pH	4.84 ± 0.04	5.36 ± 0.01 / 5.28 ± 0.02	5.28 ± 0.03 / 4.63 ± 0.02	~5.49	3.32	6.37	4.74	~3.7	4.58/~3.7

Quantifying aqSOA Mass Production:

The AMS is quantitative for nitrate, sulfate, ammonium, chloride, and total organics as explained in the introduction. However, the atomizing/drying system, which is assumed to simulate aqSOA particle production from evaporating cloud droplets as described below, displayed variable particle output. Variable atomizer output was observed in sporadic single-run (1-min average mass spectrum) mass ‘spikes’ with no commensurate RH change (Figure 5-1a).

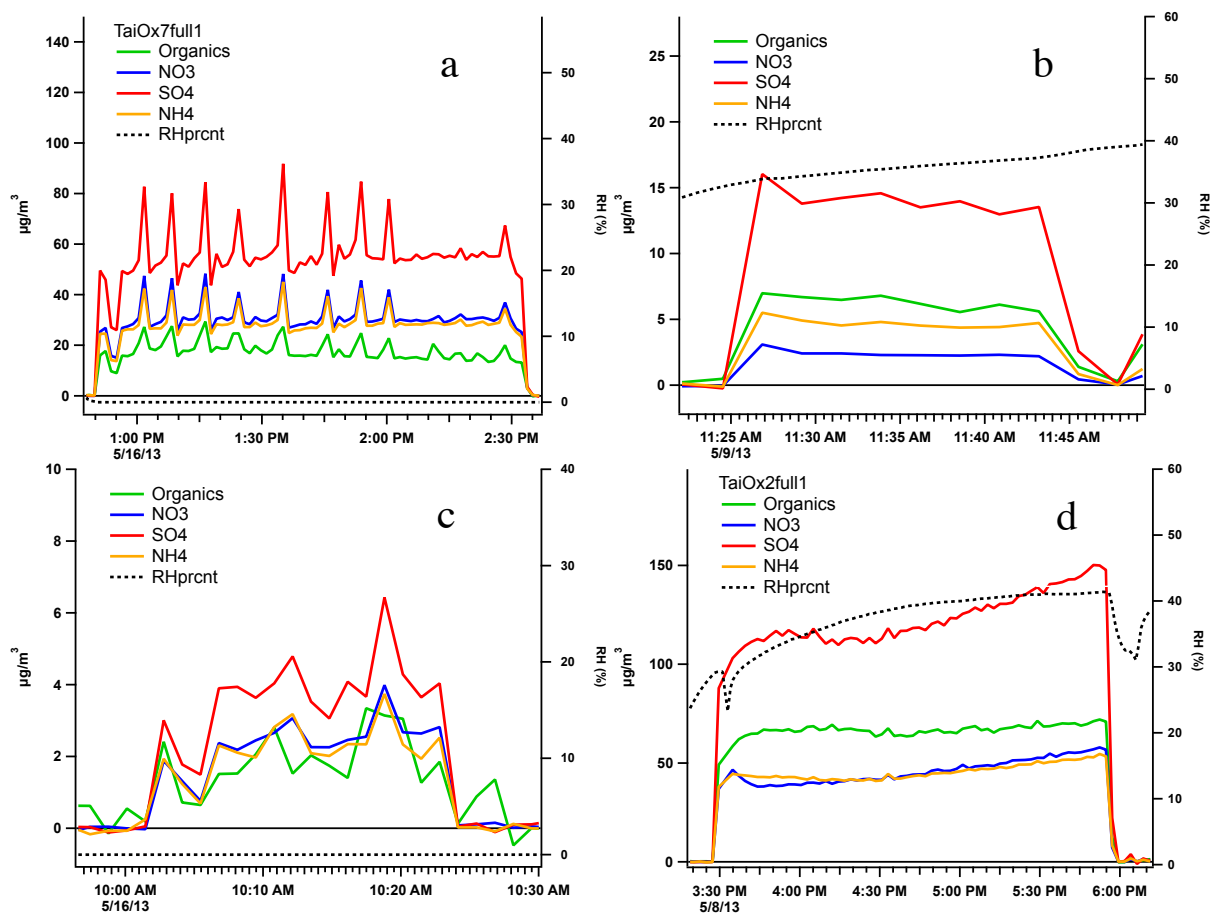


Figure 5-1: Example experiment timelines showing (a) a full photo-oxidation with mass ‘spikes,’ (b) a ‘baseline’ period with increasing RH, (c) a ‘baseline’ period with steady RH (≈ 0), and (d) a full photo-oxidation with more constant output.

The atomizer was draining inconsistently during these ‘spikes,’ emptying approximately every minute instead of continuously, as observed at the waste container. The spikes may arise from re-entrainment of sample that failed to atomize and collected in the bottom of the chamber when the waste liquid level rose to the atomizer orifice. Because the atomizer was draining every minute or so, the re-entrained sample might not be significantly different in composition from the current sample, which might explain why composition and mass progress smoothly when normalized to sulfate, as explained below. The atomizer was cleaned and re-plumbed a number of times according to manufacturer recommendations for various sample delivery methods; none of these succeeded in rectifying the problem.

To compensate for this methodological difficulty, changes in total organic mass and composition are determined by employing sulfate as an internal standard in all samples containing inorganics (i.e. all except PA and MG); inorganics, namely ammonium sulfate and ammonium nitrate salts, were added to roughly half of the single-precursor sample solutions at 50 μM to better explore the effect of inorganics in cloud water on SOA production. Mass spike-affected experiments are marked with an “*” by their name for transparency. For one affected experiment (TaiOx5*), noise in the data overwhelms useable information, but for most experiments organics scale consistently to total sulfate and resemble similar photo-oxidations. Though there are a number of cautions as discussed below, data from affected experiments are used to support conclusions drawn from unaffected experiments.

The sulfate mass constraint assumes that all organic and inorganic sulfur compounds fragment to HSO_x (Farmer et al. 2010), which the AMS software groups into ‘total sulfate’ (SO_4 hereafter); also, sulfur species partitioning during drying must be constant, and sulfur dioxide dissolution from room air into the solution is assumed to be negligible. Were the system

output and drying verifiably constant, it would be possible to evaluate these last assumptions; lack of variation in ‘CS’ family fragments between experiment beginning and end support the assertion that all sulfate species fragment to HSO_x (percentage of total signal from CS fragments is $\leq 0.1\%$ in ambient cloud samples and $\leq 0.5\%$ in single-precursor solutions with inorganics). Under the above assumptions, the ratio of high-resolution total organics to sulfate (Org/SO_4) can describe the progression of total organic mass in the evaporated-droplet particles during the experiment (Lee et al. 2011); ratios of ‘marker’ fragments to sulfate illuminate particle composition changes as described below.

For experiments with no inorganics (pinonic acid, “PA,” and methylglyoxal, “MG”), total organics were normalized to their $t=0$ value with the understanding that changes in organics could be due to changes in total mass output or artifacts in the system as discussed above and are therefore not comparable to inorganic-containing experiments; the general progression of PA and MG experiments resemble those with added inorganics (PAIN and MGIN) in many ways, and thus this organic normalization is assumed to be sufficient for the qualitative analyses presented here. Other fragment ratios used to explore composition change (described below) were calculated using total organics in the denominator.

Caveats to Quantification of aqSOA:

During oxidations of many types, organic mass may be gained through formation of lower-volatility products by functionalization and oligomerization (Kalberer et al. 2004; Szmigielski et al. 2007; Gao et al. 2010; Müller et al. 2008; Yasmeen et al. 2010), but observations suggest that mass can also be lost under advanced oxidation through organic decomposition³ (thought to arise from C-C bond scission often followed by addition of

³ Not to be confused with thermal decomposition and/or fragmentation in the AMS vaporizer.

oxygenated functional groups to the remaining fragment) and subsequent volatile loss of fragments (Kroll et al. 2009; Guzman et al. 2006). Organic mass loss during oxidation of OA has been observed with a variety of relevant precursors and oxidants (e.g. ambient particles, chamber biogenic & aromatic SOA, hydroxyl radical, and ozone) in field (Akagi et al. 2012) and laboratory campaigns (Kroll et al. 2009; Heald et al. 2010; George & Abbatt 2010; Kang et al. 2011; Bahreini et al. 2005), and bulk aqueous photo-oxidations of standards and cloud water (Lee et al. 2011a; Lee et al. 2012). Using single-component standards, Lee et al. (2011a) compared the sum of their AMS-quantified organic species (via calibration using off-line ion chromatography) to aqueous TOC measurements of the reacting solution and found that their speciated organics (glyoxal, glyoxylic, and oxalic acids) comprised ~50-100% of TOC with a higher fraction toward end, implying especial volatile loss at the beginning of experiments when higher-volatility products are often important in laboratory experiments (they did not, however, evaluate *total* AMS organics against solution TOC, quantifying total volatile loss); in their cloud water photo-oxidations, organics were initially gained ($\leq 130\%$ of $t=0$ organic mass), then subsequently lost, suggesting first functionalization, then fragmentation reactions (Lee et al. 2012).

In all, the bulk-aqueous/AMS analytical method is expected to lose a large and variable fraction of volatile oxidation products, the amount of which is highly dependent on the oxidation precursors and the volatility of their dominant products and is assumed to mimic the behavior of evaporating cloud droplets in the real atmosphere. Loss mechanisms may include a) evaporative loss during diffusion drying (Lee et al. 2011a), and b) evaporative loss during drying as the particle beam enters the high vacuum in the AMS (Zelenyuk et al. 2006). Mechanism a) might be more atmospherically relevant than b), but the current dataset cannot determine the contributions

of each of these mechanisms to organic evaporative loss. Also, while the continuously-mixed bulk solution methodology might prevent the phase separation observed in atmospheric aerosol water (e.g. organic shells, etc. which may change water evaporation and/or solute interaction and therefore reactivity), this effect is not thought to be important in cloud-relevant concentrations, where relative dilution leads to ~homogeneous mixing (Marcolli & Peter 2005; Zuend et al. 2008; Shiraiwa et al. 2013; Ziemann 2010). Under these assumptions, the AMS does capture evaporated-cloud-relevant particulate organics, assuming our drying methods resemble those in the real atmosphere.

Further discussion of the variable atomizer output is also warranted. We have observed similar mass ‘spikes’ in high-RH marine environments when liquid collects on, then is released from, the AMS flow-control orifice; we hypothesize that RH is too low for this to be the case here (see below), and there were none of the pressure and flow fluctuations usually caused by AMS orifice blockage during spike-affected periods.

Some chamber experiments have observed continuous, low magnitude increases in mass output of sulfate correlated with growing sample stream RH (Volkamer et al. 2009); we assume that sulfate has no or very low sources from SO₂ dissolution (from laboratory air, for which SO₂ sources are low) and that evaporative loss of volatile S(IV) compounds such as SO₂•H₂O is not significant, such that if sulfate mass increases during ‘baseline’ periods (no UV, no H₂O₂) it would necessarily arise from changing atomizer output or particle collection efficiency.

Next, increased RH may enhance water content in oxidized organic particles, which are generally quite hygroscopic (Section 1.2), making them more spherical and increasing collection efficiency by reducing ‘bounce’ out of the AMS vaporizer; enhancement of collection efficiency by deliquescence when RH exceeds ~80% has been observed (Allan et al. 2004; Matthew et al.

2008). Since these cloud samples originate over a forested mountain in the industrialized North China Plain and approximately 40km from a city of almost 7 million (Jinan, China), a fair amount of oxidized content might be expected and is confirmed in the mass spectra (**Figure 8-11**, Appendix Section 8.6) in which $m/z\ 44 > m/z\ 43$ (the definition of ‘low-volatility oxidized organic aerosol,’ or LV-OOA). Thus, it is necessary to evaluate whether particle wetting could contribute to fluctuating particle collection efficiency.

RH monitored before the AMS inlet averaged $32.02 \pm 13.57\%$ (max. = 66.4%). Since the particles start wet, RH relative to the crystallization point is more relevant to particle water content than deliquescence. Efflorescence RH (ERH) for ammonium-sulfate- α -pinene particles may be very low or eliminated for organic fractions ≥ 0.6 , and has been measured at $\leq 30\%$ for lower organic mass fractions (Smith et al. 2012); our organic fractions average 0.42 ± 0.30 , so it is likely that between decreased ERH and an RH usually at or above the maximum estimated ERH, our particles did not change phase (i.e. crystallize) and collection efficiency was approximately constant. In any case, increasing RH seemed to have no effect on collected particle mass during baseline periods, as evidenced in panels (b) and (c) of Figure 5-1. Installation of a second dryer to combat RH fluctuations reduced RH to near 0% (RH monitor accuracy = 3% at 0-90% RH; see Section 2.3 and **Table 2-2** for further information on RH in each experiment). Baseline experiment mass output was not related to RH in either ‘humid’ or dry conditions.

Sulfate and total mass enhancements have also been observed in cycloalkane ozonolysis experiments under constant RH, where organic particle coatings are thought to increase particle sphericity and therefore collection efficiency (Bahreini et al. 2005); this may contribute to sulfate (and total mass) increases during photo-oxidation experiments, though no sulfate increases were

noted during baseline periods as described above. Unfortunately, it is difficult to disentangle SOA formation from possible organic coating effects, if applicable.

Other complications were noted, including very sporadic, abrupt (step-wise) changes in atomizer output unrelated to the mass spikes and unaccompanied by RH changes. It is also possible that liquid water in the sampling lines, observed sporadically at and before the first dryer inlet (when the atomizer did not drain correctly), affects aqSOA quantification in a non-atmospherically relevant fashion by changing partitioning through a) particle/droplet interception or b) gaseous uptake, inducing volatilization from particles; organic coatings might also affect partitioning if they are insoluble, but since most functionalized organics are polar, organic films are usually soluble and seem to have little effect on the partitioning of organics (Donaldson & Vaida 2006; Kolb et al. 2010). Partitioning effects are not quantifiable with the current dataset and remain a caveat to the validity of results. Even if partitioning is not affected, it is difficult to distinguish between output inconsistency, altered collection efficiency, and real change in aqSOA production, thwarting direct quantification and necessitating the sulfate normalization described previously.

Exploring relative composition change:

The greatest drawback of the AMS is high fragmentation during ionization, reducing a vast array of parent compounds in the ambient samples to a relatively small number of common fragments; the contribution of multiple unidentified parent compounds to a given fragment makes quantitation of specific oxidation products – and/or reductions in precursor compounds – essentially impossible; AMS quantitation of specific oxidation products has been achieved only in simple solutions using atomized standards (with steady atomizer output) to determine contributions from each possible parent to a given fragment (Lee et al. 2011). While parent

compound quantitation is confounded by a) the complexity of the ambient matrix, b) our lack of varying-concentration standards, and c) inconsistency in particle mass output (precluding standard use for single-component solutions), certain fragments do indicate general particle types; for instance, CO_2^+ (m/z 44) fragments from mono- and poly-carboxylic acids, acid-derived esters, etc. (Duplissy et al. 2011; Canagaratna et al. 2007; Alfarra 2004; Aiken et al. 2007; Zhang, Alfarra, et al. 2005), while $\text{C}_2\text{H}_3\text{O}^+$ (m/z 43) indicates carbonyl compounds (as found in NMR analyses, Russell et al. 2011; Decesari et al. 2007).

As explained earlier, sulfate can be used to normalize organic mass when atomizing-system mass output is inconsistent. We use sulfate-relative changes in fragment abundance ($\text{C}_x\text{H}_y\text{O}_z^+/\text{SO}_4^+$) to explore organic composition change; relevant fragments and possible parent molecule types are shown in Table 5-2. Also, as noted in Section 1.3.3, the UMR-based method of calculating f_{43} and f_{44} may confuse interpretation of oxidation progression by conflating signal from more- and less-oxidized fragments in the same UMR bin (width ≤ 1 m/z); as composition changes, an increase in one fragment may be offset by decrease in another, making fragment abundance a better measure of oxidative progression. The ‘traditional’ f_{44} and f_{43} ratios (m/z 44 or 43/Org) are supplemented with analogous ratios of CO_2^+ and $\text{C}_2\text{H}_3\text{O}^+$ to sulfate; other fragments may indicate highly functionalized molecules (Table 5-2). Changes in organic composition and possible reaction regimes are also explored in van Krevelen (H:C vs O:C) space (Section 1.3.4).

‘Formic acid’ (CH_2O_2^+ @ m/z 46) receives special attention here for its volatility and impact on organic mass retention; upon collection, the cloud samples contained formic acid in some quantity (Appendix Section 8.4, **Table 8-4**). Though other molecules may fragment to CH_2O_2^+ and the complexity of the ambient matrix prevents determination of CH_2O_2^+

Table 5-2: Fragments used as indicators of chemical composition; the unit mass resolution bin (m/z) is followed by the fragment formula (in parentheses) and species or compound type possibilities. Note that a given fragment may come from a variety of parent compounds; the indicated fragment does not necessarily exist in the particle phase, but may indicate the types of parent compounds present. Methylglyoxal is abbreviated ‘MG.’

m/z	(formula) compound	m/z	(formula) compound
46	(CH_2O_2^+) Formic Acid fragment	90	($\text{C}_3\text{H}_6\text{O}_3^+$) MG monohydrate/Lactic or Hydracrylic Acid
55	(C_4H_7^+) Alkene, ($\text{C}_3\text{H}_3\text{O}^+$) Aldehyde	104	($\text{C}_3\text{H}_4\text{O}_4^+$) Malonic/Hydroxypyruvic Acid
56	(C_4H_8^+) Alkene, ($\text{C}_3\text{H}_4\text{O}^+$) Aldehyde	108	($\text{C}_3\text{H}_8\text{O}_4^+$) MG dihydrate
60	($\text{C}_2\text{H}_4\text{O}_2^+$) Acetic Acid/Glycolaldehyde	118	($\text{C}_3\text{H}_2\text{O}_5^+$) Mesoxalic, ($\text{C}_4\text{H}_6\text{O}_4^+$)
72	($\text{C}_3\text{H}_4\text{O}_2^+$) Methylglyoxal, ($\text{C}_4\text{H}_8\text{O}^+$)	126	($\text{C}_6\text{H}_6\text{O}_3^+$) MG Oligomer
74	($\text{C}_2\text{H}_2\text{O}_3^+$) Glyoxylic Acid	131	($\text{C}_6\text{H}_{11}\text{O}_3^+$) MG product oligomer
76	($\text{C}_2\text{H}_4\text{O}_3^+$) Glycolic Acid	144	($\text{C}_6\text{H}_8\text{O}_4^+$) MG product oligomer
88	($\text{C}_3\text{H}_4\text{O}_3^+$) Pyruvic Acid, ($\text{C}_4\text{H}_8\text{O}_2^+$)	147	($\text{C}_8\text{H}_3\text{O}_3^+$), ($\text{C}_5\text{H}_9\text{NO}_2^+$)

contribution from specific parent molecules, we move forward using CH_2O_2^+ signal to interpret ‘formic acid’ production with the understanding that the given signal likely overestimates the amount of formic acid in the particle. The contribution of fragmenting ‘formic acid’ to CO_2^+ (m/z 44) may be calculated using the ratio of signal at m/z 44 to m/z 46 in the NIST electron ionization reference spectrum for formic acid (=0.1642; NIST 2013), assuming that other species fragmenting to formic acid contribute similarly to CO_2^+ (which is unknown, since the fragmenting species are unknown). This is expressed:

$$\text{fraction of } \text{CO}_2^+ \text{ from formic acid} = \frac{\text{signal}_{\text{CH}_2\text{O}_2} \times 0.1642}{\text{signal}_{\text{CO}_2}} \quad (\text{Equation 15})$$

Delta Analysis

Delta analysis relies on the tendency of organic molecules to lose CH_2 groups sequentially during fragmentation such that the resulting signal peaks are separated by 14 atomic mass units (amu); functional group composition dictates the m/z values of the peaks such that $\text{delta } (\Delta) = m/z - 14n + 1$, where n is the number of methylene (CH_2) bridges on the functional group (McLafferty & Turecek 1993; Bahreini et al. 2005; Canagaratna et al. 2007; Silva et al.

2008). Generally, unsaturated hydrocarbons and aromatics have $\Delta \leq 0$, oxygenated unsaturated organics such as aldehydes, ketones, and alcohols are $\Delta = 0$, while for highly oxygenated/functionalized organics $\Delta \geq 2$ (McLafferty & Turecek 1993); a summary is provided in Table 5-3, but readers are referred to McLafferty & Turecek (1993) for a more in-depth discussion.

Table 5-3: Summary of delta values indicated fragments and/or functional groups, adapted from McLafferty & Turecek (1993).

Delta	Indicated Functional Groups	Delta	Indicated Functional Groups
-7	Phenyls	0	Alkenes, Cycloalkanes, Alkyl cyanides
-6	Phenylalkyls, Benzoyls, ROCOOR-species, Chloroalkyls	1	Alkenes, Cycloalkyl, Diketones, Unsaturated esters, Cyclic amines
-5	R-phenyls, Aminoaromatics	2	Alkyls, Saturated carbonyl
-4	Terpenes and derivatives, Phthalates	3	Aldehydes, Cycloalkanols, Alkyl amines, Amides, Nitrites
-3	R-phenyls, Cycloalkenes	4	Alcohols, Acids, Esters, ROCO-R`-CO
-2	Alkynes, Cycloalkenes, Unsaturated/cyclic w/ O: alcohol, ether	5	Cyclic sulfides, Nitrates, ROCOCHR`, CR ₂ ONO
-1	Ketones (unsaturated), Alkyl cyanides, Retro-Diels-Alder product (cyclohexene)	6	Unsaturated aryls, Alcohols, RCOOR`-rearrangments, Sulfides

A number of studies suggest that the dominant peak structure is driven by aerosol source type and can be illustrated through delta values, where positive Δ indicates (usually aged) anthropogenic sources and (especially, fresh) biogenic sources tend to produce negative Δ (Canagaratna et al. 2007; Kiendler-Scharr et al. 2009). Δ values of 0, 2, and 3 may suggest aged anthropogenic sources and have been observed during urban ambient studies (Drewnick et al. 2004; Schneider et al. 2004). From Bahreini et al. (2005):

“The dominant fragments in [urban plume] mass spectra are those with $\Delta = 2$ (alkyl groups and saturated carbonyls), $\Delta = 0$ (unsaturated hydrocarbons, unsaturated alcohols, and unsaturated carbonyls), $\Delta = 3$ (oxygenated organics and nitro compounds), and $\Delta = -1$. In addition, the organic mass spectra obtained from brush fire plumes show more contribution from fragments with negative Δ values as compared to the mass spectra of Cleveland and background Ohio pollution, indicating the presence of more terpene derivative, aromatic, unsaturated, or cyclic structures.”

Organic Nitrogen Analysis:

N:C vs O:C and CHN/CHON fragments are used to explore organic nitrogen; elemental analysis does not attempt to estimate contributions of nominally inorganic nitrogen fragments NO_n and NH_x , which may fragment from ON molecules, potentially leading to underestimation of N:C. Small amounts of total organic, CHN, and CHON mass were noted in periodic system flushes using deionized water and may result from dissolution of NH_x from room air, solution retention in the atomizer, and/or gaseous contaminants from the HEPA-filtered compressed air used in the atomizer, which had a ‘burned marshmallow’ smell. This smell was not observed until midway through the experiments, when the compressed air was used for drying glassware; the air source was not changed mainly because contaminants were usually a low percentage (~0.5%) of total mass for single-precursor experiments, depending on the atomizer mass output during the sample (Appendix Section 8.7). PA and MG experiments without added inorganics are therefore analyzed for organic nitrogen to evaluate possible contamination; ON_{min} (the sum of CHON and CHN fragments) was found to be $<0.2 \mu\text{g}/\text{m}^3$ in all DI baseline periods. No sulfate contamination was noted. In the few cases, especially after analysis of high-concentration samples, where the DI baseline total organics were elevated to $\sim 1\text{--}2.5 \mu\text{g}/\text{m}^3$ (equivalent to $\sim 10\%$ of organics in some of the lower-concentration samples), the DI flush was extended and/or the atomizer was disassembled and cleaned until organics were $< \sim 0.5 \mu\text{g}/\text{m}^3$; this contamination may arise from retention of a previous sample in the vaporizer, especially when draining was inconsistent.

Reaction types and naming guide:

Reaction names are a combination of a prefix containing the reaction precursors and suffix containing experiment type (control type, etc.) and replicate number.

Prefixes:

Pinonic Acid: PA

Methylglyoxal: MG

Added Inorganics: MGIN, PAIN

Ambient Cloud: TaiOx# (#: 1-7, Table 2-2, Appendix Section 8.4)

Ambient Cloud with added Pinonic Acid: TaiOx#PA

Suffixes:

b#: (baseline period) no UV, no H₂O₂; replicate #

ho#: (control) H₂O₂ added, no UV; replicate #

uv#: (control) UV on, no H₂O₂; replicate #

f#: (full photo-oxidation) H₂O₂ added, UV on; replicate #

For example, “TaiOx6PAf1” indicates TaiOx6 ambient cloud with added pinonic acid precursor, full photo-oxidation, replicate 1.

5.1 Ambient Cloud-water Photo-oxidations

This and each of the following sections begins with timelines of total organic production (normalized Org/SO₄) and general oxidation (*f*₄₄), then continues to a more detailed exploration of possible reaction regimes and product types through van Krevelen and elemental analysis, difference mass spectra, and timelines of important fragments. TaiOx5* is excluded from the following analyses for its high degree of noise and lack of statistical trends for all data types.

Changes in Total Organics and Degree of Oxidation

Organics/sulfate and *f*₄₄ (*mz*₄₄/Org) for TaiOx 1, 2, 3, 4-1 (of 3 TaiOx4 replicates; #2-3 had variable atomizer output), and 7 are shown in Figure 5-2; sample volume limited the duration of TaiOx1. For TaiOx1 and 3, Org/SO₄ appears to increase for the first 15-30 minutes

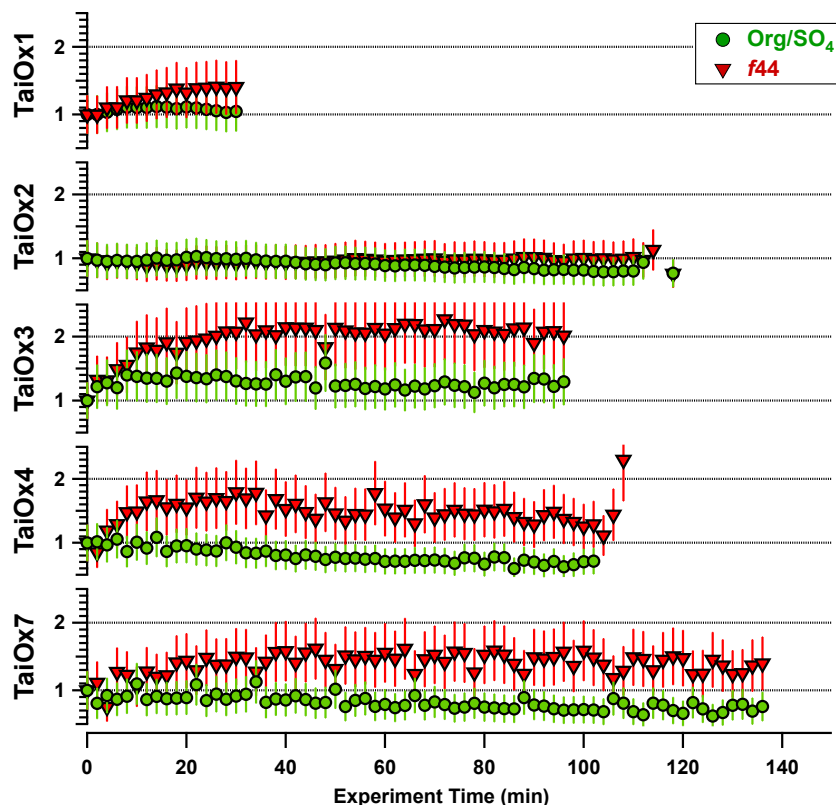


Figure 5-2: TaiOx: Timelines of normalized (to $t = 0$) Org/SO₄ (green) and f_{44} (red) for TaiOx1, 2, 3, 4-1, and 7 aqueous photo-oxidations. Error bars equal 28% of the value, from propagation of 20% AMS quantification error through the indicated calculations. Experiment time approximates ambient oxidation time as discussed in Section 2.3.

(to ~110 and 140% of the $t = 0$ value, respectively), then decrease for the remainder of the experiment. Considering the $\pm 20\%$ error generally ascribed to mass quantification in the AMS (which propagates to ~28% in these calculation), this mass increase is significant for only TaiOx3 (Drewnick & Hings 2009); however, the evident mass and f_{44} progression suggests oxidation leading to the eventual significant decrease in mass as discussed below for both TaiOx1 and 3. Early increases in organic mass indicate formation of lower volatility products, while the following decrease may arise from volatile product formation and/or decomposition of highly oxidized molecules to hydrocarbons and other more volatile fragments that are lost during evaporation. In TaiOx2, 4-1, and 7, organic mass is unchanging for the first 30-60 minutes and decreasing significantly thereafter.

Oxidation proxy f_{44} generally increases for the first 15-30 minutes and then may stay constant as in TaiOx3 or decrease slightly as in TaiOx4-1 (Figure 5-2). f_{44} in TaiOx2 may decrease slightly at the beginning and increased slightly thereafter, but, statistically speaking, was constant throughout the experiment. TaiOx1 did not run for long enough to determine a pattern after the initial increase in f_{44} . TaiOx experiments 1, 2, 4-1, and 7 (and the beginning of 3) are grouped in the ‘LV-OOA’ region of the f_{43} vs. f_{44} ambient triangle (Figure 5-3); TaiOx1 and 2 progress slightly toward higher f_{44} and f_{43} (as indicated by data point shading), while TaiOx4-1 and 7 do not show clear movement. Coupled with the chemical evolution explored below, this lack of progression in f_{44} and f_{43} may reflect contributions of both more- and less-oxidized fragments to each of m/z 43 and m/z 44; for instance, oxidation of hydrocarbons to carbonyls may not change signal at m/z 43 significantly since both have fragments with the same UMR mass ($C_4H_7^+$ and $C_2H_3O^+$, respectively); relevant fragments do change significantly and are investigated later.

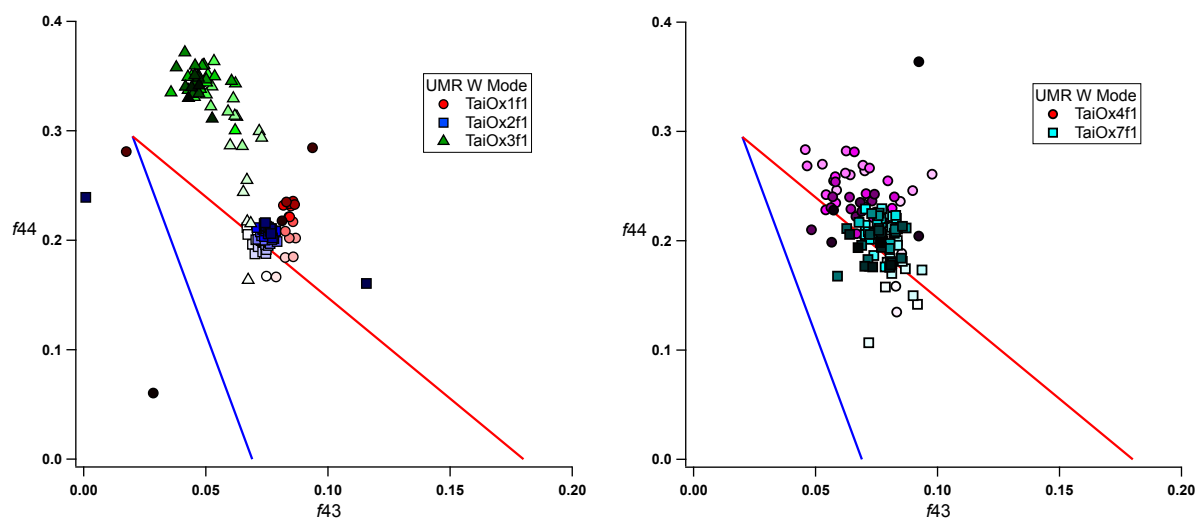


Figure 5-3: TaiOx: f_{43} (mz_{43}/Org) vs. f_{44} (mz_{44}/Org) for TaiOx 1-3 and 7; the blue- and red-bounded triangle represents the range of values typically inhabited by ambient aerosols (Ng et al. 2011).

TaiOx3 behaves more like ‘typical’ oxidizing aerosol as f_{44} increases and f_{43} decreases, which is generally expected as less-oxygenated carbonyl and hydrocarbon fragments at m/z 43 are oxidized to the carboxylic acids and carbonyls seen at m/z 44. TaiOx3’s f_{44} value is higher toward the end of the experiment than in many observed ambient aerosols, but consistent with OH-driven potential aerosol mass (PAM) chamber photo-oxidations (Ng et al. 2011; Lambe et al. 2011); the cloud event persisted another ~9 hours after TaiOx3 was collected, so the 2-hour oxidation, which is approximately time-equivalent to atmospheric oxidation (Section 2.3), is relevant to the real atmosphere. Lastly, Lambe et al. (2011) suggest that data placement in the right-hand side of the ‘ambient triangle,’ where the TaiOx samples fall, is indicative of “methylated aromatic, biogenic, and/or alkane precursors”; this is consistent with delta analysis, below, which indicated presence (and oxidation) of cycloalkyls, dienes, cycloalkenes, terpenes, etc. TaiOx4-2, 4-3, and 5 are very noisy in f_{43} vs. f_{44} space (Appendix Section 8.5, **Figure 8-9**).

Changes in Organic Composition

So far, it appears that organic mass generally increases slightly, then decreases significantly, and that oxidation indicator f_{44} increases, then may either stay approximately constant or decrease; however, this gives little information about important organic compound types and transformations. The next step is to explore organic composition changes through progression of specific fragments that indicate certain molecule types.

Figure 5-4 shows timelines of ‘modified’ f_{43} and f_{44} values $\text{CO}_2^+/\text{SO}_4$ (most oxidized fragment at m/z 44), $\text{C}_2\text{H}_3\text{O}^+/\text{SO}_4$ (most oxidized fragment at m/z 43), and $\text{C}_2\text{H}_3\text{O}^+/\text{C}_4\text{H}_7^+$ (ratio of most to least oxidized fragment at m/z 43), as well as $\text{CH}_2\text{O}_2^+/\text{SO}_4$, which is, nominally, formic acid (a major oxidation product of glyoxal compounds). Note that some studies exclude CH_2O_2^+ for its proximity to and therefore possible interference from NO_2^+ (Zhang et al. 2005;

Duplissy et al. 2011); it is included here following the standard half-max, half-width fitting rule, but it is notable that ‘formic acid’ is weakly correlated to total nitrate in TaiOx1 and 3 ($r^2 \approx 0.7$), the only runs for which we see significant formic acid formation. Both organic and inorganic nitrogen fragments (CHON and CHN, NO_n) increase in some experiments, possibly from formation of less-volatile organic nitrogen products as discussed later. However, the presence of nitrate in the runs with no formic acid (and little change in fitting residuals over the course of all experiments) suggests that the ‘formic acid’ is not a fitting error and that correlations between formic acid and nitrate may arise from real co-increases. Note that a given fragment, such as formic acid, may come from multiple parents; this analysis explores organic composition change *qualitatively* through functional group fragments, but cannot be used to quantify product formation in such a complex mixture.

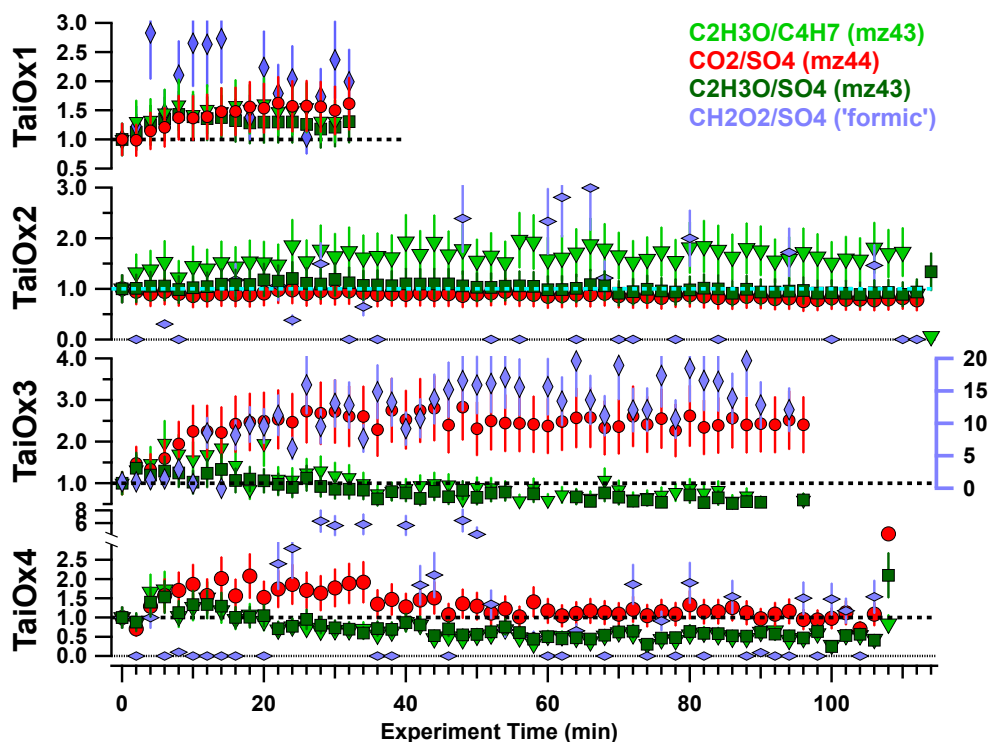


Figure 5-4: Timelines of normalized (to $t=0$ value) fragment ratios indicating level of oxidation or relative abundance of carboxylic acids (CO_2/SO_4) for TaiOx1f1, TaiOx2f1, TaiOx3f1, and TaiOx4f1. Error bars represent propagated 20% relative error for AMS mass quantitation (total propagated error = 28%).

Type 1: Carboxylic acid products maintained

Experiments may be grouped according to their $\text{CO}_2^+/\text{SO}_4$ behavior into Types 1 and 2. For TaiOx1, oxidation increases continuously as evidenced by an increase in $\text{CO}_2^+/\text{SO}_4$ and the ratio of oxidized to hydrocarbon fragments at m/z 43 (Figure 5-4). Reduction in $\text{C}_2\text{H}_3\text{O}^+/\text{SO}_4$ beginning at ~ 10 min may result from oxidation of carbonyls to carboxylic acids; contemporaneous rapid oxidation of C_xH_y species is indicated by decrease in $\text{C}_2\text{H}_3\text{O}^+/\text{SO}_4$ and *increase* in $\text{C}_2\text{H}_3\text{O}^+/\text{C}_4\text{H}_7^+$ from ~ 10 -25 minutes, indicating that C_4H_7^+ must be decreasing faster than $\text{C}_2\text{H}_3\text{O}^+$. ‘Formic acid’ fragments appear to increase for the first 10 minutes, then decrease somewhat, suggesting that formic acid and/or molecules fragmenting to ‘formic acid’ are early-generation products that persist or reach equilibrium; similar formic acid production patterns (increase, then decrease) have been observed in aqueous oxidations of glyoxal (Lee et al. 2011), but not in the other TaiOx experiments. For TaiOx1, ‘formic acid’ may contribute on average $1.15 \pm 0.52\%$ of CO_2^+ signal (Equation 15).

TaiOx3 progresses similarly to TaiOx1, including the timing and magnitude of early $\text{C}_2\text{H}_3\text{O}^+/\text{SO}_4$ increases and subsequent decrease (at ~ 10 min) as $\text{CO}_2^+/\text{SO}_4$ growth begins to slow (i.e. as reactions forming acid products reach equilibrium). ‘Formic acid’ and $\text{CO}_2^+/\text{SO}_4$ remain elevated at $\sim 300\%$ and 250% of their starting values, respectively, with formic acid contributing an average of $0.62 \pm 0.29\%$ of CO_2^+ signal. Recalling from Figure 5-2 that TaiOx3 total organics (Org/SO_4) begin to decrease at ~ 30 minutes, a picture emerges of a continuously oxidizing solution that begins with rapid oxidation of hydrocarbons and increase in carbonyls and carboxylic acids, followed by continuing oxidation of carbonyls to carboxylic acids. Constant $\text{CO}_2^+/\text{SO}_4$ accompanied by decreased total organic mass indicates increasing fractional carboxylic acid content over time in TaiOx3. Both $\text{C}_2\text{H}_3\text{O}^+/\text{SO}_4$ and $\text{C}_2\text{H}_3\text{O}^+/\text{C}_4\text{H}_7^+$ decrease to

~60% of their starting value, indicating a net loss of hydrocarbons and carbonyls, and remain constant at that value after ~30 min, indicating that most chemical change (discernable via AMS) may occur in the first half-hour or so of oxidation for TaiOx3. However, diverse oxidation and chemical change pathways are possible, and lack of experimental control in complex ambient samples precludes mechanistic determination. Lastly, the general progression to higher CO_2^+ and lower $\text{C}_2\text{H}_3\text{O}^+$ and C_4H_7^+ has been observed in myriad ambient plume-tracking experiments, lending credibility to the general progression of the aqueous photo-oxidations herein (Aiken et al. 2010; DeCarlo et al. 2010; He et al. 2010).

Type 2: Carboxylic acids lost

In contrast, $\text{CO}_2^+/\text{SO}_4$ does not change significantly in TaiOx2, and is gained, then lost in TaiOx4-1 (Figure 5-4), and TaiOx7 (Figure 5-11). The formic acid fragment shows no significant trend in TaiOx4-1; formic acid fragment mass is zero for most points, and the scattered points greater than zero may arise from the magnification of even very low masses by a near-zero $t=0$ value during normalization (masses below the AMS detection limit were not altered or eliminated); also, noise may arise from the neighboring large NO_2^+ peak, for which slight m/z calibration variations (shifting peaks) or high nitrate signal (broadening peak) may produce erroneously 'high' (still sub-detection limit for TaiOx runs, except 1 and 3) formic acid mass in the fitting algorithm. Formic acid is evident in TaiOx7, contributing on average $2.28 \pm 1.15\%$ of organic mass and $1.15 \pm 0.52\%$ of CO_2^+ signal. The indicated chemistry varies between these experiments as discussed below.

In TaiOx2, carbonyl content ($\text{C}_2\text{H}_3\text{O}^+/\text{SO}_4$) is steady or slightly decreasing (not significantly), while $\text{C}_2\text{H}_3\text{O}^+/\text{C}_4\text{H}_7^+$ increases in the first ~20 minutes (indicating decrease in C_xH_y compounds), then is constant (indicating balanced carbonyl sources and sinks in solution).

CO_2^+ is also constant, statistically, though it may decrease slightly toward the end. Coupled with the total organic loss, static oxidation indicators suggest an overall oxidation increase in TaiOx2 (as CO_2^+ and $\text{C}_2\text{H}_3\text{O}^+$ become more ‘concentrated’ with total mass loss) which will be corroborated in the elemental analysis, below; however, the oxidized fragments involved in the mass loss may be different from the other samples, as explored later in this section.

TaiOx4-1 has early formation, then pronounced loss of $\text{CO}_2^+/\text{SO}_4$ beginning at ~35 min. The first half hour looks similar to TaiOx1 and 3, with progressive carbonyl, then carboxylic acid increase, but is followed by a strong decrease in $\text{C}_2\text{H}_3\text{O}^+$ (to ~50% of t=0 value) and CO_2^+ (max ~200% at t=20 min; back to starting value by experiment’s end). TaiOx7 will be discussed with TaiOx7PA in Section 5.2.

Mass Spectra and Delta Patterns

Organic composition change may also be explored through mass spectra. Higher molecular weight compounds were detected, many of which are important in their mass bins (and without influence of a larger coincident peak), suggest highly functionalized molecules and/or oligomer formation, and are explored below; however, most of these fragments are too low in total mass to construct meaningful normalized timelines and so will be presented using important fragment series expressed through delta patterns. Some of these molecules are listed in Table 5-2 along with tentative identification from other studies in which they have been observed.

Figure 5-5 shows changes in total organic composition by subtracting the experiment beginning (t = 0) normalized 5-minute average total organic mass spectrum from the experiment’s end (usually at ~100-120 min) average spectrum; normalization such that all m/z

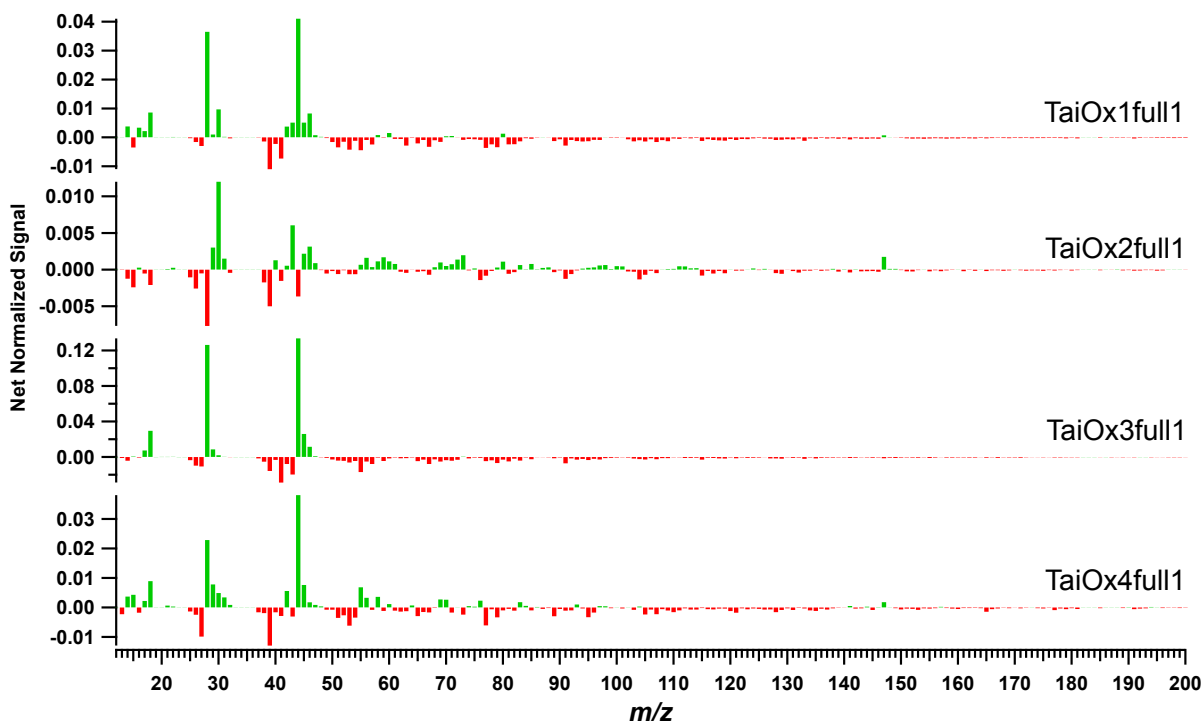


Figure 5-5: Total organic difference mass spectra calculated via subtraction of normalized experiment beginning 5-minute average organic spectrum from experiment end spectrum. Green indicates *relative* increase of the given m/z at experiment's end, while red indicates a decrease.

'sticks' sum to 1 allows comparison of mass spectra in a system for which total mass production was variable.

For TaiOx1, 3, and 4-1, relative increases in m/z 44 (mostly CO_2^+) indicate overall oxidation consistent with conclusions earlier in this section; total organics above $\sim m/z$ 50 decrease with time for these runs, consistent with progressive oxidation of organics towards highly functionalized compounds that produce CO_2^+ fragments in the AMS. This is corroborated in difference spectra for each of the organic 'families' (CH, CHO, CHON, CHN; Figure 5-6), in which CH fragments decrease and $\text{CHO} < m/z$ 50 increases, especially at m/z 44 (CO_2^+). $\text{CHO} > m/z$ 50 decrease slightly but consistently (organic 'wave' pattern can be seen with decreased y-axis range) for TaiOx3 and 4-1; there are also some increases in select fragments $> m/z$ 50 as explored later. CHO at m/z 28 (CO^+) also increases for TaiOx1, 3, and 4-1, sometimes with

commensurate decreases in CH at m/z 28 ($C_2H_4^+$) indicating oxidation of hydrocarbons to carbonyls; however, the large coincident N_2^+ peak makes quantification difficult and these species are often excluded from AMS data analyses for interference and the relative ubiquity of these fragments from a range of parent compounds (Allan et al. 2004).

TaiOx1, 3, and 4-1 show a clear shift in delta toward positive values at the end of the experiment, indicating the predominance of functionalized organics, where fragments with $\Delta \leq 0$ generally decrease and those with $\Delta > 0$ increase (Figure 5-7). Decreases are most notable at Δ_0 (alkenes, cycloalkanes), Δ_{-2} (dienes, alkynes), Δ_{-4} (terpenes, phthalates), and Δ_{-6} (phenyl alkyls, etc.); the greatest enhancements are seen in Δ_1 , which generally contains cycloalkyl/alkanones, diketones, unsaturated esters, and cyclic amines, and Δ_3 , representing aldehydes, cycloalkanols, amines, amides, and nitrites. As in the difference mass spectra, delta analysis indicates a loss of hydrocarbons and aromatics and an increase in functionalized molecules including the possibility of organic nitrogen, discussed below.

TaiOx2 progresses quite differently. First, TaiOx2 gains total organic mass above $\sim m/z$ 50, where TaiOx3 and 4-1 decrease (Figure 5-5). It also loses m/z 44 and gains m/z 43, a reduction in highly oxygenated CO_2^+ unlike most oxidation experiments both here and in the literature; however, the increase in fragments $> m/z$ 50 derives from highly oxidized (sub-family $CHO_{n>1}$, 'CHOgt1'; not shown), CHON, and CHN fragments, while hydrocarbons (CH) decrease systematically (Figure 5-6). Note that the scales in TaiOx2 CH and CHO family difference spectra are roughly half the magnitude of those for other TaiOx samples, implying relatively little change in relative fragment abundance with time. Prominent increasing fragments include m/z 71 ($C_3H_3O_2^+$), m/z 83 ($C_5H_7O^+$, some $C_4H_3O_2^+$), and, with the largest increase among fragments $> m/z$ 50, $C_6H_{11}O_4^+$ (some $C_{10}H_{11}O^+$) at m/z 147. These fragments are unidentified and

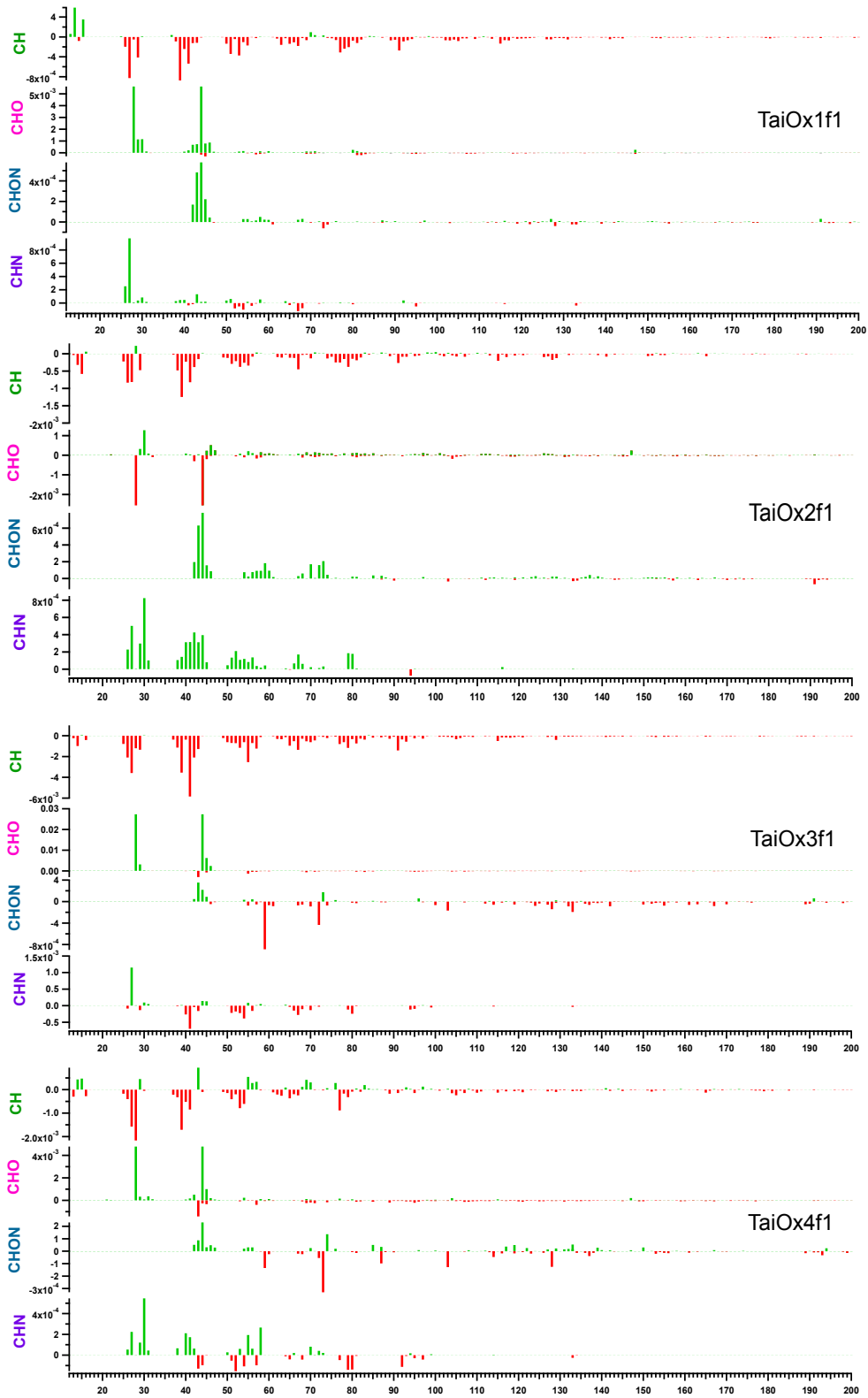


Figure 5-6: TaiOx fragment-family difference mass spectra, subtracting the normalized 5-minute average spectrum from t=0 from that at the experiment's end.

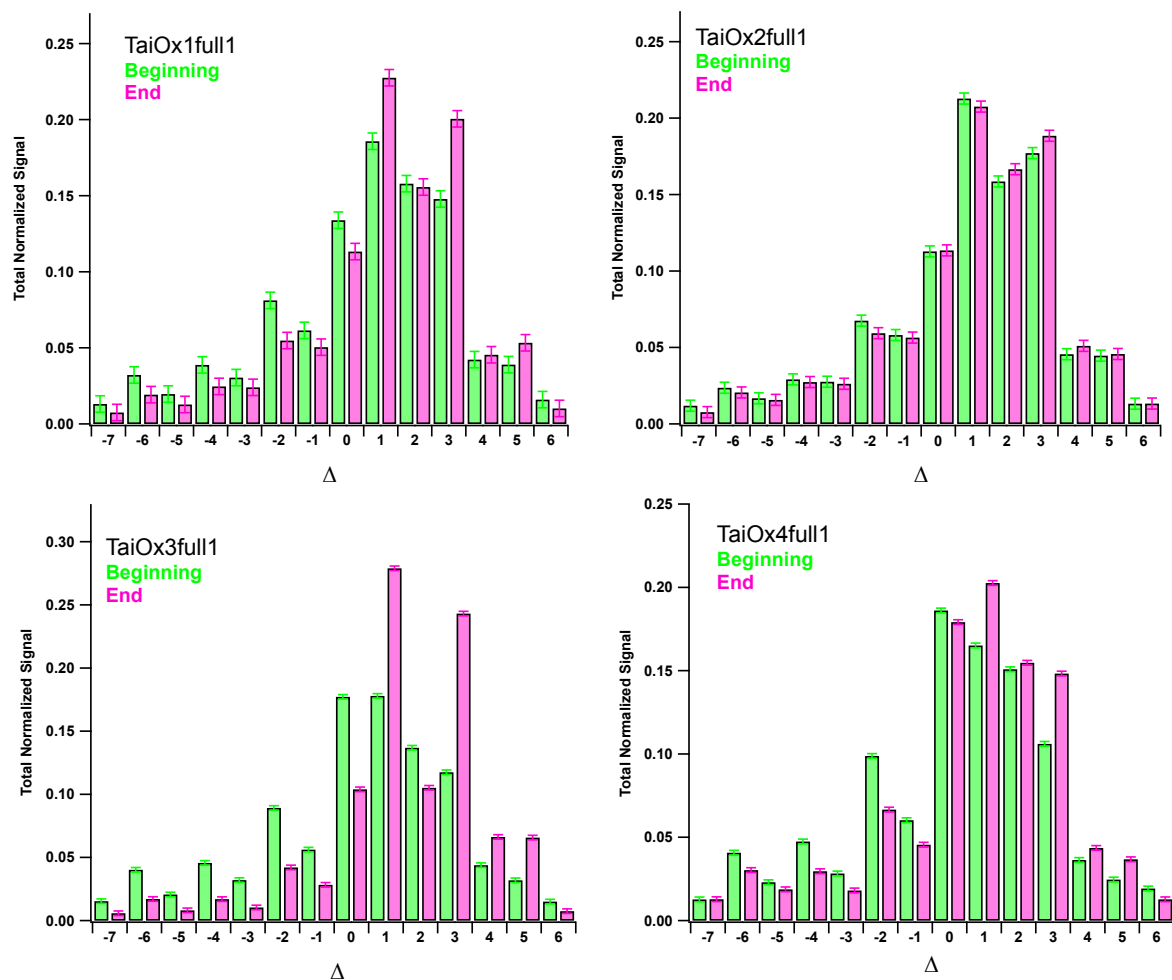


Figure 5-7: TaiOx: Total normalized signal in fragments with the given delta (Δ) value in the 5-minute average experiment beginning or end total organic mass spectrum. Error bars are the normalized average signal error over all mass bins for the given experiment.

have no clear delta pattern, but have been observed in the literature as discussed later (Bahreini et al. 2005). The progression to highly oxidized (CHOgt1) fragments $> m/z$ 50 and decreased CO_2^+ suggests higher product stability against fragmentation within the AMS. Oxidation is taking place (as inferred earlier in the section), but the products differ from other TaiOx samples (i.e. are not carboxylic acids), and the overall change in composition is minor. Delta distributions for TaiOx2 show a predominance of positive values indicating highly oxygenated (as discussed above) species, but there is no significant change between the experiment beginning and end except a slight increase in Δ_3 fragments (Figure 5-7); the TaiOx2 delta signal distribution is

much like the ‘experiment end’ delta distributions for the other TaiOx samples, implying that TaiOx2 started at a higher level of oxidation very like that produced at the end of the other experiments (which may not change significantly in composition after ~60 minutes).

Despite the variations in chemical composition and progression, all of the TaiOx samples share a series of dominant peaks in the experiment end total organic mass spectrum that are generally different from the experiment-beginning spectrum and quite similar to those published in Bahreini et al. (2005) for cyclohexene ozonolysis, with the shared m/z peak series: 44 ($C_2H_3O^+ < CO_2^+$), 55 ($C_3H_3O^+ > C_4H_7^+$), 60 ($C_2H_4O_2^+$), 73 (ours: $C_3H_9Si^+$ and some $C_3H_5O_2^+$; fragments not specified in Bahreini), 91 ($C_7H_7^+$, some $C_6H_3O^+$), 115 ($C_5H_7O_3^+$, $C_9H_7^+$), 131 ($C_9H_7O^+$), and 147 ($C_6H_{11}O_4^+$, $C_{10}H_{11}O^+$). Other peaks common to TaiOx experiments (but not the cyclohexene experiment) are found at m/z 69 ($C_4H_5O^+$, $C_5H_9^+$), 95 ($C_7H_{11}^+$), 104 ($C_7H_4O^+ > C_8H_8^+$), 133 ($C_7H_3NO_2^+ > C_8H_7NO^+ \approx C_8H_7NO^+$), and 191 ($C_{10}H_9NO_3^+$, tentatively $C_{12}HNO_2^+$). m/z 69 also appears in oxidation of biogenics (α -pinene and others, both dark and photo-oxidative) in the literature, though it may be common to a variety of unsaturated hydrocarbons, cyclic alcohols, and carbonyls (Bahreini et al. 2005; Canagaratna et al. 2007; Kiendler-Scharr et al. 2009; McLafferty & Turecek 1993). m/z s 104 and 191 were observed in dark trimethylamine-nitrate chamber reactions (Silva et al. 2008). Biogenics have been observed and amines might be expected at Mt. Tai based on the diverse combustion, agriculture, and natural sources impacting the site (Fu et al. 2010). The remaining fragments at m/z 133 are as yet unidentified and not known to have been observed in other SOA experiments or observations.

Cyclohexene was employed in the Bahreini et al. (2005) experiment as a representative cycloalkene, which are thought to be SOA precursors from industrial and fuel emissions (Odum 1997; Tkacik et al. 2012); it was added to the cycloalkane ozonolysis SOA experiment as an OH

scavenger but may also enhance SOA (Bahreini et al. 2005). The similarity between cyclohexene and TaiOx samples may arise from cyclohexene's alcohol/peroxide and carboxylic acid products (Ziemann 2002), formation of which may be indicated for TaiOx1 and 2 (and to a lesser extent 3 and 7) in the van Krevelen diagram (Figure 5-9, discussed later); high O₃ and NO_x have also been observed at Mt. Tai, which were present in the Bahreini experiments as oxidants (Fu et al. 2010). However, alcohols, carboxylic acids, etc. are fairly ubiquitous product types.

Organic Nitrogen

TaiOx1, 2, and possibly 7 gain organic nitrogen, with modest but clear progressions to higher N:C and O:C in Figure 5-8; TaiOx1 and 2 have the best correlations in this space and also the largest gains in CHON and CHN fragments (which drive N:C, Figure 5-6). TaiOx1 may form some organonitrate as evidenced by increases in CHON fragments at *m/z* 43-44 (CHNO⁺, CH₂NO⁺) and 191 (C₁₀H₉NO₃⁺, tentatively C₁₂HNO₂⁺), and have some structure to the mass spectral patterns; CHON fragments contribute slightly more to total signal at experiment's end (0.2% increase to a total of 0.4%). Though CHON fragments are fairly ubiquitous to organonitrates and thus give little additional parent molecule/chemistry information, significant nitrophenol content is indicated in previous HPLC-ESI-ToF analysis of co-located cloud samples (Desyaterik et al. 2013). CHN contributes more mass overall (0.1% increase to 0.6%) and CHN fragments - nominally amine, imidazole, etc. - increase at 27 (CHN⁺), but lack the organized mass spectral structure that might suggest formation of amines different from those in the starting solution (Figure 5-7). TaiOx3 and 4-1 gain some organic nitrogen at *m/z* 44 (CH₂NO⁺), but lose some at *m/z* 59 (C₂H₅NO⁺) and *m/z* 72-73 (C₃H₆NO⁺). However, the CHN difference series in TaiOx4-1 at *m/z*s 30, 40, (some 55) 58, 70 (72,73) is similar to the trimethylamine AMS spectra in Silva et al. (2008; *m/z* 30, 58, 72, 86, 100) and Murphy et al. (2007; trimethylamine at

m/z 58); note that while the large NO^+ peak is in the same bin as m/z 30 and tends to obscure CH_2O^+ , the CH_4N^+ amine peak is independent and therefore more readily identified. To summarize: TaiOx1 gains both organonitrate and amine mass, though amine fragments are not as important; TaiOx 3 gains smaller CHON and CHN fragments while losing larger fragments with no significant change in total ON; and 4-1 gains ‘organonitrates’ and a CHN series similar to methylamine but loses other fragments and has no significant trend in ON with time.

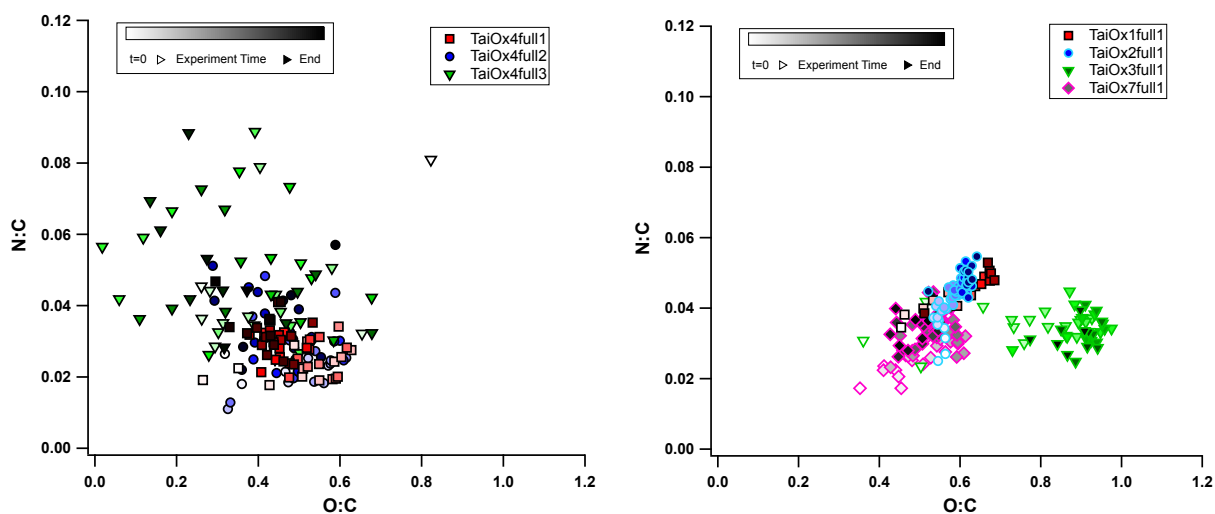


Figure 5-8: Nitrogen-to-Carbon vs Oxygen-to-Carbon ratios for ambient cloud sample aqueous photo-oxidations. Turquoise points represent baseline periods (no UV, no H_2O_2) for corresponding sample shape. Linear fits: TaiOx1: $m = 0.06$, $r^2 = 0.85$; TaiOx2: $m = 0.15$, $r^2 = 0.55$; TaiOx3: $m = 0.00$, $r^2 = 0.00$; TaiOx7: $m = 0.05$, $r^2 = 0.21$; TaiOx4-1: $m = -0.02$, $r^2 = 0.10$; TaiOx4-2: $m = -0.01$, $r^2 = 0.01$; TaiOx4-3: $m = -0.03$, $r^2 = 0.08$.

TaiOx2 appears to form some organic nitrogen, as evidenced through a positive slope in N:C/O:C space ($m = 0.15$, $r^2 = 0.55$; Figure 5-8). Organonitrate content is suggested by the organized CHON spectrum, and the dominant peaks (m/z 59 and 72) are the same that decreased in TaiOx3 and 4-1 samples; CHON increases by 0.2% of total signal to yield 0.5% of total signal at experiment’s end. TaiOx2 inorganic nitrate (NO_3/SO_4) also increases steadily (though not significantly) to $\sim 114\%$ of its $t=0$ value; nominally inorganic NO_n may fragment from organonitrates (as suggested in the Grand Teton study) which are generally lower volatility and thus might remain in the condensed phase during drying (Ng et al. 2008; Fry et al. 2009; De

Haan et al. 2011). The CHN spectrum almost doubles to ~1% of total signal in an unknown series (m/z 30, 42, 54, 67, 79) dissimilar to TaiOx4-1, the Tetons dataset, and amine reactions in the literature.

The van Krevelen Diagram

In van Krevelen space, TaiOx 1-3, though with different compositions and therefore different starting positions in the diagram, move similarly toward enhanced O:C with slopes near -0.5, which is indicative of either carboxylic addition with C-C bond breakage or addition of both acid and alcohol/peroxide functional groups without fragmentation (total 1 H loss per 2 O addition, Figure 5-9). In general, the reduction in Δ_2 , Δ_0 , and Δ_6 , which may be partially attributed to alcohols, suggests at least that alcohol production does not exceed consumption of unsaturated hydrocarbons and carbonyls (at Δ_0 , Δ_2), which may imply that carboxylic addition with C-C fragmentation is a more important reaction pathway for this dataset; fragmentation with non-functionalized fragment loss may also contribute to the organic mass loss observed. However, the AMS lacks the chemical specificity to determine reaction regimes with surety. Chamber SOA photo-oxidations producing similar slopes in van Krevelen space include α - and β -pinene, toluene, and m-xylene (Lambe et al. 2011; Chhabra et al. 2010; Massoli et al. 2010; Chhabra et al. 2011). The prevalent slope of -0.5 is consistent with ambient datasets (factorized to SV-OOA, LV-OOA, etc. in an attempt to reduce the influence of changing air masses) showing chamber oxidation of ambient OA via acid + alcohol and/or peroxide addition (Ng et al. 2011); however, few controlled oxidations of ambient air masses exist, and most of those are not in the aqueous phase, making comparison difficult. TaiOx 4-1, and possibly 7, move toward lower O:C as oxidized functional groups are lost (as explained previously).

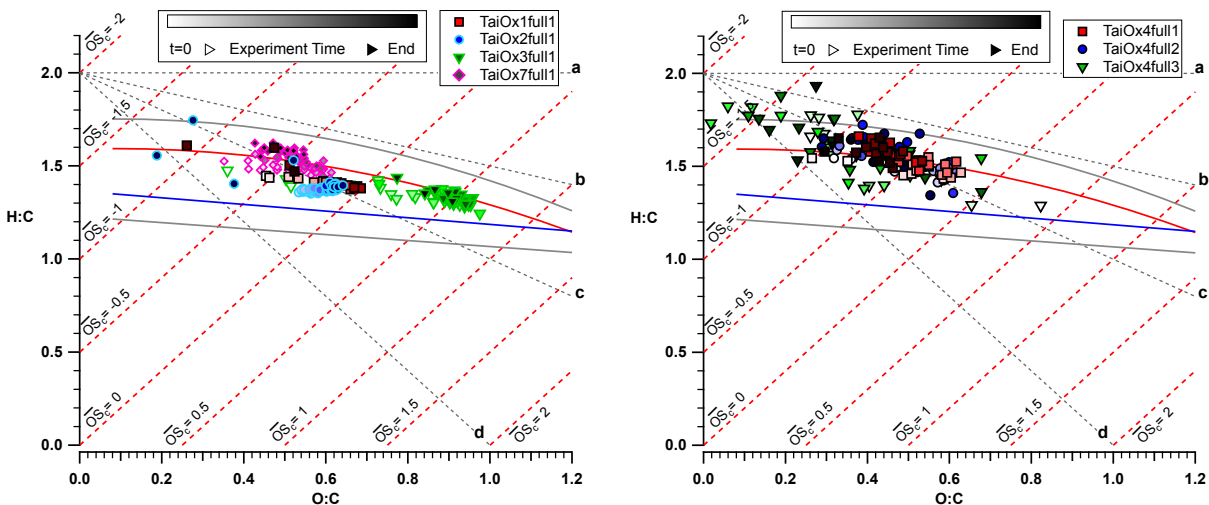


Figure 5-9: van Krevelen diagram showing (left) TaiOx1-3 full photo-oxidations and (right) TaiOx4 replicates 1-3 & TaiOx7, colored by time during experiment. Dashed red lines: Estimated oxidation state, $OSc=2 \cdot O:C-H:C$ (Kroll et al. 2011). Red and blue lines indicate the region usually inhabited by ambient data in the $f43$ vs $f44$ plot; grey lines represent 10% error. Linear fits: TaiOx1: $m = -0.52$, $r^2 = 0.87$ (w/out three ‘outlier’ points at exp. end: $m = 0.00$, $r^2 = 0.00$); TaiOx2: $m = -0.53$, $r^2 = 0.51$ (w/out four ‘outlier’ points at exp. end: $m = -0.36$, $r^2 = 0.70$); TaiOx3: $m = -0.28$, $r^2 = 0.64$; TaiOx7: $m = -0.33$, $r^2 = 0.14$. Linear fits: TaiOx 4-1: $m = -0.51$, $r^2 = 0.46$; TaiOx 4-2: $m = -0.65$, $r^2 = 0.48$; TaiOx 4-3: $m = -0.65$, $r^2 = 0.57$.

Section 5.1 Conclusions

The results above suggest two broad patterns in these photo-oxidations of ambient cloud water: in the first (Type 1, TaiOx1 & 3), organic mass is gained, then begins to decrease, and there is a sustained increase in highly oxidized fragments such as CO_2^+ as well as volatile fragments like formic acid; this indicates overall carboxylic acid formation and that volatile product evaporation may contribute to mass decrease. In the second type (Type 2, TaiOx4-1 & 7), oxidized fragments may also decrease as mass decreases, indicating that oxidized functional groups may be chemically fragmented and lost. On average, Type 1 samples had higher starting TOC and hydrogen peroxide than Type 2 samples which could influence product type as outlined in Section 1.2.3 and is discussed further in Section 5.5; however, the difference was not significant, and samples with equivalent TOC concentrations were found between the types.

5.2 Ambient Cloud-water Photo-oxidations with added Pinonic Acid Precursor

Since there are relatively few TaiOxPA experiments, each will be summarized in its entirety (timelines, spectra, elemental ratios, etc.), with comparisons between TaiOxPA and unaltered TaiOx experiments in the concluding paragraphs. To begin, Figure 5-10 shows Org/SO₄ and *f*₄₄ for ambient-cloud experiments with added pinonic acid and an unaltered TaiOx7 ‘control’ photo-oxidation. Normalized (to t = 0) fragment ratios CO₂⁺/SO₄ (modified *f*₄₄), C₂H₃O⁺/SO₄ (modified *f*₄₃), C₂H₃O⁺/C₄H₇⁺, and CH₂O₂⁺/SO₄ (‘formic acid’) are shown for added-pinonic acid experiments in Figure 5-11.

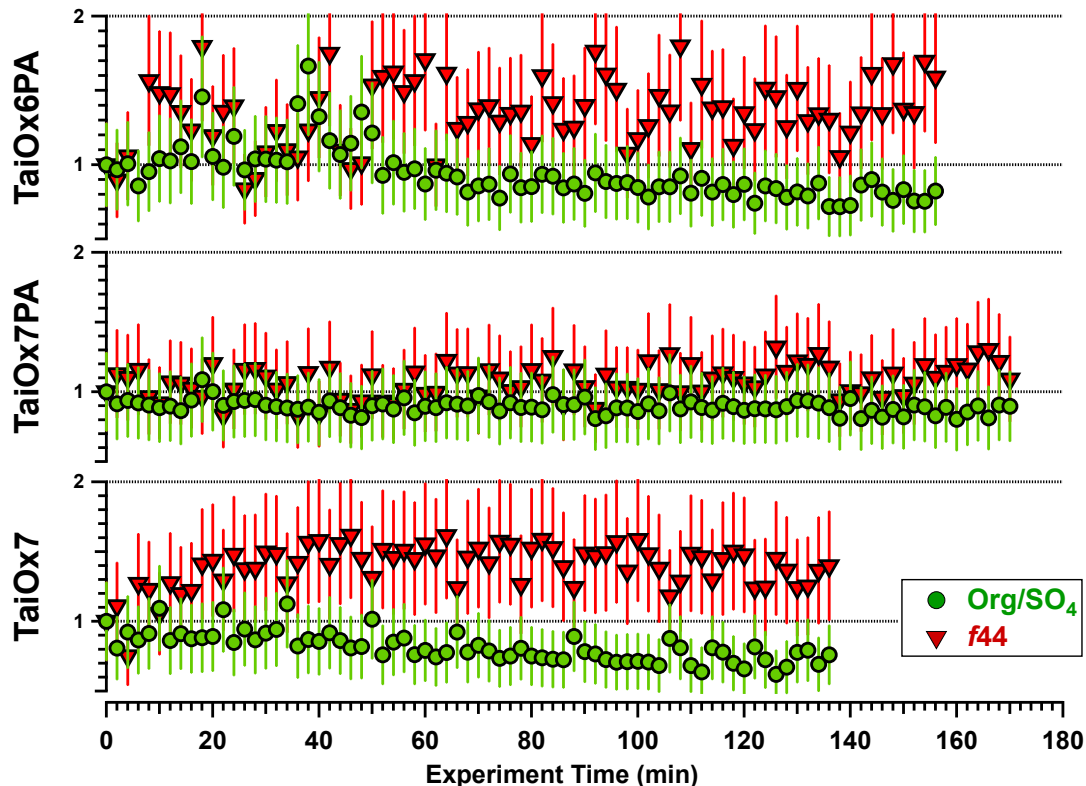


Figure 5-10: TaiOxPA: Timelines of Org/SO₄ (red) and *f*₄₄ (green) for TaiOx6PA, 7, and 7PA aqueous photo-oxidations. Error bars are not included for simplicity but equal ~28% as propagated through the indicated calculations.

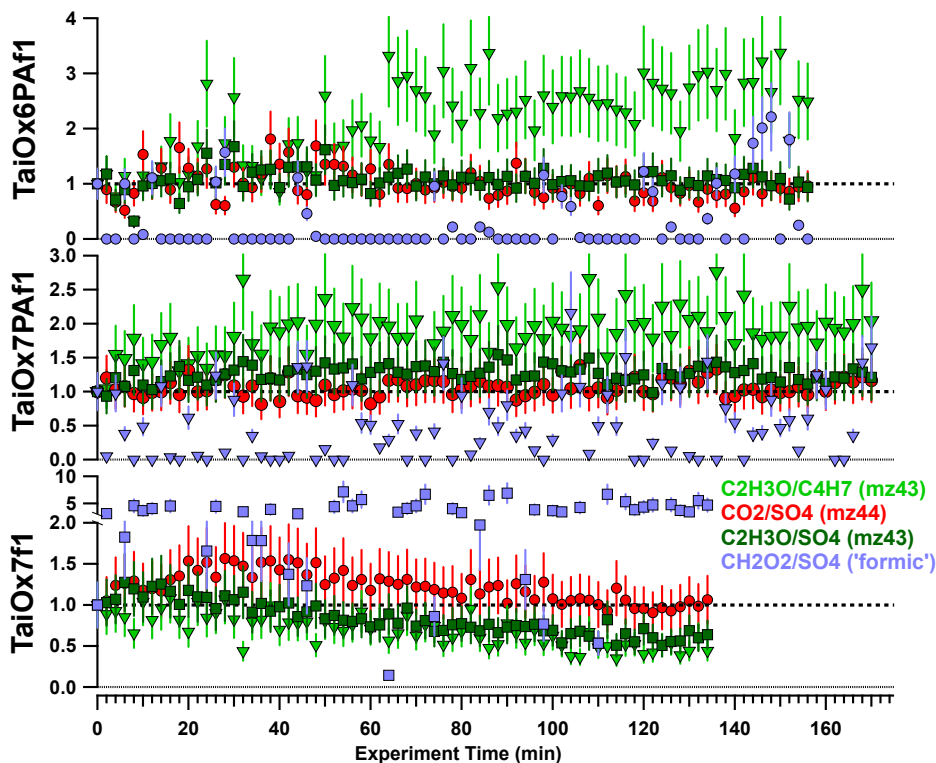


Figure 5-11: TaiOxPA: Timelines of normalized (to t=0 value) fragment ratios indicating level of oxidation including relative abundance of carboxylic acids ($\text{CO}_2^+/\text{SO}_4$) for TaiOx6PAf1, TaiOx7PAf1, and TaiOx7f1. Error bars represent propagated 20% relative error for AMS mass quantitation (total propagated error = 28%).

TaiOx6PA

TaiOx6PA is fairly noisy for most ratios until $t \sim 60$ minutes. Though mass spikes were not observed, atomizer output was somewhat variable during the first 60 minutes of this experiment (**Figure 8-12**, Appendix Section 8.6); although changes in sulfate, organics, and other constituents were synchronous and might therefore be useful with sulfate normalization, the scatter in organic ratios (Figure 5-11) before ~ 60 minutes is unlike the other photo-oxidations, casting doubt in the validity of these results. Recorded t=0 values are used for normalization with the knowledge that ratio changes relative to t=0 may be erroneous. Org/ SO_4 may be slightly reduced toward the end of the oxidation, although this depends on the validity of t=0 data, while f_{44} , $\text{CO}_2^+/\text{SO}_4$, $\text{C}_2\text{H}_3\text{O}^+/\text{SO}_4$ are statistically unchanging. Elevated $\text{C}_2\text{H}_3\text{O}^+/\text{C}_4\text{H}_7^+$ and constant $\text{C}_2\text{H}_3\text{O}^+/\text{SO}_4$ indicate loss of hydrocarbons and resemble TaiOx2 and 7PA; reduced

total mass accompanied by steady ratios of oxygenated compound to sulfate indicates overall oxidation as described earlier.

In the f_{43} vs. f_{44} triangle, all TaiOxPA samples inhabit the ‘LV-OOA’ range, indicating that the solutions were fairly oxidized even before photo-oxidation (Figure 5-12). TaiOx6PA is noisy but moves in general to higher f_{43} with seemingly less change in f_{44} , which may indicate that hydrocarbon-to-carbonyl oxidation is more important than oxidation to carboxylic acids. This assertion is somewhat corroborated in total organic difference spectra (Figure 5-13), in which the overall increase in m/z 43 is similar to that of m/z 44; an increase in CHO and decrease in CH at m/z 43 in the family difference spectra (Figure 5-14) suggests oxidation of hydrocarbons to carbonyls. However, the total organic m/z 44 increase (Figure 5-13) implies that carboxylic acids increase as well, which was not observed in the $\text{CO}_2^+/\text{SO}_4$ ratio (unless Org/SO_4 actually *is* decreasing or $t = 0$ data is flawed) or the CHO-family difference spectrum, where there is no enhancement at m/z 44; the presence of increased m/z 44 in the overall difference spectrum has yet to be explained.

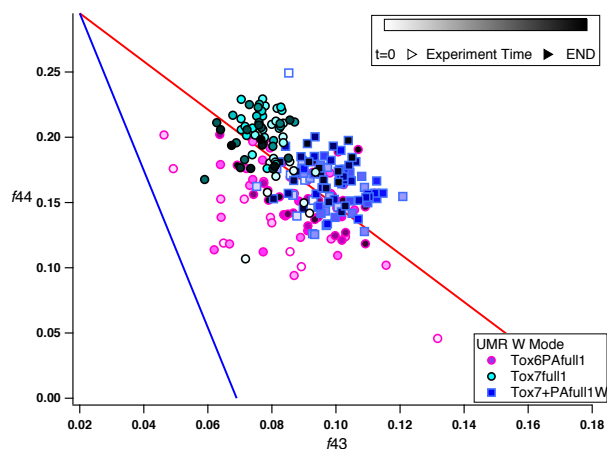


Figure 5-12: TaiOxPA: f_{43} ($mz43/\text{Org}$) vs. f_{44} ($mz44/\text{Org}$) for TaiOx6PA, 7, and 7PA; the blue- and red-bounded triangle represents the range of values typically inhabited by ambient aerosols (Ng et al. 2011).

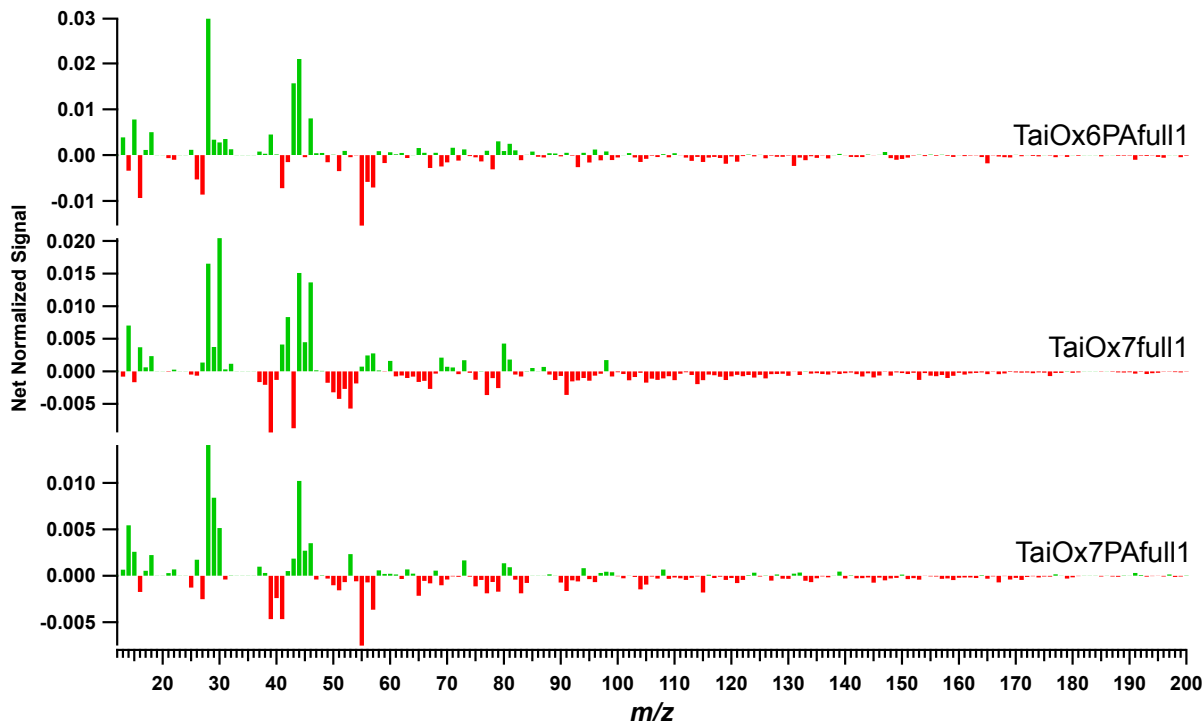


Figure 5-13: TaiOxPA: Normalized total organic difference mass spectra calculated via subtraction of experiment beginning 5-minute average organic spectrum from experiment end spectrum. Green indicates *relative* increase of the given m/z at experiment's end, while red indicates a decrease.

CHO at m/z 46 also increases; in averaged raw signal from the final five minutes of TaiOx6PA (not shown), this appears to be formic acid. Since formic acid is otherwise unimportant (Figure 5-11), this may be fitting error (although as before, the half-max, half-width rule is maintained); also note that this scale is $\sim 2.5X$ smaller than other CHO difference spectrum scales, so the mass changes in CHO are small overall. The TaiOx6PA hydrocarbon CH family is decreased at all masses.

TaiOx6PA CHON and CHN fragments are predominantly decreased, most notably in $C_3H_6NO^+$ (m/z 72) and $C_4H_5NO_4^+$ (m/z 131), both of which have large neighboring peaks and may be subject to interference. Although there are modest increases in $CHNO^+$ (m/z 43) and CH_3NO^+ (m/z 45), neither loss nor gain are particularly organized, nor do the CHON average (not difference) spectra show evidence of significant organonitrates (i.e. there are no 'organic

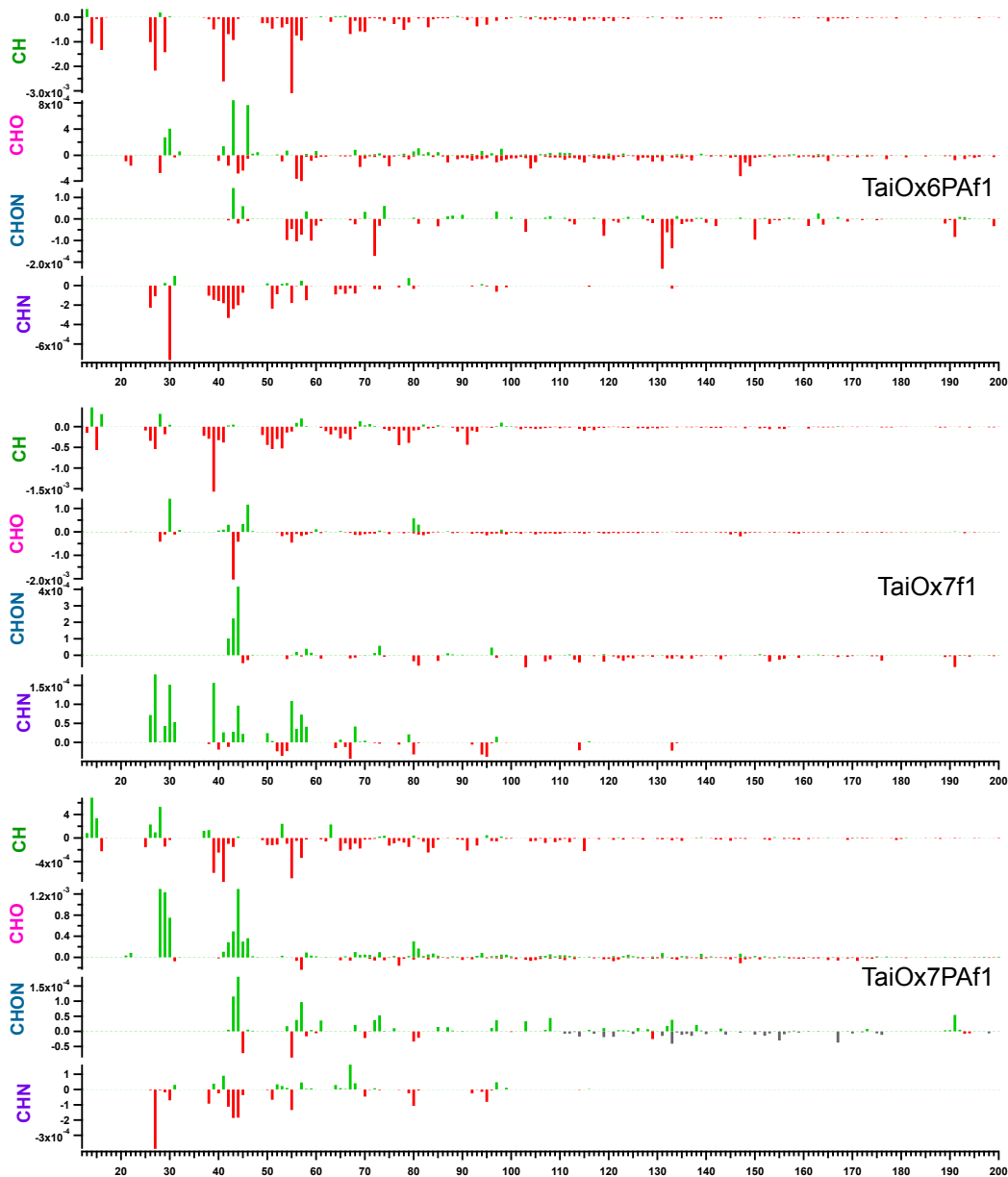


Figure 5-14: TaiOxPA: TaiOx6PA, 7, and 7PA normalized fragment-family difference mass spectra calculated via subtraction of experiment beginning 5-minute average spectrum from experiment end spectrum.

wave' patterns, Appendix Section 8.7); overall ON mass is low at ~3x DI 'background' concentrations for both CHN and CHON fragments, contributing 0.7% and 0.4% of total mass, respectively.

There is no discernable change in N:C (Figure 5-16). CHN average mass spectra (Appendix Section 8.7) has a series at m/z 30, 42, 44, 58, 68, and 79 which resembles the

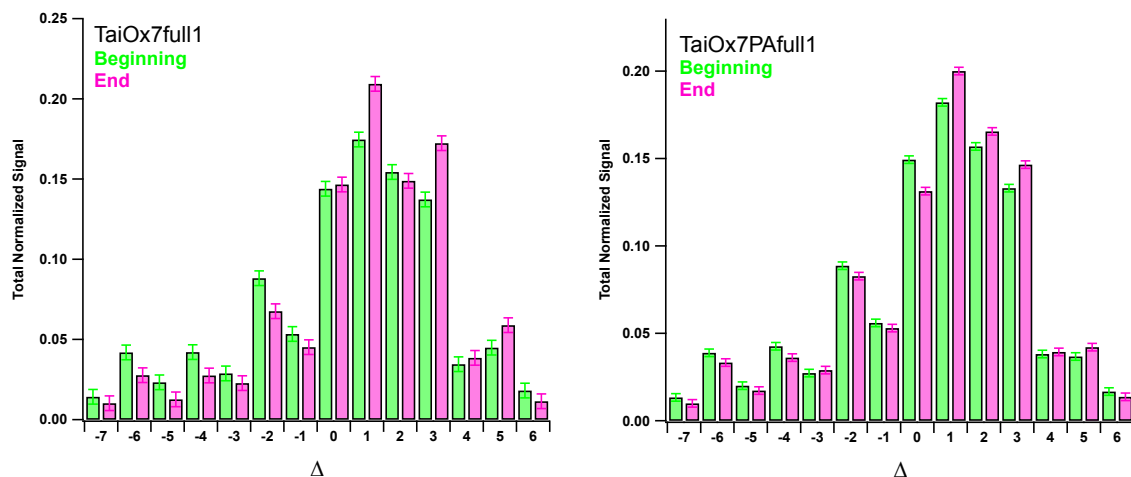


Figure 5-15: TaiOxPA: Total normalized signal in fragments with the given delta (Δ) value in the 5-minute average experiment beginning or end total organic mass spectrum.

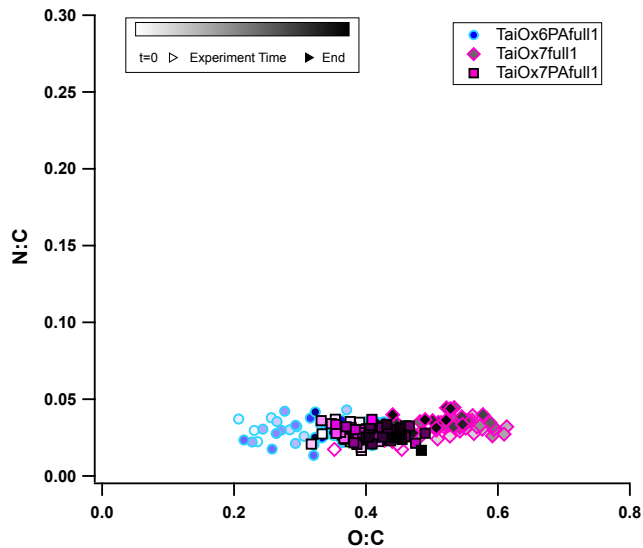


Figure 5-16: Nitrogen-to-Carbon vs. Oxygen-to-Carbon ratios for aqueous photo-oxidation of ambient cloud samples with and without added pinonic acid. Turquoise points represent baseline periods (no UV, no H_2O_2) for corresponding sample shape. Linear fits: TaiOx6+PA: $m = -0.001$, $r^2 = 0.00$; TaiOx7: $m = 0.05$, $r^2 = 0.21$; TaiOx7+PA: $m = -0.02$, $r^2 = 0.02$.

‘amine’ patterns outlined in the previous section in the incidence of m/z s 30 and 58; CHN peaks at m/z s 42, 44, 68, and 79 are not regularly observed. The CHN difference mass spectrum indicates that some of this nominally ‘amine’ content is lost at experiment’s end. In van Krevelen space, TaiOx6PA progresses to lower H:C and higher O:C along a slope of -0.65, similar to the

unaltered TaiOx samples ($r^2 = 0.52$, Figure 5-17); O:C is somewhat lower than in the unaltered TaiOx samples (Figure 5-9).

TaiOx7 and TaiOx7PA

TaiOx7 and 7PA differ in their oxidative progression. Like the unaltered TaiOx samples (esp. TaiOx4-1), TaiOx7 initially gains (0-35 min) and subsequently loses total organic mass; initial increase in all fragment ratios (except formic acid) indicates carbonyl and carboxylic acid formation, with carboxylic acids increasing relatively more. Loss of m/z 43 and increase in m/z 44 in the TaiOx7 total organic difference mass spectrum supports advanced oxidation through acid formation (Figure 5-13); the loss in m/z 43 is evident in the CHO family difference spectrum (Figure 5-14), but the increase in m/z 44 is not explained by CO_2^+ (which decreases very slightly here; van Krevelen O:C may decrease as well), CHON, or CHN (reminiscent of TaiOx6PA, though total organic and family difference spectra converge well for the rest of the unaltered TaiOx experiments). Family mass spectra reveal decreases in hydrocarbons (CH, Figure 5-14).

Both organonitrates (CHON) and amines (CHN) are organized in the TaiOx7 average family mass spectra (Appendix Section 8.7); however, organic nitrogen enhancement is minor at $\sim 0.1\%$ of total organic mass (using change in normalized CHON and CHN sticks); constant ON is also indicated by limited vertical movement in N:C/O:C (Figure 5-16, in comparison to TaiOx1 and 2, for example). In the van Krevelen diagram, TaiOx7 has a slope similar to the other unaltered TaiOx samples ($m = -0.32$, $r^2 = 0.14$; Figure 5-17), but the marker color, indicating oxidation time, seems to indicate a slight but not significant shift to higher H:C and lower O:C similar to TaiOx4-1 (and confirming TaiOx7 as a Type 2 experiment).

In contrast, TaiOx7PA has fairly constant Org/SO_4 , unlike any other TaiOx sample except possibly TaiOx6PA (Figure 5-10). f_{44} , $\text{CO}_2^+/\text{SO}_4$, and $\text{C}_2\text{H}_3\text{O}^+/\text{SO}_4$ do not vary

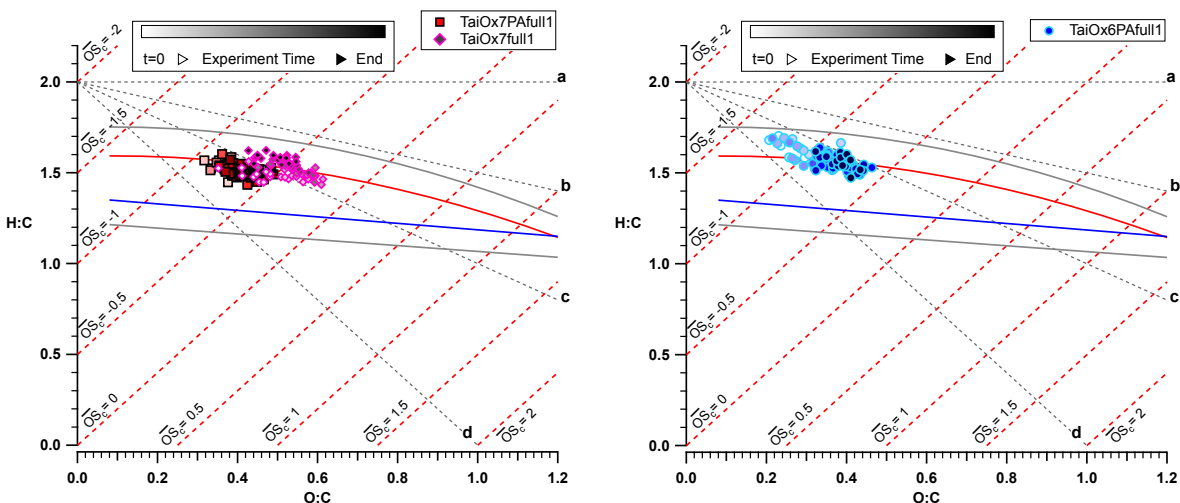


Figure 5-17: Van Krevelen diagram showing (left) TaiOx6PA, and (right) TaiOx7PA and TaiOx7 full photo-oxidations, colored by time during experiment. Linear fits: TaiOx6PA: $m = -0.65$, $r^2 = 0.52$; TaiOx7: $m = -0.32$, $r^2 = 0.14$; TaiOx7PA: $m = -0.45$, $r^2 = 0.26$.

significantly, though $C_2H_3O^+/C_4H_7^+$ increases and levels off similar to TaiOx2, implying oxidation of hydrocarbons (Figure 5-11). This is corroborated in the total organic difference spectrum (Figure 5-13), where fragments $>m/z$ 50, and especially m/z 55 (a marker of less-oxidized material dominated by hydrocarbons), are lost and m/z 44 is gained. Family difference spectra reveal mass spectral loss $>m/z$ 50 to be from hydrocarbons (CH), with addition of organized waves of $>m/z$ 50 CHO fragments. As to organic nitrogen, TaiOx7PA shares a similar organized ‘amine’ series with TaiOx7 (as would be expected), but does not change significantly over the course of the experiment (at -0.1% of total normalized signal); organonitrates (CHON) also do not change significantly.

Delta analysis for TaiOx7 looks fairly similar to other unaltered samples, with decreases in signal in negative-delta fragments and increases in Δ_1 and Δ_3 indicating a shift from unsaturated aromatics and hydrocarbons to aldehydes, cycloalkanes, diketones, and oxygenated cyclic compounds, etc. However, in keeping with the limited composition change noted in the fragment ratios, changes in delta are muted in TaiOx7PA. Notable differences from TaiOx7 (and other unaltered samples) include significant reduction in Δ_0 (alkenes, cycloalkanes) and increase

in Δ_2 (alkyls, saturated carbonyls), for which carbonyl increase would be consistent with the family difference mass spectra.

TaiOx7PA resides in a region similar to TaiOx7 in the van Krevelen diagram (Figure 5-17), though it appears to move to higher O:C with time. TaiOx7PA's somewhat lower starting O:C implies that the 'average' organic molecule in unaltered TaiOx7 is even more functionalized than pinonic acid, which contains both a carboxylic acid and a carbonyl group. The correlation coefficient for TaiOx7PA in H:C/O:C space is poor, so although it is consistent with our other experiments, we treat the calculated linear regression ($m = -0.45$) with caution.

Although we lack an unaltered TaiOx6 oxidation and the first half of TaiOx6PA is of questionable value, TaiOx6PA and TaiOx7PA may resemble each other in static $\text{CO}_2^+/\text{SO}_4$, elevated but constant $\text{C}_2\text{H}_3\text{O}^+/\text{C}_4\text{H}_7^+$, and lack of overall organic mass loss; they differ slightly in progression of $\text{C}_2\text{H}_3\text{O}^+/\text{SO}_4$, which is elevated for 7PA (indicating greater increase in carbonyls than in carboxylic acids) but may not change from the $t = 0$ value in 6PA. As shown in the following sections, single-precursor pinonic acid oxidations also formed predominantly carbonyl products.

The TaiOxPA samples differ from unaltered TaiOx in a number of ways. First, despite similar beginning levels of oxidation (as expressed through f_{44}), TaiOxPA Org/ SO_4 is unchanging whereas TaiOx experiments lose Org/ SO_4 as the oxidation proceeds; this suggests lower volatility and/or higher stability of products in the pinonic acid-containing experiments. Chamber pinonic acid-OH oxidation has been observed to form highly functionalized, low-volatility molecules such as 3-methyl-1,2,3-butanetricarboxylic acid (Müller et al. 2012); similar, unpublished pinonic acid aqueous photo-oxidations in our laboratory have also produced highly functionalized though unidentified products such as $\text{C}_{10}\text{H}_{14}\text{O}_5^+$ (in agreement with observations

in Muller et al. 2012), which were identified via ESI-ToF-MS (Ali Boris, personal communication, 15 June, 2013). Though we are unable to identify the molecules responsible due to high fragmentation in the AMS, addition of pinonic acid appears to foster enhanced carbonyl formation in TaiOx7PA and to change the type and volatility of products, forming more stable CHO > m/z 50 molecules that do not fragment to CO₂⁺ and suppressing the ‘formic acid’ signal seen in unaltered TaiOx7.

Studies of aqueous pinonic acid (and parent α -pinene) are few and aqueous chemistry may differ considerably from that observed in ‘dry’ chamber experiments; however our observations of dominant carbonyl formation compare favorably to one aqueous α -pinene oxidation showing campholenic aldehyde as a major product (Bleier & Elrod 2013). Products formed in α -pinene chamber SOA experiments vary, with some showing dominant carboxylic acid formation and little change in f_{43} (George & Abbatt 2010), while others show carbonyl formation in the form of acetone, formaldehyde, formic acid, etc. (Nozière et al. 1999); much of this variation may be due to varying equivalent OH exposures, with higher exposures leading to enhanced carboxylic acid formation, in general. Since our precursor, pinonic acid, is a fairly early-generation α -pinene product and our equivalent OH exposure is approximately 1-to-1 with ambient exposure (Section 2.3), our samples experience only a few hours of ageing compared to the days-to-weeks exposures in many chamber experiments that observe oxidation to carboxylic acids (which may be less relevant to cloud lifetimes, as well).

Lastly, chamber studies of, for example, α -pinene ozonolysis found that the functional groups formed are temperature dependent, with lower temperatures (-5.15 to -2.15 C) favoring di-carbonyl and carbonyl-acid functionalization versus high-temperature (20.85 to 23.85 C) formation of carboxylic acids (Jang 1999); the recirculating water sheath around the photo-

reactor should stabilize aqueous solution temperature at ~20 C, but it is unknown whether slight variations in laboratory (and therefore coolant) temperature affected photoreaction products, or whether the temperature dependence in aqueous reactions resembles that found in ‘dry’ chamber experiments.

Meant to simulate the addition of biogenic precursors to oxidized aerosol in clouds, such as orographic cloud formation over a forest downwind of an urban site, our data imply that biogenic addition may suppress or delay the oxidative loss of organics observed in aqueous photo-oxidation of the unaltered cloud samples. Caveats to these conclusions include the small experiment number and lack of control in total organic carbon; PA addition increases TOC, and organic carbon concentration has been related to increased oligomerization and functionalized molecules, which may cause the enhanced CHO $>m/z$ 50 fragments and mass retention observed here. In the real atmosphere, the enhancement of TOC via addition of biogenics is probably relevant; however, we cannot determine whether the observed changes in composition were due to overall TOC enhancement or to chemistry specific to pinonic acid.

5.3 Single-Precursor Photo-oxidations: Methylglyoxal

Change in Total Organics and Degree of Oxidation

All of the methylglyoxal reactions had various degrees of noise from mass spikes as discussed above, though MGfull1* was the least affected. Figure 5-18 shows the progression of total organics and f_{44} . All experiments gain both sulfate-normalized (MGIN) or $t = 0$ normalized (MG) total organic mass and f_{44} with time, with equivalent values and progressions of f_{44} between MG and MGIN experiments. For MGfull2* and MGINfull1*, Org/SO₄ increases for the first ~80 minutes and then stays constant, in contrast to the initial increase and subsequent decrease observed in most TaiOx samples. Organic mass does not change significantly in

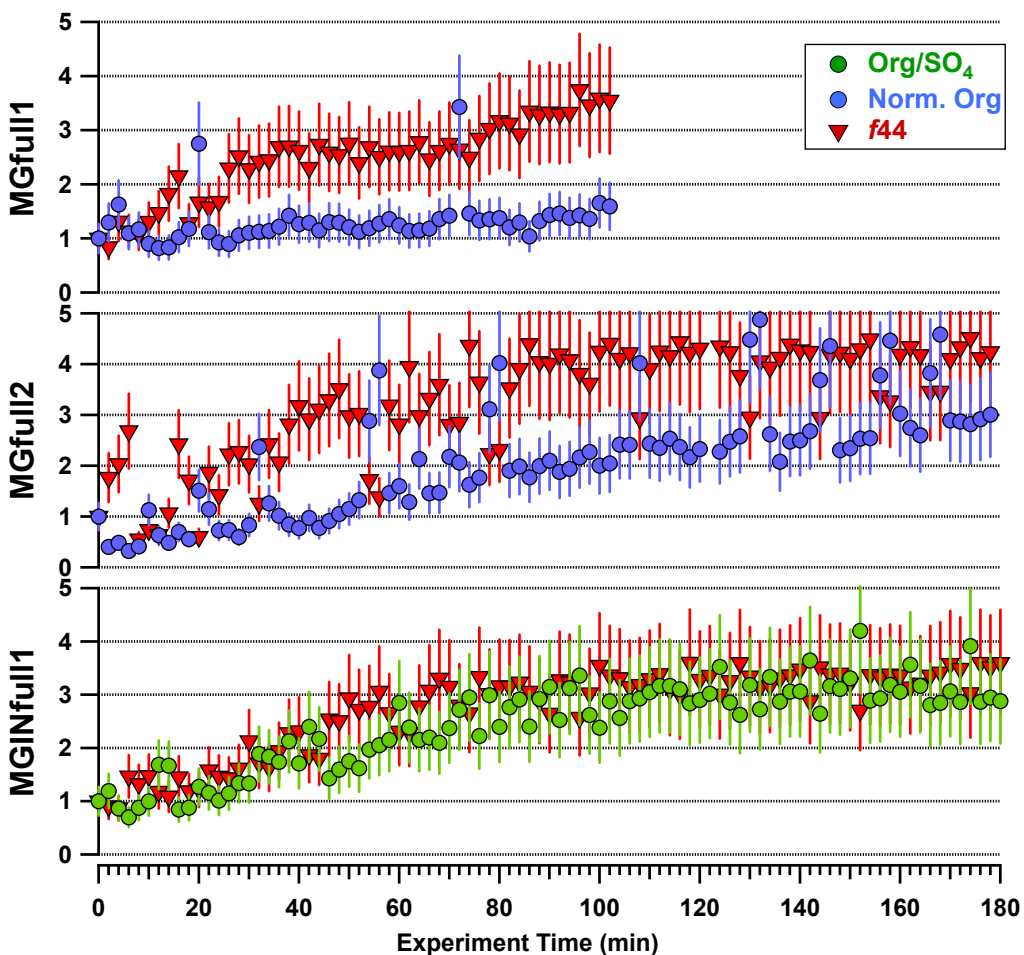


Figure 5-18: MG/MGIN: Timelines of normalized Org/SO₄ (MGIN) or total organics (MG) and *f*₄₄ for methylglyoxal (MG) and methylglyoxal + inorganics (MGIN) aqueous photo-oxidations.

MGfull1*, though *f*₄₄ increases, albeit more slowly than in the other MG/MGIN experiments. In MGfull2* and MGINfull1*, *f*₄₄ ceases to increase after ~60 minutes, in contrast to unaltered TaiOx1, 3, 4-1, and 7, for which *f*₄₄ stabilized at ~20-30 minutes; the relatively high starting carboxylic acid content of TaiOx samples may reduce the oxidation time needed to reach a carboxylic acid ‘steady state.’

In the *f*₄₃ vs. *f*₄₄ diagram, the methylglyoxal experiments move similarly to each other, with generally good correlation, toward lower *f*₄₃ (indicating carbonyl reduction) and higher *f*₄₄ (indicating acid formation; Figure 5-19). MG/MGIN samples are enriched in *m/z* 43 (and *m/z* 44, at experiment’s end) compared to bulk ambient aerosol (i.e. reside to the right of the ‘ambient’

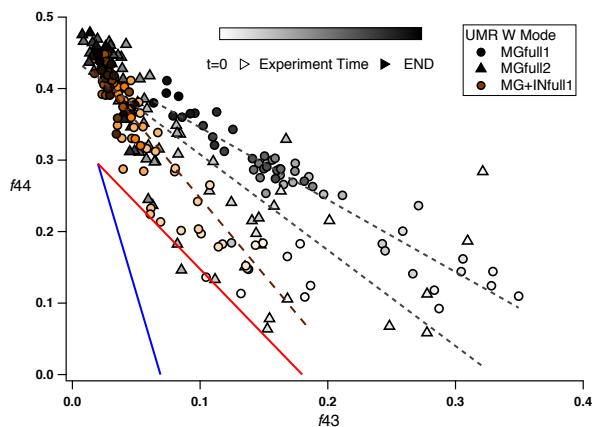


Figure 5-19: MG/MGIN: f_{43} (mz_{43}/Org) vs. f_{44} (mz_{44}/Org); the blue- and red-bounded triangle represents the range of values typically inhabited by ambient aerosols (Ng et al. 2011). Linear fits: MGfull1: $m = -1.01$, $r^2 = 0.87$; MGfull2: $m = -1.34$, $r^2 = 0.65$; MGINfull1: $m = -2.14$, $r^2 = 0.85$.

triangle); MGIN, which may better represent real aerosol containing inorganics, is closer to the ambient triangle. It is thought that methylglyoxal and its aqueous products (pyruvate, oxalate, etc.) may contribute significantly to the observed level of ambient aerosol oxidation not captured by gaseous photochemistry, which often produces lower f_{44} and/or f_{43} than ambient aerosols (i.e. data reside to the left of the ambient triangle, Ng et al. 2010; Tan et al. 2010; Lim et al. 2013; Chhabra et al. 2011).

Changes in Organic Composition

Progression of fragment ratios (CO_2^+/SO_4 , $C_2H_3O^+/SO_4$, etc.; Figure 5-20) for MGfull1* and MGfull2* are fairly similar in magnitude despite atomizer output variability, although total organic mass production is lower in MGfull1*. CO_2^+/SO_4 increases steadily as $C_2H_3O^+/SO_4$ and $C_2H_3O^+/C_4H_7^+$ decrease, indicating immediate oxidation of dicarbonyl methylglyoxal (which should produce $C_2H_3O^+$ fragments) to carboxylic acid compounds, consistent with the movement seen in f_{43} vs. f_{44} above; all ratios cease to change at ~80 minutes in MGfull2*, though MGfull1* seems to progress slightly faster ($C_2H_3O^+/SO_4$ falls below 1 earlier, etc.) and is too short to discern a pattern beyond ~90 minutes (Figure 5-20). ‘Formic acid’ fragments also

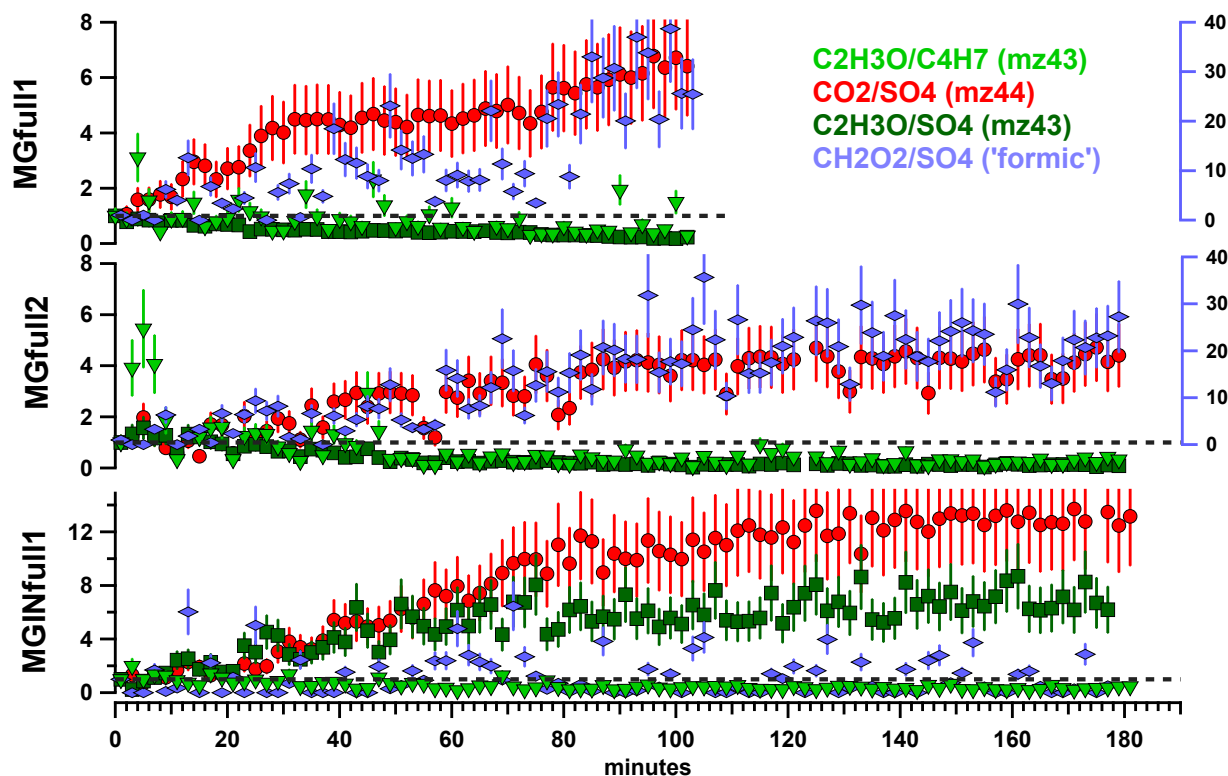


Figure 5-20: MG/MGIN: Timelines of normalized (to $t=0$ value) fragment ratios indicating relative abundance of carbonyl compounds (C_2H_3O/SO_4), carboxylic acids (CO_2/SO_4), $C_2H_3O^+/C_4H_7^+$ (ratio of most to least oxidized fragment at m/z 43), and $CH_2O_2^+/SO_4$ (nominally formic acid) for methylglyoxal experiments with inorganics (MGIN); ratios are calculated with total organics in the denominator for experiments without inorganics (MG). Formic acid is measured on the blue right-hand axes for MGfull1 and 2.

increase greatly (violet axes, Figure 5-20), consistent with studies that have found significant formic acid formation from aqueous methylglyoxal oxidation (Tan et al. 2010; Lee et al. 2011); however, the magnitude of the CO_2^+ fragment and relatively low formic acid mass ($\sim 0.5\text{-}1\%$ of total organic mass on average) are such that formic acid fragments comprise an average of only $0.56 \pm 0.39\%$ of total CO_2^+ signal (across all MG and MGIN experiments).

The progression of carbonyls to carboxylic acids is also evident in the total difference mass spectrum, where all MG and MGIN samples shows a large increase in m/z 44 and decrease in m/z 43 and fragments $> m/z$ 50 (Figure 5-21). Family difference spectra indicate loss at m/z 43 from the CHO family (Figure 5-22), confirming that methylglyoxal precursor (fragmenting to $C_2H_3O^+$) is being consumed in the photo-oxidation reactions; however, this consumption is not

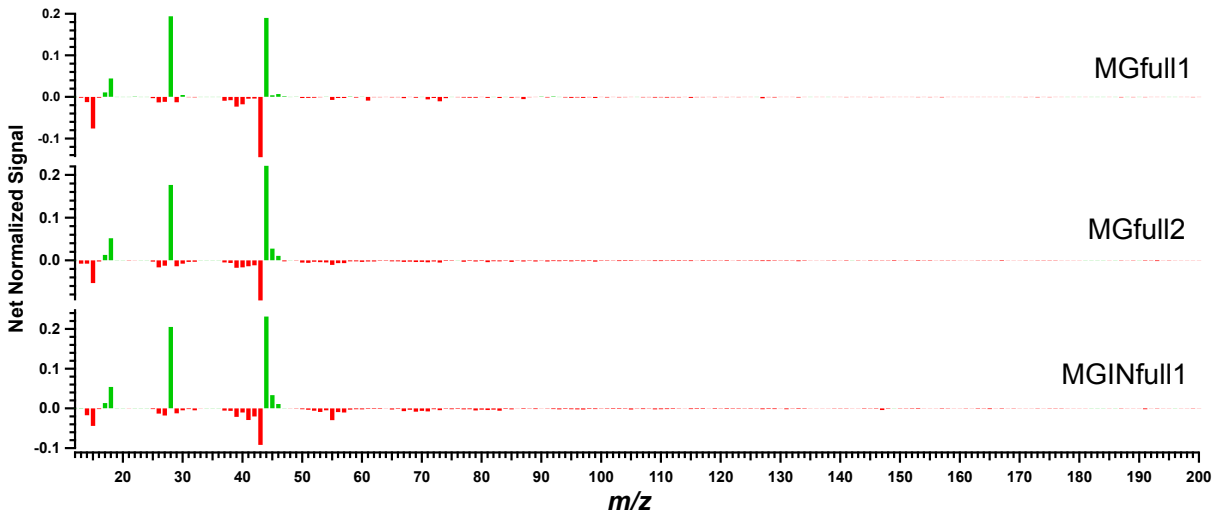


Figure 5-21: MG/MGIN: Normalized total organic difference mass spectra calculated via subtraction of experiment beginning 5-minute average organic spectrum from experiment end spectrum. Green indicates relative increase of the given m/z at experiment's end, while red indicates a decrease.

directly translatable to an SOA yield because of the possibility of carbonyl product formation in successive reaction generations (e.g. pyruvate). In both MGfull1* and 2*, reductions in CH fragment signal were noted at all m/z s, with a small but organized loss of CHN in MGfull2*; the MG experiments had reduced-nitrogen contamination comprising 9.6% of total normalized signal at $t=0$, which may arise from dissolution of ammonia from laboratory air into solution as discussed at the beginning of this section (for comparison, MGIN NH_x is 43% of total normalized signal at $t=0$). However, CHON (indicating organonitrates), NO_n (1.8% of signal), and SO_n (0.1% of signal) were very small (subscript 'n' notation used to avoid confusion with NO_x and SO_x ; refers to combined inorganic fragments for nitrate and sulfate, respectively).

In the experiment with added inorganics (MGINfull1*), production of CO_2^+ is almost doubled relative to MG (although normalization is different); unlike the MG experiments, $\text{C}_2\text{H}_3\text{O}^+/\text{SO}_4$ increases as well, reaching ~700% of its initial value by experiment's end. $\text{C}_2\text{H}_3\text{O}^+/\text{C}_4\text{H}_7^+$ decreases similarly to MGfull1 and 2. The $\text{C}_2\text{H}_3\text{O}^+/\text{SO}_4$ augmentation suggests that different, carbonyl-forming reactions are important in methylglyoxal photo-oxidations

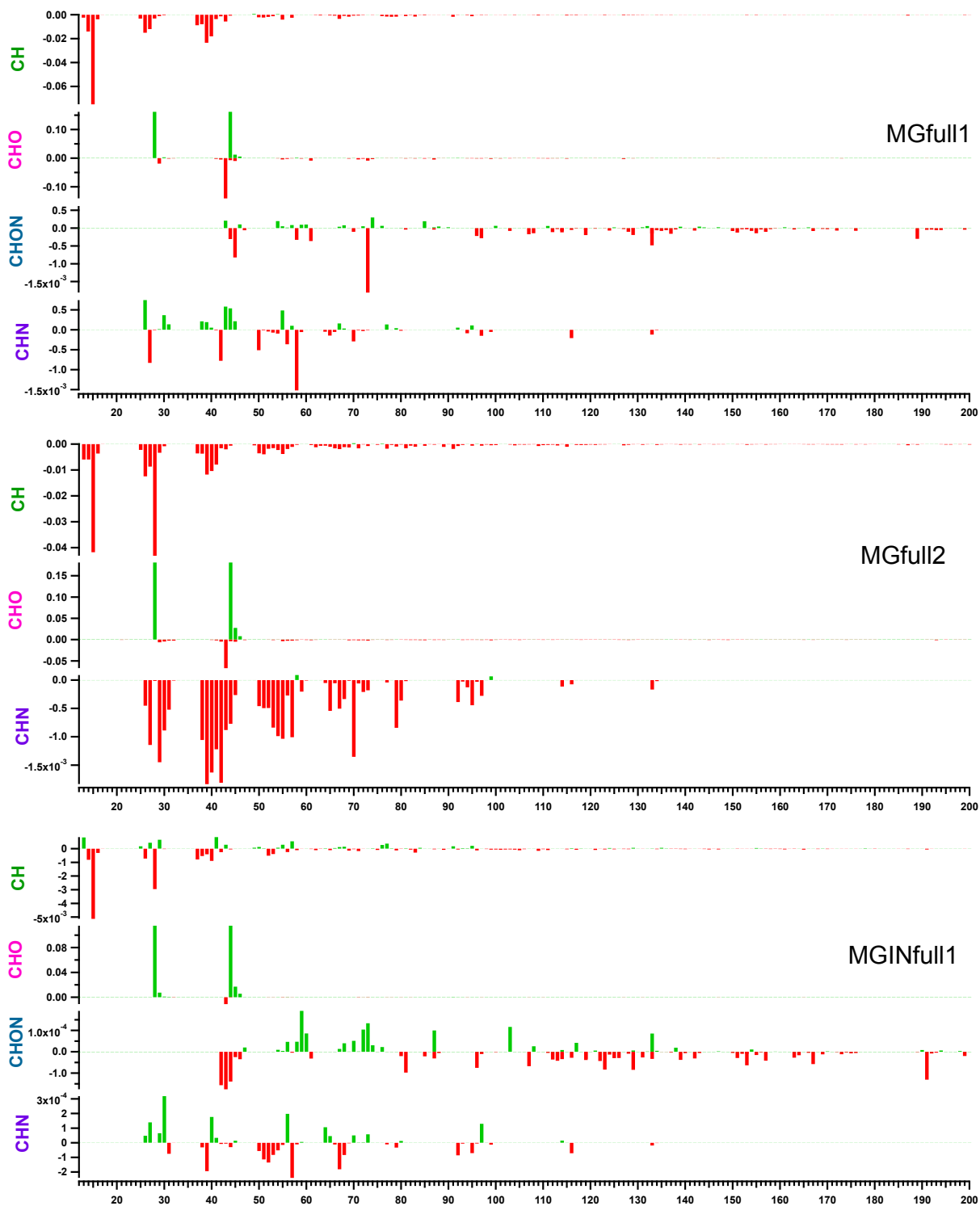


Figure 5-22: MG/MGIN: Normalized fragment-family difference mass spectra calculated via subtraction of experiment beginning 5-minute average spectrum from experiment end spectrum. Green indicates relative increase of the given m/z at experiment's end, while red indicates a decrease. The CHON family was omitted in MGfull2 (top panel) because it contained negligible mass.

containing inorganics. The reduction in $C_2H_3O^+/C_4H_7^+$ is surprising, since $C_2H_3O^+$ is increasing overall and a decreased ratio might imply even greater augmentation of $C_4H_7^+$; however, the family difference spectra do indicate a small relative increase in $C_4H_7^+$ (~7% of t=0 normalized signal). Also note the reduction in scale between MG and MGIN CH family difference spectra and decrease in *relative* $C_2H_3O^+$ (~-72% of t=0 normalized signal; Figure 5-22). This suggests that while overall mass of carbonyl and other content is increasing, carbonyls become a smaller fraction of mass during time, consistent with other experiments where carboxylic acids are a major 'end product' fragment in the AMS. Formic acid production is not observed in MGINfull1*.

Elemental and Delta Analysis

In the van Krevelen diagram (Figure 5-23), all of the MG and MGIN samples progress toward higher O:C and lower H:C along slopes near -0.5, as observed in the TaiOx samples and other studies of ambient and chamber SOA; correlation coefficients (r^2) are ≥ 0.93 . Again, this slope may indicate either carboxylic addition with C-C bond breakage or addition of both acid and alcohol/peroxide functional groups without fragmentation. According to mechanistic studies of aqueous methylglyoxal oxidation, both pathways may be important (Altieri et al. 2008; Lim et al. 2013). All of the MG/MGIN runs inhabit the 'ambient' triangle space as transposed from f_{44} vs. f_{43} space in Ng et al. (2011), moving toward the apex of the triangle as observed in the TaiOx experiments but at an accelerated rate (i.e. the change in O:C is much greater over the same experiment duration).

Delta analysis for MG and MGIN is similar to the unaltered samples, with decreases in signal in negative delta fragments and increase in Δ_1 and Δ_3 indicating a shift from unsaturated aromatics and hydrocarbons to aldehydes, cycloalkanes, diketones, and oxygenated cyclic

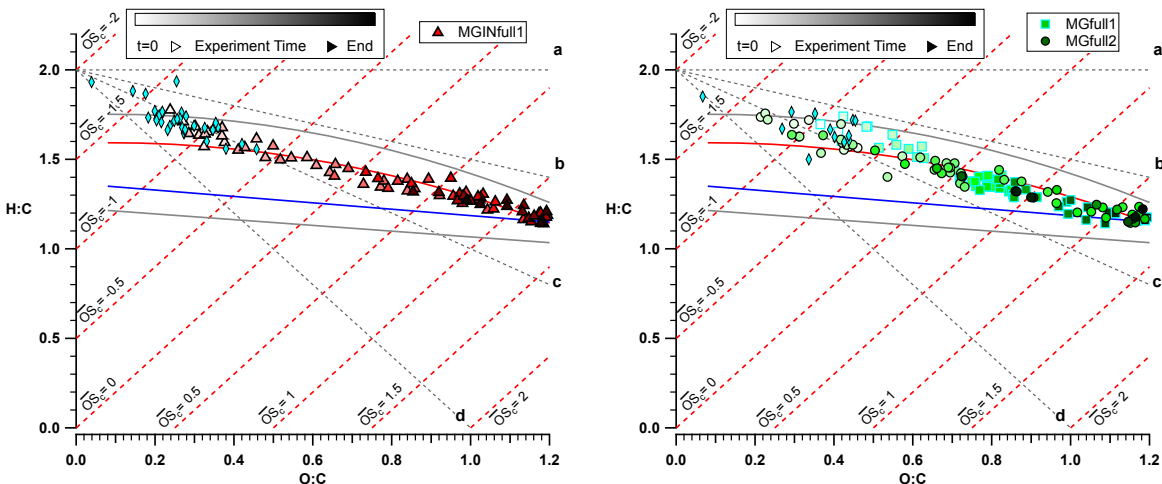


Figure 5-23: MG/MGIN: Van Krevelen diagram showing methylglyoxal + inorganics (MGIN, left panel) and methylglyoxal (MG, in replicate, right panel) photo-oxidations colored by time during experiment. Linear fits: MG1: $m = -0.72$, $r^2 = 0.93$; MG2: $m = -0.56$, $r^2 = 0.97$; MGIN: $m = -0.55$, $r^2 = 0.97$. Turquoise diamonds represent 'baseline' runs (no UV, no H_2O_2).

compounds, etc. Significant reduction in Δ_0 (alkenes, cycloalkanes) and Δ_2 (alkyls, saturated carbonyls) reflects the dominant carboxylic acid formation noted earlier (Figure 5-24). In keeping with the reduced complexity of the MG/MGIN solutions, high signal is observed in fewer delta bins, as opposed to the broader signal distribution in the complex TaiOx samples.

Organic Nitrogen

Organic nitrogen does not appear to form significantly in MGINfull1* as visualized in N:C/O:C space (Figure 5-25), although a change in CHON molecules may be indicated through loss of smaller fragments around m/z 43 (though loss of high-signal adjacent $C_2H_3O^+$ may contribute to 'CHON' loss) and increases at m/z 59 ($CH_3N_2O^+ \gg C_2H_5NO^+$), 73 ($C_3H_7NO^+$), 87 ($C_3H_7N_2O^+$, $C_3H_5NO_2^+$), 103 ($C_4H_9NO_2^+$, $C_2HNO_4^+$), 117 ($C_3H_3NO_4^+$), and 133 ($C_7H_3NO_2^+$), where the $-N_2O$ compounds could be oxygenated imidazoles and the $-NO_n$ compounds are organonitrates (Figure 5-22). Note that there are three apparent, though short, fragment 'delta series' separated by CH_2 : 1) $-N_2O$ at m/z 59 and 87 separated by $(CH_2)_2$; 2) $-NO$ at m/z 59 and 73; 3) $-NO_2$ at m/z 87 and 103; and 4) $-NO_4$ at m/z 103 and 117.

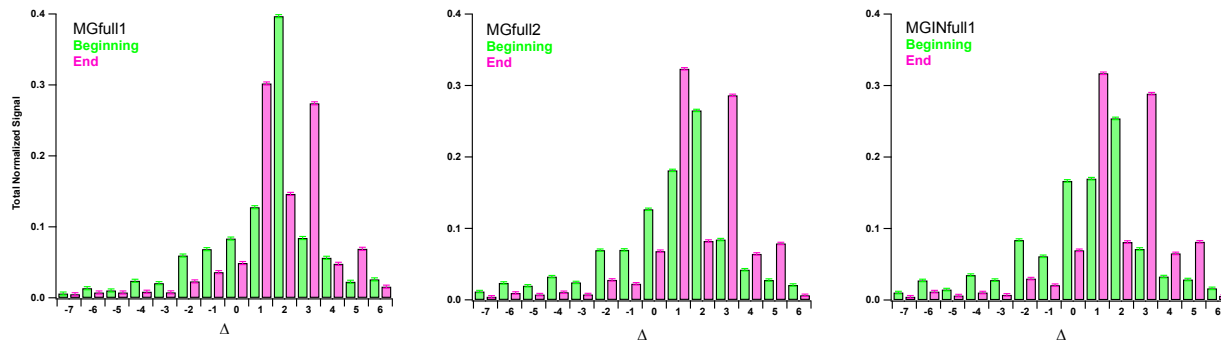


Figure 5-24: MG/MGIN: Total normalized signal in fragments with the given delta (Δ) value in the 5-minute average experiment beginning or end total organic mass spectrum.

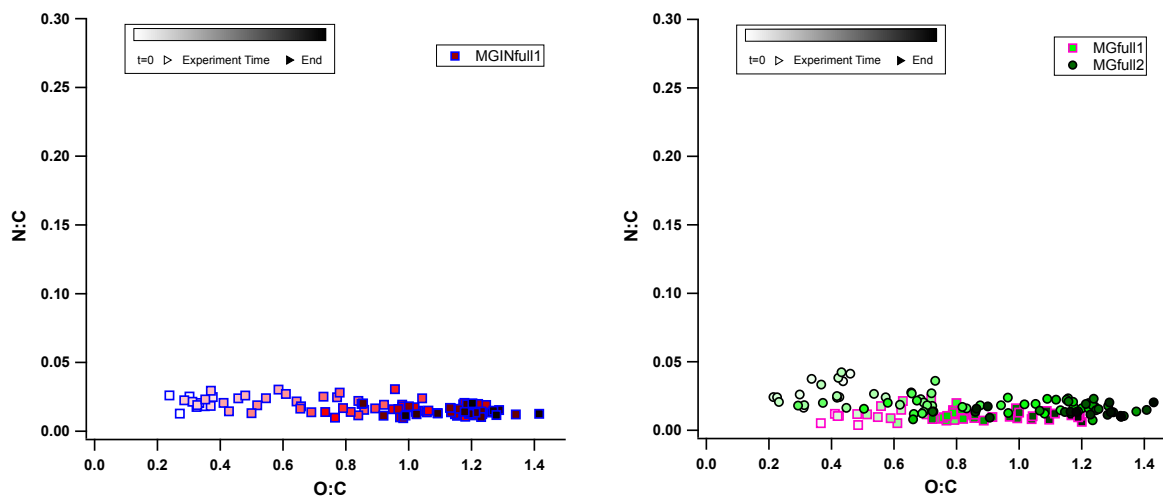


Figure 5-25: MG/MGIN: Nitrogen-to-Carbon vs. Oxygen-to-Carbon ratios for (left) methylglyoxal + inorganics and (right) methylglyoxal-only aqueous photo-oxidation. Linear fits: MGIN: $m = -0.01$, $r^2 = 0.26$; MG1: $m = 0.00$, $r^2 = 0.00$; MG1: $m = -0.01$, $r^2 = 0.28$.

Conclusions

All MG and MGIN experiments gain Org/SO_4 and $\text{CO}_2^+/\text{SO}_4$ continuously while the proportion of $\text{C}_2\text{H}_3\text{O}^+/\text{SO}_4$ (nominally, carbonyls) is decreased, suggesting overall oxidation of carbonyls to carboxylic acids, though MGIN forms carboxylic acids faster and in more quantity than MG without inorganics. MGfull1* and MGINfull1* reach ~2-300% of their $t = 0$ normalized organics, while MGfull2* increases to ~150%, indicating only fair replicability (of MGfull1*) using this methodology (Figure 5-18). In f_{43} vs. f_{44} space, all experiments move similarly to observed ambient aerosol (to higher f_{44} and lower f_{43}), while lower f_{43} (~carbonyl)

values in MGIN make the slope and placement of the progression more similar to ambient aerosol. 'Formic acid' fragment formation was significant in MG, but not observed in MGIN experiments. Changes in organic nitrogen were minor in all MG/MGIN samples. In van Krevelen analysis, slopes of ~ -0.5 are consistent with our ambient cloud samples (TaiOx) and some literature data as cited earlier.

5.4 Single-Precursor Photo-oxidations: Pinonic Acid

Change in Total Organics and Degree of Oxidation

PAfull1* and PAINfull1* were both affected by mass spikes. Like the methylglyoxal experiments, normalized Org/SO₄ (PAIN samples) or t = 0 normalized total organics (PA samples) increase and then remain elevated for all pinonic acid photo-oxidations (Figure 5-26); PAfull2, PAINfull1*, and PAINfull2 reach 250-300% of the t=0 value, while PAfull1* gains approximately 1000% of the t=0 value. *f*₄₄ is statistically constant for all runs except PAfull1*, in which it decreases to $\sim 30\%$ of the t=0 value. Altogether, these suggest significant production of non-acid species, as explored below. In the *f*₄₃ vs. *f*₄₄ triangle diagram there is significant spread and no clear trend with experiment time for all pinonic acid experiments (Appendix Section 8.5, **Figure 8-10**); most data points lie to the right of the triangle, with *f*₄₄ similar to ambient observations but higher *f*₄₃ as corroborated in the fragment ratios below and observed in α -pinene chamber photo-oxidations (Lambe et al. 2011).

Changes in Organic Composition

In the fragment ratios (Figure 5-27), PA and PAIN increase similarly in C₂H₃O⁺/SO₄ (except for PAfull1* which is significantly lower though still increasing to $\sim 200\%$ of its t=0 value) indicating carbonyl formation; C₂H₃O⁺/C₄H₇⁺ increases to varying degrees in each

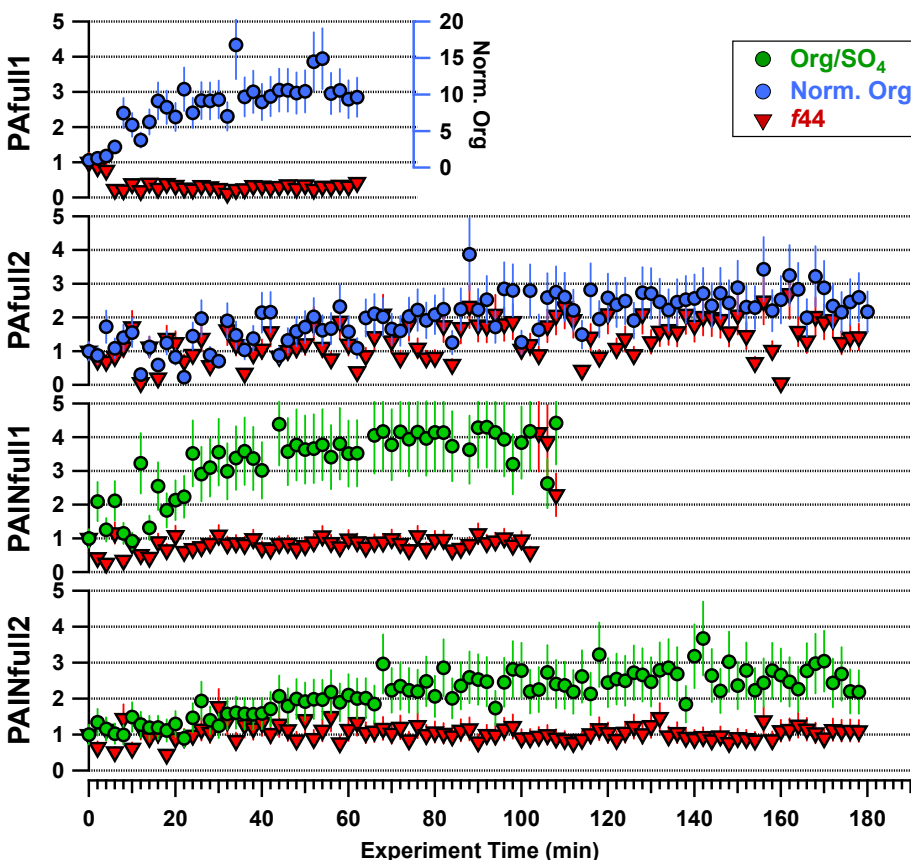


Figure 5-26: PA/PAIN: Timelines of normalized Org/SO_4 (for PAIN) or total organics (for PA), and f_{44} for pinonic acid and pinonic acid + inorganics aqueous photo-oxidations. PA organics are normalized to their $t = 0$ value. Error bars are 28% error from propagated 20% AMS quantification error on each measured quantity (SO_4 , Org, etc.).

experiment, which may arise from a combination of carbonyl formation and hydrocarbon consumption. For the PA runs, $\text{CO}_2^+/\text{SO}_4$ is constant at approximately the $t=0$ value (PAfull2) or decreasing to ~40-50% of the $t=0$ value (PAfull1*), indicating predominant carbonyl formation; in the PAIN runs, the 200-300% increase in $\text{CO}_2^+/\text{SO}_4$ suggests carboxylic acid formation, as well as the carbonyl production indicated earlier. Formic acid is not evident in any PA or PAIN experiments.

This carbonyl production differs from the TaiOx samples (except TaiOx2) and the methylglyoxal experiments, in which carboxylic acid production is higher; however, limited carboxylic acid production was also noted in the TaiOxPA experiments, and aqueous formation

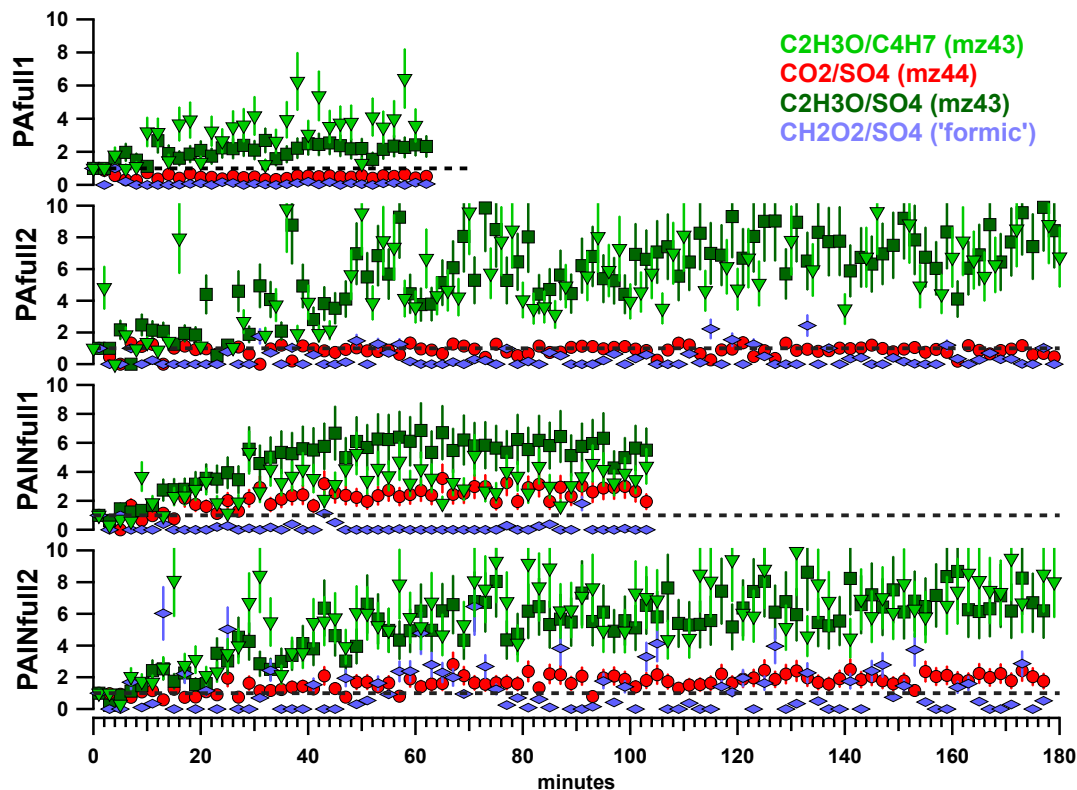


Figure 5-27: PA/PAIN: Timelines of normalized (to $t=0$ value) fragment ratios indicating relative abundance of carbonyl compounds (C_2H_3O/SO_4), carboxylic acids (CO_2/SO_4), $C_2H_3O^+/C_4H_7^+$ (ratio of most to least oxidized fragment at m/z 43), and $CH_2O_2^+/SO_4$ (nominally formic acid) for pinonic acid aqueous photo-oxidations with inorganics (PAIN); ratios are calculated with total organics in the denominator for experiments without inorganics (PA).

of carbonyls such as campholenic aldehyde from α -pinene has been observed (Bleier & Elrod 2013). Altogether, the oxidation products of pinonic acid and TaiOxPA samples are inconsistent with the unaltered samples, suggesting that pinonic acid, a relatively early-generation α -pinene oxidation product, may not be (or no longer be, having already reacted) important in our Mt. Tai samples, which were already quite oxidized initially. This difference in aqSOA composition may be influenced by increasing total organic carbon (regardless of organic composition), as added PA constitutes 65% and 57% increases in TOC for TaiOx6PA and TaiOx7PA, respectively. As noted in Section 1.2.3, increasing precursor concentration often results in higher mass production and degree of oxidation (through ionic strength kinetic enhancement or additional radical pathways, as the bulk phase precludes gaseous-precursor solubility effects); the unchanging

degree of oxidation in –PA experiments suggests that the content of the added precursor is also influencing products formed, obviously, but the lack of mechanistic control precludes deconvolution of the contribution of increasing [TOC] to aqSOA formation.

Mass Spectra and Delta Analysis

In the total difference spectra (Figure 5-28), both m/z 43 and m/z 44 increase for all experiments. m/z 44 increases more than m/z 43 in PAIN and PAfull1* experiments; for PAIN runs, m/z 44 is also greater than m/z 43 in the experiment-end total organic spectrum (not shown), indicating formation of ‘LV-OOA’-type particles and supporting the carboxyl formation indicated by increasing $\text{CO}_2^+/\text{SO}_4$. However, m/z 43 > m/z 44 in the experiment-end total organic spectrum for both PA experiments, consistent with the carbonyl formation and lack of carboxylic acid production as suggested by the fragment ratios; due to mass spikes in PAfull1*, we use PAfull2 henceforth to examine the PA progression. In all experiments, increases in m/z 43 and m/z 44 are seen in the CHO family difference spectra, with a reduction in CH at m/z 43 (C_4H_7^+) suggesting oxidation of some hydrocarbons (Figure 5-29); however, in total, the CH family increased slightly for all experiments (except PAfull1*), though the CHO normalized signal increases were roughly three times higher. Hydrocarbons increases may arise from greater retention of CH chains after functionalization. The notable reduction at m/z 41 in the total difference spectra for PAIN experiments is not explained in the family difference spectra.

In histograms of total signal at each delta, PAfull2 and PAINfull2 (neither with mass spikes) look similar to TaiOx samples, with decreases at Δ_0 (alkenes, cycloalkanes) and increases at Δ_1 and Δ_3 (Figure 5-30); these increases – and depletions in negative-delta fragments - are much higher in magnitude than in the TaiOx samples, indicating greater functional group

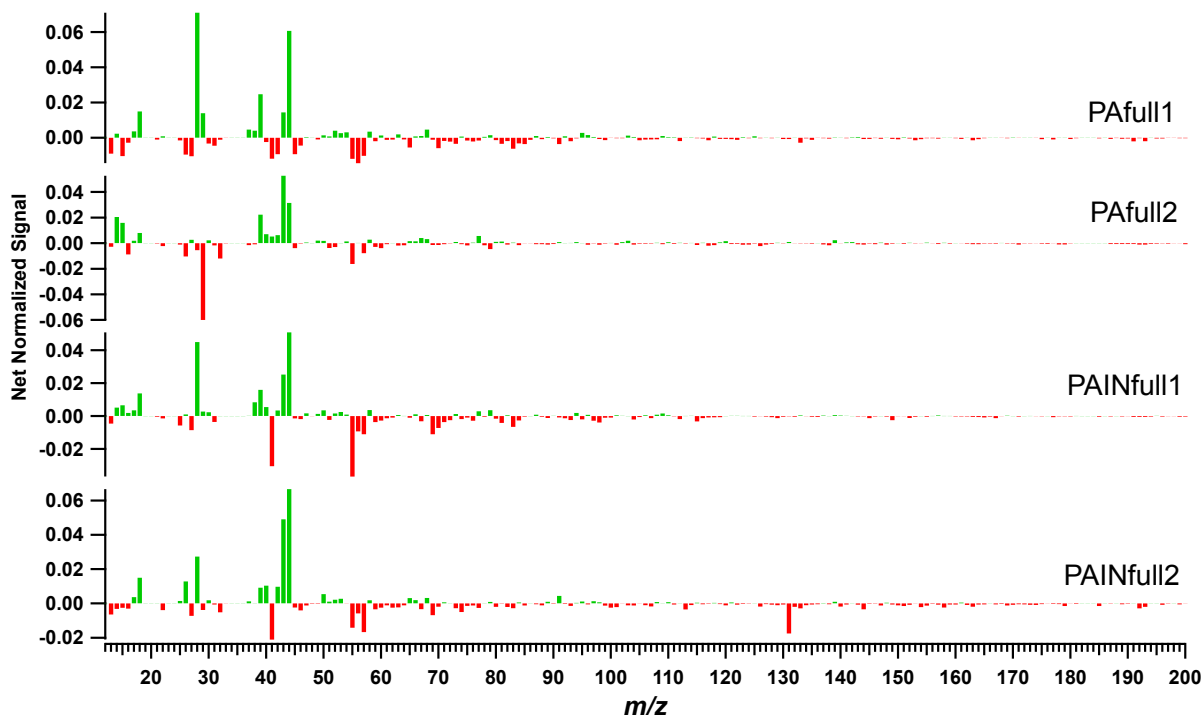


Figure 5-28: PA/PAIN: Normalized total organic difference mass spectra calculated via subtraction of experiment beginning 5-minute average organic spectrum from experiment end spectrum. Green indicates relative increase of the given m/z at experiment's end, while red indicates a decrease.

homogeneity with increasing oxidation. Δ_2 (alkyls, saturated carbonyls) also increases in PAINfull2, like TaiOx7PA (which has inorganics from the ambient cloud) and unlike most of the unaltered TaiOx samples, reflecting the carbonyl formation evidenced in the fragment ratio timelines.

Figure 5-31 shows all PA and PAIN replicates in van Krevelen space, where they have similar elemental ratio ranges and slopes between -0.63 and -0.90; this is similar to chamber α -pinene photo-oxidations, which usually have slopes between -0.5 and -1 produced by varying combinations of carbonyl and acid products, where enhanced acid formation generally produces a steeper slope (Chhabra et al. 2011; Ng et al. 2011; Lambe et al. 2011). PAfull2 has a lower slope ($m = -0.63$) than PAINfull2 ($m = -0.83$), possibly reflecting the reduced carboxylic acid functionalization indicated in the mass spectra and fragment ratios.

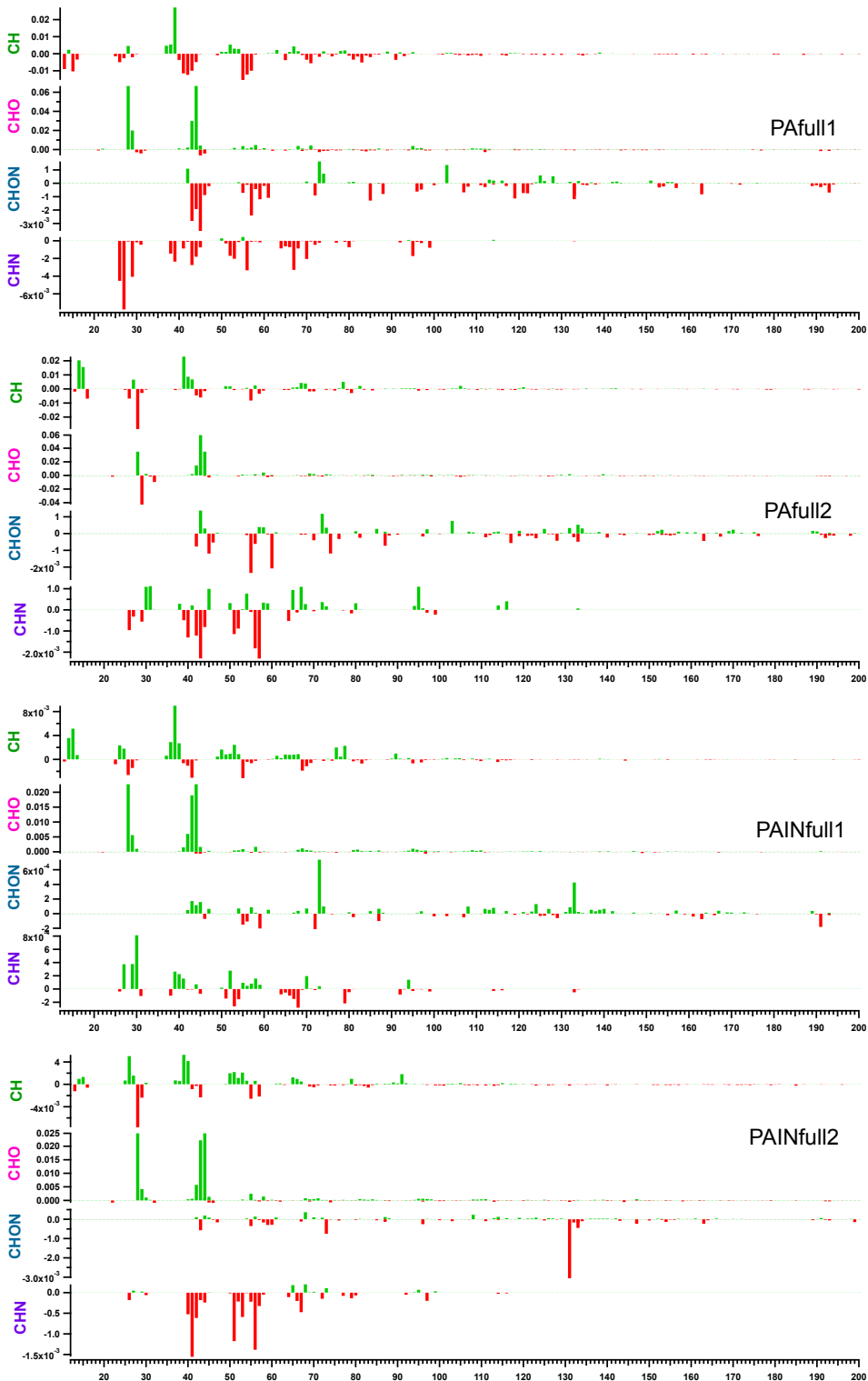


Figure 5-29: PA/PAIN: Normalized fragment-family difference mass spectra calculated via subtraction of experiment beginning 5-minute average spectrum from experiment end spectrum. Green indicates relative increase of the given m/z at experiment's end, while red indicates a decrease

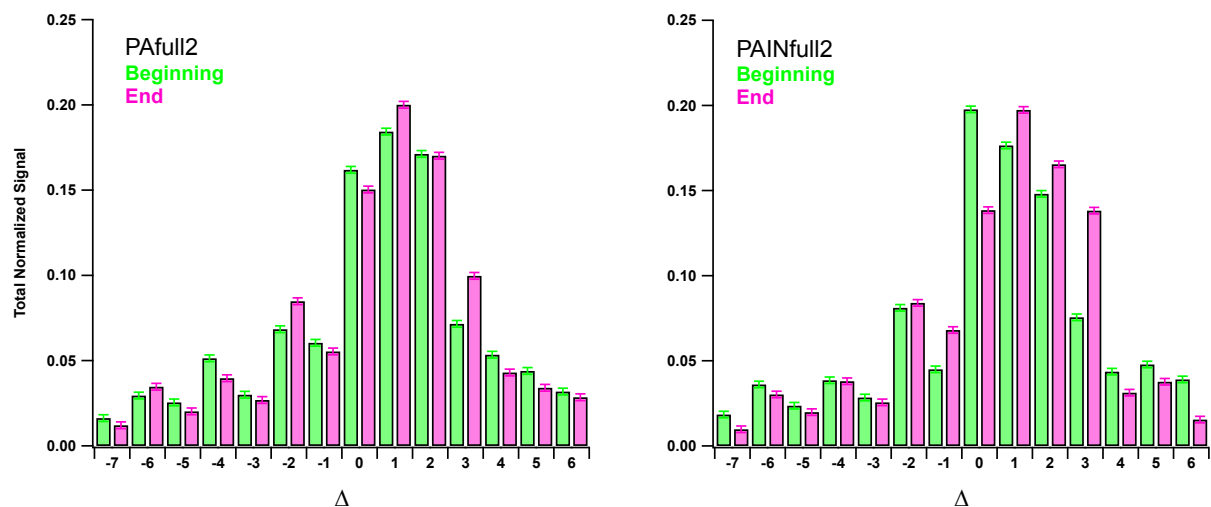


Figure 5-30: Total normalized signal in fragments with the given delta (Δ) value in the 5-minute average experiment beginning or end total organic mass spectrum.

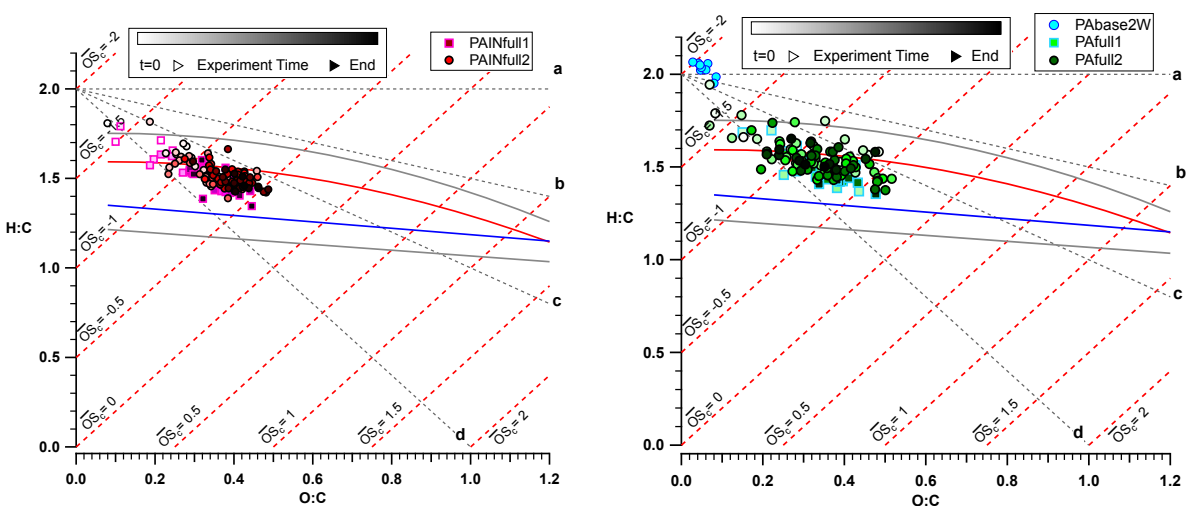


Figure 5-31: PA/PAIN: Van Krevelen diagram showing pinonic acid (PA) and pinonic acid + inorganics (PAIN) photo-oxidations in replicate colored by time during experiment. Linear fits: PA1: $m = -0.90$, $r^2 = 0.66$; PA2: $m = -0.63$, $r^2 = 0.45$; PAIN1: $m = -0.90$, $r^2 = 0.75$; PAIN2: $m = -0.83$, $r^2 = 0.58$.

Organic Nitrogen

Nominal ‘amine’ content (CHN mass) was low in both PA and PAIN experiments, at $\sim 0.17 \mu\text{g}/\text{m}^3$ (DI measures $0.084 \pm 0.012 \mu\text{g}/\text{m}^3$). Organonitrate (CHON) mass was also quite small and roughly equivalent to CHN in total mass. The limited amount of CHN/CHON fragments in deionized water (DI) ‘baseline’ periods is thought to arise from dissolution of either NH_x from room air or gaseous contaminants from the HEPA-filtered compressed air used in the

atomizer, as discussed earlier. N:C did not change significantly in any PA or PAIN experiment (Figure 5-32). These results are consistent with an α -pinene + inorganics aqueous oxidation in which no organonitrogen or organosulfur products were observed though their inorganic concentrations were $\sim 1000\times$ higher than those used here (Bleier & Elrod 2013).

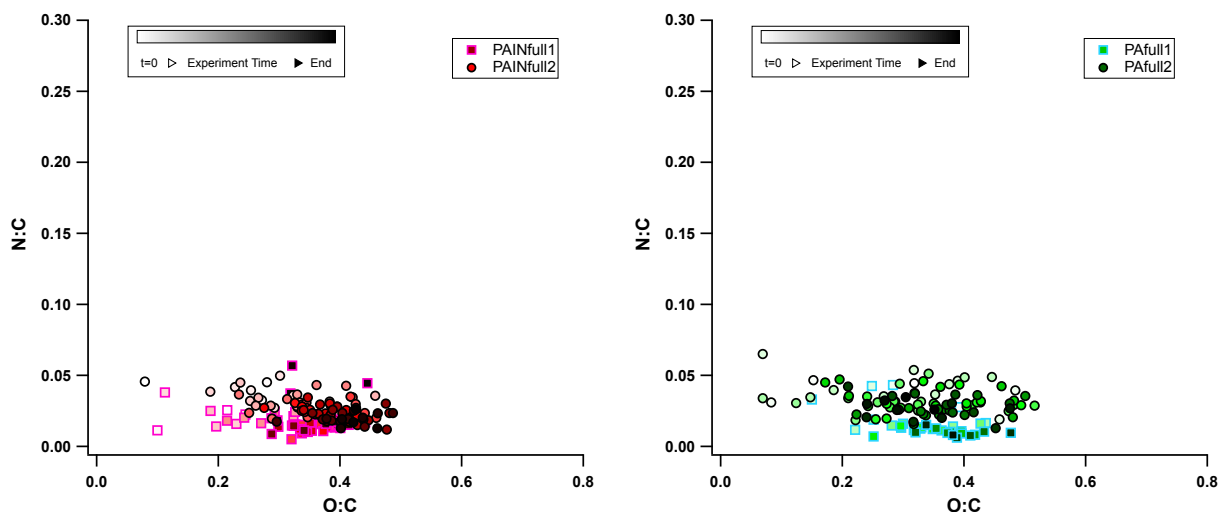


Figure 5-32: PA/PAIN: Nitrogen-to-Carbon vs. Oxygen-to-Carbon ratios for (left) pinonic acid + inorganics and (right) pinonic acid-only aqueous photo-oxidations. Linear fits: PAfull1*: $m = -0.06$, $r^2 = 0.22$; PAfull2: $m = -0.02$, $r^2 = 0.04$; PAINfull1*: $m = -0.01$, $r^2 = 0.01$; PAINfull2: $m = -0.06$, $r^2 = 0.33$.

5.5 Aqueous Photo-Oxidation Conclusions

Ambient Cloud

After initial increases to 110-140% of $t=0$ organic mass (expressed as Org/SO_4), all unaltered ambient cloud water samples lost organic mass; three of the five samples suffered a net loss of SOA to 60-80% of their $t=0$ value. Fragment ratios and difference mass spectra suggest two types of aqueous photo-oxidative behavior. In Type 1 experiments (TaiOx1 & 3), organic mass is gained then lost, with sustained increases in CO_2^+ and ‘formic acid’ fragment indicating carboxylic acid and volatile product formation; volatile products may contribute to the overall mass decrease. In Type 2 experiments (TaiOx4-1 & 7), oxidation indicators CO_2^+ and $\text{C}_2\text{H}_3\text{O}^+$ also decrease as mass decreases, suggesting that chemical decomposition may lead to loss of

oxidized functional groups. Type 1 and Type 2 samples have similar starting O:C ranging from 0.35-0.53, with Type 1 generally ending at higher O:C (0.69-0.95, versus ~0.64 for Type 2) due to retention of functional groups. Meteorological back-trajectories indicate the same source region (the heavily populated and industrial South China Plain) for air masses involved in all cloud samples. Type 1 samples have, on average, higher starting concentrations of most constituents, though the range of concentrations within each type leads to high standard deviations (**Figure 5-33**); magnesium, calcium, and manganese, total organic carbon are almost an order of magnitude higher in Type 1 samples, which may explain the tendency toward higher functionalization and therefore SOA mass retention as described in Section 1.2.3. However, using the Mann-Whitney-Wilcoxon rank-sum difference test (for non-paired, independent, and non-normal samples), concentrations of all constituents are not significantly different between Type 1 and Type 2 samples; it should be noted that this is a fairly conservative test.

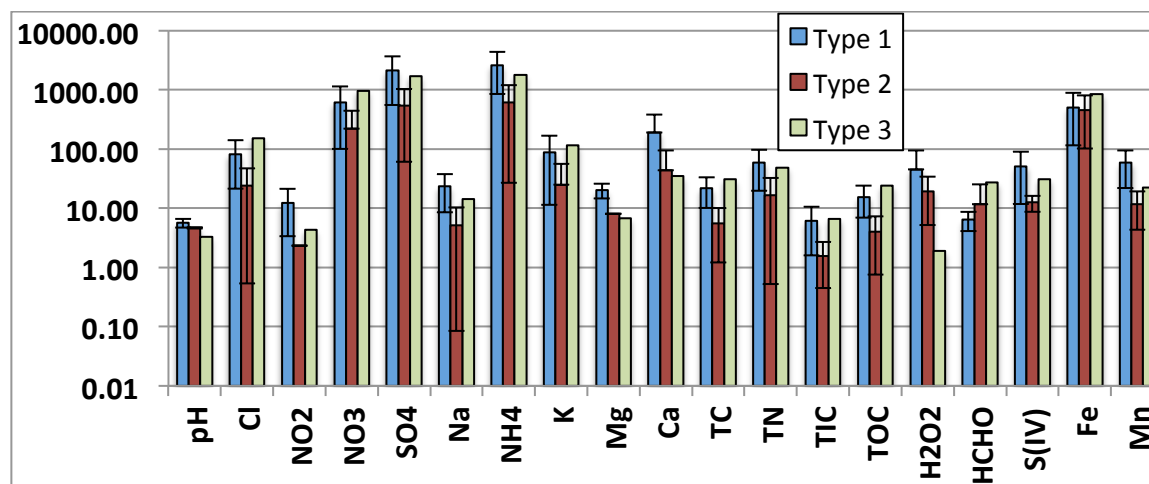


Figure 5-33: Starting concentrations of the given cloud water constituents for given sample types, where Type 3 is TaiOx2. Units are, from left to right: Cl-Ca, HCHO, & S(IV) (μN); TC-TOC (ppm); Fe & Mn ($\mu\text{g/L}$). Error bars are standard deviations where data from multiple samples of the same Type were averaged; Type 3 consists of only one sample, so error bars are omitted.

Delta analysis, which reveals classes of molecular functionalization, indicates decreases in Δ_0 (alkenyls, cycloalkyls), Δ_2 (dienes, cycloalkenes), Δ_4 (terpenes, phthalates), and Δ_6

(chloroalkyls, etc.) fragments in all TaiOx samples except TaiOx2 (which is quite oxidized initially); carbonyls, carboxylic acids, alkenes, cycloalkanes, diketones, unsaturated esters, cyclic amines, cycloalkanols, amines, amides, and nitrites are possible products indicated by enhancements in Δ_1 and Δ_3 . Organonitrates and amines are indicated by organized CHON and CHN fragments, but these fragments contribute little (~0.5%) to total signal, not accounting for possible contributions of organic nitrogen species to nominally inorganic fragments.

Formic acid production (or retention during drying) may be related to pH, with substantial ‘formic acid’ fragments occurring only in samples with pH > ~4.5 (TaiOx1, 3, and 7); TaiOx3 had the highest pH, and also the greatest increase in nominally formic acid fragments, while TaiOx7 had the lowest pH among formic acid-producing runs and also the lowest production. This is logical, since the Henry’s Law partitioning of formic acid is driven toward the particle phase by higher pH via (Liu et al. 2012):

$$\frac{[HCOO^-]_p}{[HCOOH]_g} = K_H \times LWC \times \frac{K_a}{[H^+]}$$

where K_a is formic acid’s dissociation constant. Furthermore, particulate formic acid is enhanced significantly beyond the Henry’s Law equilibrium in recent studies of urban-influenced particles (including one in Beijing, China; Liu et al. 2012; Wang et al. 2007); possible explanations include varying pH between particle bulk and surface (such that bulk measurements do not capture the pH relevant to the reaction) and variability in LWC (due to varying degrees of drying over the course of our experiments; Liu et al. 2012). Cations such as Ca^{2+} are regularly measured in cloud samples containing formic acid and could undergo acid-base reactions that lead to formic acid retention in the particle phase (Löflund et al. 2002; Fornaro & Gutz 2003; Malm et al. 2009); this chemistry has been indirectly evidenced in one case, coincidentally involving long-range transport of formic acid and dust from China (Kawamura et al. 2012).

Validation of total aqSOA production in the literature is difficult because controlled experiments (and many models) explore yields for individual precursors – lacking herein due to the complexity of ambient samples – which are useful for understanding aqueous systems, but often omit total production from a given starting TOC (which might be possible to compute from previous datasets depending on data type). However, differences between organic production in laboratory studies and the complex ambient matrices used here may reveal limitations in the current laboratory-based understanding of in-cloud aqueous reactions. The following paragraph summarizes published aqueous reactions with similar droplet drying methodology, assuming that evaporative loss of volatiles is somewhat similar between studies.

A series of experiments involving chamber cloud formation, photo-reaction, and subsequent drying provide decent comparison, though they may have surface and interstitial gas chemistry not possible in our bulk aqueous reactions (Liu et al. 2009; El Haddad et al. 2009; Monod et al. 2000; Monod et al. 2007); a methacrolein photo-oxidation therein found a non-linear 47-fold increase in SOA mass over the course of 5 hours, with almost no mass formation before ~hour 3 but subsequent continual SOA increasing over the rest of the 22-hour experiment (El Haddad et al. 2009). Using methods quite similar to ours though with higher OH concentrations, Lee et al. (2011) noted a reduction in AMS-measured Org/SO₄ for the first ~70 minutes of glyoxal photo-oxidation, followed by a mass increase to ~83% of the t = 0 value; simultaneous decreases in solution TOC (detected via ion chromatography) throughout the experiment may indicate formation of lower-volatility products after 70 minutes that lead to greater particulate signal. Ambient cloud samples were oxidized using the same method and found to form highly oxidized SOA chemically similar to that found in ambient aerosols, with

organic mass production maxima of ~110-130% of the initial value followed by decreasing mass, similar to this work (Lee et al. 2011).

Though models containing aqueous organic chemistry are few, a study simulating rural $\text{SOA}_{(\text{aq}+\text{g})}$ with monoterpene emissions showed ~21-25% total SOA increase in the first ~1 hour when clouds (pH = 4.5) were added, with a slight reduction in mass after ~2 hours, much like our experiments (Chen et al. 2007a); urban aerosol with anthropogenic emissions (NO_x , aromatics, alkanes) increased about 10% with no subsequent decrease. Overall, models generally under-predict SOA mass (Heald et al. 2005), which might argue that organic loss may be important only in some situations (e.g. highly aged anthropogenic plumes with no additional biogenic VOCs like those explored here; see next section); it is also possible that aqSOA formation outstrips oxidative/volatile mass loss. Whether or not the organic loss noted here is globally significant depends on a number of factors.

As outlined in Section 2.3, the ‘equivalent ageing times’ (i.e. OH exposures) that lead to organic mass loss must be compared to the real atmosphere. The $[\text{OH}]_{\text{aq}}$ herein is similar to that in ambient cloud water. We use $[\text{OH}] \approx 10^{-14} \text{ M}$ (in total from both added H_2O_2 and that present in the ambient sample); cloud estimates = 10^{-14} – 10^{-12} M (Arakaki & Faust 1998; Ervens, George, et al. 2003). We assume that ageing time in these experiments is directly equivalent to ambient ageing time, at least in terms of OH, which is often the dominant aqueous oxidant, though organic radicals may also be produced through photolysis and/or OH reaction. Neither organic mass nor oxidation indicator *f*₄₄ change significantly under UV-only or H_2O_2 -only control conditions, indicating that neither Fenton reactions nor hydrogen peroxide-initiated reactions produced significant amounts of aqSOA (see Section 2.3) and, hence, that aqSOA formation in the full photo-oxidation arises from OH-initiated reactions. We also must assume that

concentrations and forms of radical-producing organics did not change significantly during sample storage and that differences in irradiation between our UV source and the sun are small.

This methodology also disregards the continuous evaporation and re-condensation of cloud droplets, which could affect evaporative losses and the cycling of interstitial VOCs, semi-volatile compounds, and oxygen (O_2) through the gas and droplet phases, which may in turn change aqSOA production (De Haan et al. 2009). With typical cloud droplet lifetimes of ~10 minutes (Roelofs & Kamphuis 2009), a real cloud could undergo 12 droplet cycles over the course of the experiments herein, implying a more continuous source of fresh interstitial VOCs than can be recreated in our bulk-phase experiments. The effect of evaporative cycling on aqSOA is a focus of current research.

Ambient Cloud with Pinonic Acid

Assuming that interstitial gases in a cloud over a forest might contain biogenic VOCs which continuously partition to the droplet and react, the following section explores the affect of pinonic acid addition (as a surrogate for dissolving α -pinene) on aqSOA production; our conclusion that BVOC addition may lead to organic mass retention argues that the oxidative mass loss found in the unaltered ambient samples is less (or only situationally) pertinent to the real atmosphere.

In the one direct comparison between unaltered and altered cloud sample, adding pinonic acid appeared to impede mass loss and favor carbonyl over carboxylic acid products. TaiOx7 lost Org/SO₄ like the other TaiOx samples, with a clear progression of carbonyl to carboxylic acid products indicated in fragment ratio time series; however, TaiOx7PA had approximately constant Org/SO₄ and CO₂⁺/SO₄, with increases in carbonyl groups indicating overall oxidation. Carbonyl formation in TaiOx7PA is supported by the increase in Δ_2 , whereas TaiOx7 sees increases at Δ_1

and Δ_3 , indicating aldehydes, diketones, and/or the CO_2^+ fragment. TaiOx7 had some ‘formic acid’ increase, while TaiOx7PA does not; both experiments feature reductions in hydrocarbons (CH family) and no significant change in already low-mass organonitrate and ‘amine’ fragments.

We postulate that the addition of pinonic acid produced fewer volatile products and/or functionalization that did not lead to the fragmentative loss of functional groups seen in TaiOx7. The results suggest that in ambient situations involving addition of gaseous precursors such as interstitial alpha-pinene to aged cloud droplets (such as urban outflow over a forested region), aqSOA mass could be sustained, whereas photo-oxidation of the same droplets in an environment with low gaseous background might lead to overall aqSOA mass decrease.

Single-Precursor

Methylglyoxal oxidations were all plagued by inconsistent vaporizer output, but show consistent increase of organics to ~150-300% of their t=0 value (normalized to Org during MG and sulfate during MGIN experiments). Carboxylic acids (CO_2^+) increased 500-600% and ~1200% during MG and MGIN experiments, respectively. Experiments with no added inorganics appear to lose carbonyl molecules and gain large amounts of ‘formic acid’ fragment, while MG + IN experiments show less formic acid and significant (~600% of t=0 value) carbonyl formation. Delta progressions resemble ambient cloud sample with increases at Δ_1 and Δ_3 ; the relatively large magnitude of these increases may result from a smaller variety of products compared to the ambient cloud matrices. Both MG and MGIN progress to higher O:C and f_{44} than observed in the ambient samples, possibly contributing to the advanced levels of ambient oxidation rarely replicated in non-aqueous chamber experiments, though in all respects (carboxylic acid formation, etc.) solutions with added inorganics (MGIN) better replicate ambient cloud behavior. The van Krevelen progressions along a slope of ~-0.5 are similar to the

TaiOx samples and indicate carboxylic addition with C-C bond breakage and/or addition of both acid and alcohol/peroxide functional groups without fragmentation.

Like methylglyoxal, pinonic acid experiments with and without inorganics increased in normalized organics to ~300% of their t=0 value (though the normalization calculation differed between PA and PAIN, rendering them incomparable). However, products appeared to consist mostly of carbonyl compounds, with little of the increase in CO₂⁺/Org observed in the MG experiments (in which CO₂⁺/SO₄ increased significantly to ~200% of its t=0 value, but carbonyls increased more, to 600-800%). Delta values were more spread across the delta range, indicating a wider variety of molecule types than seen in methylglyoxal experiments; the similarity in delta distributions and progressions between PA/PAIN and TaiOx experiments, and especially the enhanced negative delta signal (relative to MG and aged anthropogenic aerosol in the literature), may support biogenic contributions to the TaiOx cloud water samples. Formic acid was not observed and organic nitrogen was low and unchanging. Pinonic acid samples had steeper slopes in van Krevelen space than methylglyoxal and TaiOx samples at m = -0.63 to -0.9; steeper negative slopes (between -0.5 and -1) indicate enhanced carboxylic addition, converse to the fragment progression seen above. The observed O:C range (beginning ≈ 0.1; end ≈ 0.5) is similar to α-pinene oxidations (George & Abbatt 2010) but much lower than that observed in TaiOx samples, and pinonic acid addition in TaiOx7PA lowers the solution starting and ending O:C by ~0.1; these suggest that the addition of BVOCs to a cloud droplet may lower the overall level of oxygenation as well as provide reduced precursors for further reaction and aqSOA formation.

Conclusions

Under the hypothesis that matrix effects in real, complex ambient cloud water lead to higher SOA production via formation of more functionalized, lower-volatility products, a variety

of unaltered ambient cloud, ‘biogenically influenced’ ambient cloud, and single-precursor solutions were photo-oxidized in the bulk aqueous phase, atomized, and dried to simulate the formation of aqSOA from clouds. Converse to our hypothesis, overall organic decreases were noted in unaltered cloud samples which are thought to arise from formation of volatile products in some cases and molecular decomposition in others. Increases in organic fragments indicating a high degree of functionalization were noted, and all samples (except the heavily oxidized TaiOx2) gained carbonyls, then organic acids, which then may or may not be lost with total organics as the oxidation progresses. The rate of aqSOA production in unaltered cloud water decreases as oxygenation increases, until organic mass loss beginning at a consistent average of $f_{44} \approx 0.23 \pm 0.05$ ($f_{43} \approx 0.08 \pm 0.02$).

In contrast, addition of pinonic acid to an ambient sample appeared to prevent mass losses and favor carbonyl formation. Single-precursor solutions, which began at a much lower level of oxidation (as indicated by O:C, CHO vs CH signal in average mass spectra, etc.), gained much more total organic mass over the course of the ~2 hour oxidations. From experiment-end O:C, methylglyoxal (MG & MGIN) became most oxygenated, followed by the TaiOx, TaiOxPA, and PA experiments in order of descending oxygenation. The rate of aqSOA production in the single-precursor solutions also appears to decrease as oxygenation increases, until organic mass reaches a steady value at an average $f_{44} = 0.19 \pm 0.03$ for pinonic acid and $f_{44} = 0.35 \pm 0.08$ for methylglyoxal; the consistency of these relationships within each solution type suggests that an ‘average’ relationship between oxygenation and aqSOA production for ambient clouds may be quantifiable, and certainly bears investigation. Combined, these experiments may offer a cohesive description of the ‘lifecycle’ of aqSOA: first, mass is gained through formation of lower-volatility carbonyls and acids (and oligomers, etc. as shown in the literature); then, organic

mass may be lost through further oxidation, or addition of fresh precursors from the gas phase may drive mass retention and/or further aqSOA formation.

While these experiments suggest some potentially important facets of aqSOA formation that warrant further exploration, there were a number of methodological setbacks that could be ameliorated in future work. Most importantly, droplet output must be stabilized. First, a nebulizer has been recommended for more consistent droplet output. Second, a counter-flow membrane dryer (such as the PermaPure Nafion series) could better regulate sample stream relative humidity above zero. The $RH = 0$ produced with the addition of a second drier may be lower than in most ambient evaporating clouds and induce enhanced organic volatilization not relevant to real clouds; constant sample stream relative humidity may also stabilize particle collection efficiency, though this probably not a large source of error in this study (as CE was modeled to be approximately constant for all experiments).

Also, TOC was somewhat inconsistent between added-PA, unaltered ambient, and single-precursor samples (though most samples were within an order of magnitude of each other); better care should be taken to remove the influence of varying TOC on product type and abundance that has been observed in the literature. Also, some NH_x was observed in single precursor samples with no added inorganics, which may have dissolved into solution from room air; though the photo-reactor was in a closed, opaque box to prevent light contamination (and which might reduce air-flow turbulence), it was not hermetically sealed. Sealing the photo-reactor would also eliminate the possibility of sulfur dioxide contamination (though this is already low due to lack of local SO_2 sources), but is not recommended because of the risk of increased vessel pressure due to gas production and increased temperature. Lastly, the bulk reaction method does

not incorporate the continuous interstitial sources of precursors and oxidants present in real cloud droplets that may change the types and amounts of aqSOA formed.

6. Conclusions

6.1 Summary and Conclusions

Particulate matter in the atmosphere has wide-ranging health, environmental, and climate effects, many of which are attributed disproportionately to fine-mode secondary organic aerosols. Fine particles may contribute to climate forcing both directly through scattering and absorption of radiation and indirectly through their cloud condensation nuclei (CCN) functionality, which in turn may affect cloud albedo, lifetime, and precipitation. Fine particles may cause respiratory difficulties, obstruct visibility, and harm ecosystems through nutrient deposition and attendant eutrophication and acidification of water and soil; they also persist long enough to undergo long-range transport. These effects motivate exploration of submicron particle composition and chemistry in the sensitive Rocky Mountain region; consistent underestimation of SOA and suggestion of a missing aqueous source in the literature prompts experiments concerning aqSOA formation in ambient cloud water.

Field campaigns employed a High-Resolution Time-of-Flight Aerosol Mass Spectrometer for particle composition and size characterization with 5-minute time resolution; data quality was constrained by extensive calibration, logging, and measurement of inlet $\text{CO}_{2(g)}$ (which must be differentiated from organic particle contributions). Mass spectral, timeline, meteorological, and positive matrix factorization data analysis yield the conclusions summarized below. To explore the influence of matrix effects in real, complex ambient cloud water on aqueous SOA production, aqueous ambient cloud (from Mt. Tai, China; Shen 2011) and single-precursor methylglyoxal and pinonic acid samples at similar starting total organic carbon (TOC) concentrations were photooxidized using UVC light and added hydrogen peroxide (producing

hydroxyl radical, OH) in a temperature-stabilized vessel; the solution was continuously atomized, dried, and analyzed via AMS with 1-minute time resolution.

A Rocky Mountain National Park aerosol mass spectrometer sampling campaign spanning 2 July - 31 August 2010 found the submicron particulate to be low in concentration (average $PM_{10} = 5.13 \pm 2.72 \mu\text{g}/\text{m}^3$) and dominated by organics (max = $93.09 \mu\text{g}/\text{m}^3$, average = $3.86 \pm 2.66 \mu\text{g}/\text{m}^3$ or $75.2 \pm 11.1\%$ of total mass). PMF identified low-volatility oxidized organic aerosol (LV-OOA, average = $2.15 \pm 1.11 \mu\text{g}/\text{m}^3$) and semi-volatile OOA (SV-OOA, average = $1.51 \pm 1.63 \mu\text{g}/\text{m}^3$), with short, high-concentration biomass burning episodes (BBOA, max = $8.33 \mu\text{g}/\text{m}^3$, though max is underestimated as explained in Chapter 4; average $0.46 \pm 0.21 \mu\text{g}/\text{m}^3$). Mixtures of LV-OOA with ammonium sulfate and of SV-OOA with ammonium nitrate are indicated by time-series correlation and similar size distributions; BBOA is not correlated with any measured inorganic species. Anthropogenic tracers nitrate, sulfate, and ammonium, for which local sources are sparse, are concurrent with southeasterly surface winds indicating upslope flow from the Front Range.

Transport of oxidized organic aerosols from the densely populated Front Range is indicated by advanced oxidation and relative monodispersity (both indicative of ageing), association with inorganic anthropogenic tracers, and concentration correlation with upslope surface winds from the Front Range; the presence of sulfate (an aqueous processing tracer), periodic high relative humidity and cloud cover, and advanced oxidation of the LV-OOA may suggest aqueous processing for the LV-OOA/ammonium sulfate particles, while growth by vapor condensation may be more likely for SV-OOA/ammonium nitrate particles.

A local BBOA source is suggested by cellulose combustion markers (m/z s 60 and 73) limited to brief, high-concentration, polydisperse events (suggesting fresh combustion emission),

association with local S or NW winds consistent with local campfire locations, no association with regional winds, and an unequivocal diurnal maximum at 22:00 LST, when campfires were set at adjacent summer camps. Contemporary carbon contributed by local biomass burning is insufficient to account for total contemporary carbon at the site (Schichtel et al. 2008), suggesting a biogenic contribution to OOA factors, possibly from NO_x/SO_x oxidation with BVOCs as Front Range plumes are transported over the forest. Organic nitrogen is associated with BBOA and may indicate amine, nitrile, and/or heterocyclic aromatic content, but is low in mass (ON_{min} : max = $1.04 \mu\text{g}/\text{m}^3$; average $0.02 \pm 0.02 \mu\text{g}/\text{m}^3$). The particle characteristics and sources determined here represent typical conditions at the Rocky Mountain site based on analysis of inter-annual variability over the previous decade in meteorological patterns, PILS-IC, filter, and fire data.

Submicron particulate mass is also low at the Grand Teton site, averaging $2.08 \mu\text{g}/\text{m}^3$ of which 75.0% is organic (organics: max. = $17.98 \mu\text{g}/\text{m}^3$; avg. = $1.56 \pm 1.19 \mu\text{g}/\text{m}^3$). Sulfate dominates inorganic mass (max. = $1.00 \mu\text{g}/\text{m}^3$; avg. = $0.26 \pm 0.12 \mu\text{g}/\text{m}^3$), with low ammonium and nitrate ammonium (NH_4 : max. = $0.78 \mu\text{g}/\text{m}^3$, avg. = $0.18 \pm 0.06 \mu\text{g}/\text{m}^3$; NO_3 : max. = $2.14 \mu\text{g}/\text{m}^3$, avg. = $0.08 \pm 0.12 \mu\text{g}/\text{m}^3$). Ammonium and sulfate have correlated time-series and CPF-indicated association with upslope winds from the Snake River valley, suggesting transport from an anthropogenic source. Concentrations of both were low with no significant diurnal patterns, though a weak afternoon maximum was observed. Ammonium sulfate appears to be the dominant form of particulate nitrogen, with ammonium in excess of stoichiometric balance with sulfate (NH_4^*) and nitrate possibly contributing to amine/nitrile/pyridine mass and one episode (during the Aug. 15 BBOA event) with evidence of organonitrate content where nitrate is excess of stoichiometric balance with NH_4^* .

PMF analysis identifies ‘background’ low-volatility oxidized organic aerosol (LV-OOA, max. = 2.85 $\mu\text{g}/\text{m}^3$; avg. = $0.74 \pm 0.33 \mu\text{g}/\text{m}^3$) averaging ~49% of PM_{10} and episodic biomass burning aerosol (BBOA, max. = 12.54 $\mu\text{g}/\text{m}^3$; avg. = $0.40 \pm 0.86 \mu\text{g}/\text{m}^3$ or ~26% of PM_{10}) as the major contributors to organic mass. LV-OOA has fairly static organic composition and is relatively less oxidized than OOA at many rural sites including Rocky Mountain National Park; Grand Teton particles average O:C = 0.50 ± 0.11 , while most LV-OOA has O:C ≈ 0.65 -1 (Table 1-2). LV-OOA is enhanced in the afternoon, but not correlated with upslope winds, anthropogenic NO_x , or ammonium sulfate; OOA at the site is also smaller and more polydisperse during the day and in comparison to a biomass burning plume inferred to have travelled ~480 km (below). These data evoke *in situ* photochemical organic aerosol formation and/or growth (perhaps from local biogenic VOCs), though transported anthropogenic OA and/or gaseous precursors cannot be excluded if they are regionally disperse; daytime boundary layer expansion to encompass the site could also produce this diurnal pattern.

Fires near Boise, ID (evident in MODIS fire maps) are thought to be the source of a high-concentration biomass-burning event on August 15-16, 2011. This event was associated with W-SW winds (upslope from the Snake River Valley) and increased sulfate, ammonium*, nitrate, and CHN fragment abundance (nominally, amine compounds), suggesting enhanced organic nitrogen content. Particles were larger and more monodisperse during this time period, consistent with extended transport and oxidation time.

Organic nitrogen in the form of nitriles and/or pyridines is indicated during the day by CHN fragment spectra, with the addition of amines at night. Nominally organonitrate (CHON) fragment intensities were constant throughout the campaign; lack of enhancement with BBOA events suggests that organonitrates are part of the regional LV-OOA background, though

enhanced nominally inorganic nitrate fragments during the BBOA event in excesses of balance with ammonium indicate compounds that did not fragment to CHON such as $\text{Ca}(\text{NO}_3)_2$ or organonitrates. Both amines and pyridines/nitriles may arise from local agricultural, natural, and combustion sources; photochemical oxidation reactions (in particular of biogenic SVOCs) may result in organonitrates, and calcium nitrate may arise from reaction of nitric acid (or its precursors) with particulate calcium carbonate.

Both of these remote sites are impacted by transported lower-concentration anthropogenic components and high-concentration, shorter-duration biomass burning plumes. At Rocky Mountain, oxidized SOA formed from combinations of anthropogenic particulate and biogenic precursors is indicated, while at Grand Teton, lack of association with anthropogenic species and relatively low level of oxidation may suggest a photo-oxidative source of OOA.

GEOS-Chem does not replicate particle transport by valley-funneled upslope winds at Rocky Mountain, and tends to underestimate sulfate, nitrate, ammonium, and, to a larger degree, total organic mass; predictions of ammonium seem more accurate during downslope winds, implying that GEOS-Chem may model the regional free tropospheric background somewhat better than the Denver surface grid box used for comparison to upslope flow periods. At Grand Teton, likewise, components are generally (though often not statistically) under-predicted and time-series variability is not well captured by either BL or FT grid boxes (or combinations thereof). Organics in the FT grid box are statistically lower than those measured via AMS, implying that if the site is indeed in the FT periodically, the model under-predicts free tropospheric organics. Overall, modeling of particles in areas with complex terrain must include small-scale flows (such as diurnal upslopes) as important sources of both particulate matter and precursors for formation of biogenic SOA; total organic mass and inorganic species were

generally under-predicted, with model free tropospheric organic matter significantly lower than implied by data from these high-altitude sites.

Aqueous SOA Formation via Photooxidation

The analysis above suggests that transported and in-situ SOA are both important in rural/remote mountainous regions and that models do not capture OA particle composition and variability in this and other studies. The literature asserts that model omission of aqueous SOA processes may cause the general under-prediction of organic particulate mass, though wall losses in the experiments used to determine photochemical SOA yields may also play a role. It is therefore imperative to quantify aqueous SOA production in the real atmosphere for inclusion in the models on which we rely for air quality and climate analyses. The experiments herein are among the first to attempt to quantify organic mass production in ambient cloud water.

Under the hypothesis that matrix effects in real, complex ambient cloud water lead to higher SOA production via formation of more functionalized, lower-volatility products, a variety of bulk aqueous samples were photooxidized, atomized, and dried to simulate the formation of SOA in evaporating cloud droplets. Unaltered ambient cloud samples were compared with ‘biogenically influenced’ cloud water, in which added pinonic acid was used to simulate uptake of monoterpene oxidation products from interstitial spaces. Single-precursor methylglyoxal and pinonic acid solutions (with and without inorganics) provide a point of comparison with the literature.

Converse to our hypothesis, any increases in sulfate-normalized organics in unaltered cloud samples (to a maximum of 110-140% of the $t=0$ value) are followed by mass decreases attributed to formation of volatile products in some cases and molecular decomposition in others. Increases in organic fragments indicating a high degree of functionalization were noted, and all

samples (except the heavily oxidized TaiOx2) gained carbonyls, then organic acids. Two general types of aqSOA behavior were observed: In Type 1 experiments (TaiOx1 & 3), organic mass is gained then lost, with sustained increases in CO_2^+ and 'formic acid' fragment suggesting carboxylic acid retention and formation of volatile products that may be lost to the gas phase, respectively. In Type 2 experiments (TaiOx4-1 & 7), in which TOC concentrations were $\sim 10\times$ lower than for Type 1, oxidation indicators CO_2^+ and $\text{C}_2\text{H}_3\text{O}^+$ also decrease as mass decreases, suggesting that chemical decomposition may lead to loss of oxidized functional groups; experiment-end O:C is also lower in Type 2 experiments, at ~ 0.64 , than for Type 1 (for which final O:C = 0.69-0.95). This is consistent with literature results showing production of more functionalized products in higher-concentration aqueous solutions (like Type 1).

In contrast, addition of pinonic acid to an ambient sample appeared to prevent organic mass losses and favor carbonyl formation. Single-precursor solutions, which began at a much lower level of oxidation (as indicated by O:C, CHO vs CH signal in average mass spectra, etc.), gained much more total organic mass over the course of the ~ 2 hour oxidations ($\text{Org}/\text{SO}_4 = 150\text{-}300\%$ of $t=0$ values for methylglyoxal, $\sim 300\%$ for pinonic acid). Combined, these experiments may suggest a cohesive description of the 'lifecycle' of aqSOA: first, mass is gained through formation of lower-volatility carbonyls and acids (and oligomers, etc. as shown in the literature); then, organic mass may be lost through further oxidation, or addition of fresh precursors from the gas phase may drive mass retention and/or further aqSOA formation. These experiments suggest that aqSOA formation in complex ambient cloud water is not well represented by the simple solutions often used for aqSOA parameterization. AqSOA production depends, predictably, on the availability of less-oxidized precursors such as interstitial VOCs, which may ultimately be expressed as the degree of organic oxygenation in the cloud water; the rate of aqSOA production

in unaltered cloud water decreases as oxygenation increases, until organic mass loss beginning at $f_{44} \approx 0.23 \pm 0.05$ ($f_{43} \approx 0.08 \pm 0.02$). This possible relationship between f_{44} and aqSOA production rate bears further investigation and, if robust, parameterization for better understanding (and modeling) of the secondary organic aerosols that contribute to so many important health, environmental, and climate effects.

6.2 Recommendation for Future Work

Aqueous Secondary Organic Aerosol Formation

Further exploration of the relationship between degree of aqSOA oxygenation and aqSOA production is a first priority for future work. While these experiments were among the first to explore aqSOA production in ambient cloud water, there were a number of methodological setbacks that could be ameliorated for better quantification of aqSOA production. Most importantly, droplet output can be stabilized through use of a nebulizer and counter-flow membrane dryer as explained in Section 5.5. Also, more care should be taken to group experiments by starting TOC, and to control the influence of TOC on production in altered experiments by dilution after precursor addition to maintain the starting concentration.

The experiments in Chapter 5 are the first of a series designed to explore cloud matrix effects on various facets of aqSOA formation. The subsequent experiments are outlined below. The experimental sequence begins with simple experiments on SOA yields in bulk ambient cloud water in real cloud, then goes on to explore surface reactions and the effect of reaction phase:

- (1) Explore ambient cloud matrix effects on aqSOA production (hypothesis and results in Chapter 5);
- (2) Evaluate surface effects on yield (flow reactor; atomized cloud water + B/VOCs);

(3) Compare yields from wet and dry reactions (flow reactor; dry atomized cloud before (dry) or after (wet) reaction).

Hypothesis 2: Surface effects (including enhanced oxidant/precursor uptake, etc.) increase SOA yield in ambient cloud water versus single-component solutions.

Experimental Approach 2: Cloud matrix or single-component solution is atomized, oxidized in the presence of biogenic gases under UV in flow reactor, dried, analyzed via AMS.

Experiment 2 Considerations/Concerns:

2i. Wall losses are often significant in flow reactor and chamber experiments, and must be constrained using constant-output nebulization of a known or standard-spiked solution (e.g. ambient cloud water). Wall losses are often reduced by reducing residence time, requiring higher oxidant concentrations to achieve a given amount of oxidation.

2ii. What is an appropriate balance between wall losses and relevance to atmospheric conditions? The hypothesis can still be nominally addressed using unrealistic oxidant concentrations, but caveats due to differing product yields, etc. under differing concentrations should be addressed.

2iii. Drying is expected to cause semivolatile organics loss, which must be assumed to mimic evaporating ambient cloud droplets.

2iv. Controls: (1) no additions (ambient cloud or single-precursor solution only)/lights off; (2) no additions/lights on; (3) oxidants added (but no bVOCs)/lights off; (4) oxidants added (no bVOCs)/lights on; (5) biogenic VOCs + oxidants added/lights off.

2v. Possible way to determine wall loss: Split sample between AMS and CPC, with and without flow reactor (UV off) between the flow split point and AMS; this will yield a ratio of AMS/CPC mass with and without wall loss. Caveat: particles lost to wall must be

within aerodynamic lens size range of AMS – this can be determined from nebulizer output size distribution.

- 2vi. Check for flow reactor contamination: HEPA air through reactor, UV on/off.
- 2vii. Inorganic oxidants in solution: Using the nitrate/sulfate already in the cloud as oxidants; must make similar concentration in simulated matrix (as Chapter 5 experiments).

Hypothesis 3: An ambient cloud droplets, aqueous (in-droplet) BVOCs oxidation produces more SOA than ‘dry’ oxidation.

Experimental Approach 3: Cloud matrix is atomized, then oxidized in the presence of biogenic gases under UV in flow reactor and analyzed via AMS; particles are dried alternately before or after reaction in the flow chamber to explore the effect of reaction phase on SOA production.

Experiment 3 Considerations/Concerns:

- 3i. Wall losses may be very different for wet and dry particles, preventing quantitative comparisons unless wall loss corrections are applied; different wall losses may affect concentrations of substrate (particles), affecting mass production and possibly product type.
- 3ii. Drying cloud particles before the flow reactor may cause volatilization, reducing substrate mass and changing both substrate and gaseous composition in the chamber; some attempt should be made to control for substrate concentration in the chamber.

Quantifying Organic Nitrogen in Sensitive Rural Areas

As outlined in the introduction, particulate organic nitrogen may be an important source of nitrogen deposition, but quantification is difficult and particulate ON measurements are rare, especially in remote and rural areas. Further, high time resolution ON measurements could aid in

source apportionment, but most ON measurement techniques have fairly poor time resolution. The following combines organic mass and elemental N measurements from the AMS with a technique for determining the fraction of N from organic species to quantify ON at higher time resolution.

Though ON quantification has not been achieved with the AMS due to high molecular fragmentation under electron impact ionization, the AMS can provide the total mass of N (TN_{AMS}) at high time resolution via:

$$TN_{AMS} (\mu g m^{-3}) = \sum_{i=0}^n M_i \frac{14.0067}{MW_i}$$

where M_i is the mass of the i^{th} N-containing fragment (including all nominally inorganic and organic fragments) and MW_i is the molecular weight of i . The fraction of N that is organic could be determined from co-located total nitrogen and inorganic nitrogen measurements using, for instance, the Shimadzu Carbon Analyzer with a nitrogen module (giving total nitrogen) and a PILS-IC system (giving inorganic nitrogen).

In an AMS dataset, the mass of N from organic molecules (TN_{org}) can be calculated by multiplying Total N (in the above equation) by the organic N fraction from the Carbon Analyzer/PILS method; TN_{org} can be integrated into the elemental analysis determination of N:C (currently, only N from nominally-organic CHON and CHN fragments are included in N:C), from which the total mass of nitrogen-containing organic compounds can be determined using OM:OC (from AMS elemental analysis). The integrated time resolution of the PILS-IC (~6 minutes) and TC instrument (limiting at 12-20 minutes) is lower than that of the AMS, and the ON-fraction values produced are averages of the sampled time periods; this methodology could introduce error into the ON mass determination in the event of brief or rapidly evolving events with an ON fraction different from the time-step average, such as a biomass burning plume, but

the higher time resolution of this estimated ON content would be useful for source apportionment of ON via meteorological analysis or other techniques.

7. References

- Adler, G. et al., 2011. Chemical, physical, and optical evolution of biomass burning aerosols: a case study. *Atmospheric Chemistry and Physics*, 11(4), pp.1491–1503. Available at: <http://www.atmos-chem-phys.net/11/1491/2011/> [Accessed April 16, 2012].
- Aerodyne Research Inc, I., 2004. *The Aerodyne Aerosol Mass Spectrometer (AMS)*,
- Ahlm, L. et al., 2013. Temperature-dependent accumulation mode particle and cloud nuclei concentrations from biogenic sources during WACS 2010. *Atmospheric Chemistry and Physics*, 13(6), pp.3393–3407. Available at: <http://www.atmos-chem-phys.net/13/3393/2013/acp-13-3393-2013.html> [Accessed January 20, 2014].
- Aiken, A.C. et al., 2009. Mexico City aerosol analysis during MILAGRO using high resolution aerosol mass spectrometry at the urban supersite (T0) – Part 1: Fine particle composition and organic source apportionment. *Atmospheric Chemistry and Physics Discussions*, 9(2), pp.8377–8427. Available at: <http://www.atmos-chem-phys-discuss.net/9/8377/2009/acpd-9-8377-2009.html> [Accessed September 13, 2013].
- Aiken, A.C. et al., 2010. Mexico city aerosol analysis during MILAGRO using high resolution aerosol mass spectrometry at the urban supersite (T0) – Part 2: Analysis of the biomass burning contribution and the non-fossil carbon fraction. *Atmospheric Chemistry and Physics*, 10(12), pp.5315–5341. Available at: <http://www.atmos-chem-phys.net/10/5315/2010/acp-10-5315-2010.html> [Accessed August 1, 2013].
- Aiken, A.C. et al., 2008. O/C and OM/OC ratios of primary, secondary, and ambient organic aerosols with high-resolution time-of-flight aerosol mass spectrometry. *Environmental science & technology*, 42(12), pp.4478–85. Available at: <http://www.ncbi.nlm.nih.gov/pubmed/18605574>.
- Aiken, A.C., DeCarlo, P.F. & Jimenez, J.L., 2007. Elemental analysis of organic species with electron ionization high-resolution mass spectrometry. *Analytical chemistry*, 79(21), pp.8350–8. Available at: <http://www.ncbi.nlm.nih.gov/pubmed/17914892>.
- Akagi, S.K. et al., 2012. Evolution of trace gases and particles emitted by a chaparral fire in California. *Atmospheric Chemistry and Physics*, 12(3), pp.1397–1421. Available at: <http://www.atmos-chem-phys.net/12/1397/2012/acp-12-1397-2012.html> [Accessed July 30, 2013].
- Albrecht, B.A., 1989. Aerosols, cloud microphysics, and fractional cloudiness. *Science (New York, N.Y.)*, 245(4923), pp.1227–30. Available at: <http://www.sciencemag.org/content/245/4923/1227.short> [Accessed June 3, 2013].
- Alfarra, M. & Paulsen, D., 2006. A mass spectrometric study of secondary organic aerosols formed from the photooxidation of anthropogenic and biogenic precursors in a reaction chamber. *Atmospheric ...*, pp.5279–5293. Available at: <http://www.atmos-chem-phys.net/6/5279/2006/> [Accessed September 6, 2013].
- Alfarra, M.R. et al., 2004. Characterization of urban and rural organic particulate in the Lower Fraser Valley using two Aerodyne Aerosol Mass Spectrometers. *Atmospheric Environment*, 38(34), pp.5745–5758. Available at: <http://dx.doi.org/10.1016/j.atmosenv.2004.01.054> [Accessed September 15, 2013].
- Alfarra, M.R. et al., 2007. Identification of the mass spectral signature of organic aerosols from wood burning emissions. *Environmental science & technology*, 41(16), pp.5770–7. Available at: <http://www.ncbi.nlm.nih.gov/pubmed/17874785> [Accessed October 24, 2012].

- Alfarra, M.R., 2004. *Insights Into Atmospheric Organic Aerosols Using An Aerosol Mass Spectrometer*. University of Manchester Institute of Science and Technology.
- Alkezweeny, A.J., Burrows, D.A. & Grainger, C.A., 1993. Measurements of Cloud-Droplet-Size Distributions in Polluted and Unpolluted Stratiform Clouds. *Journal of Applied Meteorology*, 32(1), pp.106–115. Available at: [http://journals.ametsoc.org/doi/abs/10.1175/1520-0450\(1993\)032<0106:MOCDSD>2.0.CO;2](http://journals.ametsoc.org/doi/abs/10.1175/1520-0450(1993)032<0106:MOCDSD>2.0.CO;2) [Accessed July 15, 2013].
- Allan, J.D., Delia, A.E., et al., 2004. A generalised method for the extraction of chemically resolved mass spectra from Aerodyne aerosol mass spectrometer data. *Journal of Aerosol Science*, 35(7), pp.909–922. Available at: <http://dx.doi.org/10.1016/j.jaerosci.2004.02.007> [Accessed August 6, 2012].
- Allan, J.D. et al., 2003. Quantitative sampling using an Aerodyne aerosol mass spectrometer 1. Techniques of data interpretation and error analysis. *Journal of Geophysical Research*, 108(D3), pp.1–10. Available at: <http://www.agu.org/pubs/crossref/2003/2002JD002358.shtml> [Accessed May 3, 2012].
- Allan, J.D., 2003. Quantitative sampling using an Aerodyne aerosol mass spectrometer 2. Measurements of fine particulate chemical composition in two U.K. cities. *Journal of Geophysical Research*, 108(D3), p.4091. Available at: <http://doi.wiley.com/10.1029/2002JD002359> [Accessed August 12, 2013].
- Allan, J.D., Bower, K.N., et al., 2004. Submicron aerosol composition at Trinidad Head, California, during ITCT 2K2: Its relationship with gas phase volatile organic carbon and assessment of instrument performance. *Journal of Geophysical Research*, 109(D23), pp.1–16. Available at: <http://www.agu.org/pubs/crossref/2004/2003JD004208.shtml> [Accessed April 30, 2012].
- Altieri, K.E. et al., 2006. Evidence for oligomer formation in clouds: reactions of isoprene oxidation products. *Environmental science & technology*, 40(16), pp.4956 – 60. Available at: http://www.researchgate.net/publication/6834222_Evidence_for_oligomer_formation_in_clouds_reactions_of_isoprene_oxidation_products [Accessed June 22, 2013].
- Altieri, K.E. et al., 2008. Oligomers formed through in-cloud methylglyoxal reactions: Chemical composition, properties, and mechanisms investigated by ultra-high resolution FT-ICR mass spectrometry. *Atmospheric Environment*, 42(7), pp.1476–1490. Available at: <http://dx.doi.org/10.1016/j.atmosenv.2007.11.015> [Accessed June 22, 2013].
- Altieri, K.E., Turpin, B.J. & Seitzinger, S.P., 2009. Oligomers, organosulfates, and nitrooxy organosulfates in rainwater identified by ultra-high resolution electrospray ionization FT-ICR mass spectrometry. *Atmospheric Chemistry and Physics*, 9(7), pp.2533–2542. Available at: <http://www.atmos-chem-phys.net/9/2533/2009/acp-9-2533-2009.html> [Accessed June 23, 2013].
- Anastasio, C., Faust, B.C. & Allen, J.M., 1994. Aqueous phase photochemical formation of hydrogen peroxide in authentic cloud waters. *Journal of Geophysical Research*, 99(D4), p.8231. Available at: <http://doi.wiley.com/10.1029/94JD00085> [Accessed June 22, 2013].
- Andreae, M.O., 1997. Atmospheric Aerosols: Biogeochemical Sources and Role in Atmospheric Chemistry. *Science*, 276(5315), pp.1052–1058. Available at: <http://www.sciencemag.org/content/276/5315/1052.abstract> [Accessed May 27, 2013].
- Andreae, M.O. & Gelencsér, A., 2006. Black carbon or brown carbon? The nature of light-absorbing carbonaceous aerosols. *Atmospheric Chemistry and Physics*, 6(10), pp.3131–

3148. Available at: <http://www.atmos-chem-phys.net/6/3131/2006/acp-6-3131-2006.html> [Accessed June 12, 2013].
- Anttila, P. et al., 2005. Determination of organic acids in aerosol particles from a coniferous forest by liquid chromatography-mass spectrometry. *Journal of separation science*, 28(4), pp.337–46. Available at: <http://www.ncbi.nlm.nih.gov/pubmed/15792248> [Accessed September 12, 2013].
- Arakaki, T. & Faust, B.C., 1998. Sources, sinks, and mechanisms of hydroxyl radical (\bullet OH) photoproduction and consumption in authentic acidic continental cloud waters from Whiteface Mountain, New York: The role of the Fe(r) (r = II, III) photochemical cycle. *Journal of Geophysical Research*, 103(D3), p.3487. Available at: <http://www.readcube.com/articles/10.1029/97JD02795?locale=en> [Accessed June 24, 2013].
- Arellanes, C. et al., 2006. Exceeding of Henry's Law by Hydrogen Peroxide Associated with Urban Aerosols. *Environmental Science & Technology*, 40(16), pp.4859–4866. Available at: <http://dx.doi.org/10.1021/es0513786> [Accessed June 24, 2013].
- Aschmann, S.M. et al., 1998. Products of the gas phase reaction of the OH radical with alpha- and beta- pinene in the presence of NO_x. *J. Geophys. Res.*, 103, pp.25553–25561.
- Ashbaugh, L.L., Malm, W.C. & Sadeh, W.Z., 1985. A residence time probability analysis of sulfur concentrations at grand Canyon National Park. *Atmospheric Environment (1967)*, 19(8), pp.1263–1270. Available at: [http://dx.doi.org/10.1016/0004-6981\(85\)90256-2](http://dx.doi.org/10.1016/0004-6981(85)90256-2) [Accessed September 13, 2013].
- Atkinson, R. et al., 1987. Atmospheric chemistry of aniline, N,N-dimethylaniline, pyridine, 1,3,5-triazine, and nitrobenzene. *Environmental Science & Technology*, 21(1), pp.64–72. Available at: <http://dx.doi.org/10.1021/es00155a007> [Accessed September 26, 2013].
- Atkinson, R., 2000. Atmospheric chemistry of VOCs and NO_x. *Atmospheric Environment*, 34(12-14), pp.2063–2101. Available at: [http://dx.doi.org/10.1016/S1352-2310\(99\)00460-4](http://dx.doi.org/10.1016/S1352-2310(99)00460-4) [Accessed August 11, 2013].
- Atkinson, R. et al., 2006. Evaluated kinetic and photochemical data for atmospheric chemistry: Volume II – gas phase reactions of organic species. *Atmospheric Chemistry and Physics*, 6(11), pp.3625–4055. Available at: <http://www.atmos-chem-phys.net/6/3625/2006/acp-6-3625-2006.html> [Accessed June 24, 2013].
- Atkinson, R. & Arey, J., 2003. Atmospheric degradation of volatile organic compounds. *Chemical reviews*, 103(12), pp.4605–38. Available at: <http://www.ncbi.nlm.nih.gov/pubmed/14664626> [Accessed August 7, 2013].
- Bader, D.C., McKee, T.B. & Tripoli, G.J., 1987. Mesoscale boundary layer evolution over complex terrain. Part I: Numerical simulation of the diurnal cycle. *J. Atmos. Sci.; (United States)*, 44:19. Available at: http://www.osti.gov/energycitations/product.biblio.jsp?osti_id=5859415 [Accessed September 11, 2012].
- Bae, M.-S. et al., 2007. Interference of organic signals in highly time resolved nitrate measurements by low mass resolution aerosol mass spectrometry. *Journal of Geophysical Research*, 112(D22), pp.1–16. Available at: <http://www.agu.org/pubs/crossref/2007/2007JD008614.shtml> [Accessed May 9, 2012].
- Bae, M.-S. et al., 2004. Validation of a semi-continuous instrument for elemental carbon and organic carbon using a thermal-optical method. *Atmospheric Environment*, 38(18),

- pp.2885–2893. Available at: <http://dx.doi.org/10.1016/j.atmosenv.2004.02.027> [Accessed September 12, 2013].
- Bahadur, R., Russell, L.M. & Prather, K., 2010. Composition and Morphology of Individual Combustion, Biomass Burning, and Secondary Organic Particle Types Obtained Using Urban and Coastal ATOFMS and STXM-NEXAFS Measurements. *Aerosol Science and Technology*, 44(7), pp.551–562. Available at: <http://scrippsscholars.ucsd.edu/lmrussell/content/composition-and-morphology-individual-combustion-biomass-burning-and-secondary-organic-par-0> [Accessed July 5, 2013].
- Bahreini, R. et al., 2005. Measurements of secondary organic aerosol from oxidation of cycloalkenes, terpenes, and m-xylene using an Aerodyne aerosol mass spectrometer. *Environmental science & technology*, 39(15), pp.5674–88. Available at: <http://www.ncbi.nlm.nih.gov/pubmed/16124302>.
- Baltensperger, U. et al., 1997. Aerosol climatology at the high-alpine site Jungfraujoch, Switzerland. *Journal of Geophysical Research*, 102(D16), p.19707. Available at: <http://doi.wiley.com/10.1029/97JD00928> [Accessed October 3, 2013].
- Baron, J.S. et al., 2000. Ecosystem responses to nitrogen deposition in the Colorado Front Range. *Ecosystems*, 3(4), pp.352–368. Available at: http://www.fort.usgs.gov/Products/Publications/pub_abstract.asp?PubID=577 [Accessed October 24, 2012].
- Barth, M.C. et al., 2000. Sulfur chemistry in the National Center for Atmospheric Research Community Climate Model: Description, evaluation, features, and sensitivity to aqueous chemistry. *Journal of Geophysical Research*, 105(D1), p.1387. Available at: <http://doi.wiley.com/10.1029/1999JD900773> [Accessed January 14, 2014].
- Beem, K.B. et al., 2010. Deposition of reactive nitrogen during the Rocky Mountain Airborne Nitrogen and Sulfur (RoMANS) study. *Environmental pollution (Barking, Essex : 1987)*, 158(3), pp.862–72. Available at: <http://www.ncbi.nlm.nih.gov/pubmed/19833422> [Accessed April 4, 2012].
- Benedict, K.B. et al., 2013. Observations of atmospheric reactive nitrogen species in Rocky Mountain National Park and across northern Colorado. *Atmospheric Environment*, 64(null), pp.66–76.
- Benedict, K.B. et al., 2013. The Spatial Distribution of Reactive Nitrogen Species and Nitrogen Deposition in Grand Teton National Park.
- Benkovitz, C.M. et al., 1994. Sulfate over the North Atlantic and adjacent continental regions: Evaluation for October and November 1986 using a three-dimensional model driven by observation-derived meteorology. *Journal of Geophysical Research*, 99(D10), pp.20725–20756. Available at: <http://www.agu.org/pubs/crossref/1994/94JD01634.shtml> [Accessed September 17, 2012].
- Bergin, M.H. et al., 2001. Aerosol radiative, physical, and chemical properties in Beijing during June 1999. *Journal of Geophysical Research*, 106(D16), p.17969. Available at: <http://doi.wiley.com/10.1029/2001JD900073> [Accessed July 14, 2013].
- Bergstrom, A.-K. & Jansson, M., 2006. Atmospheric nitrogen deposition has caused nitrogen enrichment and eutrophication of lakes in the northern hemisphere. *Global Change Biology*, 12(4), pp.635–643. Available at: <http://doi.wiley.com/10.1111/j.1365-2486.2006.01129.x> [Accessed June 13, 2013].
- Bertram, A.K. et al., 2011. Predicting the relative humidities of liquid-liquid phase separation, efflorescence, and deliquescence of mixed particles of ammonium sulfate, organic material,

- and water using the organic-to-sulfate mass ratio of the particle and the oxygen-to-carbon ele. *Atmospheric Chemistry and Physics*, 11(21), pp.10995–11006. Available at: <http://www.atmos-chem-phys.net/11/10995/2011/acp-11-10995-2011.html> [Accessed September 5, 2013].
- Blando, J.D. et al., 1998. Secondary Formation and the Smoky Mountain Organic Aerosol: An Examination of Aerosol Polarity and Functional Group Composition During SEAVS. *Environmental Science & Technology*, 32(5), pp.604–613. Available at: <http://www.citeulike.org/user/gourig/article/11900810> [Accessed August 7, 2013].
- Bleier, D.B. & Elrod, M.J., 2013. Kinetics and Thermodynamics of Atmospherically Relevant Aqueous Phase Reactions of α -Pinene Oxide. *J. Phys. Chem. A*, 117(20), pp.4223–4232.
- Bossert, J.E. & Cotton, W.R., 1994. Regional-Scale Flows in Mountainous Terrain. Part I: A Numerical and Observational Comparison. *Monthly Weather Review*, 122(7), pp.1449–1471. Available at: [http://journals.ametsoc.org/doi/abs/10.1175/1520-0493\(1994\)122<1449:RSFIMT>2.0.CO;2](http://journals.ametsoc.org/doi/abs/10.1175/1520-0493(1994)122<1449:RSFIMT>2.0.CO;2) [Accessed September 11, 2012].
- Bossert, J.E., Sheaffer, J.D. & Reiter, E.R., 1989. Aspects of regional-scale flows in mountainous terrain. *J. Appl. Meteorol.; (United States)*, 28:7. Available at: http://www.osti.gov/energycitations/product.biblio.jsp?osti_id=5906285 [Accessed September 11, 2012].
- Bowman, W.D. et al., 2012. Nitrogen critical loads for alpine vegetation and soils in Rocky Mountain National Park. *Journal of environmental management*, 103(null), pp.165–71. Available at: <http://dx.doi.org/10.1016/j.jenvman.2012.03.002> [Accessed August 21, 2012].
- Brown, S.S. et al., 2009. Nocturnal isoprene oxidation over the Northeast United States in summer and its impact on reactive nitrogen partitioning and secondary organic aerosol. *Atmospheric Chemistry and Physics*, 9(9), pp.3027–3042. Available at: <http://www.atmos-chem-phys.net/9/3027/2009/acp-9-3027-2009.html> [Accessed September 15, 2013].
- Bruns, E.A. et al., 2010. Comparison of FTIR and particle mass spectrometry for the measurement of particulate organic nitrates. *Environmental science & technology*, 44(3), pp.1056–61. Available at: <http://dx.doi.org/10.1021/es9029864> [Accessed November 16, 2012].
- Burns, D.A., 2003. Atmospheric nitrogen deposition in the Rocky Mountains of Colorado and southern Wyoming—a review and new analysis of past study results. *Atmospheric Environment*, 37(7), pp.921–932. Available at: [http://dx.doi.org/10.1016/S1352-2310\(02\)00993-7](http://dx.doi.org/10.1016/S1352-2310(02)00993-7) [Accessed August 18, 2013].
- Buzcu-Guven, B. et al., 2007. Analysis and apportionment of organic carbon and fine particulate matter sources at multiple sites in the midwestern United States. *Journal of the Air & Waste Management Association (1995)*, 57(5), pp.606–19. Available at: <http://www.ncbi.nlm.nih.gov/pubmed/17518227> [Accessed September 16, 2013].
- Canagaratna, M.R. et al., 2004. Chase Studies of Particulate Emissions from in-use New York City Vehicles. *Aerosol Science and Technology*, 38(6), pp.555–573. Available at: <http://dx.doi.org/10.1080/02786820490465504> [Accessed September 15, 2013].
- Canagaratna, M.R. et al., 2007. Guest Editor : Albert Viggiano CHEMICAL AND MICROPHYSICAL CHARACTERIZATION OF AMBIENT AEROSOLS WITH THE AERODYNE AEROSOL MASS SPECTROMETER. *Mass spectrometry reviews*, 26(2), pp.185–222. Available at: <http://www.ncbi.nlm.nih.gov/pubmed/17230437> [Accessed July 5, 2013].

- Cape, J.N. et al., 2011. Organic nitrogen in the atmosphere—Where does it come from? A review of sources and methods. *Atmospheric Research*. Available at: <http://www.sciencedirect.com/science/article/pii/S0169809511002407> [Accessed July 15, 2013].
- Carlton, A.G. et al., 2007. Atmospheric oxalic acid and SOA production from glyoxal: Results of aqueous photooxidation experiments. *Atmospheric Environment*, 41(35), pp.7588–7602. Available at: <http://dx.doi.org/10.1016/j.atmosenv.2007.05.035> [Accessed June 6, 2013].
- Carlton, A.G. et al., 2008. CMAQ Model Performance Enhanced When In-Cloud Secondary Organic Aerosol is Included: Comparisons of Organic Carbon Predictions with Measurements. *Environmental Science & Technology*, 42(23), pp.8798–8802. Available at: <http://dx.doi.org/10.1021/es801192n> [Accessed June 6, 2013].
- Casale, M. et al., 2007. Kinetics of acid-catalyzed aldol condensation reactions of aliphatic aldehydes. *Atmospheric Environment*, 41(29), pp.6212–6224. Available at: <http://dx.doi.org/10.1016/j.atmosenv.2007.04.002> [Accessed June 25, 2013].
- Chameides, W.L., 1999. Case study of the effects of atmospheric aerosols and regional haze on agriculture: An opportunity to enhance crop yields in China through emission controls? *Proceedings of the National Academy of Sciences*, 96(24), pp.13626–13633. Available at: <http://www.pnas.org/content/96/24/13626.full> [Accessed July 15, 2013].
- Chan, A.W.H. et al., 2009. Secondary organic aerosol formation from photooxidation of naphthalene and alkylnaphthalenes: implications for oxidation of intermediate volatility organic compounds (IVOCs). *Atmospheric Chemistry and Physics*, 9(9), pp.3049–3060. Available at: <http://www.atmos-chem-phys.net/9/3049/2009/acp-9-3049-2009.html> [Accessed January 8, 2014].
- Chan, Y. et al., 2011. Using multiple type composition data and wind data in PMF analysis to apportion and locate sources of air pollutants. *Atmospheric Environment*, 45(2), pp.439–449. Available at: <http://dx.doi.org/10.1016/j.atmosenv.2010.09.060> [Accessed October 22, 2012].
- Chang, J.L. & Thompson, J.E., 2010. Characterization of colored products formed during irradiation of aqueous solutions containing H₂O₂ and phenolic compounds. *Atmospheric Environment*, 44(4), pp.541–551. Available at: <http://dx.doi.org/10.1016/j.atmosenv.2009.10.042> [Accessed June 13, 2013].
- Chen, J. et al., 2007. Modeling secondary organic aerosol formation through cloud processing of organic compounds. *Atmospheric Chemistry and Physics*, 7(20), pp.5343–5355. Available at: <http://www.atmos-chem-phys.net/7/5343/2007/acp-7-5343-2007.html> [Accessed June 24, 2013].
- Chen, Q. et al., 2009. Mass spectral characterization of submicron biogenic organic particles in the Amazon Basin. *Geophysical Research Letters*, 36(20), p.L20806. Available at: <http://doi.wiley.com/10.1029/2009GL039880> [Accessed September 26, 2013].
- Chen, Z.M. et al., 2007. Aqueous-phase ozonolysis of methacrolein and methyl vinyl ketone: a potentially important source of atmospheric aqueous oxidants. *Atmospheric Chemistry and Physics Discussions*, 7(6), pp.17599–17623. Available at: <http://www.atmos-chem-phys-discuss.net/7/17599/2007/acpd-7-17599-2007.html> [Accessed June 22, 2013].
- Chhabra, P.S. et al., 2011. Elemental composition and oxidation of chamber organic aerosol. *Atmospheric Chemistry and Physics*, 11(17), pp.8827–8845. Available at: <http://www.atmos-chem-phys.net/11/8827/2011/acp-11-8827-2011.html> [Accessed August 2, 2013].

- Chhabra, P.S., Flagan, R.C. & Seinfeld, J.H., 2010. Elemental analysis of chamber organic aerosol using an aerodyne high-resolution aerosol mass spectrometer. *Atmospheric Chemistry and Physics*, 10(9), pp.4111–4131. Available at: <http://www.atmos-chem-phys.net/10/4111/2010/> [Accessed April 4, 2012].
- Chirico, R.D. et al., 1996. Thermodynamic properties of pyridine—I. Vapor pressures, high-temperature heat capacities, densities, critical properties, derived thermodynamic functions, vibrational assignment, and derivation of recommended values. *The Journal of Chemical Thermodynamics*, 28(8), pp.797–818. Available at: <http://www.sciencedirect.com/science/article/pii/S0021961496900737> [Accessed September 26, 2013].
- Chueinta, W., Hopke, P.K. & Paatero, P., 2000. Investigation of sources of atmospheric aerosol at urban and suburban residential areas in Thailand by positive matrix factorization. *Atmospheric Environment*, 34(20), pp.3319–3329. Available at: <http://www.sciencedirect.com/science/article/pii/S1352231099004331> [Accessed September 17, 2013].
- Chung, S.H., 2002. Global distribution and climate forcing of carbonaceous aerosols. *Journal of Geophysical Research*, 107(D19), p.4407. Available at: <http://doi.wiley.com/10.1029/2001JD001397> [Accessed May 26, 2013].
- CIRA, 2013. VIEWS Database. Available at: <http://views.cira.colostate.edu/web/> [Accessed January 22, 2014].
- Claeys, M., Wang, W., et al., 2004. Formation of secondary organic aerosols from isoprene and its gas-phase oxidation products through reaction with hydrogen peroxide. *Atmospheric Environment*, 38(25), pp.4093–4098. Available at: <http://dx.doi.org/10.1016/j.atmosenv.2004.06.001> [Accessed May 26, 2013].
- Claeys, M., Graham, B., et al., 2004. Formation of secondary organic aerosols through photooxidation of isoprene. *Science (New York, N.Y.)*, 303(5661), pp.1173–6. Available at: <http://www.sciencemag.org/content/303/5661/1173.abstract> [Accessed May 23, 2013].
- Coakley, J.A., Bernstein, R.L. & Durkee, P.A., 1987. Effect of ship-stack effluents on cloud reflectivity. *Science (New York, N.Y.)*, 237(4818), pp.1020–2. Available at: <http://www.readcube.com/articles/10.1126/science.237.4818.1020> [Accessed July 15, 2013].
- Cohan, D.S. et al., 2002. Impact of atmospheric aerosol light scattering and absorption on terrestrial net primary productivity. *Global Biogeochemical Cycles*, 16(4), pp.37–1–37–12. Available at: <http://doi.wiley.com/10.1029/2001GB001441> [Accessed July 15, 2013].
- Collaud Coen, M. et al., 2011. Aerosol climatology and planetary boundary influence at the Jungfraujoch analyzed by synoptic weather types. *Atmospheric Chemistry and Physics*, 11(12), pp.5931–5944. Available at: <http://www.atmos-chem-phys.net/11/5931/2011/acp-11-5931-2011.html> [Accessed October 3, 2013].
- Collett, J.L. et al., 1990. Intensive studies of Sierra Nevada cloudwater chemistry and its relationship to precursor aerosol and gas concentrations. *Atmospheric Environment. Part A. General Topics*, 24(7), pp.1741–1757. Available at: <http://www.sciencedirect.com/science/article/pii/096016869090507J> [Accessed September 30, 2013].
- Collett, J.L. et al., 2008. Processing of atmospheric organic matter by California radiation fogs. *Atmospheric Research*, 87(3-4), pp.232–241. Available at: <http://dx.doi.org/10.1016/j.atmosres.2007.11.005> [Accessed June 16, 2013].

- Collett, J.L. et al., 1998. Spatial and temporal variations in San Joaquin Valley fog chemistry. *Atmospheric Environment*, 33(1), pp.129–140. Available at: <http://www.sciencedirect.com/science/article/pii/S1352231098001368> [Accessed September 30, 2013].
- Cook, J. & Highwood, E.J., 2004. Climate response to tropospheric absorbing aerosols in an intermediate general-circulation model. *Quarterly Journal of the Royal Meteorological Society*, 130(596), pp.175–191. Available at: <http://doi.wiley.com/10.1256/qj.03.64> [Accessed June 11, 2013].
- Cornell, S. et al., 2003. Organic nitrogen deposition on land and coastal environments: a review of methods and data. *Atmospheric Environment*, 37(16), pp.2173–2191. Available at: [http://dx.doi.org/10.1016/S1352-2310\(03\)00133-X](http://dx.doi.org/10.1016/S1352-2310(03)00133-X) [Accessed August 16, 2012].
- Cottrell, L.D. et al., 2008. Submicron particles at Thompson Farm during ICARTT measured using aerosol mass spectrometry. *Journal of Geophysical Research*, 113(D8), p.D08212. Available at: <http://doi.wiley.com/10.1029/2007JD009192> [Accessed September 12, 2013].
- Cubison, M.J. et al., 2011. Effects of aging on organic aerosol from open biomass burning smoke in aircraft and lab studies. *Atmospheric Chemistry and Physics Discussions*, 11(4), pp.12103–12140. Available at: <http://www.atmos-chem-phys-discuss.net/11/12103/2011/acpd-11-12103-2011.html> [Accessed July 30, 2013].
- Currie, L.A. et al., 1984. Interlaboratory comparison of source apportionment procedures: Results for simulated data sets. *Atmospheric Environment (1967)*, 18(8), pp.1517–1537. Available at: [http://dx.doi.org/10.1016/0004-6981\(84\)90376-7](http://dx.doi.org/10.1016/0004-6981(84)90376-7) [Accessed September 13, 2013].
- Dall'Osto, M. et al., 2009. Real-time secondary aerosol formation during a fog event in London. *Atmospheric Chemistry and Physics*, 9(7), pp.2459–2469. Available at: <http://www.atmos-chem-phys.net/9/2459/2009/>.
- Davidson, C.I., Phalen, R.F. & Solomon, P.A., 2005. Airborne Particulate Matter and Human Health: A Review. *Aerosol Science and Technology*, 39(8), pp.737–749. Available at: <http://dx.doi.org/10.1080/02786820500191348> [Accessed July 24, 2012].
- Decarlo, P.F. et al., 2006. Field-deployable, high-resolution, time-of-flight aerosol mass spectrometer. *Analytical chemistry*, 78(24), pp.8281–9. Available at: <http://www.ncbi.nlm.nih.gov/pubmed/17165817>.
- DeCarlo, P.F. et al., 2010. Investigation of the sources and processing of organic aerosol over the Central Mexican Plateau from aircraft measurements during MILAGRO. *Atmospheric Chemistry and Physics*, 10(12), pp.5257–5280. Available at: <http://www.atmos-chem-phys.net/10/5257/2010/> [Accessed May 9, 2012].
- DeCarlo, P.F. et al., 2004. Particle Morphology and Density Characterization by Combined Mobility and Aerodynamic Diameter Measurements. Part 1: Theory. *Aerosol Science & Technology*, 38(12), pp.1185–1205. Available at: http://www.researchgate.net/publication/228861381_Particle_morphology_and_density_characterization_by_combined_mobility_and_aerodynamic_diameter_measurements_Part_1_Theory [Accessed March 8, 2012].
- Decesari, S. et al., 2000. Characterization of water-soluble organic compounds in atmospheric aerosol: A new approach. *Journal of Geophysical Research*, 105(D1), p.1481. Available at: <http://doi.wiley.com/10.1029/1999JD900950> [Accessed September 9, 2013].
- Decesari, S. et al., 2001. Chemical features and seasonal variation of fine aerosol water-soluble organic compounds in the Po Valley, Italy. *Atmospheric Environment*, 35(21), pp.3691–

3699. Available at: [http://dx.doi.org/10.1016/S1352-2310\(00\)00509-4](http://dx.doi.org/10.1016/S1352-2310(00)00509-4) [Accessed September 12, 2013].
- Decesari, S. et al., 2007. Source attribution of water-soluble organic aerosol by nuclear magnetic resonance spectroscopy. *Environmental science & technology*, 41(7), pp.2479–84. Available at: <http://www.ncbi.nlm.nih.gov/pubmed/17438803> [Accessed July 13, 2013].
- Deguillaume, L., Leriche, M. & Chaumerliac, N., 2005. Impact of radical versus non-radical pathway in the Fenton chemistry on the iron redox cycle in clouds. *Chemosphere*, 60(5), pp.718–24. Available at: <http://www.ncbi.nlm.nih.gov/pubmed/15963810> [Accessed September 1, 2013].
- Demoz, B.B., Collett, J.L. & Daube, B.C., 1996. On the Caltech Active Strand Cloudwater Collectors. *Atmospheric Research*, 41(1), pp.47–62. Available at: <http://www.sciencedirect.com/science/article/pii/0169809595000445> [Accessed September 30, 2013].
- Denkenberger, K.A. et al., 2007. Real-Time, Single-Particle Measurements of Oligomers in Aged Ambient Aerosol Particles. *Environmental Science & Technology*, 41(15), pp.5439–5446. Available at: <http://dx.doi.org/10.1021/es070329l> [Accessed May 21, 2013].
- Desyaterik, Y. et al., 2013. Speciation of “brown” carbon in cloud water impacted by agricultural biomass burning in eastern China. *Journal of Geophysical Research: Atmospheres*, 118(13), pp.7389–7399. Available at: <http://doi.wiley.com/10.1002/jgrd.50561> [Accessed August 6, 2013].
- Dinar, E., Anttila, T. & Rudich, Y., 2008. CCN Activity and Hygroscopic Growth of Organic Aerosols Following Reactive Uptake of Ammonia. *Environmental Science & Technology*, 42(3), pp.793–799. Available at: <http://dx.doi.org/10.1021/es071874p> [Accessed January 19, 2014].
- Djikaev, Y.S., 2003. Effect of adsorption on the uptake of organic trace gas by cloud droplets. *Journal of Geophysical Research*, 108(D22), p.4689. Available at: <http://doi.wiley.com/10.1029/2003JD003741> [Accessed September 10, 2013].
- Docherty, K.S. et al., 2008. Apportionment of Primary and Secondary Organic Aerosols in Southern California during the 2005 Study of Organic Aerosols in Riverside (SOAR-1). *Environmental Science & Technology*, 42(20), pp.7655–7662. Available at: <http://dx.doi.org/10.1021/es8008166> [Accessed August 7, 2013].
- Doezema, L.A. et al., 2012. Analysis of secondary organic aerosols in air using extractive electrospray ionization mass spectrometry (EESI-MS). *RSC Advances*, 2(7), p.2930. Available at: <http://pubs.rsc.org/en/content/articlehtml/2012/ra/c2ra00961g> [Accessed January 4, 2014].
- Dominici, F. et al., 2006. Fine particulate air pollution and hospital admission for cardiovascular and respiratory diseases. *JAMA : the journal of the American Medical Association*, 295(10), pp.1127–34. Available at: <http://jama.jamanetwork.com/article.aspx?articleid=202503> [Accessed August 16, 2012].
- Donaldson, D.J. & Vaida, V., 2006. The influence of organic films at the air-aqueous boundary on atmospheric processes. *Chemical reviews*, 106(4), pp.1445–61. Available at: <http://www.ncbi.nlm.nih.gov/pubmed/16608186> [Accessed August 13, 2013].
- Draxler, R.R. & Hess, G.D., 1998. An overview of the Hysplit 4 modeling system for trajectories, dispersion, and deposition. *Australian Meteorological Magazine*, 47, pp.295–308.

- Drewnick, F. et al., 2005. A New Time-of-Flight Aerosol Mass Spectrometer (TOF-AMS)—Instrument Description and First Field Deployment. *Aerosol Science and Technology*, 39(7), pp.637–658. Available at: <http://www.tandfonline.com/doi/abs/10.1080/02786820500182040> [Accessed March 10, 2012].
- Drewnick, F. et al., 2003. Intercomparison and evaluation of four semi-continuous PM_{2.5} sulfate instruments. *Atmospheric Environment*, 37(24), pp.3335–3350. Available at: [http://dx.doi.org/10.1016/S1352-2310\(03\)00351-0](http://dx.doi.org/10.1016/S1352-2310(03)00351-0) [Accessed August 14, 2013].
- Drewnick, F. et al., 2004. Measurement of Ambient Aerosol Composition During the PMTACS-NY 2001 Using an Aerosol Mass Spectrometer. Part I: Mass Concentrations Special Issue of *Aerosol Science and Technology* on Findings from the Fine Particulate Matter Supersites Program. *Aerosol Science and Technology*, 38(sup1), pp.92–103. Available at: <http://dx.doi.org/10.1080/02786820390229507> [Accessed August 1, 2013].
- Drewnick, F. & Hings, S., 2009. Aerosol quantification with the Aerodyne Aerosol Mass Spectrometer: detection limits and ionizer background effects. *Atmospheric ...*, (2006), pp.33–46. Available at: <http://www.atmos-meas-tech.net/2/33/2009/amt-2-33-2009.html> [Accessed October 24, 2013].
- Dreyfus, M.A. & Johnston, M. V., 2008. Rapid Sampling of Individual Organic Aerosol Species in Ambient Air with the Photoionization Aerosol Mass Spectrometer. *Aerosol Science and Technology*, 42(1), pp.18–27. Available at: <http://dx.doi.org/10.1080/02786820701785112> [Accessed September 12, 2013].
- Duan, F. et al., 2009. Measurements and characteristics of nitrogen-containing compounds in atmospheric particulate matter in Beijing, China. *Bulletin of environmental contamination and toxicology*, 82(3), pp.332–7. Available at: <http://www.ncbi.nlm.nih.gov/pubmed/18806908> [Accessed September 15, 2013].
- Dubovik, O. et al., 2002. Variability of Absorption and Optical Properties of Key Aerosol Types Observed in Worldwide Locations. *Journal of the Atmospheric Sciences*, 59(3), pp.590–608. Available at: [http://journals.ametsoc.org/doi/abs/10.1175/1520-0469\(2002\)059<0590:VOAAOP>2.0.CO;2](http://journals.ametsoc.org/doi/abs/10.1175/1520-0469(2002)059<0590:VOAAOP>2.0.CO;2) [Accessed January 19, 2014].
- Duplissy, J. et al., 2011. Relating hygroscopicity and composition of organic aerosol particulate matter. *Atmospheric Chemistry and Physics*, 11(3), pp.1155–1165. Available at: <http://www.atmos-chem-phys.net/11/1155/2011/> [Accessed May 9, 2012].
- Dusek, U. et al., 2010. Enhanced organic mass fraction and decreased hygroscopicity of cloud condensation nuclei (CCN) during new particle formation events. *Geophysical Research Letters*, 37(3), p.L03804. Available at: <http://www.agu.org/pubs/crossref/2010/2009GL040930.shtml> [Accessed November 6, 2012].
- Dzepina, K. et al., 2007. Detection of particle-phase polycyclic aromatic hydrocarbons in Mexico City using an aerosol mass spectrometer. *International Journal of Mass Spectrometry*, 263(2-3), pp.152–170. Available at: <http://www.deepdyve.com/lp/elsevier/detection-of-particle-phase-polycyclic-aromatic-hydrocarbons-in-mexico-ccIN200tPC/fulltext> [Accessed May 21, 2013].
- Eatough, D.J. et al., 1996. Fine particulate chemical composition and light extinction at Canyonlands National Park using organic particulate material concentrations obtained with a multisystem, multichannel diffusion denuder sampler. *Journal of Geophysical Research*,

- 101(D14), p.19515. Available at: <http://doi.wiley.com/10.1029/95JD01385> [Accessed September 11, 2013].
- Echalar, F. et al., 1995. Aerosol emissions by tropical forest and savanna biomass burning: Characteristic trace elements and fluxes. *Geophysical Research Letters*, 22(22), p.3039. Available at: <http://www.agu.org/pubs/crossref/1995/95GL03170.shtml> [Accessed September 20, 2012].
- Edney, E. et al., 2003. Polar organic oxygenates in PM_{2.5} at a southeastern site in the United States. *Atmospheric Environment*, 37(28), pp.3947–3965. Available at: http://www.researchgate.net/publication/222012777_Polar_organic_oxygenates_in_PM2.5_at_a_southeastern_site_in_the_United_States [Accessed June 25, 2013].
- Eisele, F.L., 1988. First tandem mass spectrometric measurement of tropospheric ions. *Journal of Geophysical Research*, 93(D1), p.716. Available at: <http://doi.wiley.com/10.1029/JD093iD01p00716> [Accessed September 26, 2013].
- Engel-Cox, J.A. & Weber, S.A., 2007. Compilation and Assessment of Recent Positive Matrix Factorization and UNMIX Receptor Model Studies on Fine Particulate Matter Source Apportionment for the Eastern United States. *Journal of the Air & Waste Management Association*, 57(11), p.1307. Available at: <http://connection.ebscohost.com/c/articles/27359224/compilation-assessment-recent-positive-matrix-factorization-unmix-receptor-model-studies-fine-particulate-matter-source-apportionment-eastern-united-states> [Accessed September 25, 2012].
- Erdakos, G.B. & Pankow, J.F., 2004. Gas/particle partitioning of neutral and ionizing compounds to single- and multi-phase aerosol particles. 2. Phase separation in liquid particulate matter containing both polar and low-polarity organic compounds. *Atmospheric Environment*, 38(7), pp.1005–1013. Available at: <http://dx.doi.org/10.1016/j.atmosenv.2003.10.038> [Accessed September 5, 2013].
- Ervens, B., 2004. A modeling study of aqueous production of dicarboxylic acids: 1. Chemical pathways and speciated organic mass production. *Journal of Geophysical Research*, 109(D15), p.D15205. Available at: <http://doi.wiley.com/10.1029/2003JD004387> [Accessed August 10, 2013].
- Ervens, B., George, C., et al., 2003. CAPRAM 2.4 (MODAC mechanism): An extended and condensed tropospheric aqueous phase mechanism and its application. *Journal of Geophysical Research*, 108(D14), p.4426. Available at: <http://doi.wiley.com/10.1029/2002JD002202> [Accessed May 30, 2013].
- Ervens, B. et al., 2013. Dissolved organic carbon (DOC) and select aldehydes in cloud and fog water: the role of the aqueous phase in impacting trace gas budgets. *Atmospheric Chemistry and Physics*, 13(10), pp.5117–5135. Available at: <http://www.atmos-chem-phys.net/13/5117/2013/acp-13-5117-2013.html> [Accessed September 2, 2013].
- Ervens, B., Gligorovski, S. & Herrmann, H., 2003. Temperature-dependent rate constants for hydroxyl radical reactions with organic compounds in aqueous solutions. *Physical Chemistry Chemical Physics*, 5(9), pp.1811–1824. Available at: <http://pubs.rsc.org/en/content/articlehtml/2003/cp/b300072a> [Accessed June 21, 2013].
- Ervens, B., Turpin, B.J. & Weber, R.J., 2011. Secondary organic aerosol formation in cloud droplets and aqueous particles (aqSOA): a review of laboratory, field and model studies. *Atmospheric Chemistry and Physics*, 11(21), pp.11069–11102. Available at: <http://adsabs.harvard.edu/abs/2011ACP....1111069E> [Accessed January 28, 2013].

- Ervens, B. & Volkamer, R., 2010. Glyoxal processing by aerosol multiphase chemistry: towards a kinetic modeling framework of secondary organic aerosol formation in aqueous particles. *Atmospheric Chemistry and Physics*, 10(17), pp.8219–8244. Available at: <http://www.atmos-chem-phys.net/10/8219/2010/acp-10-8219-2010.html> [Accessed June 14, 2013].
- Facchini, M.C. et al., 2008. Important Source of Marine Secondary Organic Aerosol from Biogenic Amines. *Environmental Science & Technology*, 42(24), pp.9116–9121. Available at: <http://dx.doi.org/10.1021/es8018385> [Accessed September 16, 2013].
- Facchini, M.C. et al., 1999. Partitioning of the organic aerosol component between fog droplets and interstitial air. *Journal of Geophysical Research*, 104(D21), p.26821. Available at: <http://doi.wiley.com/10.1029/1999JD900349> [Accessed September 9, 2013].
- Fan, X., Brook, J.R. & Mabury, S.A., 2003. Sampling atmospheric carbonaceous aerosols using an integrated organic gas and particle sampler. *Environmental science & technology*, 37(14), pp.3145–51. Available at: <http://www.ncbi.nlm.nih.gov/pubmed/12901663> [Accessed September 11, 2013].
- Farmer, D.K. et al., 2010. Response of an aerosol mass spectrometer to organonitrates and organosulfates and implications for atmospheric chemistry. Available at: http://cires.colorado.edu/~jjose/Papers/2010_PNAS_Farmer_Complete_Final.pdf [Accessed August 3, 2012].
- Fenn, M.E. et al., 2003. Ecological Effects of Nitrogen Deposition in the Western United States. *BioScience*, 53(4), p.404. Available at: [http://dx.doi.org/10.1641/0006-3568\(2003\)053\[0404:EEONDI\]2.0.CO;2](http://dx.doi.org/10.1641/0006-3568(2003)053[0404:EEONDI]2.0.CO;2) [Accessed August 16, 2012].
- Finlayson-Pitts, B.J. & Pitts, J.N., 2000. *Chemistry of the Upper and Lower Atmosphere: Theory, Experiments, and Applications (Google eBook)* 2nd ed., Academic Press. Available at: <http://books.google.com/books?id=mRoJUB5fxRwC&pgis=1> [Accessed June 22, 2013].
- Fischer, M. & Warneck, P., 1996. Photodecomposition of Nitrite and Undissociated Nitrous Acid in Aqueous Solution. *The Journal of Physical Chemistry*, 100(48), pp.18749–18756. Available at: <http://pubs.acs.org/doi/abs/10.1021/jp961692+> [Accessed June 24, 2013].
- Fornaro, A. & Gutz, I.G.R., 2003. Wet deposition and related atmospheric chemistry in the São Paulo metropolis, Brazil: Part 2—contribution of formic and acetic acids. *Atmospheric Environment*, 37(1), pp.117–128. Available at: <http://www.sciencedirect.com/science/article/pii/S1352231002008853> [Accessed October 2, 2013].
- Foster, D.R. et al., 1997. Forest response to disturbance and anthropogenic stress. *BioScience*, pp.437–445. Available at: <http://www.jstor.org/stable/10.2307/1313059> [Accessed August 15, 2012].
- Froyd, K.D. et al., 2010. Contribution of isoprene-derived organosulfates to free tropospheric aerosol mass. *Proceedings of the National Academy of Sciences of the United States of America*, 107(50), pp.21360–5. Available at: <http://www.pnas.org/content/107/50/21360.full> [Accessed June 17, 2013].
- Fry, J.L. et al., 2009. Organic nitrate and secondary organic aerosol yield from NO₃ oxidation of β-pinene evaluated using a gas-phase kinetics/aerosol partitioning model. *Atmospheric Chemistry and Physics*, 9(4), pp.1431–1449. Available at: <http://www.atmos-chem-phys.net/9/1431/2009/acp-9-1431-2009.html> [Accessed September 6, 2013].
- Fu, P. et al., 2010. Contributions of biogenic volatile organic compounds to the formation of secondary organic aerosols over Mt. Tai, Central East China. *Atmospheric Environment*,

- 44(38), pp.4817–4826. Available at:
<http://eprints.lib.hokudai.ac.jp/dspace/handle/2115/44492> [Accessed May 24, 2013].
- Fu, T.-M. et al., 2008. Global budgets of atmospheric glyoxal and methylglyoxal, and implications for formation of secondary organic aerosols. *Journal of Geophysical Research*, 113(D15), p.D15303. Available at: <http://doi.wiley.com/10.1029/2007JD009505> [Accessed May 26, 2013].
- Fu, T.M. & Jacob, D.J., 2009. Aqueous-Phase Reactive Uptake of Dicarbonyls as a Source of Organic Aerosol Over Eastern North America. *Atmospheric Environment*, 43, pp.1814–1822. Available at: http://www.researchgate.net/publication/41060207_Aqueous-Phase_Reactive_Uptake_of_Dicarbonyls_as_a_Source_of_Organic_Aerosol_Over_Eastern_North_America [Accessed September 9, 2013].
- Fuzzi, S. et al., 2001. A simplified model of the water soluble organic component of atmospheric aerosols. *Geophysical Research Letters*, 28(21), pp.4079–4082. Available at: <http://doi.wiley.com/10.1029/2001GL013418> [Accessed September 9, 2013].
- Fuzzi, S. et al., 2007. Overview of the inorganic and organic composition of size-segregated aerosol in Rondônia, Brazil, from the biomass-burning period to the onset of the wet season. *Journal of Geophysical Research*, 112(D1), p.D01201. Available at: <http://doi.wiley.com/10.1029/2005JD006741> [Accessed September 20, 2012].
- Fuzzi, S. & Andreae, M., 2006. Critical assessment of the current state of scientific knowledge, terminology, and research needs concerning the role of organic aerosols in the atmosphere, climate, and global change. *Atmospheric ...*, pp.2017–2038. Available at: <http://www.atmos-chem-phys.net/6/2017/2006/acp-6-2017-2006.pdf> [Accessed July 14, 2013].
- Gallagher, J.P. et al., 2011. Seasonal and Diurnal Variations in Aerosol Concentration on Whistler Mountain: Boundary Layer Influence and Synoptic-Scale Controls. *Journal of Applied Meteorology and Climatology*, 50(11), pp.2210–2222. Available at: <http://journals.ametsoc.org/doi/abs/10.1175/JAMC-D-11-028.1> [Accessed August 25, 2013].
- Gallimore, P.J. & Kalberer, M., 2013. Characterizing an extractive electrospray ionization (EESI) source for the online mass spectrometry analysis of organic aerosols. *Environmental science & technology*, 47(13), pp.7324–31. Available at: <http://dx.doi.org/10.1021/es305199h> [Accessed January 4, 2014].
- Galloway, J.N. et al., 2004. *Nitrogen cycles : past , present , and future*,
- Galloway, J.N. et al., 2008. Transformation of the nitrogen cycle: recent trends, questions, and potential solutions. *Science (New York, N.Y.)*, 320(5878), pp.889–92. Available at: <http://www.sciencemag.org/content/320/5878/889.abstract> [Accessed July 20, 2012].
- Galloway, M.M. et al., 2011. Analysis of photochemical and dark glyoxal uptake: Implications for SOA formation. *Geophysical Research Letters*, 38(17), p.n/a–n/a. Available at: <http://doi.wiley.com/10.1029/2011GL048514> [Accessed June 24, 2013].
- Galloway, M.M. et al., 2009. Glyoxal uptake on ammonium sulphate seed aerosol: reaction products and reversibility of uptake under dark and irradiated conditions. *Atmospheric Chemistry and Physics*, 9(10), pp.3331–3345. Available at: <http://www.atmos-chem-phys.net/9/3331/2009/acp-9-3331-2009.html> [Accessed June 24, 2013].
- Gao, S. et al., 2004. Low-Molecular-Weight and Oligomeric Components in Secondary Organic Aerosol from the Ozonolysis of Cycloalkenes and α -Pinene. *The Journal of Physical*

- Chemistry A*, 108(46), pp.10147–10164. Available at: <http://dx.doi.org/10.1021/jp047466e> [Accessed June 24, 2013].
- Gao, Y., Hall, W.A. & Johnston, M. V, 2010. Molecular composition of monoterpene secondary organic aerosol at low mass loading. *Environmental science & technology*, 44(20), pp.7897–902. Available at: <http://adsabs.harvard.edu/abs/2010EnST...44.7897G> [Accessed August 7, 2013].
- Ge, X. et al., 2012. Effect of aqueous-phase processing on aerosol chemistry and size distributions in Fresno, California, during wintertime. *Environmental Chemistry*, 9(3), p.221. Available at: http://www.publish.csiro.au/view/journals/dsp_journal_fulltext.cfm?nid=188&f=EN11168 [Accessed February 19, 2013].
- Gebhart, K.A. et al., 2011. Back-trajectory-based source apportionment of airborne sulfur and nitrogen concentrations at Rocky Mountain National Park, Colorado, USA. *Atmospheric Environment*, 45(3), pp.621–633. Available at: <http://dx.doi.org/10.1016/j.atmosenv.2010.10.035> [Accessed October 9, 2012].
- Gelencsér, A. et al., 2003. In-situ Formation of Light-Absorbing Organic Matter in Cloud Water. *Journal of Atmospheric Chemistry*, 45(1), pp.25–33. Available at: <http://link.springer.com/article/10.1023/A:1024060428172> [Accessed September 10, 2013].
- George, I.J. & Abbatt, J.P.D., 2010. Chemical evolution of secondary organic aerosol from OH-initiated heterogeneous oxidation. *Atmospheric Chemistry and Physics*, 10(12), pp.5551–5563. Available at: <http://www.atmos-chem-phys.net/10/5551/2010/acp-10-5551-2010.html> [Accessed July 30, 2013].
- Givati, A. & Rosenfeld, D., 2004. Quantifying Precipitation Suppression Due to Air Pollution. *Journal of Applied Meteorology*, 43(7), pp.1038–1056. Available at: [http://journals.ametsoc.org/doi/abs/10.1175/1520-0450\(2004\)043<1038:QPSDTA>2.0.CO;2](http://journals.ametsoc.org/doi/abs/10.1175/1520-0450(2004)043<1038:QPSDTA>2.0.CO;2) [Accessed June 12, 2013].
- Glotfelty, D.E., Seiber, J.N. & Liljedahl, L.A., 1987. Pesticides in fog. *Nature*, 325(6105), pp.602–5. Available at: <http://dx.doi.org/10.1038/325602a0> [Accessed September 10, 2013].
- Goldberg, E.D., 1985. *Black Carbon in the Environment: Properties and Distribution (Environmental Science and Technology Series)*, John Wiley & Sons Inc. Available at: <http://www.amazon.com/Black-Carbon-Environment-Distribution-Environmental/dp/0471819794> [Accessed July 15, 2013].
- Goldstein, A. & Galbally, I., 2007. Known and Unexplored Organic Constituents in the Earth's Atmosphere. *Environmental Science and Technology*, pp.1515 – 1521. Available at: <http://www.citeulike.org/user/rdsaylor/article/1283626> [Accessed September 12, 2013].
- Gómez-González, Y. et al., 2008. Characterization of organosulfates from the photooxidation of isoprene and unsaturated fatty acids in ambient aerosol using liquid chromatography/(-) electrospray ionization mass spectrometry. *Journal of mass spectrometry : JMS*, 43(3), pp.371–82. Available at: <http://www.ncbi.nlm.nih.gov/pubmed/17968849> [Accessed May 26, 2013].
- Gorzelska, K. et al., 1992. Water-soluble primary amine compounds in rural continental precipitation. *Atmospheric Environment. Part A. General Topics*, 26(6), pp.1005–1018. Available at: [http://dx.doi.org/10.1016/0960-1686\(92\)90032-G](http://dx.doi.org/10.1016/0960-1686(92)90032-G) [Accessed September 15, 2013].

- De Gouw, J.A. et al., 2008. Sources of particulate matter in the northeastern United States in summer: 1. Direct emissions and secondary formation of organic matter in urban plumes. *Journal of Geophysical Research*, 113(D8), p.D08301. Available at: <http://doi.wiley.com/10.1029/2007JD009243> [Accessed August 14, 2013].
- Graedel, T.E. & Goldberg, K.I., 1983. Kinetic studies of raindrop chemistry: 1. Inorganic and organic processes. *Journal of Geophysical Research*, 88(C15), p.10865. Available at: <http://doi.wiley.com/10.1029/JC088iC15p10865> [Accessed June 24, 2013].
- Graedel, T.E. & Weschler, C.J., 1981. Chemistry within aqueous atmospheric aerosols and raindrops. *Reviews of Geophysics*, 19(4), p.505. Available at: <http://doi.wiley.com/10.1029/RG019i004p00505> [Accessed June 24, 2013].
- Grant, A.N., Pszenny, A.A.P. & Fischer, E. V., 2005. The 1935–2003 Air Temperature Record from the Summit of Mount Washington, New Hampshire. *Journal of Climate*, 18(21), pp.4445–4453. Available at: <http://journals.ametsoc.org/doi/abs/10.1175/JCLI3547.1> [Accessed October 3, 2013].
- Grieshop, a. P., Logue, J.M., et al., 2009. Laboratory investigation of photochemical oxidation of organic aerosol from wood fires 1: measurement and simulation of organic aerosol evolution. *Atmospheric Chemistry and Physics*, 9(4), pp.1263–1277. Available at: <http://www.atmos-chem-phys.net/9/1263/2009/>.
- Grieshop, a. P., Donahue, N.M. & Robinson, a. L., 2009. Laboratory investigation of photochemical oxidation of organic aerosol from wood fires 2: analysis of aerosol mass spectrometer data. *Atmospheric Chemistry and Physics*, 9(6), pp.2227–2240. Available at: <http://www.atmos-chem-phys.net/9/2227/2009/>.
- Grosjean, D., 1975. Solvent extraction and organic carbon determination in atmospheric particulate matter: the organic extraction-organic carbon analyzer (OE-OCA) technique. *Analytical chemistry*, 47(6), pp.797–805. Available at: <http://www.ncbi.nlm.nih.gov/pubmed/1137157> [Accessed September 11, 2013].
- Gross, D.S. et al., 2006. Real-time measurement of oligomeric species in secondary organic aerosol with the aerosol time-of-flight mass spectrometer. *Analytical chemistry*, 78(7), pp.2130–7. Available at: <http://www.ncbi.nlm.nih.gov/pubmed/16579590> [Accessed August 7, 2013].
- Guenther, A. et al., 1995. A global model of natural volatile organic compound emissions. *Journal of Geophysical Research*, 100(D5), p.8873. Available at: <http://doi.wiley.com/10.1029/94JD02950> [Accessed September 5, 2013].
- Guenther, A., 2000. Natural emissions of non-methane volatile organic compounds, carbon monoxide, and oxides of nitrogen from North America. *Atmospheric Environment*, 34(12-14), pp.2205–2230. Available at: [http://dx.doi.org/10.1016/S1352-2310\(99\)00465-3](http://dx.doi.org/10.1016/S1352-2310(99)00465-3) [Accessed September 6, 2013].
- Guzman, M.I., Colussi, A.J. & Hoffmann, M.R., 2006. Photoinduced oligomerization of aqueous pyruvic acid. *The journal of physical chemistry. A*, 110(10), pp.3619–26. Available at: <http://www.ncbi.nlm.nih.gov/pubmed/16526643> [Accessed June 24, 2013].
- De Haan, D.O. et al., 2011. Formation of nitrogen-containing oligomers by methylglyoxal and amines in simulated evaporating cloud droplets. *Environmental science & technology*, 45(3), pp.984–91. Available at: <http://dx.doi.org/10.1021/es102933x> [Accessed June 24, 2013].
- De Haan, D.O., Corrigan, A.L., Tolbert, M.A., et al., 2009. Secondary organic aerosol formation by self-reactions of methylglyoxal and glyoxal in evaporating droplets. *Environmental*

- science & technology*, 43(21), pp.8184–90. Available at: <http://dx.doi.org/10.1021/es902152t> [Accessed June 24, 2013].
- De Haan, D.O., Corrigan, A.L., Smith, K.W., et al., 2009. Secondary Organic Aerosol-Forming Reactions of Glyoxal with Amino Acids. *Environmental Science & Technology*, 43(8), pp.2818–2824. Available at: <http://pubs.acs.org/doi/abs/10.1021/es803534f> [Accessed May 9, 2012].
- De Haan, D.O., Tolbert, M.A. & Jimenez, J.L., 2009. Atmospheric condensed-phase reactions of glyoxal with methylamine. *Geophysical Research Letters*, 36(11), p.L11819. Available at: <http://doi.wiley.com/10.1029/2009GL037441> [Accessed May 26, 2013].
- El Haddad, I. et al., 2009. In-cloud processes of methacrolein under simulated conditions – Part 2: Formation of secondary organic aerosol. *Atmospheric Chemistry and Physics*, 9(14), pp.5107–5117. Available at: <http://www.atmos-chem-phys.net/9/5107/2009/acp-9-5107-2009.html> [Accessed June 25, 2013].
- Hakola, H. et al., 1994. Product formation from the gas-phase reactions of OH radicals and O₃ with a series of monoterpenes. *Journal of Atmospheric Chemistry*, 18(1), pp.75–102. Available at: <http://link.springer.com/10.1007/BF00694375> [Accessed June 25, 2013].
- Hallquist, M., 2009. The formation, properties and impact of secondary organic aerosol: current and emerging issues. ... *and Physics*, (November 2008), pp.5155–5236. Available at: <http://www.atmos-chem-phys.net/9/5155/> [Accessed September 10, 2013].
- Hamilton, J.F. et al., 2004. Partially oxidised organic components in urban aerosol using GCXGC-TOF/MS. *Atmospheric Chemistry and Physics*, 4(5), pp.1279–1290. Available at: <http://www.atmos-chem-phys.net/4/1279/2004/acp-4-1279-2004.html> [Accessed July 14, 2013].
- Hansen, J., 2005. Efficacy of climate forcings. *Journal of Geophysical Research*, 110(D18), p.D18104. Available at: <http://doi.wiley.com/10.1029/2005JD005776> [Accessed May 28, 2013].
- Hansen, J., Sato, M. & Ruedy, R., 1997. Radiative forcing and climate response. *Journal of Geophysical Research*, 102(D6), p.6831. Available at: <http://doi.wiley.com/10.1029/96JD03436> [Accessed July 14, 2013].
- Härdle, W., 1992. *Applied Nonparametric Regression (Econometric Society Monographs)*, Cambridge University Press. Available at: <http://www.amazon.com/Applied-Nonparametric-Regression-Econometric-Monographs/dp/0521429501> [Accessed September 17, 2013].
- Harris, D.C., 2007. *Quantitative Chemical Analysis*, W. H. Freeman. Available at: <http://www.amazon.com/Quantitative-Chemical-Analysis-E-Book-Daniel/dp/1429203080> [Accessed August 30, 2013].
- Hatch, L.E. et al., 2011a. Measurements of Isoprene-Derived Organosulfates in Ambient Aerosols by Aerosol Time-of-Flight Mass Spectrometry - Part 1: Single Particle Atmospheric Observations in Atlanta. *Environmental Science & Technology*, 45(12), pp.5105–5111. Available at: <http://dx.doi.org/10.1021/es103944a> [Accessed June 25, 2013].
- Hatch, L.E. et al., 2011b. Measurements of Isoprene-Derived Organosulfates in Ambient Aerosols by Aerosol Time-of-Flight Mass Spectrometry—Part 2: Temporal Variability and Formation Mechanisms. *Environmental Science & Technology*, 45(20), pp.8648–8655. Available at: <http://dx.doi.org/10.1021/es2011836> [Accessed June 25, 2013].

- Havers, N. et al., 1998. Spectroscopic Characterization of Humic-Like Substances in Airborne Particulate Matter. *Journal of Atmospheric Chemistry*, 29(1), pp.45–54. Available at: <http://link.springer.com/article/10.1023/A:1005875225800> [Accessed September 9, 2013].
- He, L.-Y. et al., 2010. Characterization of high-resolution aerosol mass spectra of primary organic aerosol emissions from Chinese cooking and biomass burning. *Atmospheric Chemistry and Physics*, 10(23), pp.11535–11543. Available at: <http://www.atmos-chem-phys.net/10/11535/2010/> [Accessed May 9, 2012].
- Heald, C.L. et al., 2005. A Large Organic Aerosol Source in the Free Troposphere Missing from Current Models. Available at: <http://dash.harvard.edu/handle/1/3829250> [Accessed June 26, 2013].
- Heald, C.L. et al., 2010. A simplified description of the evolution of organic aerosol composition in the atmosphere. *Geophysical Research Letters*, 37(8), p.L08803. Available at: <http://www.agu.org/pubs/crossref/2010/2010GL042737.shtml> [Accessed February 12, 2013].
- Heald, C.L. et al., 2006. Concentrations and sources of organic carbon aerosols in the free troposphere over North America. *Journal of Geophysical Research*, 111(D23), p.D23S47. Available at: <http://doi.wiley.com/10.1029/2006JD007705> [Accessed May 23, 2013].
- Heald, C.L. et al., 2011. Exploring the vertical profile of atmospheric organic aerosol: comparing 17 aircraft field campaigns with a global model. *Atmospheric Chemistry and Physics*, 11(24), pp.12673–12696. Available at: <http://www.atmos-chem-phys.net/11/12673/2011/acp-11-12673-2011.html> [Accessed June 14, 2013].
- Hearn, J.D. & Smith, G.D., 2006. Reactions and mass spectra of complex particles using Aerosol CIMS. *International Journal of Mass Spectrometry*, 258(1-3), pp.95–103. Available at: <http://dx.doi.org/10.1016/j.ijms.2006.05.017> [Accessed September 12, 2013].
- Hellén, H. et al., 2008. Using Proton Transfer Reaction Mass Spectrometry for Online Analysis of Secondary Organic Aerosols. *Environmental Science & Technology*, 42(19), pp.7347–7353. Available at: <http://dx.doi.org/10.1021/es801279m> [Accessed September 12, 2013].
- Hennigan, C.J. et al., 2008. Enhanced secondary organic aerosol formation due to water uptake by fine particles. *Geophysical Research Letters*, 35(18), p.L18801. Available at: <http://doi.wiley.com/10.1029/2008GL035046> [Accessed August 14, 2013].
- Hennigan, C.J. et al., 2009. Gas/particle partitioning of water-soluble organic aerosol in Atlanta. *Atmospheric Chemistry and Physics*, 9(11), pp.3613–3628. Available at: <http://www.atmos-chem-phys.net/9/3613/2009/acp-9-3613-2009.html> [Accessed September 5, 2013].
- Henry, R.C., 1987. Current factor analysis receptor models are ill-posed. *Atmospheric Environment (1967)*, 21(8), pp.1815–1820. Available at: [http://dx.doi.org/10.1016/0004-6981\(87\)90122-3](http://dx.doi.org/10.1016/0004-6981(87)90122-3) [Accessed September 13, 2013].
- Henry, R.C., Chang, Y.-S. & Spiegelman, C.H., 2002. Locating nearby sources of air pollution by nonparametric regression of atmospheric concentrations on wind direction. *Atmospheric Environment*, 36(13), pp.2237–2244. Available at: [http://dx.doi.org/10.1016/S1352-2310\(02\)00164-4](http://dx.doi.org/10.1016/S1352-2310(02)00164-4) [Accessed September 13, 2013].
- Henry, R.C. & Kim, B.M., 1990. Extension of self-modeling curve resolution to mixtures of more than three components. *Chemometrics and Intelligent Laboratory Systems*, 8(2), pp.205–216. Available at: [http://dx.doi.org/10.1016/0169-7439\(90\)80136-T](http://dx.doi.org/10.1016/0169-7439(90)80136-T) [Accessed September 13, 2013].

- Henze, D.K. & Seinfeld, J.H., 2006. Global secondary organic aerosol from isoprene oxidation. *Geophysical Research Letters*, 33(9), p.L09812. Available at: <http://doi.wiley.com/10.1029/2006GL025976> [Accessed August 14, 2013].
- Herckes, P., Leenheer, J. & Collett, J.J., 2007. Comprehensive characterization of atmospheric organic matter in Fresno, California fog water. *Environ Sci Technol*, 41(2), pp.393–9.
- Herckes, P., Valsaraj, K.T. & Collett, J.L., 2013. A review of observations of organic matter in fogs and clouds: Origin, processing and fate. *Atmospheric Research*, 132-133(null), pp.434–449. Available at: <http://dx.doi.org/10.1016/j.atmosres.2013.06.005> [Accessed August 10, 2013].
- Hering, S.V. & Friedlander, S.K., 1982. Origins of aerosol sulfur size distributions in the Los Angeles basin. *Atmospheric Environment (1967)*, 16(11), pp.2647–2656. Available at: [http://dx.doi.org/10.1016/0004-6981\(82\)90346-8](http://dx.doi.org/10.1016/0004-6981(82)90346-8) [Accessed September 10, 2013].
- Heringa, M.F. et al., 2012. A new method to discriminate secondary organic aerosols from different sources using high-resolution aerosol mass spectra. *Atmospheric Chemistry and Physics*, 12(4), pp.2189–2203. Available at: <http://www.atmos-chem-phys.net/12/2189/2012/> [Accessed March 11, 2012].
- Herrmann, H., 2003. Kinetics of aqueous phase reactions relevant for atmospheric chemistry. *Chemical reviews*, 103(12), pp.4691–716. Available at: http://www.researchgate.net/publication/8968396_Kinetics_of_aqueous_phase_reactions_relevant_for_atmospheric_chemistry [Accessed June 24, 2013].
- Herrmann, H. et al., 2010. Tropospheric aqueous-phase free-radical chemistry: radical sources, spectra, reaction kinetics and prediction tools. *Chemphyschem : a European journal of chemical physics and physical chemistry*, 11(18), pp.3796–822. Available at: <http://www.ncbi.nlm.nih.gov/pubmed/21120981> [Accessed June 24, 2013].
- Hoffer, A., 2004. Chemical characterization of humic-like substances (HULIS) formed from a lignin-type precursor in model cloud water. *Geophysical Research Letters*, 31(6), p.L06115. Available at: <http://doi.wiley.com/10.1029/2003GL018962> [Accessed September 10, 2013].
- Hoffmann, T. et al., 1997. Formation of Organic Aerosols from the Oxidation of Biogenic Hydrocarbons. *Journal of Atmospheric Chemistry*, 26(2), pp.189–222. Available at: <http://link.springer.com/article/10.1023/A:1005734301837> [Accessed September 5, 2013].
- Hogrefe, O. et al., 2004. Semicontinuous PM_{2.5} sulfate and nitrate measurements at an urban and a rural location in New York: PMTACS-NY summer 2001 and 2002 campaigns. *Journal of the Air & Waste Management Association (1995)*, 54(9), pp.1040–60. Available at: <http://www.ncbi.nlm.nih.gov/pubmed/15468658> [Accessed September 12, 2013].
- Hopke, P.K., 2003. Recent developments in receptor modeling. *Journal of Chemometrics*, 17(5), pp.255–265. Available at: <http://doi.wiley.com/10.1002/cem.796> [Accessed September 13, 2013].
- Hopke, P.K. et al., 1998. Three-way (PARAFAC) factor analysis: examination and comparison of alternative computational methods as applied to ill-conditioned data. *Chemometrics and Intelligent Laboratory Systems*, 43(1-2), pp.25–42. Available at: [http://dx.doi.org/10.1016/S0169-7439\(98\)00077-X](http://dx.doi.org/10.1016/S0169-7439(98)00077-X) [Accessed September 13, 2013].
- Hoppel, W.A. et al., 1994. Marine boundary layer measurements of new particle formation and the effects nonprecipitating clouds have on aerosol size distribution. *Journal of Geophysical Research*, 99(D7), p.14443. Available at: <http://doi.wiley.com/10.1029/94JD00797> [Accessed September 10, 2013].

- Horan, A.J. et al., 2012. Online characterization of particles and gases with an ambient electrospray ionization source. *Analytical chemistry*, 84(21), pp.9253–8. Available at: <http://dx.doi.org/10.1021/ac302024y> [Accessed January 4, 2014].
- Hoyle, C.R. et al., 2011. A review of the anthropogenic influence on biogenic secondary organic aerosol. *Atmospheric Chemistry and Physics*, 11(1), pp.321–343. Available at: <http://www.atmos-chem-phys.net/11/321/2011/> [Accessed May 9, 2012].
- Hoyle, C.R. et al., 2007. Secondary organic aerosol in the global aerosol – chemical transport model Oslo CTM2. *Atmospheric Chemistry and Physics*, 7(21), pp.5675–5694. Available at: <http://www.atmos-chem-phys.net/7/5675/2007/acp-7-5675-2007.html> [Accessed September 5, 2013].
- Huang, D. et al., 2011. The kinetics and mechanism of an aqueous phase isoprene reaction with hydroxyl radical. *Atmospheric Chemistry and Physics*, 11(15), pp.7399–7415. Available at: <http://www.atmos-chem-phys.net/11/7399/2011/acp-11-7399-2011.html> [Accessed June 25, 2013].
- Huang, S., Rahn, K.A. & Arimoto, R., 1999. Testing and optimizing two factor-analysis techniques on aerosol at Narragansett, Rhode Island. *Atmospheric Environment*, 33(14), pp.2169–2185. Available at: [http://dx.doi.org/10.1016/S1352-2310\(98\)00324-0](http://dx.doi.org/10.1016/S1352-2310(98)00324-0) [Accessed September 13, 2013].
- Huang, X.-F. et al., 2011. Characterization of submicron aerosols at a rural site in Pearl River Delta of China using an Aerodyne High-Resolution Aerosol Mass Spectrometer. *Atmospheric Chemistry and Physics*, 11(5), pp.1865–1877. Available at: <http://www.atmos-chem-phys.net/11/1865/2011/acp-11-1865-2011.html> [Accessed September 26, 2013].
- Huffman, J.A. et al., 2005. Design, modeling, optimization, and experimental tests of a particle beam width probe for the aerodyne aerosol mass spectrometer. *Aerosol Science & Technology*, 39(12).
- Inuma, Y. et al., 2004. Aerosol-chamber study of the α -pinene/O₃ reaction: influence of particle acidity on aerosol yields and products. *Atmospheric Environment*, 38(5), pp.761–773. Available at: <http://dx.doi.org/10.1016/j.atmosenv.2003.10.015> [Accessed August 7, 2013].
- Inuma, Y. et al., 2007. Source characterization of biomass burning particles: The combustion of selected European conifers, African hardwood, savanna grass, and German and Indonesian peat. *Journal of Geophysical Research*, 112(D8), p.D08209. Available at: <http://www.agu.org/pubs/crossref/2007/2006JD007120.shtml> [Accessed November 21, 2012].
- Ip, H.S.S., Huang, X.H.H. & Yu, J.Z., 2009. Effective Henry's law constants of glyoxal, glyoxylic acid, and glycolic acid. *Geophysical Research Letters*, 36(1), p.L01802. Available at: <http://doi.wiley.com/10.1029/2008GL036212> [Accessed June 25, 2013].
- IPCC, W.G. 1, 2007. *Climate Change 2007 - The Physical Science Basis: Working Group I Contribution to the Fourth Assessment Report of the IPCC*, Cambridge University Press. Available at: http://books.google.com/books/about/Climate_Change_2007_The_Physical_Science.html?id=8-m8nXB8GB4C&pgis=1 [Accessed July 14, 2013].
- Iraci, L. et al., 1999. Measurements of the Henry's law coefficients of 2-methyl-3-buten-2-ol, methacrolein, and methylvinyl ketone. *J. Atmospheric Chemistry*, 33, pp.321–330.
- Jacob, D.J., 1986. Chemistry of OH in remote clouds and its role in the production of formic acid and peroxy monosulfate. *Journal of Geophysical Research*, 91(D9), p.9807. Available at: <http://doi.wiley.com/10.1029/JD091iD09p09807> [Accessed September 1, 2013].

- Jacob, D.J., 2005. Global budget of methanol: Constraints from atmospheric observations. *Journal of Geophysical Research*, 110(D8), p.D08303. Available at: <http://doi.wiley.com/10.1029/2004JD005172> [Accessed June 26, 2013].
- Jacobson, M.C. et al., 2000. Organic atmospheric aerosols: Review and state of the science. *Reviews of Geophysics*, 38(2), p.267. Available at: <http://doi.wiley.com/10.1029/1998RG000045> [Accessed August 8, 2013].
- Jang, M. et al., 2002. Heterogeneous atmospheric aerosol production by acid-catalyzed particle-phase reactions. *Science (New York, N.Y.)*, 298(5594), pp.814–7. Available at: <http://www.sciencemag.org/content/298/5594/814.abstract> [Accessed June 24, 2013].
- Jang, M., 1999. Newly characterized products and composition of secondary aerosols from the reaction of α -pinene with ozone. *Atmospheric Environment*, 33(3), pp.459–474. Available at: [http://dx.doi.org/10.1016/S1352-2310\(98\)00222-2](http://dx.doi.org/10.1016/S1352-2310(98)00222-2) [Accessed June 25, 2013].
- Jang, M. & Kamens, R.M., 2001. Characterization of Secondary Aerosol from the Photooxidation of Toluene in the Presence of NO_x and 1-Propene. Available at: <http://pubs.acs.org/doi/abs/10.1021/es010676+> [Accessed June 24, 2013].
- Jayne, J. et al., 2000. Development of an aerosol mass spectrometer for size and composition analysis of submicron particles. *Aerosol Science and Technology*, 33, pp.49–70. Available at: http://hero.epa.gov/index.cfm?action=reference.details&reference_id=190978 [Accessed October 29, 2012].
- Jimenez, J.L., 2003. Ambient aerosol sampling using the Aerodyne Aerosol Mass Spectrometer. *Journal of Geophysical Research*, 108(D7), p.8425. Available at: <http://doi.wiley.com/10.1029/2001JD001213> [Accessed May 23, 2013].
- Jimenez, J.L. et al., 2009. Evolution of organic aerosols in the atmosphere. *Science (New York, N.Y.)*, 326(5959), pp.1525–9. Available at: <http://www.ncbi.nlm.nih.gov/pubmed/20007897> [Accessed April 4, 2012].
- Jirak, I.L. & Cotton, W.R., 2006. Effect of Air Pollution on Precipitation along the Front Range of the Rocky Mountains. *Journal of Applied Meteorology and Climatology*, 45(1), pp.236–245. Available at: <http://journals.ametsoc.org/doi/abs/10.1175/JAM2328.1> [Accessed September 11, 2012].
- John, W. et al., 1990. Modes in the size distributions of atmospheric inorganic aerosol. *Atmospheric Environment. Part A. General Topics*, 24(9), pp.2349–2359. Available at: [http://dx.doi.org/10.1016/0960-1686\(90\)90327-J](http://dx.doi.org/10.1016/0960-1686(90)90327-J) [Accessed September 10, 2013].
- Johnson, B.T., 2005. The Semidirect Aerosol Effect: Comparison of a Single-Column Model with Large Eddy Simulation for Marine Stratocumulus. *Journal of Climate*, 18(1), pp.119–130. Available at: <http://journals.ametsoc.org/doi/abs/10.1175/JCLI-3233.1> [Accessed July 14, 2013].
- Kalberer, M. et al., 2000. Aerosol Formation in the Cyclohexene-Ozone System. *Environmental Science & Technology*, 34(23), pp.4894–4901. Available at: http://www.researchgate.net/publication/225089678_Aerosol_formation_in_the_cyclohexene-ozone_system [Accessed September 6, 2013].
- Kalberer, M. et al., 2004. Identification of polymers as major components of atmospheric organic aerosols. *Science (New York, N.Y.)*, 303(5664), pp.1659–62. Available at: <http://www.sciencemag.org/content/303/5664/1659.abstract> [Accessed August 7, 2013].
- Kamens, R. et al., 1999. Aerosol Formation from the Reaction of α -Pinene and Ozone Using a Gas-Phase Kinetics-Aerosol Partitioning Model. *Environmental Science & Technology*, 33(9), pp.1430–1438. Available at:

- http://www.researchgate.net/publication/231291395_Aerosol_Formation_from_the_Reaction_of_Pinene_and_Ozone_Using_a_Gas-Phase_Kinetics-Aerosol_Partitioning_Model [Accessed August 7, 2013].
- Kamens, R.M. & Coe, D.L., 1977. A Large Gas-Phase Stripping Device to Investigate Rate of PAH Evaporation from Airborne Diesel Soot Particles. *Environmental Science and Technology*, 31(6). Available at: <http://trid.trb.org/view.aspx?id=575835> [Accessed September 11, 2013].
- Kanakidou, M. et al., 2005. Organic aerosol and global climate modelling: a review. *Atmospheric Chemistry and Physics*, 5(4), pp.1053–1123. Available at: <http://www.atmos-chem-phys.net/5/1053/2005/>.
- Kang, E. et al., 2007. Introducing the concept of Potential Aerosol Mass (PAM). *Atmospheric Chemistry and Physics*, 7(22), pp.5727–5744. Available at: <http://www.atmos-chem-phys.net/7/5727/2007/>.
- Kang, E., Toohey, D.W. & Brune, W.H., 2011. Dependence of SOA oxidation on organic aerosol mass concentration and OH exposure: experimental PAM chamber studies. *Atmospheric Chemistry and Physics*, 11(4), pp.1837–1852. Available at: <http://www.atmos-chem-phys.net/11/1837/2011/> [Accessed May 9, 2012].
- Karamchandani, P. & Venkatram, A., 1992. The role of non-precipitating clouds in producing ambient sulfate during summer: Results from simulations with the Acid Deposition and Oxidant Model (ADOM). *Atmospheric Environment. Part A. General Topics*, 26(6), pp.1041–1052. Available at: [http://dx.doi.org/10.1016/0960-1686\(92\)90036-K](http://dx.doi.org/10.1016/0960-1686(92)90036-K) [Accessed September 10, 2013].
- Kavouras, I.G., Mihalopoulos, N. & Stephanou, E.G., 1998. Formation of atmospheric particles from organic acids produced by forests. *Atmospheric Environment*, 32(19), pp.683–686. Available at: <http://dx.doi.org/10.1038/27179> [Accessed August 2, 2013].
- Kawamura, K. et al., 2012. Low molecular weight (C1–C10) monocarboxylic acids, dissolved organic carbon and major inorganic ions in alpine snow pit sequence from a high mountain site, central Japan. *Atmospheric Environment*, 62, pp.272–280. Available at: <http://www.sciencedirect.com/science/article/pii/S135223101200790X> [Accessed October 2, 2013].
- Kawamura, K., 2003. Water-soluble dicarboxylic acids in the tropospheric aerosols collected over east Asia and western North Pacific by ACE-Asia C-130 aircraft. *Journal of Geophysical Research*, 108(D23), p.8639. Available at: <http://doi.wiley.com/10.1029/2002JD003256> [Accessed June 14, 2013].
- Kawamura, K., IMAI, Y. & BARRIE, L., 2005. Photochemical production and loss of organic acids in high Arctic aerosols during long-range transport and polar sunrise ozone depletion events. *Atmospheric Environment*, 39(4), pp.599–614. Available at: <http://dx.doi.org/10.1016/j.atmosenv.2004.10.020> [Accessed June 25, 2013].
- Kawamura, K. & Sakaguchi, F., 1999. Molecular distributions of water soluble dicarboxylic acids in marine aerosols over the Pacific Ocean including tropics. *Journal of Geophysical Research*, 104(D3), p.3501. Available at: <http://doi.wiley.com/10.1029/1998JD100041> [Accessed September 9, 2013].
- Kerminen, V.-M. & Kulmala, M., 2002. Analytical formulae connecting the “real” and the “apparent” nucleation rate and the nuclei number concentration for atmospheric nucleation events. *Journal of Aerosol Science*, 33(4), pp.609–622. Available at: [http://dx.doi.org/10.1016/S0021-8502\(01\)00194-X](http://dx.doi.org/10.1016/S0021-8502(01)00194-X) [Accessed September 9, 2013].

- Kerminen, V.-M., Pirjola, L. & Kulmala, M., 2001. How significantly does coagulation scavenging limit atmospheric particle production? *Journal of Geophysical Research*, 106(D20), p.24119. Available at: <http://doi.wiley.com/10.1029/2001JD000322> [Accessed September 9, 2013].
- Kesselmeier, J. & Staudt, M., 1999. Biogenic Volatile Organic Compounds (VOC): An Overview on Emission, Physiology and Ecology. *Journal of Atmospheric Chemistry*, 33(1), pp.23–88. Available at: <http://link.springer.com/article/10.1023/A:1006127516791> [Accessed September 5, 2013].
- Khlystov, A., Wyers, G.P. & Slanina, J., 1995. The steam-jet aerosol collector. *Atmospheric Environment*, 29(17), pp.2229–2234. Available at: [http://dx.doi.org/10.1016/1352-2310\(95\)00180-7](http://dx.doi.org/10.1016/1352-2310(95)00180-7) [Accessed September 12, 2013].
- Kiendler-Scharr, A. et al., 2009. Aerosol mass spectrometric features of biogenic SOA: observations from a plant chamber and in rural atmospheric environments. *Environmental science & technology*, 43(21), pp.8166–72. Available at: <http://www.ncbi.nlm.nih.gov/pubmed/19924939>.
- Kim, B.M. & Henry, R.C., 1999. Extension of self-modeling curve resolution to mixtures of more than three components. *Chemometrics and Intelligent Laboratory Systems*, 49(1), pp.67–77. Available at: [http://dx.doi.org/10.1016/S0169-7439\(99\)00029-5](http://dx.doi.org/10.1016/S0169-7439(99)00029-5) [Accessed September 13, 2013].
- Kim, B.M. & Henry, R.C., 2000. Extension of self-modeling curve resolution to mixtures of more than three components. *Chemometrics and Intelligent Laboratory Systems*, 52(2), pp.145–154. Available at: [http://dx.doi.org/10.1016/S0169-7439\(00\)00077-0](http://dx.doi.org/10.1016/S0169-7439(00)00077-0) [Accessed September 13, 2013].
- Kim, E. & Hopke, P.K., 2004. Comparison between Conditional Probability Function and Nonparametric Regression for Fine Particle Source Directions. *Atmospheric Environment*, 38(28), pp.4667–4673. Available at: <http://dx.doi.org/10.1016/j.atmosenv.2004.05.035> [Accessed November 7, 2012].
- Kim, E. & Hopke, P.K., 2007. Source identifications of airborne fine particles using positive matrix factorization and U.S. Environmental Protection Agency positive matrix factorization. *Journal of the Air & Waste Management Association (1995)*, 57(7), pp.811–9. Available at: <http://www.ncbi.nlm.nih.gov/pubmed/17687996> [Accessed September 16, 2013].
- Kim, S., Kramer, R.W. & Hatcher, P.G., 2003. Graphical Method for Analysis of Ultrahigh-Resolution Broadband Mass Spectra of Natural Organic Matter, the Van Krevelen Diagram. *Analytical Chemistry*, 75(20), pp.5336–5344. Available at: <http://dx.doi.org/10.1021/ac034415p> [Accessed September 15, 2013].
- Kleefeld, C., 2002. Relative contribution of submicron and supermicron particles to aerosol light scattering in the marine boundary layer. *Journal of Geophysical Research*, 107(D19), p.8103. Available at: <http://doi.wiley.com/10.1029/2000JD000262> [Accessed July 14, 2013].
- Kleissl, J. et al., 2007. Occurrence of upslope flows at the Pico mountaintop observatory: A case study of orographic flows on a small, volcanic island. *Journal of Geophysical Research*, 112(D10), p.D10S35. Available at: <http://doi.wiley.com/10.1029/2006JD007565> [Accessed October 3, 2013].

- Kok, G.L., Gitlin, S.N. & Lazrus, A.L., 1986. Kinetics of the formation and decomposition of hydroxymethanesulfonate. *Journal of Geophysical Research*, 91(D2), p.2801. Available at: <http://doi.wiley.com/10.1029/JD091iD02p02801> [Accessed June 24, 2013].
- Kokkola, H. et al., 2013. The role of low volatile organics on secondary organic aerosol formation. *Atmospheric Chemistry and Physics Discussions*, 13(6), pp.14613–14635. Available at: <http://www.atmos-chem-phys-discuss.net/13/14613/2013/acpd-13-14613-2013.html> [Accessed June 4, 2013].
- Kolb, C.E. et al., 2010. An overview of current issues in the uptake of atmospheric trace gases by aerosols and clouds. *Atmospheric Chemistry and Physics*, 10(21), pp.10561–10605. Available at: <http://www.atmos-chem-phys.net/10/10561/2010/acp-10-10561-2010.html> [Accessed August 13, 2013].
- Kondo, Y. et al., 2007. Oxygenated and water-soluble organic aerosols in Tokyo. *Journal of Geophysical Research*, 112(D1), p.D01203. Available at: <http://doi.wiley.com/10.1029/2006JD007056> [Accessed September 12, 2013].
- Van Krevelen, D.W., 1950. Graphical-statistical method for the study of structure and reaction processes of coal. *Fuel*, 29. Available at: http://www.researchgate.net/publication/204978624_Graphical-statistical_method_for_the_study_of_structure_and_reaction_processes_of_coal [Accessed September 15, 2013].
- Krieger, M.S. & Hites, R.A., 1992. Diffusion denuder for the collection of semivolatile organic compounds. *Environmental Science & Technology*, 26(8), pp.1551–1555. Available at: <http://dx.doi.org/10.1021/es00032a009> [Accessed September 11, 2013].
- Krivácsy, Z., 2000. Study of humic-like substances in fog and interstitial aerosol by size-exclusion chromatography and capillary electrophoresis. *Atmospheric Environment*, 34(25), pp.4273–4281. Available at: [http://dx.doi.org/10.1016/S1352-2310\(00\)00211-9](http://dx.doi.org/10.1016/S1352-2310(00)00211-9) [Accessed September 9, 2013].
- Krizner, H.E., De Haan, D.O. & Kua, J., 2009. Thermodynamics and kinetics of methylglyoxal dimer formation: a computational study. *The journal of physical chemistry. A*, 113(25), pp.6994–7001. Available at: <http://www.ncbi.nlm.nih.gov/pubmed/19480424> [Accessed September 3, 2013].
- Kroll, J.H. et al., 2011. Carbon oxidation state as a metric for describing the chemistry of atmospheric organic aerosol. *Nature chemistry*, 3(2), pp.133–9. Available at: <http://www.ncbi.nlm.nih.gov/pubmed/21258386> [Accessed March 1, 2012].
- Kroll, J.H. et al., 2005. Chamber studies of secondary organic aerosol growth by reactive uptake of simple carbonyl compounds. *Journal of Geophysical Research*, 110(D23), p.D23207. Available at: <http://doi.wiley.com/10.1029/2005JD006004> [Accessed May 26, 2013].
- Kroll, J.H. et al., 2009. Measurement of fragmentation and functionalization pathways in the heterogeneous oxidation of oxidized organic aerosol. *Physical chemistry chemical physics : PCCP*, 11(36), pp.8005–14. Available at: <http://pubs.rsc.org/en/content/articlehtml/2009/cp/b905289e> [Accessed July 30, 2013].
- Kroll, J.H. et al., 2006. Secondary Organic Aerosol Formation from Isoprene Photooxidation. *Environmental Science & Technology*, 40(6), pp.1869–1877. Available at: <http://dx.doi.org/10.1021/es0524301> [Accessed June 24, 2013].
- Kroll, J.H. & Seinfeld, J.H., 2008. Chemistry of secondary organic aerosol: Formation and evolution of low-volatility organics in the atmosphere. *Atmospheric Environment*, 42(16),

- pp.3593–3624. Available at: <http://dx.doi.org/10.1016/j.atmosenv.2008.01.003> [Accessed August 7, 2013].
- Kua, J., Krizner, H.E. & De Haan, D.O., 2011. Thermodynamics and kinetics of imidazole formation from glyoxal, methylamine, and formaldehyde: a computational study. *The journal of physical chemistry. A*, 115(9), pp.1667–75. Available at: <http://dx.doi.org/10.1021/jp111527x> [Accessed June 22, 2013].
- Kubátová, A. et al., 2000. Carbonaceous aerosol characterization in the Amazon basin, Brazil: novel dicarboxylic acids and related compounds. *Atmospheric Environment*, 34(29-30), pp.5037–5051. Available at: [http://dx.doi.org/10.1016/S1352-2310\(00\)00320-4](http://dx.doi.org/10.1016/S1352-2310(00)00320-4) [Accessed June 25, 2013].
- Kulmala, M. et al., 2004. Formation and growth rates of ultrafine atmospheric particles: a review of observations. *Journal of Aerosol Science*, 35(2), pp.143–176. Available at: <http://dx.doi.org/10.1016/j.jaerosci.2003.10.003> [Accessed August 22, 2013].
- Lack, D.A., 2004. Seasonal variability of secondary organic aerosol: A global modeling study. *Journal of Geophysical Research*, 109(D3), p.D03203. Available at: <http://doi.wiley.com/10.1029/2003JD003418> [Accessed September 6, 2013].
- Lagrange, J., Wenger, G. & Lagrange, P., 1999. Kinetic study of HMSA formation and decomposition: Tropospheric relevance. *Journal de Chimie Physique et de Physico-Chimie Biologique*, 96(4), pp.610–633. Available at: <http://dx.doi.org/10.1051/jcp:1999161> [Accessed June 24, 2013].
- Laj, P. et al., 1997. Experimental evidence for in-cloud production of aerosol sulphate. *Atmospheric Environment*, 31(16), pp.2503–2514. Available at: [http://dx.doi.org/10.1016/S1352-2310\(96\)00217-8](http://dx.doi.org/10.1016/S1352-2310(96)00217-8) [Accessed June 25, 2013].
- Lambe, a. T. et al., 2011. Characterization of aerosol photooxidation flow reactors: heterogeneous oxidation, secondary organic aerosol formation and cloud condensation nuclei activity measurements. *Atmospheric Measurement Techniques*, 4(3), pp.445–461. Available at: <http://www.atmos-meas-tech.net/4/445/2011/> [Accessed April 27, 2012].
- Lambe, A.T. et al., 2011. Laboratory studies of the chemical composition and cloud condensation nuclei (CCN) activity of secondary organic aerosol (SOA) and oxidized primary organic aerosol (OPOA). *Atmospheric Chemistry and Physics*, 11(17), pp.8913–8928. Available at: <http://www.atmos-chem-phys.net/11/8913/2011/acp-11-8913-2011.html> [Accessed July 3, 2013].
- Langford, A.O. & Fehsenfeld, F.C., 1992. Natural vegetation as a source or sink for atmospheric ammonia: a case study. *Science (New York, N.Y.)*, 255(5044), pp.581–3. Available at: <http://www.sciencemag.org/content/255/5044/581.abstract> [Accessed September 11, 2012].
- Lanz, V.A. et al., 2007. Source apportionment of submicron organic aerosols at an urban site by factor analytical modelling of aerosol mass spectra. , (2004), pp.1503–1522.
- Leaitch, W.R. et al., 2011. Temperature response of the submicron organic aerosol from temperate forests. *Atmospheric Environment*, 45(37), pp.6696–6704. Available at: <http://dx.doi.org/10.1016/j.atmosenv.2011.08.047> [Accessed August 25, 2013].
- Lee, A.K.Y. et al., 2011. Aqueous OH oxidation of ambient organic aerosol and cloud water organics: Formation of highly oxidized products. *Geophysical Research Letters*, 38(11), p.n/a–n/a. Available at: <http://doi.wiley.com/10.1029/2011GL047439> [Accessed August 23, 2013].
- Lee, A.K.Y. et al., 2011. Aqueous-phase OH oxidation of glyoxal: application of a novel analytical approach employing aerosol mass spectrometry and complementary off-line

- techniques. *The journal of physical chemistry. A*, 115(38), pp.10517–26. Available at: <http://www.ncbi.nlm.nih.gov/pubmed/21854005>.
- Lee, A.K.Y. et al., 2012. Characterization of aerosol and cloud water at a mountain site during WACS 2010: secondary organic aerosol formation through oxidative cloud processing. *Atmospheric Chemistry and Physics*, 12(15), pp.7103–7116. Available at: <http://www.atmos-chem-phys.net/12/7103/2012/acp-12-7103-2012.html> [Accessed August 25, 2013].
- Lee, T. et al., 2010. Chemical Smoke Marker Emissions During Flaming and Smoldering Phases of Laboratory Open Burning of Wildland Fuels. *Aerosol Science and Technology*, 44(9), pp.i–v. Available at: <http://dx.doi.org/10.1080/02786826.2010.499884> [Accessed November 9, 2012].
- Lee, T. et al., 2008. Semi-continuous measurement of PM_{2.5} ionic composition at several rural locations in the United States. *Atmospheric Environment*, 42(27), pp.6655–6669. Available at: <http://dx.doi.org/10.1016/j.atmosenv.2008.04.023> [Accessed August 18, 2013].
- Lee, T., Kreidenweis, S.M. & Collett, J.L., 2004. Aerosol ion characteristics during the Big Bend Regional Aerosol and Visibility Observational study. *Journal of the Air & Waste Management Association (1995)*, 54(5), pp.585–92. Available at: <http://www.ncbi.nlm.nih.gov/pubmed/15149045> [Accessed September 25, 2013].
- Lelieveld, J. & Heintzenberg, J., 1992. Sulfate Cooling Effect on Climate Through In-Cloud Oxidation of Anthropogenic SO₂. *Science (New York, N.Y.)*, 258(5079), pp.117–20. Available at: <http://www.ncbi.nlm.nih.gov/pubmed/17835896> [Accessed January 14, 2014].
- Lestari, P. & Mauliadi, Y.D., 2009. Source apportionment of particulate matter at urban mixed site in Indonesia using PMF. *Atmospheric Environment*, 43(10), pp.1760–1770. Available at: <http://www.sciencedirect.com/science/article/pii/S1352231008011485> [Accessed November 7, 2012].
- Levin, E.J.T. et al., 2009. Aerosol physical, chemical and optical properties during the Rocky Mountain Airborne Nitrogen and Sulfur study. *Atmospheric Environment*, 43(11), pp.1932–1939. Available at: <http://dx.doi.org/10.1016/j.atmosenv.2008.12.042> [Accessed October 9, 2012].
- Levin, E.J.T. et al., 2012. An annual cycle of size-resolved aerosol hygroscopicity at a forested site in Colorado. *Journal of Geophysical Research*, 117(D6), p.D06201. Available at: <http://www.agu.org/pubs/crossref/2012/2011JD016854.shtml> [Accessed December 13, 2012].
- Li, Y.J. et al., 2013. Evaluating the degree of oxygenation of organic aerosol during foggy and hazy days in Hong Kong using high-resolution time-of-flight aerosol mass spectrometry (HR-ToF-AMS). *Atmospheric Chemistry and Physics Discussions*, 13(2), pp.3533–3573. Available at: <http://www.atmos-chem-phys-discuss.net/13/3533/2013/acpd-13-3533-2013.html> [Accessed September 4, 2013].
- Liao, H. & Seinfeld, J.H., 2005. Global impacts of gas-phase chemistry-aerosol interactions on direct radiative forcing by anthropogenic aerosols and ozone. *Journal of Geophysical Research*, 110(D18), p.D18208. Available at: <http://doi.wiley.com/10.1029/2005JD005907> [Accessed May 23, 2013].

- Likens, G.E., Driscoll, C.T. & Buso, D.C., 1996. Long-Term Effects of Acid Rain: Response and Recovery of a Forest Ecosystem. *Science*, 272(5259), pp.244–246. Available at: <http://www.sciencemag.org/content/272/5259/244> [Accessed July 15, 2013].
- Lim, H.-J., Carlton, A.G. & Turpin, B.J., 2005. Isoprene Forms Secondary Organic Aerosol through Cloud Processing: Model Simulations. *Environmental Science & Technology*, 39(12), pp.4441–4446. Available at: <http://dx.doi.org/10.1021/es048039h> [Accessed June 6, 2013].
- Lim, Y.B. et al., 2010. Aqueous chemistry and its role in secondary organic aerosol (SOA) formation. *Atmospheric Chemistry and Physics*, 10(21), pp.10521–10539. Available at: <http://www.atmos-chem-phys.net/10/10521/2010/acp-10-10521-2010.html> [Accessed May 30, 2013].
- Lim, Y.B., Tan, Y. & Turpin, B.J., 2013. Chemical insights, explicit chemistry and yields of secondary organic aerosol from methylglyoxal and glyoxal. *Atmospheric Chemistry and Physics Discussions*, 13(2), pp.4687–4725. Available at: <http://www.atmos-chem-phys-discuss.net/13/4687/2013/acpd-13-4687-2013.html> [Accessed July 20, 2013].
- Limbeck, A. & Puxbaum, H., 2000. Dependence of in-cloud scavenging of polar organic aerosol compounds on the water solubility. *Journal of Geophysical Research*, 105(D15), p.19857. Available at: <http://doi.wiley.com/10.1029/2000JD900123> [Accessed June 24, 2013].
- Lin, M. et al., 2010. Organic nitrogen in PM_{2.5} aerosol at a forest site in the Southeast US. *Atmospheric Chemistry and Physics*, 10(5), pp.2145–2157. Available at: <http://www.atmos-chem-phys.net/10/2145/2010/acp-10-2145-2010.html> [Accessed September 15, 2013].
- Liu, J. et al., 2012. Global in-cloud production of secondary organic aerosols: Implementation of a detailed chemical mechanism in the GFDL atmospheric model AM3. *Journal of Geophysical Research*, 117(D15), p.D15303. Available at: <http://doi.wiley.com/10.1029/2012JD017838> [Accessed January 4, 2014].
- Liu, J. et al., 2012. On the gas-particle partitioning of soluble organic aerosol in two urban atmospheres with contrasting emissions: 2. Gas and particle phase formic acid. *Journal of Geophysical Research: Atmospheres*, 117(D21), p.n/a–n/a. Available at: <http://doi.wiley.com/10.1029/2012JD017912> [Accessed August 10, 2013].
- Liu, P.S.K. et al., 2007. Transmission Efficiency of an Aerodynamic Focusing Lens System: Comparison of Model Calculations and Laboratory Measurements for the Aerodyne Aerosol Mass Spectrometer. *Aerosol Science and Technology*, 41(8), pp.721–733. Available at: <http://dx.doi.org/10.1080/02786820701422278> [Accessed October 3, 2012].
- Liu, Y. et al., 2009. In-cloud processes of methacrolein under simulated conditions – Part 1: Aqueous phase photooxidation. *Atmospheric Chemistry and Physics*, 9(14), pp.5093–5105. Available at: <http://www.atmos-chem-phys.net/9/5093/2009/acp-9-5093-2009.html> [Accessed June 25, 2013].
- Loeffler, K.W. et al., 2006. Oligomer Formation in Evaporating Aqueous Glyoxal and Methyl Glyoxal Solutions. *Environmental Science & Technology*, 40(20), pp.6318–6323. Available at: <http://dx.doi.org/10.1021/es060810w> [Accessed June 6, 2013].
- Löflund, M. et al., 2002. Formic, acetic, oxalic, malonic and succinic acid concentrations and their contribution to organic carbon in cloud water. *Atmospheric Environment*, 36(9), pp.1553–1558. Available at: <http://www.sciencedirect.com/science/article/pii/S1352231001005738> [Accessed October 2, 2013].

- Lohmann, U. & Feichter, J., 2005. Global indirect aerosol effects: a review. *Atmospheric Chemistry and Physics*, 5(3), pp.715–737. Available at: <http://www.atmos-chem-phys.net/5/715/2005/acp-5-715-2005.html> [Accessed July 15, 2013].
- Lovelock, J.E., Maggs, R.J. & Rasmussen, R.A., 1972. Atmospheric Dimethyl Sulphide and the Natural Sulphur Cycle. *Nature*, 237(5356), pp.452–453. Available at: <http://dx.doi.org/10.1038/237452a0> [Accessed May 27, 2013].
- Mace, K.A., Artaxo, P. & Duce, R.A., 2003. Water-soluble organic nitrogen in Amazon Basin aerosols during the dry (biomass burning) and wet seasons. *Journal of Geophysical Research*, 108(D16), p.4512. Available at: <http://www.agu.org/pubs/crossref/2003/2003JD003557.shtml> [Accessed November 6, 2012].
- Makela, J. et al., 2000. Characteristics of the atmospheric particle formation events observed at a boreal forest site in southern Finland. *Boreal Environment Research*, 5(299-313).
- Malloy, Q. & Qi, L., 2009. Secondary organic aerosol formation from primary aliphatic amines with NO₃ radical. *Atmospheric ...*, (1973), pp.2051–2060. Available at: <http://www.atmos-chem-phys.net/9/2051/2009/acp-9-2051-2009.html> [Accessed September 15, 2013].
- Malm, W.C. et al., 2005. Intercomparison and closure calculations using measurements of aerosol species and optical properties during the Yosemite Aerosol Characterization Study. *Journal of Geophysical Research*, 110(D14), p.D14302. Available at: <http://doi.wiley.com/10.1029/2004JD005494> [Accessed September 25, 2013].
- Malm, W.C. et al., 2009. *Rocky Mountain Atmospheric Nitrogen and Sulfur Study*, Fort Collins, CO. Available at: <http://www.nature.nps.gov/air/studies/romans.cfm>.
- Malm, W.C. & Day, D.E., 2001. Estimates of aerosol species scattering characteristics as a function of relative humidity. , 35, pp.2845–2860.
- Malm, W.C. & Hand, J.L., 2007. An examination of the physical and optical properties of aerosols collected in the IMPROVE program. *Atmospheric Environment*, 41, pp.3407–3427. Available at: http://capita.wustl.edu/capita/capitareports/090120_AerosolMeasHandbook/Literature/MalmHandIMPROVE.pdf.
- Malm, W.C., Johnson, C.E. & Brechs, J.F., 1986. Application of principal component analysis for purposes of identifying source-receptor relationships. In T. G. Pace, ed. *Receptor Methods for Source Apportionment*. Pittsburg, PA: Air Pollution Control Association, pp. 127–148.
- Marculli, C. & Peter, T., 2005. Water activity in polyol/water systems: new UNIFAC parameterization. *Atmospheric Chemistry and Physics*, 5(6), pp.1545–1555. Available at: <http://www.atmos-chem-phys.net/5/1545/2005/acp-5-1545-2005.html> [Accessed September 5, 2013].
- Marple, V.A. & Rubow, K.L., 1984. *Final Report on DOE contract No. DE-FG22-83PC61255*, Minneapolis, MN.
- Masiello, C.A., 2004. New directions in black carbon organic geochemistry. *Marine Chemistry*, 92(1-4), pp.201–213. Available at: <http://dx.doi.org/10.1016/j.marchem.2004.06.043> [Accessed May 27, 2013].
- Massoli, P. et al., 2010. Relationship between aerosol oxidation level and hygroscopic properties of laboratory generated secondary organic aerosol (SOA) particles. *Geophysical Research Letters*, 37(24), pp.1–5. Available at: <http://www.agu.org/pubs/crossref/2010/2010GL045258.shtml> [Accessed March 29, 2012].

- Matsunaga, S., 2004. Variation on the atmospheric concentrations of biogenic carbonyl compounds and their removal processes in the northern forest at Moshiri, Hokkaido Island in Japan. *Journal of Geophysical Research*, 109(D4), p.D04302. Available at: <http://doi.wiley.com/10.1029/2003JD004100> [Accessed June 24, 2013].
- Matsunaga, S.N., 2005. Gas-aerosol partitioning of semi volatile carbonyls in polluted atmosphere in Hachioji, Tokyo. *Geophysical Research Letters*, 32(11), p.L11805. Available at: <http://doi.wiley.com/10.1029/2004GL021893> [Accessed June 24, 2013].
- Matthew, B.M., Middlebrook, A.M. & Onasch, T.B., 2008. Collection Efficiencies in an Aerodyne Aerosol Mass Spectrometer as a Function of Particle Phase for Laboratory Generated Aerosols. *Aerosol Science and Technology*, 42(11), pp.884–898. Available at: <http://dx.doi.org/10.1080/02786820802356797> [Accessed April 1, 2012].
- McDow, S.R. & Huntzicker, J.J., 1990. Vapor adsorption artifact in the sampling of organic aerosol: Face velocity effects. *Atmospheric Environment. Part A. General Topics*, 24(10), pp.2563–2571. Available at: [http://dx.doi.org/10.1016/0960-1686\(90\)90134-9](http://dx.doi.org/10.1016/0960-1686(90)90134-9) [Accessed September 11, 2013].
- McHenry, J.N. & Dennis, R.L., 1994. The Relative Importance of Oxidation Pathways and Clouds to Atmospheric Ambient Sulfate Production as Predicted by the Regional Acid Deposition Model. *Journal of Applied Meteorology*, 33(7), pp.890–905. Available at: [http://journals.ametsoc.org/doi/abs/10.1175/1520-0450\(1994\)033<0890:TRIOOP>2.0.CO;2](http://journals.ametsoc.org/doi/abs/10.1175/1520-0450(1994)033<0890:TRIOOP>2.0.CO;2) [Accessed September 10, 2013].
- McKenzie, L.M. et al., 1995. Measurement and modeling of air toxins from smoldering combustion of biomass. *Environmental science & technology*, 29(8), pp.2047–54. Available at: <http://dx.doi.org/10.1021/es00008a025> [Accessed February 22, 2014].
- McKeown, P.J., Johnston, M. V. & Murphy, D.M., 1991. On-line single-particle analysis by laser desorption mass spectrometry. *Analytical Chemistry*, 63(18), pp.2069–2073. Available at: <http://dx.doi.org/10.1021/ac00018a033> [Accessed September 12, 2013].
- McLafferty, F.W. & Turecek, F., 1993. *Interpretation of Mass Spectra* 4th ed., Herndon, VA: University Science Books.
- McMurry, P., 2000. A review of atmospheric aerosol measurements. *Atmospheric Environment*, 34(12-14), pp.1959–1999. Available at: [http://dx.doi.org/10.1016/S1352-2310\(99\)00455-0](http://dx.doi.org/10.1016/S1352-2310(99)00455-0) [Accessed August 8, 2013].
- McMurry, P.H. & Zhang, X.Q., 1989. Size Distributions of Ambient Organic and Elemental Carbon. *Aerosol Science and Technology*, 10(2), pp.430–437. Available at: <http://dx.doi.org/10.1080/02786828908959282> [Accessed September 12, 2013].
- Meng, Z. et al., 1995. Contribution of Water to Particulate Mass in the South Coast Air Basin. *Aerosol Science and Technology*, 22(1), pp.111–123. Available at: <http://dx.doi.org/10.1080/02786829408959731> [Accessed May 30, 2013].
- Meng, Z. & Seinfeld, J.H., 1994. On the Source of the Submicrometer Droplet Mode of Urban and Regional Aerosols. *Aerosol Science and Technology*, 20(3), pp.253–265. Available at: <http://dx.doi.org/10.1080/02786829408959681> [Accessed July 14, 2013].
- Middlebrook, A.M. et al., 2012. Evaluation of Composition-Dependent Collection Efficiencies for the Aerodyne Aerosol Mass Spectrometer using Field Data. *Aerosol Science and Technology*, 46(3), pp.258–271. Available at: <http://www.tandfonline.com/doi/abs/10.1080/02786826.2011.620041> [Accessed April 30, 2012].

- Minerath, E.C. & Elrod, M.J., 2009. Assessing the potential for diol and hydroxy sulfate ester formation from the reaction of epoxides in tropospheric aerosols. *Environmental science & technology*, 43(5), pp.1386–92. Available at: <http://www.ncbi.nlm.nih.gov/pubmed/19350908> [Accessed June 25, 2013].
- Minnis, P. et al., 1993. Radiative climate forcing by the mount pinatubo eruption. *Science (New York, N.Y.)*, 259(5100), pp.1411–5. Available at: <http://www.sciencemag.org/content/259/5100/1411> [Accessed July 14, 2013].
- Mohr, C. & Huffman, J., 2009. primary organic aerosol emissions from meat cooking, trash burning, and motor vehicles with high-resolution aerosol mass spectrometry and comparison with ambient. ... *science & technology*. Available at: <http://pubs.acs.org/doi/abs/10.1021/es8011518> [Accessed July 15, 2013].
- Monod, A. et al., 2000. Oxidation of methanol by hydroxyl radicals in aqueous solution under simulated cloud droplet conditions. *Atmospheric Environment*, 34(29-30), pp.5283–5294. Available at: [http://dx.doi.org/10.1016/S1352-2310\(00\)00191-6](http://dx.doi.org/10.1016/S1352-2310(00)00191-6) [Accessed August 12, 2013].
- Monod, A. et al., 2007. Photooxidation of methylhydroperoxide and ethylhydroperoxide in the aqueous phase under simulated cloud droplet conditions. *Atmospheric Environment*, 41(11), pp.2412–2426. Available at: <http://dx.doi.org/10.1016/j.atmosenv.2006.10.006> [Accessed August 12, 2013].
- Morgan, W.T. et al., 2010. Airborne measurements of the spatial distribution of aerosol chemical composition across Europe and evolution of the organic fraction. *Atmospheric Chemistry and Physics*, 10(8), pp.4065–4083. Available at: <http://www.atmos-chem-phys.net/10/4065/2010/acp-10-4065-2010.html> [Accessed September 9, 2013].
- Müller, L. et al., 2012. Formation of 3-methyl-1,2,3-butanetricarboxylic acid via gas phase oxidation of pinonic acid – a mass spectrometric study of SOA aging. *Atmospheric Chemistry and Physics*, 12(3), pp.1483–1496. Available at: <http://www.atmos-chem-phys.net/12/1483/2012/acp-12-1483-2012.html> [Accessed August 2, 2013].
- Müller, L. et al., 2008. Unambiguous identification of esters as oligomers in secondary organic aerosol formed from cyclohexene and cyclohexene/ α -pinene ozonolysis. *Atmospheric Chemistry and Physics*, 8(5), pp.1423–1433. Available at: <http://www.atmos-chem-phys.net/8/1423/2008/acp-8-1423-2008.html> [Accessed August 7, 2013].
- Munger, J.W. et al., 1990. Fogwater chemistry at Riverside, California. *Atmospheric Environment. Part B. Urban Atmosphere*, 24(2), pp.185–205. Available at: <http://www.sciencedirect.com/science/article/pii/095712729090025P> [Accessed September 30, 2013].
- Murphy, D.M., 2005. Atmospheric science. Something in the air. *Science (New York, N.Y.)*, 307(5717), pp.1888–90. Available at: <http://www.sciencemag.org/content/307/5717/1888.short> [Accessed July 14, 2013].
- Murphy, D.M. et al., 2006. Single-particle mass spectrometry of tropospheric aerosol particles. *Journal of Geophysical Research*, 111(D23), p.D23S32. Available at: <http://doi.wiley.com/10.1029/2006JD007340> [Accessed August 14, 2013].
- Murphy, S.M. et al., 2007. Secondary aerosol formation from atmospheric reactions of aliphatic amines. *Atmospheric Chemistry and Physics Discussions*, 7(1), pp.289–349. Available at: <http://www.atmos-chem-phys-discuss.net/7/289/2007/>.
- Nakayama, T. et al., 2010. Laboratory studies on optical properties of secondary organic aerosols generated during the photooxidation of toluene and the ozonolysis of α -pinene. *Journal of*

- Geophysical Research*, 115(D24), p.D24204. Available at: <http://doi.wiley.com/10.1029/2010JD014387> [Accessed June 25, 2013].
- Neff, J.C. et al., 2002. The origin, composition and rates of organic nitrogen deposition: A missing piece of the nitrogen cycle? *Biogeochemistry*, 57-58(1), pp.99–136. Available at: <http://link.springer.com/article/10.1023/A:1015791622742> [Accessed September 15, 2013].
- Ng, N.L., Canagaratna, M.R., et al., 2011. Changes in organic aerosol composition with aging inferred from aerosol mass spectra. *Atmospheric Chemistry and Physics*, 11(13), pp.6465–6474. Available at: <http://www.atmos-chem-phys.net/11/6465/2011/> [Accessed April 16, 2012].
- Ng, N.L. et al., 2010. Organic aerosol components observed in Northern Hemispheric datasets from Aerosol Mass Spectrometry. *Atmospheric Chemistry and Physics*, 10(10), pp.4625–4641. Available at: <http://www.atmos-chem-phys.net/10/4625/2010/> [Accessed May 9, 2012].
- Ng, N.L., Canagaratna, M.R., et al., 2011. Real-time methods for estimating organic component mass concentrations from aerosol mass spectrometer data. *Environmental science & technology*, 45(3), pp.910–6. Available at: <http://www.ncbi.nlm.nih.gov/pubmed/21186814>.
- Ng, N.L. et al., 2008. Secondary organic aerosol (SOA) formation from reaction of isoprene with nitrate radicals (NO₃). *Atmospheric Chemistry and Physics*, 8(14), pp.4117–4140. Available at: <http://www.atmos-chem-phys.net/8/4117/2008/acp-8-4117-2008.html> [Accessed September 6, 2013].
- Ng, N.L. et al., 2007. Secondary organic aerosol formation from *m*-xylene, toluene, and benzene. *Atmospheric Chemistry and Physics Discussions*, 7(2), pp.4085–4126. Available at: <http://www.atmos-chem-phys-discuss.net/7/4085/2007/acpd-7-4085-2007.html> [Accessed June 25, 2013].
- Nishino, N., Arey, J. & Atkinson, R., 2010. Formation yields of glyoxal and methylglyoxal from the gas-phase OH radical-initiated reactions of toluene, xylenes, and trimethylbenzenes as a function of NO₂ concentration. *The journal of physical chemistry. A*, 114(37), pp.10140–7. Available at: <http://dx.doi.org/10.1021/jp105112h> [Accessed January 8, 2014].
- NIST, 2013. National Institute of Standards and Technology Chemistry Webbook. Available at: <http://webbook.nist.gov/chemistry/>.
- NOAA, 2012. No Title3-Hourly NCEP North American Regional Reanalysis (NARR) Composites. Available at: <http://www.esrl.noaa.gov/psd/cgi-bin/data/narr/plothour.pl> [Accessed September 4, 2012].
- Noble, C. & Prather, K., 2000. Real-time single particle mass spectrometry: a historical review of a quarter century of the chemical analysis of aerosols. *Mass spectrometry reviews*, 19(4), pp.248–74. Available at: <http://www.ncbi.nlm.nih.gov/pubmed/10986694> [Accessed September 12, 2013].
- Noble, C.A. & Prather, K.A., 1996. Real-Time Measurement of Correlated Size and Composition Profiles of Individual Atmospheric Aerosol Particles. *Environmental Science & Technology*, 30(9), pp.2667–2680. Available at: <http://dx.doi.org/10.1021/es950669j> [Accessed August 7, 2013].
- Norris, G. & Vedantham, R., 2008. *EPA Positive Matrix Factorization (PMF) 3.0 Fundamentals & User Guide*, Available at: [http://www.researchgate.net/publication/238104027_EPA_Positive_Matrix_Factorization_\(PMF\)_3.0_Fundamentals__User_Guide](http://www.researchgate.net/publication/238104027_EPA_Positive_Matrix_Factorization_(PMF)_3.0_Fundamentals__User_Guide) [Accessed September 16, 2013].

- Northway, M.J. et al., 2007. Demonstration of a VUV Lamp Photoionization Source for Improved Organic Speciation in an Aerosol Mass Spectrometer. *Aerosol Science and Technology*, 41(9), pp.828–839. Available at: <http://dx.doi.org/10.1080/02786820701496587> [Accessed August 9, 2013].
- Nozière, B., Ekström, S., et al., 2010. Radical-initiated formation of organosulfates and surfactants in atmospheric aerosols. *Geophysical Research Letters*, 37(5), p.n/a–n/a. Available at: <http://doi.wiley.com/10.1029/2009GL041683> [Accessed June 25, 2013].
- Nozière, B. et al., 2006. The uptake of methyl vinyl ketone, methacrolein, and 2-methyl-3-butene-2-ol onto sulfuric acid solutions. *The journal of physical chemistry. A*, 110(7), pp.2387–95. Available at: <http://www.ncbi.nlm.nih.gov/pubmed/16480298> [Accessed October 7, 2013].
- Nozière, B., Barnes, I. & Becker, K.H., 1999. Product study and mechanisms of the reactions of α -pinene and of pinonaldehyde with OH radicals. *Journal of Geophysical Research*, 104(D19), p.23645. Available at: <http://doi.wiley.com/10.1029/1999JD900778> [Accessed June 25, 2013].
- Nozière, B., Dziedzic, P. & Cordova, A., 2010. Inorganic ammonium salts and carbonate salts are efficient catalysts for aldol condensation in atmospheric aerosols. *Physical Chemistry Chemical Physics*, 12(15), pp.3864–72. Available at: <http://www.ncbi.nlm.nih.gov/pubmed/20358081> [Accessed June 24, 2013].
- Nozière, B., Dziedzic, P. & Córdoba, A., 2009. Products and kinetics of the liquid-phase reaction of glyoxal catalyzed by ammonium ions (NH₄⁺). *The journal of physical chemistry. A*, 113(1), pp.231–7. Available at: <http://dx.doi.org/10.1021/jp8078293> [Accessed June 24, 2013].
- Nyeki, S. et al., 1998. The Jungfraujoch high-alpine research station (3454 m) as a background clean continental site for the measurement of aerosol parameters. *Journal of Geophysical Research*, 103(D6), p.6097. Available at: <http://doi.wiley.com/10.1029/97JD03123> [Accessed October 3, 2013].
- Obrist, D. et al., 2008. Atmospheric mercury concentrations at Storm Peak Laboratory in the Rocky Mountains: Evidence for long-range transport from Asia, boundary layer contributions, and plant mercury uptake. *Atmospheric Environment*, 42(33), pp.7579–7589. Available at: <http://www.sciencedirect.com/science/article/pii/S1352231008005955> [Accessed October 3, 2013].
- Odum, J.R. et al., 1996. Gas/Particle Partitioning and Secondary Organic Aerosol Yields. *Environmental Science & Technology*, 30(8), pp.2580–2585. Available at: <http://pubs.acs.org/doi/abs/10.1021/es950943+> [Accessed September 5, 2013].
- Odum, J.R., 1997. The Atmospheric Aerosol-Forming Potential of Whole Gasoline Vapor. *Science*, 276(5309), pp.96–99. Available at: <http://www.sciencemag.org/content/276/5309/96> [Accessed July 23, 2013].
- Orsini, D.A. et al., 2003. Refinements to the particle-into-liquid sampler (PILS) for ground and airborne measurements of water soluble aerosol composition. Available at: [http://shadow.eas.gatech.edu/~arec/Publications/Orsini et al, PILS refinements, AtmEnv37, 1243-59, 2003.pdf](http://shadow.eas.gatech.edu/~arec/Publications/Orsini%20et%20al,%20PILS%20refinements,%20AtmEnv37,%201243-59,%202003.pdf) [Accessed August 17, 2012].
- Oturan, M.A. et al., 2000. Complete Destruction of p -Nitrophenol in Aqueous Medium by Electro-Fenton Method. *Environmental Science & Technology*, 34(16), pp.3474–3479. Available at: <http://dx.doi.org/10.1021/es990901b> [Accessed January 30, 2014].

- Paatero, P., 1997. Least squares formulation of robust non-negative factor analysis. *Chemometrics and Intelligent Laboratory Systems*, 37(1), pp.23–35. Available at: [http://dx.doi.org/10.1016/S0169-7439\(96\)00044-5](http://dx.doi.org/10.1016/S0169-7439(96)00044-5) [Accessed August 16, 2012].
- Paatero, P., 1999. The Multilinear Engine—A Table-Driven, Least Squares Program for Solving Multilinear Problems, Including the n -Way Parallel Factor Analysis Model. *Journal of Computational and Graphical Statistics*, 8(4), pp.854–888. Available at: <http://dx.doi.org/10.1080/10618600.1999.10474853> [Accessed September 12, 2013].
- Paatero, P. et al., 2002. Understanding and controlling rotations in factor analytic models. *Chemometrics and Intelligent Laboratory Systems*, 60(1-2), pp.253–264. Available at: [http://dx.doi.org/10.1016/S0169-7439\(01\)00200-3](http://dx.doi.org/10.1016/S0169-7439(01)00200-3) [Accessed February 15, 2013].
- Paatero, P. & Hopke, P.K., 2003. Discarding or downweighting high-noise variables in factor analytic models. *Analytica Chimica Acta*, 490(1-2), pp.277–289. Available at: [http://dx.doi.org/10.1016/S0003-2670\(02\)01643-4](http://dx.doi.org/10.1016/S0003-2670(02)01643-4) [Accessed August 29, 2012].
- Paatero, P. & Tapper, U., 1993. Analysis of different modes of factor analysis as least squares fit problems. *Chemometrics and Intelligent Laboratory Systems*, 18(2), pp.183–194. Available at: [http://dx.doi.org/10.1016/0169-7439\(93\)80055-M](http://dx.doi.org/10.1016/0169-7439(93)80055-M) [Accessed February 15, 2013].
- Paatero, P. & Tapper, U., 1994. Positive matrix factorization: A non-negative factor model with optimal utilization of error estimates of data values. *Environmetrics*, 5(2), pp.111–126. Available at: <http://doi.wiley.com/10.1002/env.3170050203> [Accessed July 29, 2012].
- Pandolfi, M. et al., 2008. Receptor models application to multi-year ambient PM10 measurements in an industrialized ceramic area: Comparison of source apportionment results. *Atmospheric Environment*, 42(40), pp.9007–9017. Available at: <http://www.sciencedirect.com/science/article/pii/S1352231008008832> [Accessed September 16, 2013].
- Pang, Y., Turpin, B.J. & Gundel, L. a., 2006. On the Importance of Organic Oxygen for Understanding Organic Aerosol Particles. *Aerosol Science and Technology*, 40(2), pp.128–133. Available at: <http://www.tandfonline.com/doi/abs/10.1080/02786820500423790> [Accessed May 9, 2012].
- Pankow, J.F., 1994. An absorption model of gas/particle partitioning of organic compounds in the atmosphere. *Atmospheric Environment*, 28, pp.185–188. Available at: http://hero.epa.gov/index.cfm?action=reference.details&reference_id=45253 [Accessed September 5, 2013].
- Pankow, J.F., 2003. Gas/particle partitioning of neutral and ionizing compounds to single and multi-phase aerosol particles. 1. Unified modeling framework. *Atmospheric Environment*, 37(24), pp.3323–3333. Available at: [http://dx.doi.org/10.1016/S1352-2310\(03\)00346-7](http://dx.doi.org/10.1016/S1352-2310(03)00346-7) [Accessed August 14, 2013].
- Pankow, J.F., 1987. Review and comparative analysis of the theories on partitioning between the gas and aerosol particulate phases in the atmosphere. *Atmospheric Environment (1967)*, 21(11), pp.2275–2283. Available at: <http://www.sciencedirect.com/science/article/pii/0004698187903635> [Accessed September 26, 2013].
- Park, R. et al., 2006. Regional visibility statistics in the United States: Natural and transboundary pollution influences, and implications for the Regional Haze Rule. *Atmospheric Environment*, 40(28), pp.5405–5423. Available at: <http://dx.doi.org/10.1016/j.atmosenv.2006.04.059> [Accessed August 16, 2012].

- Park, R.J., 2003. Sources of carbonaceous aerosols over the United States and implications for natural visibility. *Journal of Geophysical Research*, 108(D12), p.4355. Available at: <http://doi.wiley.com/10.1029/2002JD003190> [Accessed May 26, 2013].
- Parrish, D.D. et al., 1990. Systematic Variations in the Concentration of NO_x (NO Plus NO₂) at Niwot Ridge, Colorado. *Journal of Geophysical Research*, 95(D2), pp.1817–1836. Available at: <http://www.agu.org/pubs/crossref/1990/JD095iD02p01817.shtml> [Accessed September 11, 2012].
- Paulot, F. et al., 2009. Isoprene photooxidation: new insights into the production of acids and organic nitrates. *Atmospheric Chemistry and Physics*, 9(4), pp.1479–1501. Available at: <http://www.atmos-chem-phys.net/9/1479/2009/acp-9-1479-2009.html> [Accessed September 15, 2013].
- Penner, J.E., Hegg, D. & Leaitch, R., 2001. Peer Reviewed: Unraveling the role of aerosols in climate change. *Environmental Science & Technology*, 35(15), p.332A–340A. Available at: <http://dx.doi.org/10.1021/es0124414> [Accessed September 6, 2013].
- Perri, M.J. et al., 2010. Organosulfates from glycolaldehyde in aqueous aerosols and clouds: Laboratory studies. *Atmospheric Environment*, 44(21-22), pp.2658–2664. Available at: <http://dx.doi.org/10.1016/j.atmosenv.2010.03.031> [Accessed June 25, 2013].
- Petters, M.D. et al., 2006. Chemical aging and the hydrophobic-to-hydrophilic conversion of carbonaceous aerosol. *Geophysical Research Letters*, 33(24), p.L24806. Available at: <http://doi.wiley.com/10.1029/2006GL027249> [Accessed August 14, 2013].
- Petters, M.D. & Kreidenweis, S.M., 2007. A single parameter representation of hygroscopic growth and cloud condensation nucleus activity. *Atmos. Chem. Phys.*, (7), pp.1961–1971. Available at: <http://www.atmos-chem-phys.net/7/1961/2007/acp-7-1961-2007.html>.
- Pfrang, C., Shiraiwa, M. & Pöschl, U., 2011. Chemical ageing and transformation of diffusivity in semi-solid multi-component organic aerosol particles. *Atmospheric Chemistry and Physics*, 11(14), pp.7343–7354. Available at: <http://www.atmos-chem-phys.net/11/7343/2011/acp-11-7343-2011.html> [Accessed September 5, 2013].
- Pierce, J.R. et al., 2012. Nucleation and condensational growth to CCN sizes during a sustained pristine biogenic SOA event in a forested mountain valley. *Atmospheric Chemistry and Physics*, 12(7), pp.3147–3163. Available at: <http://www.atmos-chem-phys.net/12/3147/2012/acp-12-3147-2012.html> [Accessed August 6, 2013].
- Pilinis, C., Pandis, S.N. & Seinfeld, J.H., 1995. Sensitivity of direct climate forcing by atmospheric aerosols to aerosol size and composition. *Journal of Geophysical Research*, 100(D9), p.18739. Available at: <http://doi.wiley.com/10.1029/95JD02119> [Accessed July 14, 2013].
- Van Pinxteren, D. et al., 2005. Schmücke hill cap cloud and valley stations aerosol characterisation during FEBUKO (II): Organic compounds. *Atmospheric Environment*, 39(23-24), pp.4305–4320. Available at: <http://dx.doi.org/10.1016/j.atmosenv.2005.02.014> [Accessed June 24, 2013].
- Placet, M., 2000. Emissions of ozone precursors from stationary sources: a critical review. *Atmospheric Environment*, 34(12-14), pp.2183–2204. Available at: [http://dx.doi.org/10.1016/S1352-2310\(99\)00464-1](http://dx.doi.org/10.1016/S1352-2310(99)00464-1) [Accessed September 6, 2013].
- Pope, C.A. et al., 2002. Lung cancer, cardiopulmonary mortality, and long-term exposure to fine particulate air pollution. *JAMA : the journal of the American Medical Association*, 287(9), pp.1132–41. Available at: <http://www.ncbi.nlm.nih.gov/pubmed/11879110> [Accessed July 8, 2013].

- Pöschl, U., 2011. Gas–particle interactions of tropospheric aerosols: Kinetic and thermodynamic perspectives of multiphase chemical reactions, amorphous organic substances, and the activation of cloud condensation nuclei. *Atmospheric Research*, 101(3), pp.562–573. Available at: <http://dx.doi.org/10.1016/j.atmosres.2010.12.018> [Accessed August 30, 2013].
- Prenni, A.J. et al., 2007. Cloud droplet activation of secondary organic aerosol. *Journal of Geophysical Research*, 112(D10), p.D10223. Available at: <http://www.agu.org/pubs/crossref/2007/2006JD007963.shtml> [Accessed September 19, 2012].
- Prenni, A.J. et al., 2013. Real-time measurements of gas-phase reactive nitrogen during the GrandTReNDS field campaign.
- Putaud, J.-P. et al., 2004. A European aerosol phenomenology—2: chemical characteristics of particulate matter at kerbside, urban, rural and background sites in Europe. *Atmospheric Environment*, 38(16), pp.2579–2595. Available at: <http://dx.doi.org/10.1016/j.atmosenv.2004.01.041> [Accessed May 23, 2013].
- Raabe, O.G., 1971. Particle size analysis utilizing grouped data and the log-normal distribution. *Journal of Aerosol Science*, 2(3), pp.289–303. Available at: [http://dx.doi.org/10.1016/0021-8502\(71\)90054-1](http://dx.doi.org/10.1016/0021-8502(71)90054-1) [Accessed September 18, 2012].
- Radke, L.F., Coakley, J.A. & King, M.D., 1989. Direct and remote sensing observations of the effects of ships on clouds. *Science (New York, N.Y.)*, 246(4934), pp.1146–9. Available at: <http://www.sciencemag.org/content/246/4934/1146.short> [Accessed June 28, 2013].
- Ramachandran, S. et al., 2000. Radiative impact of the Mount Pinatubo volcanic eruption: Lower stratospheric response. *Journal of Geophysical Research*, 105(D19), p.24409. Available at: <http://doi.wiley.com/10.1029/2000JD900355> [Accessed July 14, 2013].
- Ramanathan, V. et al., 2001. Aerosols, climate, and the hydrological cycle. *Science (New York, N.Y.)*, 294(5549), pp.2119–24. Available at: <http://www.sciencemag.org/content/294/5549/2119.short> [Accessed May 23, 2013].
- Ramanathan, V. & Carmichael, G., 2008. Global and regional climate changes due to black carbon. *Nature Geoscience*, 1(4), pp.221–227. Available at: <http://dx.doi.org/10.1038/ngeo156> [Accessed May 24, 2013].
- Rao, X. & Collett, J.L., 1995. Behavior of S(IV) and Formaldehyde in a Chemically Heterogeneous Cloud. *Environmental science & technology*, 29(4), pp.1023–31. Available at: <http://dx.doi.org/10.1021/es00004a024> [Accessed September 28, 2013].
- Rattigan, O. V. et al., 2001. Sulfur dioxide oxidation in clouds at Whiteface Mountain as a function of drop size. *Journal of Geophysical Research*, 106(D15), p.17347. Available at: <http://doi.wiley.com/10.1029/2000JD900807> [Accessed September 30, 2013].
- Reddy, M.S., 2005. Estimates of global multicomponent aerosol optical depth and direct radiative perturbation in the Laboratoire de Météorologie Dynamique general circulation model. *Journal of Geophysical Research*, 110(D10), p.D10S16. Available at: <http://doi.wiley.com/10.1029/2004JD004757> [Accessed May 24, 2013].
- Reff, A., Eberly, S.I. & Bhave, P. V., 2007. Receptor modeling of ambient particulate matter data using positive matrix factorization: review of existing methods. *Journal of the Air & Waste Management Association (1995)*, 57(2), pp.146–54. Available at: <http://www.ncbi.nlm.nih.gov/pubmed/17355075> [Accessed September 20, 2012].
- Reid, J.S. et al., 2005. A review of biomass burning emissions part II: intensive physical properties of biomass burning particles. *Atmospheric Chemistry and Physics*, 5(3), pp.799–

825. Available at: <http://www.atmos-chem-phys.net/5/799/2005/acp-5-799-2005.html> [Accessed January 19, 2014].
- Reid, J.S. & Hobbs, P. V., 1998. Physical and optical properties of young smoke from individual biomass fires in Brazil. *Journal of Geophysical Research*, 103(D24), p.32013. Available at: <http://doi.wiley.com/10.1029/98JD00159> [Accessed January 19, 2014].
- Reilly, J.E. et al., 2001. Drop size-dependent S(IV) oxidation in chemically heterogeneous radiation fogs. *Atmospheric Environment*, 35(33), pp.5717–5728. Available at: <http://www.sciencedirect.com/science/article/pii/S1352231001003739> [Accessed September 30, 2013].
- Remer, L.A. & Kaufman, Y.J., 1998. Dynamic aerosol model: Urban/industrial aerosol. *Journal of Geophysical Research*, 103(D12), p.13859. Available at: <http://doi.wiley.com/10.1029/98JD00994> [Accessed January 19, 2014].
- Riemer, N. et al., 2010. Estimating black carbon aging time-scales with a particle-resolved aerosol model. *Journal of Aerosol Science*, 41(1), pp.143–158. Available at: <http://dx.doi.org/10.1016/j.jaerosci.2009.08.009> [Accessed September 10, 2013].
- Rizzo, M.J. & Scheff, P.A., 2007. Fine particulate source apportionment using data from the USEPA speciation trends network in Chicago, Illinois: Comparison of two source apportionment models. *Atmospheric Environment*, 41(29), pp.6276–6288. Available at: <http://www.sciencedirect.com/science/article/pii/S1352231007003287> [Accessed September 16, 2013].
- Roberts, G.C. et al., 2001. Cloud condensation nuclei in the Amazon Basin: “marine” conditions over a continent? *Geophysical Research Letters*, 28(14), pp.2807–2810. Available at: <http://doi.wiley.com/10.1029/2000GL012585> [Accessed June 7, 2013].
- Robinson, A.L. et al., 2007. Rethinking organic aerosols: semivolatile emissions and photochemical aging. *Science (New York, N.Y.)*, 315(5816), pp.1259–62. Available at: <http://www.sciencemag.org/content/315/5816/1259.short> [Accessed March 20, 2012].
- Roelofs, G.-J. & Kamphuis, V., 2009. Cloud processing, cloud evaporation and Angström exponent. *Atmospheric Chemistry and Physics*, 9(1), pp.71–80. Available at: <http://www.atmos-chem-phys.net/9/71/2009/acp-9-71-2009.html> [Accessed August 14, 2013].
- Rogge, W.F. et al., 1993. Quantification of urban organic aerosols at a molecular level: Identification, abundance and seasonal variation. *Atmospheric Environment. Part A. General Topics*, 27(8), pp.1309–1330. Available at: [http://dx.doi.org/10.1016/0960-1686\(93\)90257-Y](http://dx.doi.org/10.1016/0960-1686(93)90257-Y) [Accessed June 3, 2013].
- Rollins, a. W. et al., 2010. Elemental analysis of aerosol organic nitrates with electron ionization high-resolution mass spectrometry. *Atmospheric Measurement Techniques*, 3(1), pp.301–310. Available at: <http://www.atmos-meas-tech.net/3/301/2010/>.
- Rollins, A. et al., 2009. Isoprene oxidation by nitrate radical: alkyl nitrate and secondary organic aerosol yields. *Atmospheric Chemistry and Physics*, 9(18), pp.6685 – 6703. Available at: <http://www.citeulike.org/user/alupu/article/5788840> [Accessed October 8, 2012].
- Rollins, A.W. et al., 2012. Evidence for NO(x) control over nighttime SOA formation. *Science (New York, N.Y.)*, 337(6099), pp.1210–2. Available at: <http://www.sciencemag.org/content/337/6099/1210.abstract> [Accessed October 27, 2012].
- Romero, F. & Oehme, M., 2005. Organosulfates – A New Component of Humic-Like Substances in Atmospheric Aerosols? *Journal of Atmospheric Chemistry*, 52(3), pp.283–

294. Available at: <http://link.springer.com/10.1007/s10874-005-0594-y> [Accessed August 16, 2013].
- Römpp, A., Winterhalter, R. & Moortgat, G.K., 2006. Oxodicarboxylic acids in atmospheric aerosol particles. *Atmospheric Environment*, 40(35), pp.6846–6862. Available at: <http://dx.doi.org/10.1016/j.atmosenv.2006.05.053> [Accessed September 12, 2013].
- Rosenfeld, D. & Givati, A., 2006. Evidence of Orographic Precipitation Suppression by Air Pollution–Induced Aerosols in the Western United States. *Journal of Applied Meteorology and Climatology*, 45(7), pp.893–911. Available at: <http://journals.ametsoc.org/doi/abs/10.1175/JAM2380.1> [Accessed July 15, 2013].
- Rowe, M.D. & Perlinger, J.A., 2010. Performance of a high flow rate, thermally extractable multicapillary denuder for atmospheric semivolatile organic compound concentration measurement. *Environmental science & technology*, 44(6), pp.2098–104. Available at: <http://www.ncbi.nlm.nih.gov/pubmed/20148550> [Accessed September 11, 2013].
- Rozanov, E. V., 2002. Climate/chemistry effects of the Pinatubo volcanic eruption simulated by the UIUC stratosphere/troposphere GCM with interactive photochemistry. *Journal of Geophysical Research*, 107(D21), p.4594. Available at: <http://doi.wiley.com/10.1029/2001JD000974> [Accessed June 26, 2013].
- Rudich, Y., Donahue, N.M. & Mentel, T.F., 2007. Aging of organic aerosol: bridging the gap between laboratory and field studies. *Annual review of physical chemistry*, 58, pp.321–52. Available at: <http://www.annualreviews.org/doi/abs/10.1146/annurev.physchem.58.032806.104432> [Accessed August 14, 2013].
- Russell, L.M. et al., 2009. Oxygenated fraction and mass of organic aerosol from direct emission and atmospheric processing measured on the R/V Ronald Brown during TEXAQS/GoMACCS 2006. *Journal of Geophysical Research*, 114, p.D00F05. Available at: <http://doi.wiley.com/10.1029/2008JD011275> [Accessed September 12, 2013].
- Russell, L.M., Bahadur, R. & Ziemann, P.J., 2011. Identifying organic aerosol sources by comparing functional group composition in chamber and atmospheric particles. *Proceedings of the National Academy of Sciences of the United States of America*, 108(9), pp.3516–21. Available at: <http://www.pnas.org/content/108/9/3516.full> [Accessed May 29, 2013].
- Sato, K. et al., 2011. Secondary organic aerosol formation from the photooxidation of isoprene, 1,3-butadiene, and 2,3-dimethyl-1,3-butadiene under high NO_x conditions. *Atmospheric Chemistry and Physics*, 11(14), pp.7301–7317. Available at: <http://www.atmos-chem-phys.net/11/7301/2011/acp-11-7301-2011.html> [Accessed May 9, 2012].
- Sawyer, R., 2000. Mobile sources critical review: 1998 NARSTO assessment. *Atmospheric Environment*, 34(12-14), pp.2161–2181. Available at: [http://dx.doi.org/10.1016/S1352-2310\(99\)00463-X](http://dx.doi.org/10.1016/S1352-2310(99)00463-X) [Accessed September 6, 2013].
- Saxena, P. & Hildemann, L.M., 1996. Water-soluble organics in atmospheric particles: A critical review of the literature and application of thermodynamics to identify candidate compounds. *Journal of Atmospheric Chemistry*, 24(1), pp.57–109. Available at: <http://link.springer.com/10.1007/BF00053823> [Accessed July 14, 2013].
- Schichtel, B.A. et al., 2008. Fossil and contemporary fine particulate carbon fractions at 12 rural and urban sites in the United States. *Journal of Geophysical Research*, 113(D2), p.D02311. Available at: <http://www.agu.org/pubs/crossref/2008/2007JD008605.shtml> [Accessed October 10, 2012].

- Schindler, D.W. et al., 1971. Eutrophication of Lake 227, Experimental Lakes Area, Northwestern Ontario, by Addition of Phosphate and Nitrate. *Journal of the Fisheries Research Board of Canada*, 28(11), pp.1763–1782. Available at: <http://www.nrcresearchpress.com/doi/abs/10.1139/f71-261?journalCode=jfrbc#.UeQUZLwTH-k> [Accessed July 15, 2013].
- Schneider, J. et al., 2006. Mass spectrometric analysis and aerodynamic properties of various types of combustion-related aerosol particles. *International Journal of Mass Spectrometry*, 258(1-3), pp.37–49. Available at: <http://linkinghub.elsevier.com/retrieve/pii/S1387380606003460> [Accessed May 9, 2012].
- Schneider, J. et al., 2004. Online mass spectrometric aerosol measurements during the MINOS campaign (Crete, August 2001). *Atmospheric Chemistry and Physics*, 4(1), pp.65–80. Available at: <http://www.atmos-chem-phys.net/4/65/2004/acp-4-65-2004.html> [Accessed August 1, 2013].
- Schulte, P. & Arnold, F., 1990. Pyridinium ions and pyridine in the free troposphere. *Geophysical Research Letters*, 17(8), pp.1077–1080. Available at: <http://doi.wiley.com/10.1029/GL017i008p01077> [Accessed September 26, 2013].
- Schwarzenbach, R.P., Gschwend, P.M. & Imboden, D.M., 2005. *Environmental Organic Chemistry (Google eBook)*, John Wiley & Sons. Available at: <http://books.google.com/books?id=77ShpUHTZCYC&pgis=1> [Accessed June 24, 2013].
- Seigneur, C. & Saxena, P., 1984. A study of atmospheric acid formation in different environments. *Atmospheric Environment (1967)*, 18(10), pp.2109–2124. Available at: [http://dx.doi.org/10.1016/0004-6981\(84\)90197-5](http://dx.doi.org/10.1016/0004-6981(84)90197-5) [Accessed September 10, 2013].
- Seinfeld, J.H. et al., 2001. Modeling the formation of secondary organic aerosol (SOA). 2. The predicted effects of relative humidity on aerosol formation in the alpha-pinene-, beta-pinene-, sabinene-, delta 3-carene-, and cyclohexene-ozone systems. *Environmental science & technology*, 35(9), pp.1806–17. Available at: <http://www.ncbi.nlm.nih.gov/pubmed/11355196> [Accessed September 5, 2013].
- Seinfeld, J.H. & Pandis, S.N., 2006. *Atmospheric Chemistry and Physics: From Air Pollution to Climate Change* 2nd ed., John Wiley & Sons. Available at: <http://www.wiley-vch.de/publish/en/books/bySubjectES00/bySubSubjectESZ0/0-471-72018-6/?sID=5co5me0a5b99rg9a34n9kqmf07>.
- Seinfeld, J.H. & Pankow, J.F., 2003. Organic atmospheric particulate material. *Annual review of physical chemistry*, 54, pp.121–40. Available at: <http://www.annualreviews.org/doi/abs/10.1146/annurev.physchem.54.011002.103756?journalCode=physchem> [Accessed August 8, 2013].
- Setschenow, J., 1889. Über die Konstitution der Salzlosungen auf Grund ihres Verhaltens zu Kohlensäure. *Z. Phys. Chem.*, 1, pp.117–125.
- Shapiro, E.L. et al., 2009. Light-absorbing secondary organic material formed by glyoxal in aqueous aerosol mimics. *Atmospheric Chemistry and Physics Discussions*, 9(1), pp.59–80. Available at: <http://www.atmos-chem-phys-discuss.net/9/59/2009/acpd-9-59-2009.html> [Accessed June 25, 2013].
- Shen, H. & Anastasio, C., 2011. Formation of hydroxyl radical from San Joaquin Valley particles extracted in a cell-free surrogate lung fluid. *Atmospheric chemistry and physics (Print)*, 11(18), pp.9671–9682. Available at: <http://www.atmos-chem-phys.net/11/9671/2011/acp-11-9671-2011.html> [Accessed June 24, 2013].

- Shen, X., 2011. *Aqueous Phase Sulfate Production in Clouds at Mt. Tai in Eastern China*. Colorado State University. Available at: http://digitool.library.colostate.edu/R/?func=dbin-jump-full&object_id=127482&local_base=GEN01 [Accessed August 19, 2013].
- Shen, X.J. et al., 2011. First long-term study of particle number size distributions and new particle formation events of regional aerosol in the North China Plain. *Atmospheric Chemistry and Physics*, 11(4), pp.1565–1580. Available at: <http://www.atmos-chem-phys.net/11/1565/2011/acp-11-1565-2011.html> [Accessed September 9, 2013].
- Shi & Qian, 2003. *Continuous measurements of 3 nm to 10 micron aerosol size distributions in St. Louis*. University of Minnesota, Minneapolis, MN 55455.
- Shiraiwa, M. et al., 2013. Gas-particle partitioning of atmospheric aerosols: interplay of physical state, non-ideal mixing and morphology. *Physical chemistry chemical physics : PCCP*, 15(27), pp.11441–53. Available at: <http://pubs.rsc.org/en/content/articlehtml/2013/cp/c3cp51595h> [Accessed September 5, 2013].
- Shrivastava, M.K. et al., 2006. Modeling semivolatile organic aerosol mass emissions from combustion systems. *Environmental science & technology*, 40(8), pp.2671–7. Available at: <http://www.ncbi.nlm.nih.gov/pubmed/16683607> [Accessed September 9, 2013].
- Silva, P.J. et al., 1999. Size and Chemical Characterization of Individual Particles Resulting from Biomass Burning of Local Southern California Species. *Environmental Science & Technology*, 33(18), pp.3068–3076. Available at: <http://dx.doi.org/10.1021/es980544p> [Accessed September 26, 2013].
- Silva, P.J. et al., 2008. Trimethylamine as precursor to secondary organic aerosol formation via nitrate radical reaction in the atmosphere. *Environmental science & technology*, 42(13), pp.4689–96. Available at: <http://www.ncbi.nlm.nih.gov/pubmed/18677992>.
- Simoneit, B.R.T. et al., 2003. Alkyl Amides and Nitriles as Novel Tracers for Biomass Burning. *Environmental Science & Technology*, 37(1), pp.16–21. Available at: <http://dx.doi.org/10.1021/es020811y> [Accessed November 21, 2012].
- Simoneit, B.R.T. et al., 1999. Levoglucosan, a tracer for cellulose in biomass burning and atmospheric particles. *Atmospheric Environment*, 33(2), pp.173–182. Available at: <http://linkinghub.elsevier.com/retrieve/pii/S1352231098001459>.
- Skoog, D.A., Holler, F.J. & Crouch, S.R., 2006. *Principles of Instrumental Analysis*, Cengage Learning. Available at: <http://www.amazon.com/Principles-Instrumental-Analysis-Douglas-Skoog/dp/0495012017> [Accessed August 30, 2013].
- Slowik, J.G. et al., 2010. Simultaneous factor analysis of organic particle and gas mass spectra: AMS and PTR-MS measurements at an urban site. *Atmospheric Chemistry and Physics*, 10(4), pp.1969–1988. Available at: <http://www.atmos-chem-phys.net/10/1969/2010/acp-10-1969-2010.html> [Accessed September 12, 2013].
- Slusher, D.L., 2004. A thermal dissociation–chemical ionization mass spectrometry (TD-CIMS) technique for the simultaneous measurement of peroxyacyl nitrates and dinitrogen pentoxide. *Journal of Geophysical Research*, 109(D19), p.D19315. Available at: <http://doi.wiley.com/10.1029/2004JD004670> [Accessed September 18, 2013].
- Smith, J.E. & Jordan, M.L., 1964. Mathematical and graphical interpretation of the log-normal law for particle size distribution analysis. *Journal of Colloid Science*, 19(6), pp.549–559. Available at: [http://dx.doi.org/10.1016/0095-8522\(64\)90069-8](http://dx.doi.org/10.1016/0095-8522(64)90069-8) [Accessed August 1, 2012].

- Smith, J.N. et al., 2005. Chemical composition of atmospheric nanoparticles during nucleation events in Atlanta. *Journal of Geophysical Research*, 110(D22), p.D22S03. Available at: <http://doi.wiley.com/10.1029/2005JD005912> [Accessed September 12, 2013].
- Smith, M.L., Bertram, A.K. & Martin, S.T., 2012. Deliquescence, efflorescence, and phase miscibility of mixed particles of ammonium sulfate and isoprene-derived secondary organic material. *Atmospheric Chemistry and Physics Discussions*, 12(4), pp.9903–9943. Available at: <http://www.atmos-chem-phys-discuss.net/12/9903/2012/acpd-12-9903-2012.html> [Accessed July 30, 2013].
- Smith, M.L., Kuwata, M. & Martin, S.T., 2011. Secondary Organic Material Produced by the Dark Ozonolysis of α -Pinene Minimally Affects the Deliquescence and Efflorescence of Ammonium Sulfate. *Aerosol Science and Technology*, 45(2), pp.244–261. Available at: <http://dx.doi.org/10.1080/02786826.2010.532178> [Accessed September 10, 2013].
- Sorooshian, A., Brechtel, F.J., et al., 2006. Modeling and Characterization of a Particle-into-Liquid Sampler (PILS). *Aerosol Science and Technology*, 40(6), pp.396–409. Available at: <http://dx.doi.org/10.1080/02786820600632282> [Accessed September 12, 2013].
- Sorooshian, A., Varutbangkul, V., et al., 2006. Oxalic acid in clear and cloudy atmospheres: Analysis of data from International Consortium for Atmospheric Research on Transport and Transformation 2004. *Journal of Geophysical Research*, 111(D23), p.D23S45. Available at: <http://doi.wiley.com/10.1029/2005JD006880> [Accessed August 14, 2013].
- Spracklen, D. V. et al., 2011. Aerosol mass spectrometer constraint on the global secondary organic aerosol budget. *Atmospheric Chemistry and Physics Discussions*, 11(2), pp.5699–5755. Available at: <http://adsabs.harvard.edu/abs/2011ACPD...11.5699S> [Accessed August 25, 2013].
- Starn, T.K. et al., 1998. Observations of isoprene chemistry and its role in ozone production at a semirural site during the 1995 Southern Oxidants Study. *Journal of Geophysical Research*, 103(D17), p.22425. Available at: <http://doi.wiley.com/10.1029/98JD01279> [Accessed September 6, 2013].
- Stavrakou, T. et al., 2009. The continental source of glyoxal estimated by the synergistic use of spaceborne measurements and inverse modelling. *Atmospheric Chemistry and Physics*, 9(21), pp.8431–8446. Available at: <http://www.atmos-chem-phys.net/9/8431/2009/acp-9-8431-2009.html> [Accessed June 25, 2013].
- Stefan, M.I. & Bolton, J.R., 1999. Reinvestigation of the Acetone Degradation Mechanism in Dilute Aqueous Solution by the UV/H₂O₂ Process. *Environmental Science & Technology*, 33(6), pp.870–873. Available at: <http://dx.doi.org/10.1021/es9808548> [Accessed June 25, 2013].
- Stein, A.F. et al., 2007. A hybrid modeling approach to resolve pollutant concentrations in an urban area. *Atmospheric Environment*, 41(40), pp.9410–9426. Available at: <http://www.sciencedirect.com/science/article/pii/S1352231007007881> [Accessed September 17, 2013].
- Stenchikov, G.L. et al., 1998. Radiative forcing from the 1991 Mount Pinatubo volcanic eruption. *Journal of Geophysical Research*, 103(D12), p.13837. Available at: <http://doi.wiley.com/10.1029/98JD00693> [Accessed July 14, 2013].
- Stone, E.A. et al., 2009. Investigating the chemical nature of humic-like substances (HULIS) in North American atmospheric aerosols by liquid chromatography tandem mass spectrometry. *Atmospheric Environment*, 43(27), pp.4205–4213. Available at: <http://dx.doi.org/10.1016/j.atmosenv.2009.05.030> [Accessed August 16, 2013].

- Sullivan, A.P., 2004. A method for on-line measurement of water-soluble organic carbon in ambient aerosol particles: Results from an urban site. *Geophysical Research Letters*, 31(13), p.L13105. Available at: <http://doi.wiley.com/10.1029/2004GL019681> [Accessed August 14, 2013].
- Sullivan, A.P. et al., 2008. A method for smoke marker measurements and its potential application for determining the contribution of biomass burning from wildfires and prescribed fires to ambient PM 2.5 organic carbon. *Journal of Geophysical Research*, 113(D22), p.D22302. Available at: <http://www.agu.org/pubs/crossref/2008/2008JD010216.shtml> [Accessed December 13, 2012].
- Sullivan, R.C. & Prather, K.A., 2005. Recent advances in our understanding of atmospheric chemistry and climate made possible by on-line aerosol analysis instrumentation. *Analytical chemistry*, 77(12), pp.3861–85. Available at: <http://www.ncbi.nlm.nih.gov/pubmed/15952760> [Accessed August 7, 2013].
- Sun, Y. et al., 2010. Insights into secondary organic aerosol formed via aqueous-phase reactions of phenolic compounds based on high resolution mass spectrometry. *Atmospheric Chemistry and Physics Discussions*, 10(2), pp.2915–2943. Available at: <http://www.atmos-chem-phys-discuss.net/10/2915/2010/acpd-10-2915-2010.html> [Accessed June 25, 2013].
- Sun, Y.-L. et al., 2011. Characterization of the sources and processes of organic and inorganic aerosols in New York city with a high-resolution time-of-flight aerosol mass spectrometer. *Atmospheric Chemistry and Physics*, 11(4), pp.1581–1602. Available at: <http://www.atmos-chem-phys.net/11/1581/2011/> [Accessed April 19, 2012].
- Surratt, J.D. et al., 2006. Chemical composition of secondary organic aerosol formed from the photooxidation of isoprene. *The journal of physical chemistry. A*, 110(31), pp.9665–90. Available at: <http://dx.doi.org/10.1021/jp061734m> [Accessed June 22, 2013].
- Surratt, J.D. et al., 2007. Evidence for organosulfates in secondary organic aerosol. *Environmental science & technology*, 41(2), pp.517–27. Available at: <http://www.ncbi.nlm.nih.gov/pubmed/17310716> [Accessed June 22, 2013].
- Surratt, J.D. et al., 2008. Organosulfate Formation in Biogenic Secondary Organic Aerosol. *The Journal of Physical Chemistry A*, 112(36), pp.8345–8378. Available at: <http://dx.doi.org/10.1021/jp802310p> [Accessed June 25, 2013].
- Surratt, J.D. et al., 2010. Reactive intermediates revealed in secondary organic aerosol formation from isoprene. *Proceedings of the National Academy of Sciences of the United States of America*, 107(15), pp.6640–5. Available at: <http://www.pubmedcentral.nih.gov/articlerender.fcgi?artid=2872383&tool=pmcentrez&rendertype=abstract> [Accessed March 31, 2012].
- Szmigielski, R. et al., 2007. Characterization of 2-methylglyceric acid oligomers in secondary organic aerosol formed from the photooxidation of isoprene using trimethylsilylation and gas chromatography/ion trap mass spectrometry. *Journal of mass spectrometry : JMS*, 42(1), pp.101–16. Available at: <http://europepmc.org/abstract/MED/17154243/reload=0> [Accessed August 6, 2013].
- Takahama, S., Pathak, R.K. & Pandis, S.N., 2007. Efflorescence Transitions of Ammonium Sulfate Particles Coated with Secondary Organic Aerosol. *Environmental Science & Technology*, 41(7), pp.2289–2295. Available at: <http://dx.doi.org/10.1021/es0619915> [Accessed January 21, 2014].

- Takegawa, N. et al., 2005. Characterization of an Aerodyne Aerosol Mass Spectrometer (AMS): Intercomparison with Other Aerosol Instruments. *Aerosol Science and Technology*, 39(8), pp.760–770. Available at: <http://dx.doi.org/10.1080/02786820500243404> [Accessed July 30, 2012].
- Takegawa, N. et al., 2006. Seasonal and diurnal variations of submicron organic aerosol in Tokyo observed using the Aerodyne aerosol mass spectrometer. *Journal of Geophysical Research*, 111(D11), p.D11206. Available at: <http://adsabs.harvard.edu/abs/2006JGRD..11111206T> [Accessed August 29, 2013].
- Takemura, T. et al., 2005. Simulation of climate response to aerosol direct and indirect effects with aerosol transport-radiation model. *Journal of Geophysical Research*, 110(D2), p.D02202. Available at: <http://doi.wiley.com/10.1029/2004JD005029> [Accessed May 21, 2013].
- Takemura, T. et al., 2001. Simulation of future aerosol distribution, radiative forcing, and long-range transport in East Asia. Available at: <http://repository.dl.itc.u-tokyo.ac.jp/dspace/handle/2261/26646> [Accessed July 14, 2013].
- Tan, Y. et al., 2009. Effects of precursor concentration and acidic sulfate in aqueous glyoxal-OH radical oxidation and implications for secondary organic aerosol. *Environmental science & technology*, 43(21), pp.8105–12. Available at: <http://dx.doi.org/10.1021/es901742f> [Accessed June 11, 2013].
- Tan, Y. et al., 2012. Mechanisms leading to oligomers and SOA through aqueous photooxidation: insights from OH radical oxidation of acetic acid and methylglyoxal. *Atmospheric Chemistry and Physics*, 12(2), pp.801–813. Available at: <http://www.atmos-chem-phys.net/12/801/2012/acp-12-801-2012.html> [Accessed August 2, 2013].
- Tan, Y. et al., 2010. SOA from methylglyoxal in clouds and wet aerosols: Measurement and prediction of key products. *Atmospheric Environment*, 44(39), pp.5218–5226. Available at: <http://dx.doi.org/10.1016/j.atmosenv.2010.08.045> [Accessed June 6, 2013].
- Tanner, D.J. & Eisele, F.L., 1991. Ions in oceanic and continental air masses. *Journal of Geophysical Research*, 96(D1), p.1023. Available at: <http://doi.wiley.com/10.1029/90JD02131> [Accessed September 26, 2013].
- Tanner, R.L. et al., 2005. Diurnal patterns in PM_{2.5} mass and composition at a background, complex terrain site. *Atmospheric Environment*, 39(21), pp.3865–3875. Available at: <http://dx.doi.org/10.1016/j.atmosenv.2005.03.014> [Accessed September 17, 2012].
- Tilgner, A. & Herrmann, H., 2010. Radical-driven carbonyl-to-acid conversion and acid degradation in tropospheric aqueous systems studied by CAPRAM. *Atmospheric Environment*, 44(40), pp.5415–5422. Available at: <http://dx.doi.org/10.1016/j.atmosenv.2010.07.050> [Accessed June 24, 2013].
- Timperley, M.H. et al., 1985. Organic Nitrogen Compounds in Atmospheric Precipitation: Their Chemistry and Availability to Phytoplankton. *Canadian Journal of Fisheries and Aquatic Sciences*, 42(6), pp.1171–1177. Available at: <http://www.nrcresearchpress.com/doi/abs/10.1139/f85-145> [Accessed September 15, 2013].
- Tkacik, D.S. et al., 2012. Secondary organic aerosol formation from intermediate-volatility organic compounds: cyclic, linear, and branched alkanes. *Environmental science & technology*, 46(16), pp.8773–81. Available at: <http://lib.bioinfo.pl/paper:22823284> [Accessed July 23, 2013].
- Tobias, D.E. et al., 2007. Direct thermal desorption of semivolatile organic compounds from diffusion denuders and gas chromatographic analysis for trace concentration measurement.

- Journal of chromatography. A*, 1140(1-2), pp.1–12. Available at: <http://dx.doi.org/10.1016/j.chroma.2006.11.045> [Accessed September 11, 2013].
- Tsigaridis, K. & Kanakidou, M., 2003. Global modelling of secondary organic aerosol in the troposphere: a sensitivity analysis. *Atmospheric Chemistry and Physics*, 3(5), pp.1849–1869. Available at: <http://www.atmos-chem-phys.net/3/1849/2003/acp-3-1849-2003.html> [Accessed September 4, 2013].
- Turnipseed, A.A. et al., 2006. Eddy covariance fluxes of peroxyacetyl nitrates (PANs) and NO_y to a coniferous forest. *Journal of Geophysical Research*, 111(D9), p.D09304. Available at: <http://doi.wiley.com/10.1029/2005JD006631> [Accessed September 18, 2013].
- Turpin, B.J., Huntzicker, J.J. & Hering, S. V., 1994. Investigation of organic aerosol sampling artifacts in the los angeles basin. *Atmospheric Environment*, 28(19), pp.3061–3071. Available at: [http://dx.doi.org/10.1016/1352-2310\(94\)00133-6](http://dx.doi.org/10.1016/1352-2310(94)00133-6) [Accessed September 11, 2013].
- Turpin, B.J. & Lim, H.-J., 2001. Species Contributions to PM_{2.5} Mass Concentrations: Revisiting Common Assumptions for Estimating Organic Mass. *Aerosol Science and Technology*, 35(1), pp.602–610. Available at: <http://www.tandfonline.com/doi/abs/10.1080/02786820119445>.
- Twomey, S., Davidson, K.A. & Seton, K.J., 1978. Results of Five Years' Observations of Cloud Nucleus Concentration at Robertson, New South Wales. *Journal of the Atmospheric Sciences*, 35(4), pp.650–656. Available at: [http://journals.ametsoc.org/doi/abs/10.1175/1520-0469\(1978\)035<0650:ROFYOO>2.0.CO;2](http://journals.ametsoc.org/doi/abs/10.1175/1520-0469(1978)035<0650:ROFYOO>2.0.CO;2) [Accessed July 15, 2013].
- Ulbrich, I.M., 2011. *Characterization of Positive Matrix Factorization Methods and Their Application to Ambient Aerosol Mass Spectra*. University of Colorado.
- Ulbrich, I.M. et al., 2009. Interpretation of organic components from Positive Matrix Factorization of aerosol mass spectrometric data. *Atmospheric Chemistry and Physics*, 9(9), pp.2891–2918. Available at: <http://www.atmos-chem-phys.net/9/2891/2009/>.
- Ulbrich, I.M. et al., 2006. Source Apportionment of Aerosol Mass Spectrometer Data in Pittsburgh, Mexico City, and Houston by Positive Matrix Factorization. *AGU Fall Meeting Abstracts*, -1, p.0980. Available at: <http://adsabs.harvard.edu/abs/2006AGUFM.A23C0980U> [Accessed September 12, 2013].
- Ulbrich, I.M. et al., 2012. Three-dimensional factorization of size-resolved organic aerosol mass spectra from Mexico City. Available at: <http://core.kmi.open.ac.uk/display/1141137> [Accessed February 5, 2013].
- University of Wyoming, D. of A.S. website, 2012. University of Wyoming, Department of Atmospheric Science Upper Air Soundings. *Oolman, L*. Available at: <http://weather.uwyo.edu/upperair/sounding.html> [Accessed September 4, 2012].
- USFS, 2013. USFS Remote Sensing Applications Center MODIS Fire Mapping Database. Available at: <http://activefiremaps.fs.fed.us/activefiremaps.php> [Accessed May 23, 2013].
- Val Martin, M. et al., 2013. A decadal satellite analysis of the origins and impacts of smoke in Colorado. *Atmospheric Chemistry and Physics*, 13(15), pp.7429–7439. Available at: <http://www.atmos-chem-phys.net/13/7429/2013/acp-13-7429-2013.html> [Accessed January 23, 2014].
- Valavanidis, A., Fiotakis, K. & Vlachogianni, T., 2008. Airborne particulate matter and human health: toxicological assessment and importance of size and composition of particles for oxidative damage and carcinogenic mechanisms. *Journal of environmental science and*

- health. Part C, Environmental carcinogenesis & ecotoxicology reviews*, 26(4), pp.339–62. Available at: <http://www.ncbi.nlm.nih.gov/pubmed/19034792> [Accessed May 22, 2013].
- Valsaraj, K.T. et al., 1993. On the enrichment of hydrophobic organic compounds in fog droplets. *Atmospheric Environment. Part A. General Topics*, 27(2), pp.203–210. Available at: [http://dx.doi.org/10.1016/0960-1686\(93\)90351-X](http://dx.doi.org/10.1016/0960-1686(93)90351-X) [Accessed September 10, 2013].
- Valverde-Canossa, J. et al., 2005. H₂O₂ and organic peroxide measurements in an orographic cloud: The FEBUKO experiment. *Atmospheric Environment*, 39(23-24), pp.4279–4290. Available at: <http://dx.doi.org/10.1016/j.atmosenv.2005.02.040> [Accessed June 22, 2013].
- Vinckier, C., Compernelle, F. & Saleh, A., 1997. Qualitative determination of the non-volatile reaction products of the alpha-pinene reaction with hydroxyl radicals. *Bull. Aos. Chim. Belg.*, 106. Available at: <https://lirias.kuleuven.be/handle/123456789/31708> [Accessed June 25, 2013].
- Volkamer, R. et al., 2006. Secondary organic aerosol formation from anthropogenic air pollution: Rapid and higher than expected. *Geophysical Research Letters*, 33(17), p.L17811. Available at: <http://doi.wiley.com/10.1029/2006GL026899> [Accessed August 7, 2013].
- Volkamer, R., Platt, U. & Wirtz, K., 2001. Primary and Secondary Glyoxal Formation from Aromatics: Experimental Evidence for the Bicycloalkyl–Radical Pathway from Benzene, Toluene, and p-Xylene. *The Journal of Physical Chemistry A*, 105(33), pp.7865–7874. Available at: <http://dx.doi.org/10.1021/jp010152w> [Accessed June 24, 2013].
- Volkamer, R., Ziemann, P.J. & Molina, M.J., 2009. Secondary Organic Aerosol Formation from Acetylene (C₂H₂): seed effect on SOA yields due to organic photochemistry in the aerosol aqueous phase. *Atmospheric Chemistry and Physics*, 9(6), pp.1907–1928. Available at: <http://www.atmos-chem-phys.net/9/1907/2009/acp-9-1907-2009.html> [Accessed June 24, 2013].
- Wainwright, C.D. et al., 2012. The effect of model spatial resolution on Secondary Organic Aerosol predictions: a case study at Whistler, BC, Canada. *Atmospheric Chemistry and Physics*, 12(22), pp.10911–10923. Available at: <http://www.atmos-chem-phys.net/12/10911/2012/acp-12-10911-2012.html> [Accessed August 6, 2013].
- Wand, M.P. & Jones, M.C., 1995. *Kernel Smoothing*, Chapman & Hall. Available at: http://books.google.com/books/about/Kernel_Smoothing.html?id=GTOOi5yE008C&pgis=1 [Accessed September 17, 2013].
- Wang, L., Atkinson, R. & Arey, J., 2007. Dicarbonyl Products of the OH Radical-Initiated Reactions of Naphthalene and the C 1 - and C 2 -Alkylnaphthalenes. *Environmental Science & Technology*, 41(8), pp.2803–2810. Available at: <http://dx.doi.org/10.1021/es0628102> [Accessed January 8, 2014].
- Wang, S., Zordan, C.A. & Johnston, M. V, 2006. Chemical characterization of individual, airborne sub-10-nm particles and molecules. *Analytical chemistry*, 78(6), pp.1750–4. Available at: <http://dx.doi.org/10.1021/ac052243l> [Accessed September 12, 2013].
- Wang, X. et al., 2010. Evidence for high molecular weight nitrogen-containing organic salts in urban aerosols. *Environmental science & technology*, 44(12), pp.4441–6. Available at: <http://dx.doi.org/10.1021/es1001117> [Accessed September 25, 2013].
- Wang, Y. et al., 2007. Characteristics and sources of formic, acetic and oxalic acids in PM_{2.5} and PM₁₀ aerosols in Beijing, China. *Atmospheric Research*, 84(2), pp.169–181. Available at: <http://dx.doi.org/10.1016/j.atmosres.2006.07.001> [Accessed August 10, 2013].

- Wang, Y. et al., 2010. Probing the source of hydrogen peroxide associated with coarse mode aerosol particles in southern California. *Environmental science & technology*, 44(11), pp.4070–5. Available at: <http://www.ncbi.nlm.nih.gov/pubmed/20429550> [Accessed June 24, 2013].
- Warneck, P., 2003. In-cloud chemistry opens pathway to the formation of oxalic acid in the marine atmosphere. *Atmospheric Environment*, 37(17), pp.2423–2427. Available at: <http://www.deepdyve.com/lp/elsevier/in-cloud-chemistry-opens-pathway-to-the-formation-of-oxalic-acid-in-TXVo41jrQA/fulltext> [Accessed June 24, 2013].
- Watson, J.G., 2002. Visibility: Science and Regulation. *Journal of the Air & Waste Management Association*, 52(6), pp.628–713. Available at: <http://dx.doi.org/10.1080/10473289.2002.10470813> [Accessed July 15, 2013].
- Weber, R. et al., 2001. A particle-into-liquid collector for rapid measurement of aerosol bulk chemical composition. *Aerosol Science and Technology*, 35, pp.718–727. Available at: http://hero.epa.gov/index.cfm?action=reference.details&reference_id=24640 [Accessed October 10, 2012].
- Weber, R.J. et al., 2001. A Particle-into-Liquid Collector for Rapid Measurement of Aerosol Bulk Chemical Composition. *Aerosol Science and Technology*, 35(3), pp.718–727. Available at: <http://dx.doi.org/10.1080/02786820152546761> [Accessed August 17, 2012].
- Weber, R.J. et al., 2007. A study of secondary organic aerosol formation in the anthropogenic-influenced southeastern United States. *Journal of Geophysical Research*, 112(D13), p.D13302. Available at: <http://doi.wiley.com/10.1029/2007JD008408> [Accessed August 7, 2013].
- Weber, R.J. et al., 1997. Measurements of new particle formation and ultrafine particle growth rates at a clean continental site. *Journal of Geophysical Research*, 102(D4), p.4375. Available at: <http://doi.wiley.com/10.1029/96JD03656> [Accessed September 8, 2013].
- Weimer, S. et al., 2008. Organic aerosol mass spectral signatures from wood-burning emissions: Influence of burning conditions and wood type. *Journal of Geophysical Research*, 113(D10), pp.1–10. Available at: <http://www.agu.org/pubs/crossref/2008/2007JD009309.shtml> [Accessed May 9, 2012].
- Weiss-Penzias, P. et al., 2006. Observations of Asian air pollution in the free troposphere at Mount Bachelor Observatory during the spring of 2004. *Journal of Geophysical Research*, 111(D10), p.D10304. Available at: <http://doi.wiley.com/10.1029/2005JD006522> [Accessed October 3, 2013].
- Welthagen, W., Schnelle-Kreis, J. & Zimmermann, R., 2003. Search criteria and rules for comprehensive two-dimensional gas chromatography–time-of-flight mass spectrometry analysis of airborne particulate matter. *Journal of Chromatography A*, 1019(1-2), pp.233–249. Available at: <http://dx.doi.org/10.1016/j.chroma.2003.08.053> [Accessed September 12, 2013].
- Weschler, C.J., Mandich, M.L. & Graedel, T.E., 1986. Speciation, photosensitivity, and reactions of transition metal ions in atmospheric droplets. *Journal of Geophysical Research*, 91(D4), p.5189. Available at: <http://doi.wiley.com/10.1029/JD091iD04p05189> [Accessed June 24, 2013].
- Whitby, K.T., 1978. The physical characteristics of sulfur aerosols. *Atmospheric Environment (1967)*, 12(1), pp.135–159. Available at: <http://www.sciencedirect.com/science/article/pii/0004698178901968> [Accessed January 19, 2014].

- Whitby, K.T. & Sverdrup, G.M., 1980. California aerosols: their physical and chemical characteristics. *Adv. Environ. Sci. Technol.*, 8(477-525).
- Wiedinmyer, C. et al., 2004. Emissions of Atmospheric Trace Compounds C. Granier, P. Artaxo, & C. E. Reeves, eds. *Advances in Global Change Research*, 18, pp.115–170. Available at: <http://www.springerlink.com/index/10.1007/978-1-4020-2167-1> [Accessed September 5, 2013].
- Williams, M.W., Hood, E. & Caine, N., 2001. The role of organic nitrogen in the nitrogen cycle of a high-elevation catchment, Colorado Front Range. Available at: <http://citeseerx.ist.psu.edu/viewdoc/summary?doi=10.1.1.71.3678> [Accessed June 25, 2013].
- Winterhalter, R. et al., 2003. LC-MS analysis of aerosol particles from the oxidation of α -pinene by ozone and OH-radicals. *Atmospheric Chemistry and Physics Discussions*, 3(1), pp.1–39. Available at: <http://www.atmos-chem-phys-discuss.net/3/1/2003/acpd-3-1-2003.html> [Accessed June 25, 2013].
- Wolfe, G.M. et al., 2009. Eddy covariance fluxes of acyl peroxy nitrates (PAN, PPN and MPAN) above a Ponderosa pine forest. *Atmospheric Chemistry and Physics*, 9(2), pp.615–634. Available at: <http://www.atmos-chem-phys.net/9/615/2009/acp-9-615-2009.html> [Accessed September 18, 2013].
- Wu, C. et al., 2007. Source apportionment of PM_{2.5} and selected hazardous air pollutants in Seattle. *Science of The Total Environment*, 386(1), pp.42–52. Available at: <http://www.sciencedirect.com/science/article/pii/S0048969707007711> [Accessed September 16, 2013].
- Xie, Y. & Berkowitz, C.M., 2007. The use of conditional probability functions and potential source contribution functions to identify source regions and advection pathways of hydrocarbon emissions in Houston, Texas. *Atmospheric Environment*, 41(28), pp.5831–5847. Available at: <http://dx.doi.org/10.1016/j.atmosenv.2007.03.049> [Accessed November 7, 2012].
- Xiong, J.Q. et al., 1998. Influence of Organic Films on the Hygroscopicity of Ultrafine Sulfuric Acid Aerosol. *Environmental Science & Technology*, 32(22), pp.3536–3541. Available at: <http://dx.doi.org/10.1021/es980019q> [Accessed June 24, 2013].
- Yasmeen, F. et al., 2010. Characterization of oligomers from methylglyoxal under dark conditions : a pathway to produce secondary organic aerosol through cloud processing during nighttime. , pp.3803–3812.
- Yasmeen, F. et al., 2010. Terpenylic acid and related compounds: precursors for dimers in secondary organic aerosol from the ozonolysis of α - and β -pinene. *Atmospheric Chemistry and Physics*, 10(19), pp.9383–9392. Available at: <http://www.atmos-chem-phys.net/10/9383/2010/acp-10-9383-2010.html> [Accessed August 7, 2013].
- Yu, J. et al., 1999. Gas-Phase Ozone Oxidation of Monoterpenes: Gaseous and Particulate Products. *Journal of Atmospheric Chemistry*, 34(2), pp.207–258. Available at: <http://link.springer.com/article/10.1023/A:1006254930583> [Accessed August 2, 2013].
- Yu, K. et al., 2004. Identifying the impact of large urban airports on local air quality by nonparametric regression. *Atmospheric Environment*, 38(27), pp.4501–4507. Available at: <http://www.sciencedirect.com/science/article/pii/S1352231004005229> [Accessed September 17, 2013].
- Zappoli, S. et al., 1999. Inorganic, organic and macromolecular components of fine aerosol in different areas of Europe in relation to their water solubility. *Atmospheric Environment*,

- 33(17), pp.2733–2743. Available at: [http://dx.doi.org/10.1016/S1352-2310\(98\)00362-8](http://dx.doi.org/10.1016/S1352-2310(98)00362-8) [Accessed September 9, 2013].
- Zelenyuk, A., Imre, D. & Cuadra-Rodriguez, L.A., 2006. Evaporation of water from particles in the aerodynamic lens inlet: an experimental study. *Analytical chemistry*, 78(19), pp.6942–7. Available at: <http://dx.doi.org/10.1021/ac061184o> [Accessed August 30, 2013].
- Zellner, R., Exner, M. & Herrmann, H., 1990. Absolute OH quantum yields in the laser photolysis of nitrate, nitrite and dissolved H₂O₂ at 308 and 351 nm in the temperature range 278–353 K. *Journal of Atmospheric Chemistry*, 10(4), pp.411–425. Available at: <http://link.springer.com/10.1007/BF00115783> [Accessed June 24, 2013].
- Zhang, Q., Alfarra, M.R., et al., 2005. Deconvolution and quantification of hydrocarbon-like and oxygenated organic aerosols based on aerosol mass spectrometry. *Environmental science & technology*, 39(13), pp.4938–52. Available at: <http://www.ncbi.nlm.nih.gov/pubmed/16053095>.
- Zhang, Q., Worsnop, D.R., et al., 2005. Hydrocarbon-like and oxygenated organic aerosols in Pittsburgh: insights into sources and processes of organic aerosols. *Atmospheric Chemistry and Physics*, 5(12), pp.3289–3311. Available at: <http://www.atmos-chem-phys.net/5/3289/2005/acp-5-3289-2005.html> [Accessed September 12, 2013].
- Zhang, Q. et al., 2004. Insights into the Chemistry of New Particle Formation and Growth Events in Pittsburgh Based on Aerosol Mass Spectrometry. *Environmental Science & Technology*, 38(18), pp.4797–4809. Available at: <http://dx.doi.org/10.1021/es035417u> [Accessed September 8, 2013].
- Zhang, Q., Canagaratna, M.R., et al., 2005. Time- and size-resolved chemical composition of submicron particles in Pittsburgh: Implications for aerosol sources and processes. *Journal of Geophysical Research*, 110(D7), p.D07S09. Available at: <http://doi.wiley.com/10.1029/2004JD004649> [Accessed August 29, 2013].
- Zhang, Q. et al., 2007. Ubiquity and dominance of oxygenated species in organic aerosols in anthropogenically-influenced Northern Hemisphere midlatitudes. *Geophysical Research ...*, 34(13), pp.1–6. Available at: <http://www.agu.org/pubs/crossref/2007/2007GL029979.shtml> [Accessed April 12, 2012].
- Zhang, Q. et al., 2011. Understanding atmospheric organic aerosols via factor analysis of aerosol mass spectrometry: a review. *Analytical and bioanalytical chemistry*, 401(10), pp.3045–67. Available at: <http://www.pubmedcentral.nih.gov/articlerender.fcgi?artid=3217143&tool=pmcentrez&rendertype=abstract> [Accessed January 29, 2013].
- Zhang, Q., 2002. Water-soluble organic nitrogen in atmospheric fine particles (PM 2.5) from northern California. *Journal of Geophysical Research*, 107(D11), p.4112. Available at: <http://doi.wiley.com/10.1029/2001JD000870> [Accessed September 15, 2013].
- Zhang, X., Chen, Z.M. & Zhao, Y., 2010. Laboratory simulation for the aqueous OH-oxidation of methyl vinyl ketone and methacrolein: significance to the in-cloud SOA production. *Atmospheric Chemistry and Physics Discussions*, 10(6), pp.15595–15628. Available at: <http://www.atmos-chem-phys-discuss.net/10/15595/2010/acpd-10-15595-2010.html> [Accessed June 25, 2013].
- Zhao, J. et al., 2006. Heterogeneous Reactions of Methylglyoxal in Acidic Media: Implications for Secondary Organic Aerosol Formation. *Environmental Science & Technology*, 40(24), pp.7682–7687. Available at: <http://dx.doi.org/10.1021/es060610k> [Accessed June 24, 2013].

- Zheng, W. et al., 2011. Characterization of a thermal decomposition chemical ionization mass spectrometer for the measurement of peroxy acyl nitrates (PANs) in the atmosphere. *Atmospheric Chemistry and Physics*, 11(13), pp.6529–6547. Available at: <http://www.atmos-chem-phys.net/11/6529/2011/acp-11-6529-2011.html> [Accessed September 18, 2013].
- Zhou, L. et al., 2004. Advanced factor analysis for multiple time resolution aerosol composition data. *Atmospheric Environment*, 38(29), pp.4909–4920. Available at: <http://dx.doi.org/10.1016/j.atmosenv.2004.05.040> [Accessed October 9, 2012].
- Zhou, L., 2005. Investigation of the relationship between chemical composition and size distribution of airborne particles by partial least squares and positive matrix factorization. *Journal of Geophysical Research*, 110(D7), p.D07S18. Available at: <http://doi.wiley.com/10.1029/2004JD005050> [Accessed September 16, 2013].
- Zhu, Y. et al., 2002. Study of ultrafine particles near a major highway with heavy-duty diesel traffic. *Atmospheric Environment*, 36(27), pp.4323–4335. Available at: [http://dx.doi.org/10.1016/S1352-2310\(02\)00354-0](http://dx.doi.org/10.1016/S1352-2310(02)00354-0) [Accessed February 19, 2013].
- Ziemann, P.J., 2010. Atmospheric chemistry: phase matters for aerosols. *Nature*, 467(7317), pp.797–8. Available at: <http://dx.doi.org/10.1038/467797a> [Accessed September 10, 2013].
- Ziemann, P.J., 2002. Evidence for Low-Volatility Diacyl Peroxides as a Nucleating Agent and Major Component of Aerosol Formed from Reactions of O₃ with Cyclohexene and Homologous Compounds. *The Journal of Physical Chemistry A*, 106(17), pp.4390–4402. Available at: <http://dx.doi.org/10.1021/jp012925m>.
- Ziemba, L.D. et al., 2010. Characterization of aerosol associated with enhanced small particle of number concentrations in a suburban forested environment. *Journal of Geophysical Research*, 115(D12), p.D12206. Available at: <http://doi.wiley.com/10.1029/2009JD012614> [Accessed September 12, 2013].
- Zuend, A. et al., 2008. A thermodynamic model of mixed organic-inorganic aerosols to predict activity coefficients. *Atmospheric Chemistry and Physics*, 8(16), pp.4559–4593. Available at: <http://www.atmos-chem-phys.net/8/4559/2008/acp-8-4559-2008.html> [Accessed September 10, 2013].

8. Appendices

8.1 AMS Instrument Function Summaries and Calibration Protocols

1. AMS instrument details for Rocky Mountain National Park field campaign

AMS_Type: HR: V and W

AMS_SamplingTime: 2 minute runs: V mode (10 sec ea open and closed, 20sec PToF, 3cycles/run) and W mode (20 sec ea open and closed, 3cycles/run)

AMS_LensType: standard

AMS_FlowRate: study average=1.47 ± 0.02 cm³/sec

AMS_PrsTempFlowCal: calibration conditions: P = 1012.5 hPa, T = 15.5 C, flow rate = 1.47 cm³/sec

AMS_STPConversionFactor: 0.96

AMS_IEOverAB: 5.34E-13

AMS_RIENH4: RIE_{NH4} = 5.4; DMA-sized 300 nm NH₄NO₃ BFSP with concurrently sampled condensation particle counter verification.

AMS_CE: Constant CE=0.5 based on thresholds in Middlebrook et al. (2012). Here, NH₄/NH_{4,predict} = 0.8 (r² = 0.96) > 0.75 threshold, ANMF = 0.11 ± 0.15 < 0.4 threshold, relative humidity in the inlet < 80% for 88% of data points (see *InletRH*). Supported by PILS-IC sulfate comparison (m=1.00, r²=0.88) consistent with other studies (Takegawa et al. 2005; Middlebrook et al. 2012).

AMS_PMCut: PM_{2.5}

AMS_InletRH: ambient: inlet RH averages 52 ± 22%; 88% of hourly data points are below 80% RH (inclusive of raining data points with very low aerosol concentration), using Clausius-Clapeyron with ambient temperature, ambient RH, and the mobile lab thermostat setting (15.56 °C)

AMS_LocalToUTCTime: UTC – 7h

AMS_RelatedInstrumentationInfo: Inside mobile lab held at 15.56 °C; dedicated inlet.

Other calibrations, etc.: HEPA-filtered ambient air sampled for ~30 minutes every other day (per Aerodyne Research, 2005). PSL size calibration at beginning and end of campaign.

Instrument comparisons: PILS-AMS (17-min resolution): NO₃: m=1.29, r²=0.76; NH₄: m=0.80, r²=0.50.

2. AMS instrument details for Grand Teton National Park field campaign

AMS_Type: HR: V and W

AMS_SamplingTime: 5 minute runs: V mode (20 sec each open and closed, 20 sec PToF, 1/cycle, 5 cycles/run) and W mode (10 sec ea open and closed, 3/cycle, 5cycles/run)

AMS_LensType: standard

AMS_FlowRate: study average=2.06 ± 0.12 cm³/sec

AMS_PrsTempFlowCal: calibration conditions: P = 740.9 hPa, T = 23 C, flow rate = 2.07 cm³/sec

AMS_STPConversionFactor: 0.68

AMS_IEOverAB: 7.44E-13

AMS_RIENH4: RIE_{NH4} = 5.4; DMA-sized 300 nm NH₄NO₃ BFSP with concurrently sampled condensation particle counter verification.

AMS_CE: Constant CE=0.5 based on thresholds in Middlebrook et al. (2012). Here, NH₄/NH_{4,predict} = 0.83 (r² = 0.81) > 0.75 threshold, ANMF = 0.04 ± 0.02 < 0.4 threshold.

AMS_PMCut: PM_{2.5}

AMS_InletRH: ambient: inlet humidity averages 4.4168 ± 1.35265 ppt.

AMS_LocalToUTCTime: UTC – 7h

AMS_RelatedInstrumentationInfo: Dedicated inlet.

Other calibrations, etc.: HEPA-filtered ambient air sampled for ~30 minutes every other day (per Aerodyne Research, 2005). PSL size calibration at beginning and end of campaign.

Table 8-1: Rocky Mountain thresholds for ‘high’ concentrations (inclusive) used in the Conditional Probability Function equal the component average plus one standard deviation. Thresholds vary between wind levels because averaging times for components were different (to match wind data availability); longer averaging times damp the amplitude of high-concentration events, requiring different thresholds to define the same high-concentration event

Wind Level	LV-OOA	SV-OOA	BBOA	SO ₄	NO ₃	NH ₄
700 mb (3hr)	3.16	2.68	0.56	1.40	0.33	0.30
Surface (1hr)	4.34	2.38	1.86	2.09	0.47	0.45

8.2 AMS Calibration and Data Analysis Protocols

The following checklists were developed to streamline calibration and standardize note-taking; they are based on and serve to supplement the AMS Wiki developed by the Jimenez Group at University of Colorado, Boulder, which should be consulted during calibration:

http://cires.colorado.edu/jimenez-group/wiki/index.php/Field_ToF-AMS_Operation#5.2_Data_processing_of_IE_calibration_.28for_DMA.2FCPC_data_analysis.29

A Quick Overview of AMS Controls

The AMS is controlled by hard-wired switches and two main pieces of software – the TPS (power supply) control software, which applies current to components, and the DAQ (data acquisition software), which controls the TPS, guiding it to switch between modes automatically, etc.

Most maintenance during this campaign will involve only the DAQ, but some TPS interaction may be necessary in the case of a W-mode failure. (see troubleshooting section at end of this document). No W-mode failures have been observed since installation of a new DAQ version, so you probably won't have to deal with this.

A number of hard-wired switches control power to various hardware – turbo pumps, diaphragm backing pump, the TPS (power supply), etc.; in case of an emergency (such as a power failure in the building), it may be necessary to use some of these. The UPS batteries can power the AMS for ~30 minutes; emergency shutdown takes about 30 minutes as well (SOP taped to wall near AMS). If you observe a power failure and expect it to last more than ~20 minutes (to be safe), please begin emergency shutdown procedures IMMEDIATELY.

Lastly, a series of small screws on the left front panel of the AMS (near the floor), control chopper speed, heater power, and other parameters. If undesirable drift is apparent (chopper $>\sim 153$ or <147 , heater temp $>\sim 570$ or <550), a small screw-driver (stored in slot in 80/20 frame by AMS inlet) can be used to *gently and gradually* adjust chopper Hz or heater power by turning the screws (adjust heater power by 0.01A at a time, then wait to stabilize – e.g. 1.17 to 1.18 if too cool, or 1.20-1.19 if too hot).

DAQ Software:

The DAQ software has a main panel from which all other panels are accessed. At the top of this panel, checking the “TPS” box will enable the DAQ to control the TPS. **THIS BOX MUST BE CHECKED DURING ALL CALIBRATIONS, CHECKS, AND ACQUISITION.**

-The box next to the “**Menu**” button contains the number of the currently active menu (listed in a table to the right). Select a menu by typing the number and pressing “Enter.”

-The “**Menu**” button opens a window with tabs concerning averaging and saving times, mass spectrometer settings, ionization efficiency, single-ion area, signal baseline and threshold, etc. Screenshots of current parameters for each (V and W) mode, for each menu tab, can be found in Desktop/Shortcut to screenshots/TeRNiP/Menu settings

-The “**Acquire**” button leads to the acquisition screen, where you can start data acquisition and view data in real time.

-The “**Calibration**” button produces a window with m/z calibration and mass spectrometer tuning information. DO NOT re-tune the mass spec during a campaign, as a host of calibrations must follow tuning. Some drift in signal intensity and resolution is normal. Contact Misha for instructions if, for example, emission current deteriorates steadily.

-The “**Bitwise**” button opens a screen with information on baseline signal intensity, thresholding, and the single-ion area. Baseline and threshold are determined at the beginning of the campaign and should not usually be changed. The single-ion area will be evaluated during ionization efficiency (IE) calibrations using functions in the Bitwise window.

The “**servo**” button will open a window where signal intensity is measured as the chopper is moved, ensuring that the chopper servo position is correct for open, closed, and chopping modes.

Controlling the Acquisition and Calibration Displays:

- On a graph or mass spectrum, zoom in by drawing a box around the desired item with the mouse; zoom out by right-clicking and selecting ‘unzoom’ or auto-range or whatever you like.
- CNTRL-L (1-2 times) toggles logarithmic scale on a mass spectrum y-axis.

More specific instructions for interactions with these windows are provided in each calibration SOP below. All SOPs are included in this document, but most users will only have to do m/z calibration, HEPA-filtered air sampling, data backup, and possibly (Yury) the IE calibration.

M/Z Calibration

1. Stop acquisition (click stop button on lower left corner of acquisition screen).
2. Click “stop and exit” button (upper right).
3. CLOSE main green “AMS inlet” valve (marked with yellow tape).
4. On main DAQ window, select MENU=1 for V mode (or =2 for W).
5. Click CALIBRATION button.
6. In the resulting window, you will see a raw mass spectrum (“MS,” ToF flight time on x-axis, signal intensity on Y-axis). Three smaller windows below this MS show the three ions used for the m/z calibration; N⁺ = m/z 14, O₂⁺ = m/z 32, and tungsten⁺ at m/z 184 (emitted from vaporizer/ionization source). The flight time (X-axis on MS) is shown in a little box below each ion.
7. On the upper right, click the “MOVE” button near the “Chopper” text to open the chopper.
8. On the upper left-most button above the MS, click “AVG.” This will refresh the MS. (do not average continuously – that is for tuning the mass spec). As you adjust the calibration as outlined below, please click “AVG” repeatedly – the peaks may shift somewhat from refresh to refresh, so looking at many spectra will enable you to pick the most ‘common’ peak position to use for the calibration.
9. In each of the three ion graphs, the vertical green dashed line (indicating the exact mass of the chosen ion) should match exactly with the apex of the signal peak. You can adjust the placement of the green line by changing the ToF flight time in the small box below the graph and pressing ‘enter.’
10. The ‘error’ (in ppm) of the current m/z calibration is shown in a graph below the three ion graphs. You will see three black points and two dashed blue asymptotes – these blue lines bound the acceptable range of error; i.e. **the three black points should be between the blue**

lines. (See screenshots of past m/z cals by following pathway in Step 9 for reference, if necessary).

11. If you accidentally enter a weird number and/or don't see peaks where you saw them before, click "Revert to Saved Calibration" in the upper right corner of the window. Re-open calibration window and start over.
12. When the calibration looks good, please take a screenshot: Press CNTL-ScreenShot, open Paint (on desktop), paste screenshot, and Save As: Desktop/Shortcut to screenshots/ TeRNiP (follow the naming scheme therein; just enter the correct date).
13. On upper right of calibration window, click "Save All and Exit." This will return you to the main DAQ window.
14. Repeat Steps 1-13 for W Mode (Choose MENU=2 in Step 1, above).

Re-start Data Acquisition:

15. On the main DAQ window, select V Mode (enter 1 in box, hit enter).
16. OPEN inlet valve.
17. Click the "Acquire" button to go to the acquisition window.
18. (NOT CURRENTLY ACTIVE – SKIP STEP) Save real-time files (in small pop-up window).
19. Click "acquire" button (lower left).
20. Note run number and start time in logbook.
21. Press CNTRL-L 1-2 times to adjust mass spectrum y-axis to non-log scale, and zoom in as desired (reference screenshots have x-axis range ~12-150).
22. Sample HEPA-filtered air (see next page) for 20-30 minutes before starting ambient-air acquisition, if time allows.

Troubleshooting the m/z calibration:

1. **Symptoms:** (a) The m/z cal is completely off (may not see peaks in three graphs, of peaks may be outside of the grey shaded area delineating a 'unit mass'), **AND** (if not, see 2, below) (b) the raw MS in the calibration window looks noisy (noise around the base of 32, etc. with no zoom) and has 'extra' peaks. Also, (c) there may be red numbers in the column to the right. **Explanation:** A suspected bug in the DAQ changes the TPS settings loaded by a given DAQ menu (observed in both V and W modes; for instance, the V mode starts loading the W-mode TPS settings while maintaining a V-shaped flight path, or visa versa).
To fix:
 - a. Check the m/z cal for the other mode (usually, one mode is fine, the other is off), and note the result in the lab book.
 - b. In the main DAQ window, select the malfunctioning mode, and click MENU.
 - c. In the menu TOFAMS tab, click the "Load *.set" button.
 - d. For TRNP:
 - i. For V Mode, select: TeRNiP_V_F1_120713_27_5.set (the last number is the heater bias, which is actually 27.0, not 27.5, but I didn't change the file name – you do not have to do anything, just load as-is).
 - ii. For W Mode, select: TeRNiP_W_F1_102813_10.5.set
 - iii. Save the menu (upper left button).
 - iv. Re-check the m/z cal for the malfunctioning mode.
2. **Symptoms:** The m/z cal is very far off. However, the MS looks generally 'clean' and like the figure below. **Explanation:** Sometimes temperature and other factors can cause the m/z cal to

drift so far that the “auto-calibrate during acquisition” (a box at the bottom of the screen, which should ALWAYS be activated) can’t keep up. In this case, you may have to find m/z 14, 32, and 184 (in red in figure below) by yourself, using the following mass-spectral patterns.

- Look for the signature 18 down to 14. Hold the mouse over the desired peak (m/z 14, 32 or 184) and look for the changing number below the mass spectrum window. Where it says “Sample XXX,” the XXX number – flight time in the ToF - should be entered in the small time box below the appropriate window (m/z 14, 32, or 184). Hit enter. You should see a peak in a grey shaded area, and the vertical green dashed line should line up with the peak apex (adjust, as above, until the line matches the peak).
- Look for 28 that goes up and down if you: move chopper, then click AVG (or open valve, for larger effect)
- Look for 32 right after 28
- The tungsten peaks will be in a group of 4, see figure below. They are increased in relative intensity in the figure below - in the real MS they are fairly small. You can zoom in by drawing a box around them with the mouse; zoom out by right-clicking and selecting ‘unzoom’ or auto-range or whatever you like).
- If the calibration is very wrong, peak centers will stray from unit mass values (bounded by grey shading in the three ion graphs).



Sampling HEPA-filtered Air: It is useful, during data analysis and after altering the inlet, etc., to sample filtered air for 20-30 minutes. This is recommended every ~2-3 days for this project after completion of m/z or IE calibrations.

1. If data acquisition is already started, skip 3 & 4 and just note start time and run in the logbook.
2. There are three black valves immediately before the main Green AMS inlet valve. Turning all of them 90 degrees will re-route sampled air through a HEPA filter and close the direct sample stream to the AMS inlet. (First (#1) and last (#3) valve open, middle (#2) valve closed.)
3. Make sure menu switching is ON in the main MENU window (accessed through main DAQ window).
4. Open acquisition window, save real-time files (if applicable), and begin acquisition. NOTE starting run number and time in logbook.
5. NOTE: The grey bars (air beam ions) will still appear in the real-time MS, but most species should be minimal (you may see some green bars – nominally organics - because the real-time software automatically apportions some air-beam-ion mass to organics, e.g. at m/z 44, but these should not be organized into organic ‘wave’ patterns, or contain much mass).

6. After 20-30 minutes, switch all the valves back (1 & 3 closed, middle (#2) valve open) during the 'waiting for TPS' period between runs to start sampling ambient air.
7. Note starting run number and time of ambient sample in logbook.

Data Download: Data backup is recommended every two days or so. Data can be backed up while acquiring, but **GREAT CARE** must be taken **NOT** to copy the data file currently being acquired, or the DAQ may crash.

1. Two folders should be open on the desktop:
 - a. Desktop/Shortcut to ToFAMSDData/AutosaveHDF
 - b. E/TRNP/
2. Each of these folders contains two folders: "main" contains _m files of mass spec data, and "PToF" contains _p files of PToF data.
3. Look in E/TRNP/Main for the last file copied.
4. In the ../AutosaveHDF/Main, select the next file (after the last one copied), through **the file PREVIOUS to the one currently being acquired (i.e. DO NOT select the most recent file, which is currently being recorded)**. CNTRL-C copies these files.
5. Paste (CNTRL-V) them into E/TRNP/Main.
6. Repeat for PToF files, using the relevant folders (copying PToF files may take up to ~3 min per day of data).

Flow Calibration: Must be redone with altitude change (should be 1.5-1.6 ccs; if not, clean and redo)

1. Make a table in IGOR containing the following columns: flow_ccm, Pressure Volts, flow_ccs, Nozzle flow (an example experiment: **flow_ccm_Ft052510.pxp**)
2. Save the experiment anew with the current date.
3. Loosen line to blue filter pack, and the nuts on the inlet support.
4. Gilibrator used: 20 ccm – 6 lpm
5. Remove the critical orifice from AMS inlet.
6. Replace with a needle valve; flow goes from Gilibrator, through the valve, and into AMS.
7. Close needle valve entirely.
8. Open flow valve on AMS (Biggest green valve just before aerodynamic lens).
9. Measure a series of Gilibrator flow and Pressure data points (from Torr readout on electronics box); put into IGOR (flow_ccm and Pressure Volts, respectively). Make sure to cover a wide range, but get more data points around what the AMS flow 'should' be: 1.5-1.6 ccs.
10. Close the flow valve on AMS (Biggest green valve).
11. "..._ccs" wave = "..._ccm" flow (from Gilibrator)/60
12. Append the data to graph.
13. Analysis – Curve Fitting – Function – Line (Select X and Y waves)
14. Data Options: (do **not** set intercept to zero)
15. Can get slope and intercept from the command line (VPr is the correlation).
16. Reinstall the AMS inlet (w/ critical orifice).
17. Open the flow valve on AMS.

18. Check the flow with the critical orifice and plot with calibration data; it should be on the calibration line. (incoming flow should contact 'widest' orifice opening first; pinhole should face away from flow/be nearest to aerodynamic lens).
19. Flow rate should be $\sim 1.6 \text{ cm}^3/\text{sec}$
20. Close the flow valve on AMS (Biggest green valve).
21. Note critical orifice used in AMS notebook
22. Open DAQ
23. Menus – Analog/Digital
24. Input new slope and intercept from flow calibration and save.

Aerodynamic Lens Alignment

1. Set up NH_4NO_3 300nm particle generation (size/concentration not super important, just need mass).
2. Loosen 4 screws fixing lens plate in place.
3. Chopper control (shortcut): Chopper open
4. Set up signal monitoring:
 - a. Shortcut to AeroTimer: Select ToF frequency = 20Hz, click CONTINUOUS MODE.
 - b. Shortcut to Acquiris:
 - i. Setup – Recall – vwToFconfig
 - ii. Click smooth graph button (upper L corner)
 - iii. Instrument – Select Class – Average
 - iv. Option – Connect Data Points
 - v. Click NORMAL
 - vi. Zoom window. Must find H_2O and Air (28 and 32) peaks.
 - vii. Open BIG GREEN valve to sample particles – should see new peak (NO) appear between 28 and 32. Zoom in on this peak (@ ~ 1.7525 X axis) and 10x-20x magnify.
5. Starting from a point in the last lens alignment, adjust X and Y position to find the edges of the ellipse bounding particle transmission. For instance, move the X position +/- 0.2 and scan Y until the signal goes away; this is a boundary point.
6. Log all boundary points and plot in some software. It should look like an ellipse (X diam > Y diam) (plotting helps to see if you didn't find the edges very well).
7. Find X and Y max and min, and from there the center of the ellipse.
8. Adjust the lens to the optimal values found in step 7.
9. Working in a diagonal pattern, tighten 4 screws, checking continuously that the alignment is being maintained.

Sizing Calibration: Necessary to click 'save itx files.'

1. Turn heater to appropriate value: $\text{NH}_4\text{NO}_3 = 550 \text{ C}$; PSL = 750 C [really 600,800 C but our sensor is off]).
2. Open IGOR experiment – only need to drag and drop itx. files into experiment.
3. PToF 20 sec sampling (save raw data for MS – necessary for PIKA)
4. Make sure m/z cal is done and saved (document with screenshots).

5. Generate particles of a known size, either NH_4NO_3 with a DMA or PSL 50-600 nm.
6. Start acquiring data while sampling known-size particles.
7. Note run range for given size (take minimum 2-3 minutes of data per size).
8. Take a representative itx. File (or two) from the middle of each size file group and drag and drop into IGOR (the wave is: mMassToF_runnumber, and should contain a wave for each m/z)
9. command line: display wavename[[]][37] displays m/z46 for NH_4NO_3 particles, use [][95] (m/z 104) for PSL (can check to make sure that these are the right column references).
10. command line: appendtograph wavename[[]][37] to add subsequent waves
11. May choose to average or use lognormal fit of multiple itx. samples for each particle size.
12. CNTRL-I opens info, put target on particle peak: X position of peak = arrival time.
13. Make a table similar to other sizing calib experiments; have mobility diameter (Dm), need vacuum aerodynamic diameter ($Dva = Dm * \rho * s.f.$)
14. For NH_4NO_3 : $\rho=1.72$, $s.f.=0.8$; For PSL: $\rho=1.05$, $s.f.=1$
15. Velocity = $(293\text{mm}/P\text{ToF_time}) * 1E6$
16. X = Dva and Y = Velocity graph is calibration graph, ANALYSIS tab for p[0-3]
17. Drag and drop VelFxn.ipf into experiment
18. CL: FuncFit/NTHR=0 VelFit W_coef PSL_Velocity /X=PSL_Dva_Aero /D
19. Input new p[0-3] into correct menus and save.

Ionization Efficiency BFSP Calibration:

1. Stop Acquisition: click “stop” button; note run number and time.
2. CLOSE the green inlet valve (just before aerodynamic lens).
3. Check m/z calibration for V & W modes and save (also take screenshots).
4. (SKIP) Check Servo position. (Menu=1 (V), click SERVO button, click “Start.” Two blue triangles should appear, with the middle data point the highest of the three (like a party hat). Don’t worry much if one (or, sometimes, even both) of the triangles does not look right – just save a screenshot with the m/z cal screenshots and I will review it. Click “stop,” (it will go on to do full scans, which take a while), wait for the program to stop, then click “Exit” on the upper right.
5. From main DAQ menu, select V or W and click BITWISE – you need the Single Ion measurement for each mode. On the main Bitwise window, there are two main panels and a right-handle column. Do not do anything with the Left panel.
 - a. Make sure chopper is blocked (buttons on lower right of window).
 - b. In the “Single Extraction Peaks” panel, click “Start” on the upper left. This will start acquiring signal from ion impacts on the MCP. On the upper graph in the right-hand panel, note the average single-ion peak area (largest value, in bold, units = bit-ns). It may take a while for this to stabilize (~500 or 1000 peak acquisitions in V or W mode, respectively). You can start Step 6 while waiting for values.
 - c. Note the value in the logbook, and enter into appropriate menus (click the “Mass List Value” button below “Single Ion” box in the R-hand column, then check that the new value is entered correctly in Main DAQ – MENU – ToFAMS tab. Save menu. The new V-mode single ion value should be entered into both menus 1 (V) and 3 (BFSP IE Cal).

- d. Repeat for W mode. W-mode single ion value is entered into Menu 2.
6. Setup particle generation 300-400 nm (usually use 300 nm). 200-400 particles/cc concentration is ideal (use a CPC to count; data logged in Analog 5 channel).
 - a. Connect compressed air line to atomizer. Sample flows from atomizer – dryer – neutralizer – then into “polydisperse flow” port on DMA.
 - b. Turn on DMA and CPC – connect CPC pump (small pump under chair with orange power cord) and run exhaust line out the back door. Adjust DMA to generate 300 nm particles (usually use flow = 9 LPM); after turning wheel to select a DMA setting, push wheel to change that setting.
 - c. Take off ambient inlet at the joint marked with yellow tape that says “Cal.”
 - d. Connect 4-way Swagelock fitting (put cap from compressed air line on 4th opening) to the AMS inlet at the joint marked with yellow tape that says “Cal.” One line should come in from the “monodisperse flow” port on the DMA, one line should go to the CPC, and the remaining opening goes into the AMS.
7. Main DAQ – MENU – front panel: UN-select menu switching (upper left check-box).
8. MENU = 3 IESPCal (Averaging and Saving Tab: BFSP 20 sec, MS(5/5), 2 cycles/run = 60 seconds total).
9. Main DAQ – ACQUIRE – Autosave on.
10. OPEN the green inlet valve.
11. Start acquiring data until C/ToFAMS/ToFAMSDData/BFSPData data has ~200 files (right-click – properties to see number of files acquired). Please note Start Run, Time, #/cc (from CPC), size, and particle composition (probably NH₄NO₃) in notebook.
 - a. CNTRL-L 1-2x will toggle y-axis log scale.
 - b. MS should contain only NH₄ (orange), NO₃ (blue), and air (grey) peaks. Otherwise look for incorrect plumbing in particle generation, leaks, etc.
12. Stop acquisition, close green valve, exit window (upper right button).
13. In C/ToFAMS/ToFAMSDData/, rename the BFSPData folder by adding “_MMDDYY” to the end of the folder name. This prevents future confusion.
14. Open (from desktop) IGOR ams_tof_ie_calibration_v3.1.3.ipf
15. Save a copy with the current date (in Desktop/Shortcut to Calibration/IE Calibration – see naming scheme therein, also contains .ipf in step 14, above).
16. Panels – Regular Panel.
17. Upper left - Browse for BFSPData folder in C/ToFAMS/ToFAMSDData/BFSPData_MMDDYY.
18. Click ‘Load Data’.
19. Set baseline and particle arrival ranges on graph (find screenshot in desktop – shortcut to calibration – IE calibration), CoAdd =1, enter correct single ion area (V mode value) and particle diameter (Dm).
20. Click ‘Do It’
21. Blacklist bad points and click ‘Do It’ again until RIE<6. Log IE, RIE.
22. Do NOT enter the new IE value into the menu yet.
23. Using HEPA-filtered air, measure airbeam and calculate W mode IE:
 - a. Main DAQ – MENU – front panel: SELECT menu switching.
 - b. Menu 1 (V), “Avg and Saving” tab: change “cycles/run” from 5 to 1 – this makes a 1-minute total run. Do the same in W mode. Save (upper left button).

- c. Turn all three black valves just before AMS inlet – this should route the sample through a HEPA filter. (Close #2, Open #1 and #3)
 - d. Main DAQ – ACQUIRE. Start acquiring, not run number and time.
 - e. For ~4 runs per mode, note Air Beam (AB, right-hand column on acquisition window); record in notebook.
 - f. Enter BFSP IE for V-mode, average V- and W-mode AB from step e, and Single Ion values into the “IE for VWmode.xls” Excel file (should be open, or find in: Desktop/Shortcut to Calibration/IE Calibration folder). The worksheet will calculate the W mode IE if you drag the formula down in the “W_IE” column. You may also apply corrections from a CPC-mass-based calibration here (see two columns – for V and W – immediately to right of V_ IE and W_ IE columns).
- 24. Enter new IEs (in pink column) into correct menus and save. (DAQ main – MENU – ToFAMS tab – small window near top, hit “Enter”, save menu)**
- 25. Enter new IEs into logbooks as well.
 - 26. Menus 1 and 2 (V & W), DAQ main – MENU - “Avg and Saving” tab: **change “cycles/run” from 1 to 5** – this makes a 5-minute (300 seconds/run) total run. Do the same in W mode. Save (upper left button). Make sure ‘acquisition clock’ = ‘each run’ (lower left in Avg. and Saving Tab).
 - 27. Make sure “menu switching” is ON (on front “menu” tab). Pink and Orange bars will appear at top of menu window.
 - 28. Re-attach ambient inlet at yello “cal” sticker.
 - 29. Now ready to start getting ambient data. Main DAQ – ACQUIRE, with the green inlet valve OPEN.
 - 30. If time allows, please sample HEPA-filtered air for 20-30 minutes before starting ambient-air acquisition. Please note run numbers and time for starting HEPA air, and when starting ambient sampling.
 - 31. Remove compressed-air line from atomizer and cap (this is NECESSARY to maintain pressure in Tony’s gas-rack system). Turn off DMA, CPC, and put away CPC pump.

IE CPC Mass-Based Calibration:

- 1. Get CPC and particle generation setup – 300-350 nm particle size.
- 2. Measure CPC flow: if <1LPM, must divide CPC_voltage by this number to correct for sub-expected flow. (CPC_cnts=CPC_voltage*1000/0.493 in our case)
- 3. CPC is Analog05 input – make sure AMS computer is reporting the same # the CPC displays.
- 4. Check *m/z* calibration, take screenshot.
- 5. Check and input Single Ion Area values if appropriate (Bitwise tab; Close biggest green vlave)
- 6. MENU: V/W alternate:
 - a. V = 2 min, MS(10/10), PToF 20, 3 cycles/run
 - b. W = 2 min, MS(20/20), 3 cycles/run
 - c. OR, at TRNP, **change “cycles/run” to 1 or 2, save menu.**
- 7. Autosave and Acquire ON

8. Want to get ~15 min of data for a number of concentration ranges: ~600 p/cc, ~400p/cc, ~250 p/cc, and ~60-100 p/cc. Tailor data collection to typical mass at site (i.e. more low-conc points at remote sites). Note run numbers for all this, log DMA function, etc.
9. Make a new folder named “CPC IE MMDDYY” in the IE Calibration folder.
10. In this new folder, make 3 new folders named “main,” “ptof,” and “int.”
11. Copy the HDF files from Desktop/Shortcut to ToFAMSDData/AutosaveHDF/Main into the main folder; put PToF files into PToF folder (if desired, not necessary).
12. Open an IGOR experiment
(C:\ToFAMS\ToFAMSCode\ToF_AMS_HRanalysis_V1_11k.pxp).
13. Put in data, calculate CPC_mass_nitrate and compare to AMS (CPC = X, AMS = Y).
(Open folder containing last CPC IE calibration to find an example experiment – e.g. CPC IE 121413 -, and follow code in command line).
 - a. Correct for CPC flow irregularities, as seen in previous experiments.
 - b. Check numbers against previous experiments for general similarity.
14. Line of best fit between CPC and AMS nitrate. Use slope to correct BFSP IE: IE_V or IE_W corrected by: mass_based_ IE = (BFSP IE)*b, where b is the slope from the above AMS (y) vs. CPC (x) nitrate graph for the given mode.
15. Useful equations:
 - $\text{CPC_cnts_mass (microg/m}^3\text{)} = 1/6 * \pi * (300/1000)^3 * 0.8 * 1.72 * \text{CPC_cnts}$
 - Where pi(3.14159), 300(size of particle(nm)), 0.8(density modifier), and 1.72 (Density of NH₄NO₃)
 - $\text{CPC_cnts_mass_nitrate} = \text{CPC_cnts_mass} * (61.9878/80.0222)$
 - IE_V or W corrected by: mass_based_ IE = (BFSP IE)*b, where b is the slope from the above AMS (y) vs. CPC (x) nitrate graph for the given mode.

Operating the LICOR 840 CO2 Monitor:

The CO₂ monitor constrains gaseous CO₂ contributions to m/z 44, which also contains CO₂ fragments from oxygenated organics.

In case of a power failure (if LICOR not on the UPS), start at Step 9.

1. The LICOR needs a backing pump. An orifice creating ~XX LPM flow is recommended; see manual for allowable flow parameters. Remember to add flow through LICOR to backing pump flow when choosing orifices to meet inlet cyclone flow requirements.
2. A line to the LICOR can be placed after the AMS inlet and a HEPA filter, but before the AMS inlet backing pump (needed to maintain size cut on cyclone).
3. Boot laptop WITHOUT LICOR serial cable connected. (Bug causes laptop trackpad to fail if LICOR is connected upon boot).
4. Plug LICOR in - to power and to serial connection with computer.
5. Start – Programs – LI-840 A V2.0.1
6. In the resulting window, click upper left-most button to find a connection with the instrument.
7. Select Serial Port 1.
8. After the connection is established, a window should appear with a number of boxes – the top two have continuously changing CO₂ (ppm, left side) and H₂O (usually ppt, right side).
9. Now begin logging data:
 - a. Synch clock with AMS clock.

- b. Go to C:\Program Files\LI840A_2_0_1 and re-name the “LogFile.txt”, if it exists, with the current date (see other files therein for format). LICOR will overwrite this file otherwise.
- c. Ensure averaging time equals AMS run time (i.e. 300 seconds). ‘Logging’ menu – Options – 1 record/300 seconds.
- d. On the main CO₂ monitoring window, click the red-circle icon to start logging data.
 - i. Window pops up for data-save pathway. (Default: LogFile.txt)
 - ii. Click OK on this window EXACTLY on the 5-minute mark (e.g. 12:00:00, 12:05:00, 12:10:00, etc.) to synch easily with AMS data.

TROUBLE SHOOTING:

1. The DAQ closes unexpectedly (may see an error window like “DAQ has encountered a problem and needs to close”):
 - a. Re-start the DAQ software by clicking the ‘ari’ icon on the task bar.
 - b. Click the “TPS” check box.
 - c. Follow instructions on re-starting acquisition in Steps 15-21 in the “m/z Calibration” instructions earlier in this document.
 - d. Note starting run and time in the notebook.
2. The V or W Mode fails: The mass spectrum during V or W mode acquisition has black or green bars that are roughly the same intensity (no organic ‘wave’ patterns, but more like a logarithmic function that evens off at higher m/z), BUT, the next V or W mode run (after waiting through the next sample cycle ~5-10 minutes) looks normal.
 - a. **IS YOUR CELL PHONE ON AIRPLANE MODE???** If not, this is probably causing the problem. Place cell on airplane mode (or turn cell off) and remove from the room.
 - b. Wait to see if the mass spectrum goes back to normal after a sampling cycle (5-10 minutes, after V mode has turned on once). This has been observed numerous times at TRNP.
 - c. If not, see #4, below.
3. There are no grey bars on the mass spectrum (possibly, no bars at all). This is most probable in the W mode. The V mode may be fine, or, if temperature fluctuations, etc., were extremely severe, may also manifest in the V mode.
 - a. Problem (probably): The m/z cal is so shifted that the DAQ can’t identify peaks at all.
 - b. Do an m/z calibration, then re-start acquisition.
4. The W Mode fails: The mass spectrum during W mode acquisition has black or green bars that are roughly the same intensity (no organic ‘wave’ patterns, but more like a logarithmic function that evens off at higher m/z). **VERY IMPORTANT: the W mode looks like this in many consecutive runs** (wait another acquisition cycle (one V mode, one W mode run): if it’s isolated to one run, then goes back to normal, ignore it). **This has NOT been observed at TRNP, and is unlikely to occur.**
 - a. **IS YOUR CELL PHONE ON AIRPLANE MODE???** If not, this is probably causing the problem. Place cell on airplane mode and/or remove from room. Wait to see if the mass spectrum goes back to normal after a sampling cycle (5-10 minutes, after V mode has turned on once).

- b. If cell interference is not the problem:
- c. In the acquisition window, while still acquiring, go to the “Time Series” tab – if the W mode is failing it will read zero for every species, every W-mode run (every-other run on the time series). The V-mode runs will look normal.
- d. Stop acquisition, note run number, time, and reason. Exit acquisition screen.
- e. Close DAQ.
- f. Click “shutdown” button on TPS window and wait for voltages to go to zero.
- g. Close TPS program (click “x” on upper right). You MUST close and re-open the TPS, or the w mode will not regain function.
- h. Re-open TPS program from the taskbar (blue squiggly-looking icon).
- i. Click “initialize”
- j. File – load menu – select: TeRNiP_V_F1_120713_27_5.set
- k. Click “call voltage”
- l. Wait ~20 minutes for the filament to warm up – its applied and emission currents should be steadily increasing to an applied current = 3.70 (I think), and an emission current ~2.0.
- m. Open the DAQ software as in Troublshooting #1 a-b.
- n. Check the m/z calibration for both modes
- o. Re-start data acquisition following Steps 15-21 in the “m/z Calibration” instructions earlier in this document.
- p. Note start time and run number.

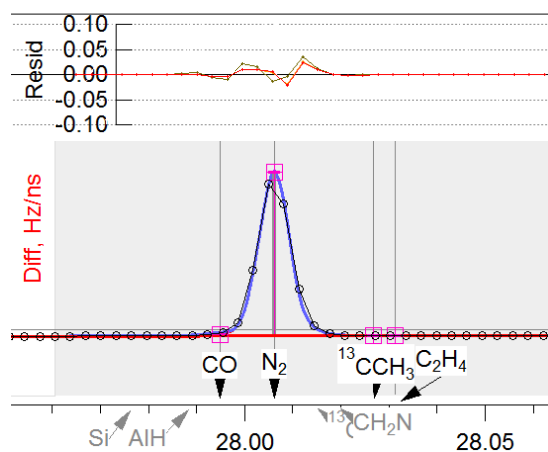


Figure 8-1: Example of peak fitting in PIKA; black circles are measured signal, the blue line is reconstructed signal based on peak width, peak shape, and fragment choices, and the red line in the upper panel is fractional residual in the difference spectrum (chopper-open minus chopper-closed spectra).

The following checklists were developed to streamline data analysis and standardize note-taking; they are based on and serve to supplement the AMS Wiki developed by the Jimenez Group at University of Colorado, Boulder, which should be consulted during data analysis: Squirrel (Low-Resolution): http://cires.colorado.edu/jimenez-group/wiki/index.php/Field_Data_Analysis_Guide; PIKA (High-Resolution): http://cires.colorado.edu/jimenez-group/wiki/index.php/High_Resolution_ToF-AMS_Analysis_Guide

Data Analysis: Squirrel

1. Click “Get Index.” Direct pathway to the HDF file folder (contains: XXX_m.hdf) and desired folder for intermediate files.
2. After indexing is done, check the m/z calibration:
 - Find fits with at least 6 species, minimizing accuracy error (less than +/- 10 ppm is ideal), chosen species should cover m/z range of data that will be used.
 - If using for HR fits: INCLUDE: CO₂⁺, SO, SO₂ (m/z 48 and 64); C₆H₅ (m/z 77), m/z 43 (C₃H₇), m/z 91 (doubly charged tungsten), and 149 (phtalate) are encouraged, but don’t include if noisy. DO NOT INCLUDE: N⁺, O⁺ (high background and multiple sources possible)
 - Use chi squared to find bad run numbers, and color the accuracy markers for species to pinpoint bad species.
 - ‘Step 4’ diagnostic: fit/logged tells how much m/z cal changed in this fit versus the original .
 - Replace bad points with interpolation if necessary (if points are outside threshold or equal nan). Log choices.
3. Check baseline integration:
 - Do V and W separately, Do V mode FIRST.
 - Stick region (pink) should encompass all of each peak.
 - Use stick complement region to adjust the baseline to underlie the whole peak with minimized residual.
 - Peak apex should lie at center of region – use mass defect table to change the center of the peak region.
 - Over m/z 300, don’t use default mass defect. (Should check and/or change <m/z300, too).
 - To find peak center: (use cursors to select from m/z x1-x2, then can ‘copy found peak to mass defect.’)
 - To change large ranges of m/z mass defects:
 - CL: “root:stickCalc:sr_massdefect[99,199] = p+1+x” (this example from m/z 100-200, where x =0.05, etc. depending on actual mass defect)
 - [199,299], x=0.1; [299,399], x=0.15, often, in datasets herein
 - Check each peak individually, special attention to: 14, 17, 18, 28, 29
 - May see W mode interference at 63 (N₂) and 72 (O₂)
 - Go back through and make sure regions used for V mode work for W mode as well. If any changes are necessary for W mode, check appropriate number of V mode runs to make sure baselines are still appropriate; iterate as necessary.
 - For one month of data, check three runs for each of : V, W, in both high and low concentration periods (~12 total)
 - Modify Single Ion Value, if the wrong value was entered during the experiment.
4. Pre-Process Data: Check:
 - ToDo: all
 - Stick MS data

- Raw MS data
 - MS m/z duty cycle
 - MS stick recalc
 - Use m/z fit params
 - Use Baseline fit params
 - CLICK “ PRE-PROCESS”
5. “Errors” Tab:
- Check: “calc MS errors”
 - Click: DO CORRECTIONS
6. “Corrections” Tab:
- Check IE/AB ratio: should be within 15% of the average value over study duration in order to apply AB corrections using ‘reference runs’ and checking ‘autoset’ for other values. Otherwise, need to uncheck ‘autoset’ and manually input a calibrated IE with corresponding AB values, etc. ToDo: all
 - AB tab: need to choose a period for AB reference right after IE calib, when AB is not varying much.
 - Can select period in diagnostic plot, R click, ‘set AB reference.’
 - PToF tab: unclick ‘apply DC markers’
 - Click: DO CORRECTIONS
7. Now it’s time for fragmentation checks. By this time, one has already:
- Done all m/z calibs, baseline, done the Pre-Process
 - Done MS Errors Corrections
 - In SQL> Checks tab > use AB correction (ToDo = allV of some kind...can use nocalib etc.)
 - Main SQL panel: Click REVIEW FRAGS
 - Tab: Checks:
 - Click CALCULATE LOADINGS FOR ALL SPECIES EXCEPT THOSE ABOVE
 - Click FRAG PLOTS PANEL

Graph: Org44 vs Org43 correlation plot with a 1:1 and a 1:2 lines for reference

- **Task for user:** Change default at frag_CO2[44] = 0.00037*1.36*1.28*1.14*frag_air[28]
- Data should go through origin (or should trend to go through the origin); users should change the ‘0.00037’ coefficient, which is [CO2(g)]; if continuous CO2(g) was measured at the inlet, that wave can be entered here (make sure it’s time-indexed to the data wave).

Graph: Org29 vs Org43 correlation plot

- **Task for user:** Change default at frag_air[29]= 0.00736*frag_air[28]
- Data should go through origin (or should trend to go through the origin); users should add a correction factor near 1 (e.g.=0.91*0.00736*frag_air[28]).

Graph: Org15 vs Org43 correlation plot

- **Task for user:** Change default at frag_air[15]= 0.00368*frag_air[14]
- Data should go through origin (or should trend to go through the origin); users should add a correction factor near 1 (e.g.=1.2*0.00368*frag_air[14]).

Graph: Frag_O16[16]: frag_NH4[17] (NH3+) vs frag_NH4[16] (NH2+) correlation plot with a 1:1.1 line

- **Task for user:** Change default at frag_O16[16]=0.353*frag_air[14] (e.g.=0.91*0.353*frag_air[14])
- Data should go through the origin (or should trend to go through the origin) for the NH₄_17 vs NH₄_16 plot and data should go through the trend of the mz16 vs mz14 plot with an intercept of zero.

A convenient way to log frag checks:

Check #	Intercept/Slope	In/Decrease Coefficient?	Frag Table Coefficient
1			
2, ...			

Other Notes:

- Measured vs predicted NH₄ gives a feeling for acidity. This may change over time. If it does, how does this explain the change in 17/16 ratio?
- SO₄ compared to PILS helps to find correct CE.

8. Making ToDo Waves for HEPA-filtered and other calibration periods

First, make ToDo waves of the HEPA-filtered regions:

- Plot a timeline of, say, org. ID relevant regions with the timeline and verify with event notes.
- Select the region in the timeline, right click, say make new, simple todo. Make Todos named, for instance, HEPA, HEPA_v, HEPA_w, and HEPA_{add}. All of these regions you select will go into 'HEPA_{add}' at first, then paste them into HEPA, or filter and put into HEPA_v or -w.
- Do this also for 'Calib' – regions of HEPA, AB, or other calibrations.
- Then one can use the procedure below to take these points out of the main run list, for a run list that contains everything EXCEPT the HEPA or Calib regions (producing NoCalib, NoHEPA wave; code from Taehyoung Lee):

```
pragma rtGlobals=1          // Use modern global access method.
Function CreateToDoWithoutFilter()
    WAVE AllV, AllW
    Duplicate/O All, NoHEPA
    Duplicate/O AllV, NoHEPAV
    Duplicate/O AllW, NoHEPAW

    WAVE HEPAAirV, HEPAAirW, HEPAAir

    Variable i
    Make/O/N=(numpnts(HEPAAirV)) pntV = nan
    pntV = BinarySearch(AllV, HEPAAirV)
    for(i=numpnts(pntV)-1; i>=0; i--=1)
        DeletePoints pntV[i], 1, NoHEPAV
    endfor
    Make/O/N=(numpnts(HEPAAirW)) pntW = nan
    pntW = BinarySearch(AllW, HEPAAirW)
    for(i=numpnts(pntW)-1; i>=0; i--=1)
        DeletePoints pntW[i], 1, NoHEPAW
    endfor
    Make/O/N=(numpnts(HEPAAir)) pnt = nan
```

```

pnt = BinarySearch(All,HEPAAir)
for(i=numpnts(pnt)-1;i>=0;i-=1)
    DeletePoints pnt[i],1,NoHEPA
endfor
KillWaves/z pntV,pntW,pnt
End

```

HR Analysis

- Select all, allV, allW
- Click PREPARE RAW DIFFERENCE SPECTRA
- Open PeakWidth/Shape panel
- Peak Width:
 - Click 2a, then 2b. After changing, click UPDATE PEAK WIDTH GRAPH to see new linear/power fits
 - Include as many points as possible while minimizing spread of points (error bars) around the (power/linear) fit lines.
 - Filter out outliers with 2c.
 - Screenshot documentation
 - After filtering and finalizing power/linear choice and fit, click DECLARE THESE PW PARAMETERS.

NOTES:

- Fragments chosen will comprise **peak shape choices**, so choose as many as possible the first time through (after seeing fits, may be able to exclude some choices).
- Widths will increase with m/z due to spread in the longer ToF flight time.
- When choosing HR ions to fit, note peak width dependence on m/z. Changing linear/power fit may resolve problems.
- Sometimes choosing ions doesn't get a great peak width. Can change the variables (a,b,c) in the linear/power fit manually.

Peak Shape:

- Click CONFIRM (ToDo) WAVE CHOICE
- Click CALC PEAK SHAPE DATA FOR...
- LEFT side: usually pick INORGANIC ions
- RIGHT side: usually pick ORGANIC ions
- Click FIND NEW PS CANDIDATE....
- Exclude ions with noisy edges, conflicting peak apexes, or peak tailing, etc. unless this reflects real signal patterns.
- Click EDIT/VIEW PW CANDIDATE to manually edit the chosen fit curve (this is very useful if L/R sides don't meet at apex, apex is skewed, or sides cannot be fit properly with ion fits).
- Final peak shape shows chosen fit (black) in comparison to a Gaussian distribution (grey).
- Screenshot documentation
- Click DECLARE PS..

- Click END

Tab: HR Ion Groups

- Usually: Click CHOOSE HR IONS TO FIT...
- However, look among other options. Can apply ions previously fit to ToDo, if made a mistake, import a table from another experiment (pop HR ions table and copy in the whole table from other experiment, make sure to delete leftover rows at the end if there were fewer ions chosen in the imported table than the default/previously chosen table from current experiment).

Tab: HR Fits One Spectra:

- Check boxes i and ii, others are optional for advanced users.
- Select whether to use a single run or averaged ToDo: Do a quick check with one run (high organics preferred), or/then make a high organics ToDo for averaged spectra check. Check a few different ToDos; if experiment/organic content changes drastically, may have to make another ToDo wave and make different fragment choices.
- Click CALC HR STICKS FOR ONE SET OF SPECTRA

A new window will pop up with raw and calculated (from PW and PS choices) signal.

- Tab: Display Tweaks: Check “Resid Axis = Ratio to Biggest”
- Other ‘Tweaks’ are optional (I always check “Show all mass tags” so I can see my ion fit choices).
- The goal: make the calculated signal (blue line) match the measured signal (black circles).
- Choose ions such that residual is minimized AND half-width rule is maintained.
- After changing ion choices, Click UPDATE MASK FOR FITTING WAVE then Click REDO FITS.
- Exclude CH₂N @ m/z 28.
- Residual (Red, top panel) should be +/- 0.05 (ratio to biggest CHECKED) for all m/z.
- Check m/z from 110 to 11 (checking from high to low prevents isotope disorganization).
- There should not be ions to the left side of m/z 48 and 64, so can use to find peak shape for left side.
- m/z 41 (C₃H₅⁺) and other fragments with a high number of Hs, should not have any ions to their right, so use for right side peak shape.
- Pay attention to trends in peak shape and width errors as you scan m/z:
- Peak Width errors that are consistent across all m/z may necessitate a PW fitting change (then redo all steps above).
- Peak Width errors that are not consistent across m/z (i.e. are present only at high m/z) may necessitate choosing a different kind of PW regression (linear or power).
- Peak Shape errors necessitate choosing new ions and iterating the intervening steps (like PW) until shape is correct.
- Even if residuals are acceptable, keep an eye toward PW and PS. Small fit improvements may be crucial to later steps such as PMF or EA.

- Look at Diagnostics 4a, b, and c.
- 4c: t-line of residuals may help you find m/z incorrectly fit, or with incorrect ions chosen.

Tab: HR fits many runs is a batch process of the previous tab.

- Select appropriate ToDo wave.
- Check “Find open and closed HR sticks also” and, if desired, “Save experiment after completion.”
- Click CALC HR STICKS. (This can take a very long time)

Useful Equations:

psl_velocity (m/s) := (0.293/psl_Ptof_time(μs))*1e6(μs/s)
 psl_Dva_aero (nm):= PSL_D_aero(nm)*1.05*1

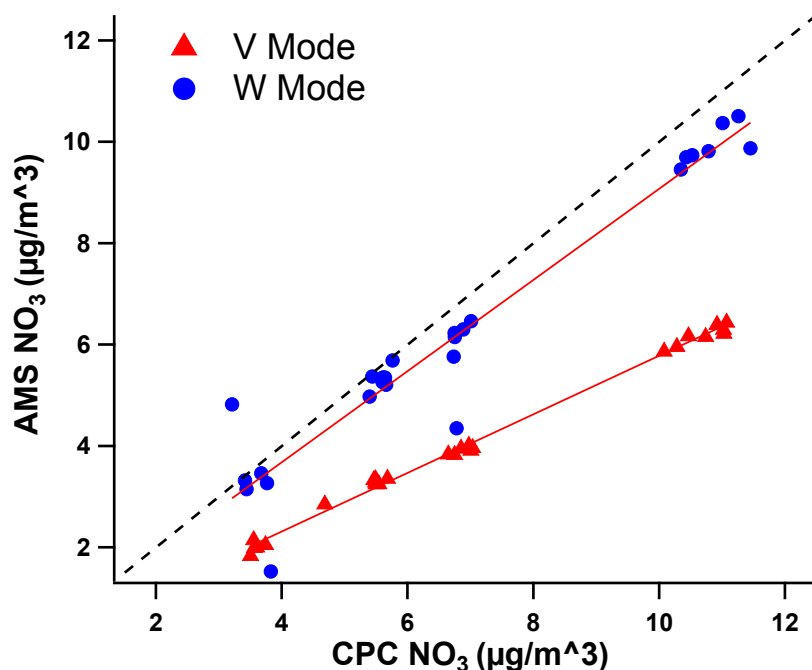


Figure 8-2: Comparison of AMS nitrate against that calculated from the condensation particle counter for 300nm ammonium nitrate particles; the slope of these relationships can be used to correct the BFSP ionization efficiency calibration. For equations, consult Section 5.2 of the AMS Wiki page administrated by the Jimenez Group at University of Colorado, Boulder: http://cires.colorado.edu/jimenez-group/wiki/index.php/Field_ToF-AMS_Operation#5.2_Data_processing_of_IE_calibration_.28for_DMA.2FCPC_data_analysis.29

8.3 Supporting ROM and TET Data Analyses

Table 8-2: Correlation coefficient and slope between ambient temperature and concentration (μg/m³) during periods with upslope (120-225 deg) and downslope (250-360 degs) winds for Rocky Mountain dataset.

r ² (slope)	LV-OOA	SV-OOA	SV+LV	BBOA
Up-Slope	0.00 (0.00)	0.00 (0.00)	0.00 (0.00)	0.00 (-0.02)
Down-Slope	0.00 (0.00)	0.02 (-0.03)	0.00 (-0.03)	0.01 (-0.02)

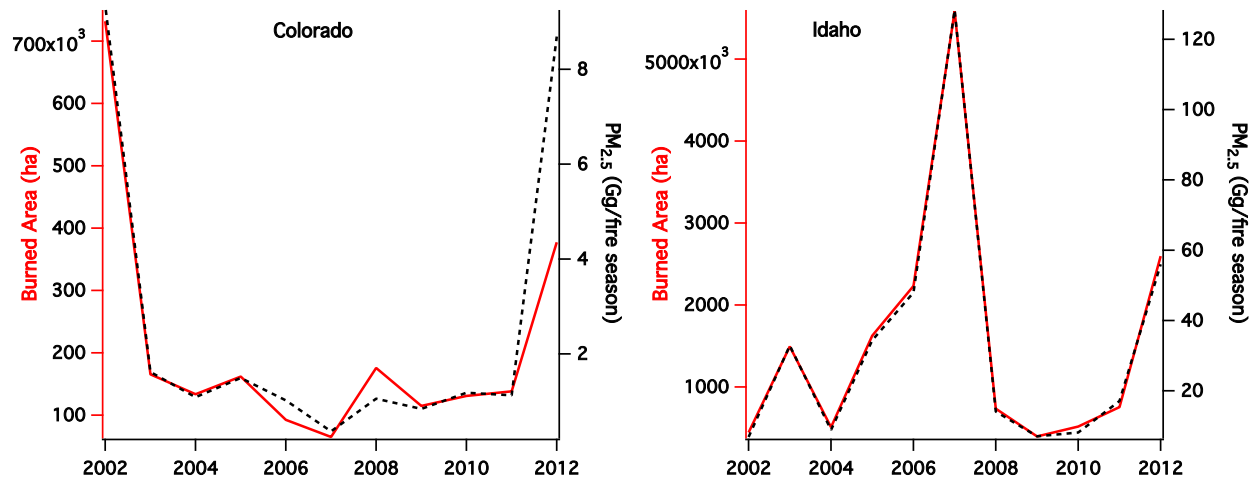


Figure 8-3: Total burned area (left axis, in red) and fire-generated carbonaceous aerosol emissions (right axis, in dashed black, in PM_{2.5} Gg/fire season) for the given state. Data courtesy Maria Val Martin from the publication Val Martin et al. 2013.

8.4 Alternate PMF Solutions

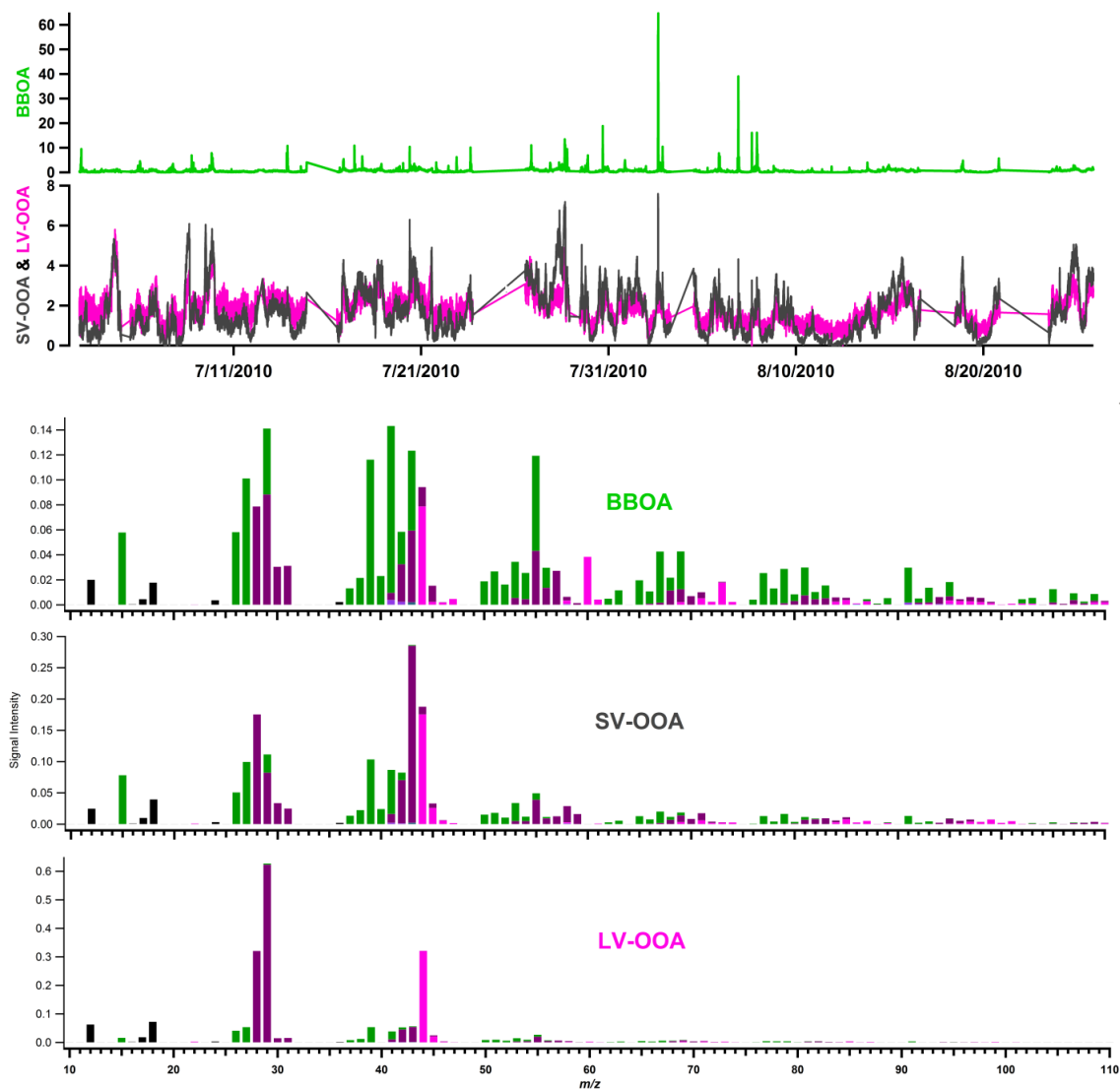


Figure 8-4: Timelines and mass spectra from PMF six-factor recombination of the Rocky Mountain dataset.

Table 8-3: Time-series correlations between inorganic species and organic factors from recombination of factors in a six-factor analysis (IGOR linear regression).

Timeline Correlation (r^2)	LVOOA	SVOOA	BBOA
SO ₄	0.43	0.29	0.02
NO ₃	0.31	0.32	0.07
NH ₄	0.49	0.34	0.03

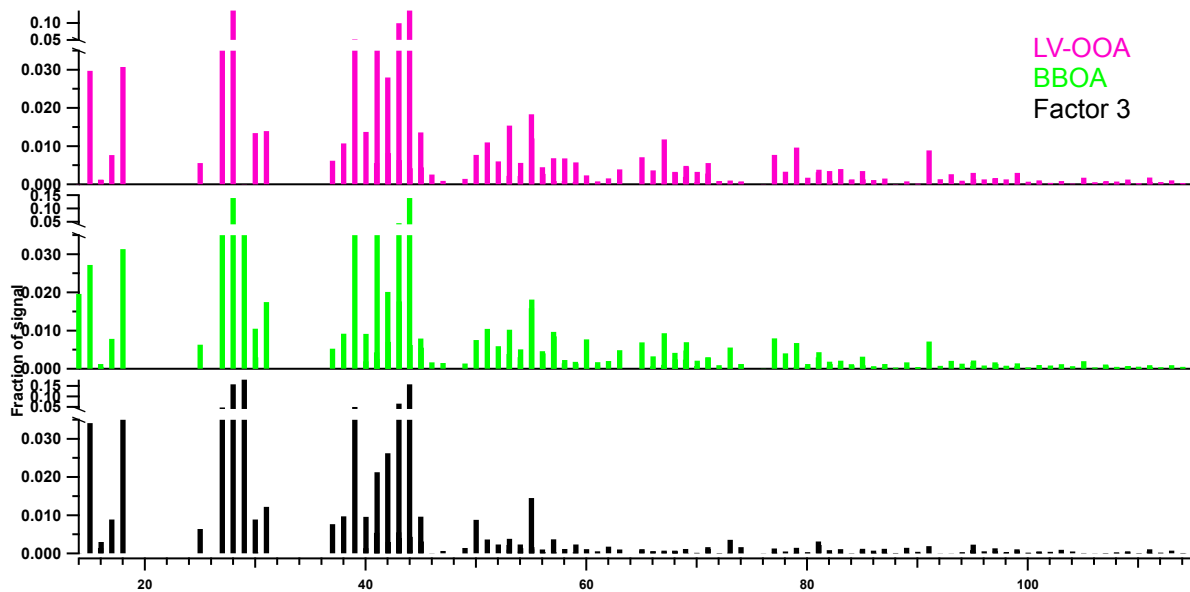


Figure 8-5: Factor mass spectra for a 3-factor PMF solution of the Grand Teton dataset. The lower portions of each split axis are on the same scale to show the lack of ‘organic wave’ patterns in the ‘Factor 3’ mass spectrum.

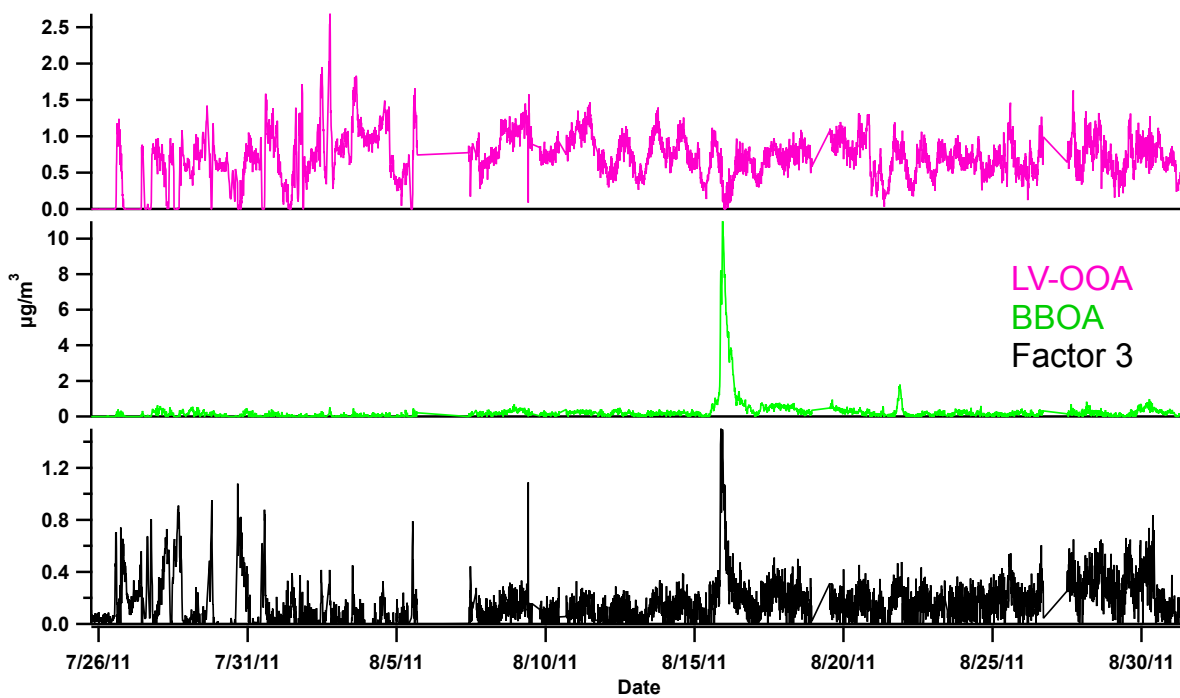


Figure 8-6: Timeline of a 3-factor PMF solution of the Grand Teton dataset.

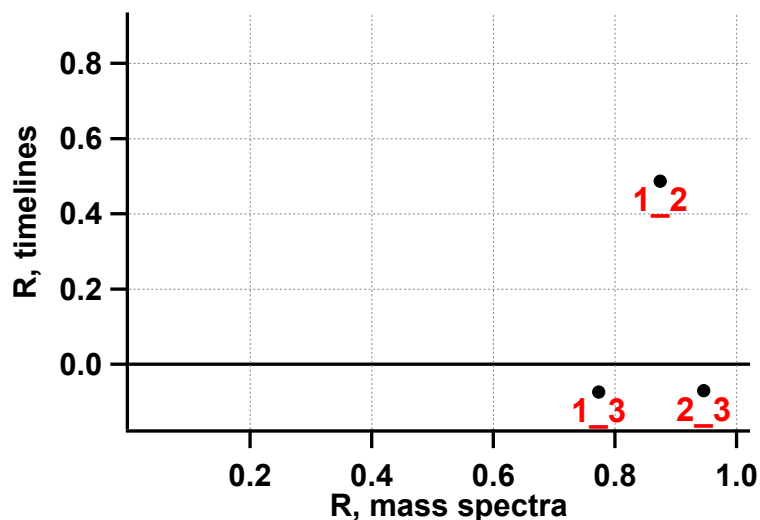


Figure 8-7: Correlation coefficients (R) between mass spectra and timelines of the indicated factor pairs, where 1 = Factor 3, 2 = BBOA, and 3 = LV-OOA, showing that Factor 3 is similar to BBOA in mass spectral profile and timeline.

8.5 Ambient Cloud Sample Concentrations of Precursors, Oxidants, etc.

Table 8-4: Analysis of each cloud water sample used herein, discussed in depth in Shen et al. (2011). The ‘Collector’ column refers to type of collector used, where C = CASCC, L = size-fractionated CASCC, large droplets ($D_p > \sim 16 \mu\text{m}$), S = size-fractionated CASCC, small droplets ($\sim 4 \mu\text{m} < D_p < \sim 16 \mu\text{m}$).

Exp. #	Sample	pH	Cl μN	NO2 μN	NO3 μN	SO4 μN	Na μN	NH4 μN	K μN
Tox1	TC062508A01	6.61	123.10	24.04	876.42	4058.18	43.42	4304.55	138.35
Tox1	TC070308A03	5.38	51.39	12.31	342.50	1811.97	22.13	2360.67	37.91
Tox1	TS061908A01	4.47	142.53	10.38	1200.29	2313.07	20.73	3587.49	171.53
Tox2	TS061808A03	3.32	154.09	4.36	970.24	1721.07	14.31	1784.93	115.27
Tox3	TL070408A09	6.37	12.48	2.41	52.22	271.27	7.48	256.62	9.39
Tox4	TC070408A13	4.74	7.45		63.57	202.43	1.58	199.83	2.60
Tox6	TC071408A01	3.70	48.90	2.14	335.75	1129.31	10.72	1133.24	13.61
Tox7	TC070808A11	4.58	40.79	2.34	375.79	884.69	8.82	1034.38	47.54
Exp. #	Sample	Mg μN	Ca μN	TC ppm	TN ppm	TIC ppm	TOC ppm	H2O2 μM	HCHO μM
Tox1	TC062508A01	26.54	465.08	29.85	92.70	9.34	20.51	6.75	8.17
Tox1	TC070308A03	17.69	177.99	28.06	51.74	10.51	17.54	79.79	5.82
Tox1	TS061908A01	16.21	108.50	24.15	84.51	2.59	21.56	0.96	8.20
Tox2	TS061808A03	6.81	34.68	30.70	48.92	6.60	24.10	1.92	27.48
Tox3	TL070408A09		11.62	4.74	6.36	1.88	2.86	94.37	3.39
Tox4	TC070408A13		8.11	2.50	5.26	0.78	1.73	9.42	2.16
Tox6	TC071408A01	22.82	100.96	7.53	28.40	1.98	5.55	50.45	11.06
Tox7	TC070808A11	8.08	79.22	8.75	28.09	2.35	6.40	29.69	21.32
Exp. #	Sample	S4 μM	Fe $\mu\text{g/L}$	Mn $\mu\text{g/L}$	Start Time		End Time		Collector

Tox1	TC062508A01	25.97	953.29	76.14	6/25/2008 23:10	7/3/2008 0:00	C
Tox1	TC070308A03	107.50	372.64	101.22	7/3/2008 23:00	7/3/2008 0:00	C
Tox1	TS061908A01	52.28	631.60	39.65	6/19/2008 19:00	6/19/2008 21:00	S
Tox2	TS061808A03	31.25	849.40	22.51	6/19/2008 0:00	6/19/2008 1:00	S
Tox3	TL070408A09	20.61	44.55	18.62	7/5/2008 10:00	7/5/2008 12:00	L
Tox4	TC070408A13	15.24	709.50	6.53	7/5/2008 17:00	7/5/2008 18:00	C
Tox6	TC071408A01	30.64	384.17	29.29	7/14/2008 18:00	7/14/2008 19:00	C
Tox7	TC070808A11	9.85	206.07	17.07	7/9/2008 0:30	7/9/2008 1:30	C

8.6 On the calculation of f_{44} and f_{43} ; Additional Data Visualizations

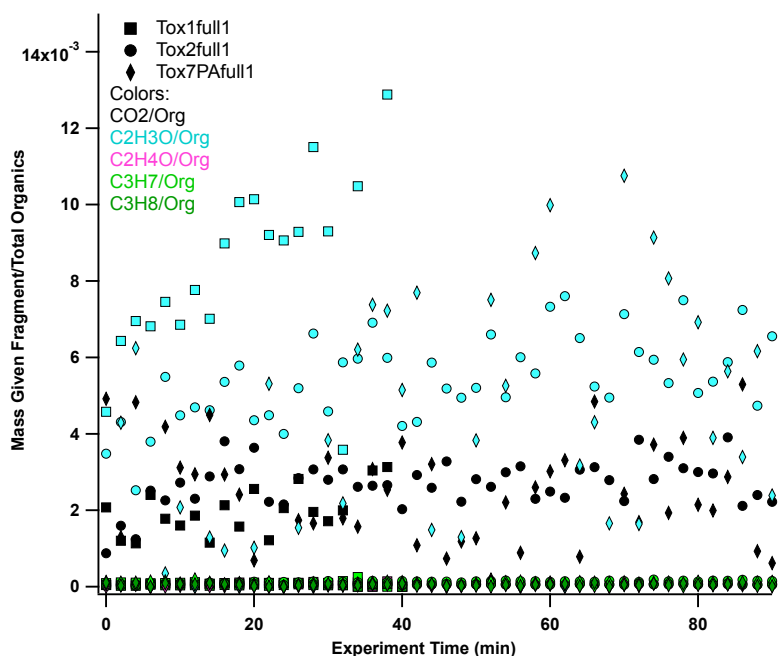


Figure 8-8: Ratios of the given fragment to total organics for TaiOx1, 2, and 7PA showing that most oxidized fragment at 43 or 44 drives progression of f_{43} or f_{44} .

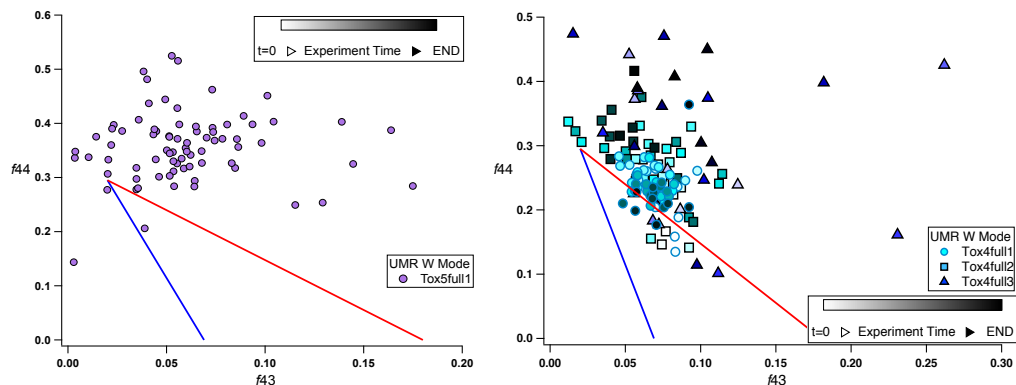


Figure 8-9: f_{43} versus f_{44} for TaiOx5 and three replicates of TaiOx4.

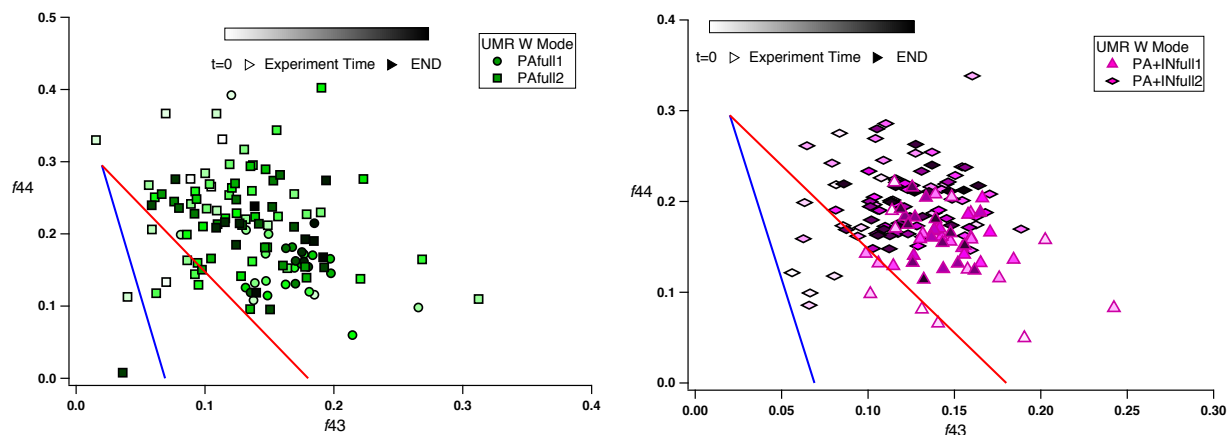


Figure 8-10: f_{43} versus f_{44} for PA and PAIN experiments.

8.7 Additional Visualizations of Aqueous Photo-oxidation Experiments

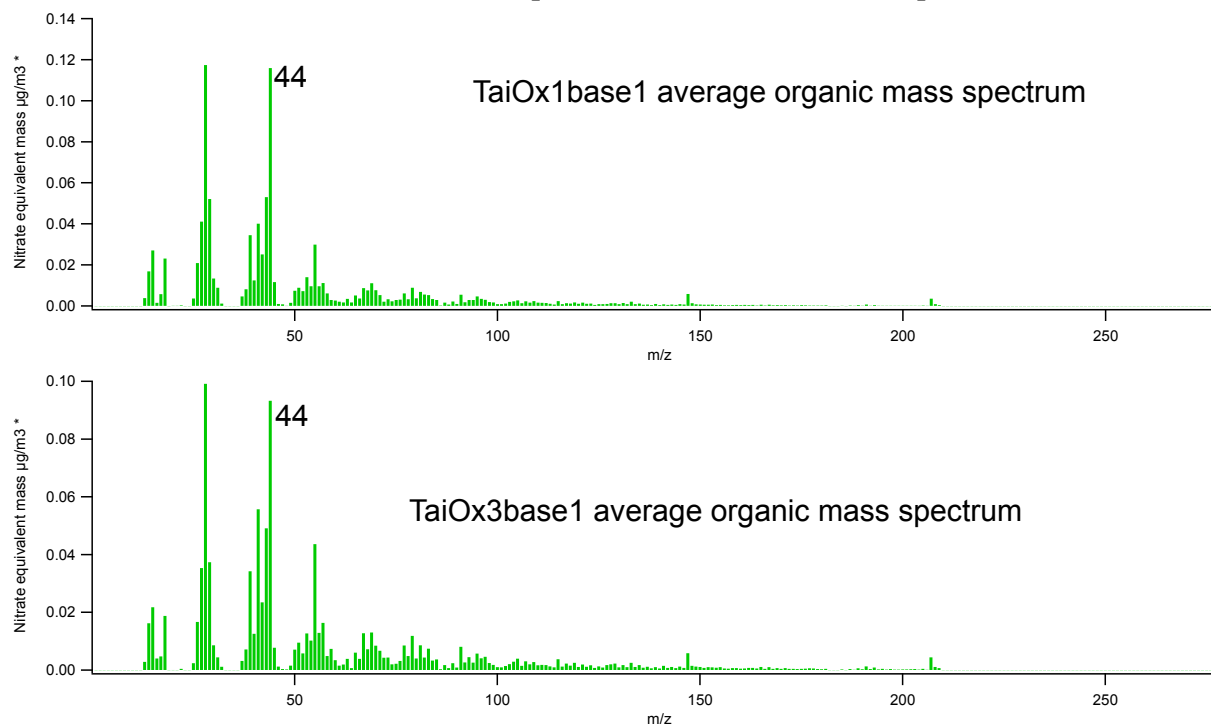


Figure 8-11: Example average total organic mass spectrum from given baseline experiment (no UV, no hydrogen peroxide) showing advanced oxidation even before photo-oxidation.

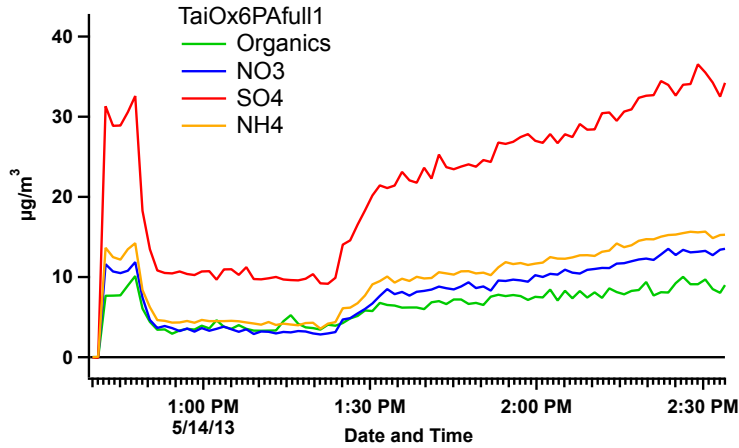


Figure 8-12: Timeline of TaiOx6PAfull1 showing variable atomizing system output.

8.8 Normalized Family Mass Spectra

Normalized average family mass spectra for $t=0-5$ minutes are included below for each experiment presented herein. The experiment number is at the top of the legend, which also contains the fraction of total mass contributed by each family.

